

# Colorimetric detection of selected gases for work and food safety applications



DISSERTATION ZUR ERLANGUNG DES DOKTORGRADES DER  
NATURWISSENSCHAFTEN (DR. RER. NAT.) DER FAKULTÄT  
CHEMIE UND PHARMAZIE DER UNIVERSITÄT REGENSBURG

vorgelegt von

**Julia Linhardt**

aus Postbauer-Heng

im Jahr 2016



Diese Doktorarbeit entstand in der Zeit von Januar 2013 bis Dezember 2015 an der Fraunhofer-Einrichtung für Mikrosysteme und Festkörper-Technologien (EMFT) in Kooperation mit dem Institut für Analytische Chemie, Chemo-und Biosensorik an der Universität Regensburg.

Die Arbeit wurde durchgeführt bei Prof. Dr. Joachim Wegner.

Promotionsgesuch eingereicht: 29. Januar 2016

Kolloquiumstermin: 18. März 2016

**Prüfungsausschuss:**

Vorsitzender: Prof. Dr. Oliver Tepner

Erstgutachter: Prof. Dr. Joachim Wegener

Zweitgutachter: Prof. Dr. Christoph Kutter

Drittprüfer: Prof. Dr. Sabine Amslinger



To Roland & my family



## Table of contents

<b>A Introduction .....</b>	<b>1</b>
<b>B Theoretical background .....</b>	<b>9</b>
1 Sensors in digital cameras.....	9
2 Multivariate analysis – Principal Component Analysis .....	12
3 Color spaces .....	17
4 References .....	21
<b>C Detection of volatile aldehydes for food safety applications .....</b>	<b>23</b>
1 Introduction .....	23
1.1 Autoxidation of fatty acids.....	25
1.2 Measuring the autoxidation state of fatty food.....	31
1.3 Hexanal as indicator substance for rancidity of fats and oils.....	37
1.4 Measuring methods for hexanal .....	40
1.5 Intelligent food packaging .....	42
1.6 Reaction mechanism of Schiff's reagent with aldehydes .....	45
2 Objective .....	47
3 Materials and Methods.....	48
3.1 Preparation of indicator particles .....	48
3.2 Preparation of measurement samples by applying PTFE as barrier .....	48
3.3 Preparation of measurement samples by immobilizing indicator particles in a polyvinyl acetate matrix.....	50
3.4 Measurement setup .....	51
3.5 Data processing .....	53
3.6 Adjustment of aldehyde concentrations.....	54
3.7 General procedure for data evaluation.....	56
4 Results and Discussion.....	61
4.1 Determination of best composition for Schiff's reagent@silica .....	61
4.2 Calibration measurements .....	63
4.2.1 Calibration with hexanal .....	64
4.2.2 Calibration with propionaldehyde.....	72
4.2.3 Calibration with acetaldehyde .....	78

4.3 Comparison of limits of detection (LOD) and sensitivities .....	84
4.4 Assessment of cross sensitivities.....	87
4.5 Investigating long-term stability of indicator particles .....	90
4.6 Immobilization of particles in a polyvinyl acetate matrix.....	92
4.7 Application to real food samples.....	96
5 Summary and conclusion .....	102
6 References.....	103

## **D Detection of carbon monoxide for work safety applications..... 109**

1 Introduction .....	109
2 Objective .....	115
3 Materials and Methods .....	116
3.1 Synthesis of indicator dyes .....	117
3.2 Sensor fabrication.....	119
3.3 Experimental setup for reflection measurements .....	120
3.4 Experimental setup for absorbance measurements .....	122
3.5 Determination of absorption coefficients .....	123
3.6 Determination of limits of detection (LOD) and sensitivity.....	124
3.7 Data evaluation.....	124
4 Results and Discussion .....	126
4.1 Photophysical properties of indicator dyes .....	126
4.2 Choice of matrix polymers .....	129
4.3 Calibration by reflection measurements (0 – 10% CO) .....	132
4.4 Calibration by absorbance measurements (0 – 100 ppm CO) .....	135
4.5 Assessment of cross sensitivities.....	138
5 Summary and conclusion .....	140
6 References.....	141

## **E Detection of ammonia for work safety applications ..... 145**

1 Introduction .....	145
1.1 Sources of ammonia and application fields for ammonia sensors.....	145
1.2 Ammonia sensing principles .....	147
1.3 Sensor systems in textiles .....	149
2 Objective .....	155
3 Materials and Methods .....	156



3.1 Dyeing with ammonia-sensitive probes.....	156
3.2 Preparation of measurement samples .....	157
3.3 Measurement setup and data processing.....	157
3.4 Adjustment of amine concentrations .....	158
3.5 General procedure for data evaluation.....	159
3.5.1 Color change evaluation of bromothymol blue dyed polyamide fabric (BTB-PA) .....	160
3.5.2 Color change evaluation of cresol red dyed polyamide fabric (CR-PA).....	161
3.5.3 Color change evaluation of methyl red dyed polyamide fabric (CR-PA).....	162
3.5.4 Determination of limits of detection (LOD) and sensitivities.....	163
3.5.5 Determination of response and reverse times .....	163
4 Results and Discussion.....	165
4.1 Calibration measurements with ammonia.....	165
4.1.1 Bromothymol blue dyed polyamide (BTB-PA) .....	165
4.1.2 Cresol red dyed polyamide (CR-PA).....	169
4.1.3 Methyl red dyed polyamide (MR-PA).....	173
4.2 Limits of detection (LOD), sensitivity, and response times.....	176
4.3 Response and reverse behavior of sensor fabrics.....	177
4.3.1 Bromothymol blue dyed polyamide.....	178
4.3.2 Cresol red dyed polyamide.....	179
4.3.3 Methyl red dyed polyamide.....	180
4.3.4 Response and reverse times .....	180
4.4 Assessment of cross sensitivities to acids.....	182
4.4.1 Bromothymol blue dyed polyamide.....	183
4.4.2 Cresol red dyed polyamide.....	185
4.4.3 Methyl red dyed polyamide.....	187
4.5 Response of sensor textiles to various amines .....	190
4.5.1 Bromothymol blue dyed polyamide.....	191
4.5.2 Cresol red dyed polyamide.....	193
4.5.3 Methyl red dyed polyamide.....	195
4.5.4 Comparison of sensor responses to various amines .....	197
4.6 Calibration of bromothymol blue dyed polyamide fabric with ethylamine, diethylamine, and triethylamine.....	199
4.7 Long-term stability of sensor textiles .....	201
5 Summary and conclusion.....	203
6 References .....	204

<b>F Summary .....</b>	<b>207</b>
1 Summary in English .....	207
2 Summary in German .....	209
 <b>G Appendix.....</b>	 <b>211</b>
1 Abbreviations and symbols.....	211
2 Regents and materials.....	215
3 Instrumentation and consumable .....	216
4 Software .....	216
5 Supplementary figures and tables.....	217
 <b>H Curriculum vitae.....</b>	 <b>247</b>
 <b>I Acknowledgements.....</b>	 <b>251</b>
 <b>J Declaration.....</b>	 <b>253</b>

## A Introduction

Detection of gases is feasible by transforming physical or chemical sensor information to electrical signals via various different methods. Physical information is provided e.g. by molecular mass, diffusion properties or the molecular structure of a gas. Chemical information in contrast includes reactivity like oxidizability or reducibility of the corresponding gas.

A general description of chemical sensors is provided by the Cambridge definition: *“Chemical sensors are miniaturized devices that can deliver real time and on-line information on the presence of specific compounds or ions in even complex samples”*.<sup>1</sup>

Figure A1 depicts the schematic setup of a chemical sensor including the analyte to be measured and a suitable sensor platform with a transducer unit. The obtained chemical information is converted into an electrical signal which correlates with the analyte concentration. As a result the present amount of analyte can be derived from the raw data via suitable signal processing methods and communicated e.g. by a visual display or an acoustic sound upon exceeding a certain threshold signal.

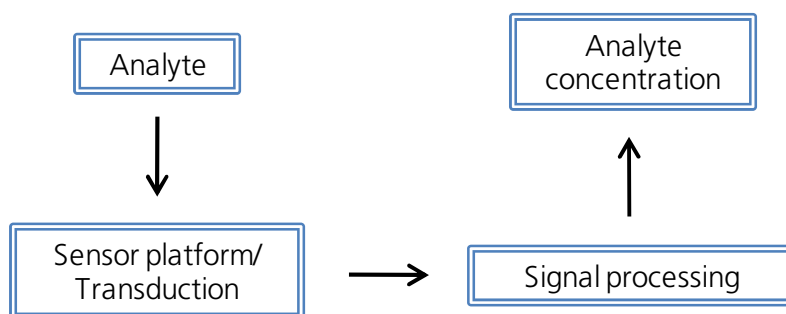


**Figure A1.** Schematic sequence of a chemical sensor setup according to Cambridge definition.<sup>1</sup>

Signal transduction can be performed via different principles. One possibility is provided by resistive methods which generally make use of conductive sensor films that change their resistance depending on the present analyte concentration.<sup>2</sup> Capacitive sensors in contrast detect the presence of gaseous analytes by induced alterations of a sensitive dielectric.<sup>3-5</sup> Potentiometric methods instead quantify the potential difference between a measuring and a reference electrode. This difference originates from the interaction of gaseous analytes with the measuring electrode while any contact to the reference electrode is avoided.<sup>6-8</sup> Another measuring principle is represented by amperometric sensors.<sup>9,10</sup> Here a current change is measured which is caused by a chemical transformation of the analyte at an electrode. While a constant voltage is applied on the electrode the current change is directly proportional to the analyte concentration.<sup>11</sup>

Additionally, gravimetric methods can be applied for signal transduction. Gravimetric sensors utilize a mass change induced by adsorbed gas molecules, for example on piezoelectric crystals which as a result exhibit modified resonance frequencies.<sup>12</sup> The optoelectronic measuring principle finally provides an example which is especially important for optical chemical sensors.<sup>13–15</sup> For this kind of sensors, optical information is transduced into electrical signals by applying visible, infrared or UV light.<sup>16,17</sup>

After signal transduction by any of the above mentioned transducer methods signal processing is performed by mathematical and statistical approaches. Thus, the electric signal is transformed to e.g. a concentration which is communicated via display.

Optical chemical sensors have been a steadily growing research area with a number of successful applications during the last decade. Advantages of optical chemical sensors are for example their low manufacturing costs and easy miniaturization. Moreover, they enable non-invasive measurements, remote and online sensing and often provide unmatched sensitivity. Furthermore, they are often non-toxic in use, easy to handle, and can be applied in hazardous environments or point-of-care diagnostics, respectively.<sup>18,19</sup>

Optical chemical sensors are mostly based on fluorescence measurements and monitor lifetime, polarization, intensity, and quenching or energy transfer processes (FRET).<sup>20–24</sup> UV/Vis absorption provides an alternative detection method for optical chemical systems.<sup>15,25–28</sup> In general, these sensors can be separated in two different categories: direct (label-free) sensors and reagent-mediated (label-based) sensing systems.<sup>1</sup>

Direct optical sensors detect the gaseous analyte by its intrinsic optical properties such as absorption or fluorescence. The absorption of IR light for example reports on the vibrational modes of a specific gas molecule and can be measured via an absorption cell which contains the corresponding analyte gas. This principle is applicable for various gases like CO<sub>2</sub>, CO, NO<sub>2</sub>, NH<sub>3</sub>, and CH<sub>4</sub>.<sup>1,29,30</sup>

In reagent-mediated systems an intermediate agent is used to monitor analyte concentrations, e.g. an analyte sensitive dye molecule. An optical response of the applied reagent can be detected upon either reversible or irreversible reaction with analyte molecules.<sup>31–35</sup> Reagent-mediated techniques are useful for analytes which do not provide sufficiently appropriate intrinsic, optical properties. A well known example for this principle is oxygen sensing which detect a change in luminescence intensity and/or lifetime of a reagent in the presence of oxygen.<sup>36–39</sup>

The indirect measuring principle requires an immobilized reagent to facilitate interaction with gaseous molecules. In recent years this was usually performed by applying solid phase

immobilization by covalent or ionic binding, or encapsulation of the reagent dye.<sup>22,40–42</sup> A wide range of sensor configurations and applications is feasible especially with immobilization matrices that can be conveniently coated onto various substrates (e.g. sol-gel glasses or polymer coatings).<sup>43</sup> Figure A2 shows the setup of sensors consisting of a reagent immobilized in a suitable matrix and coated on a solid support. After reacting with a present analyte the sensor dye changes its structural and optical properties.

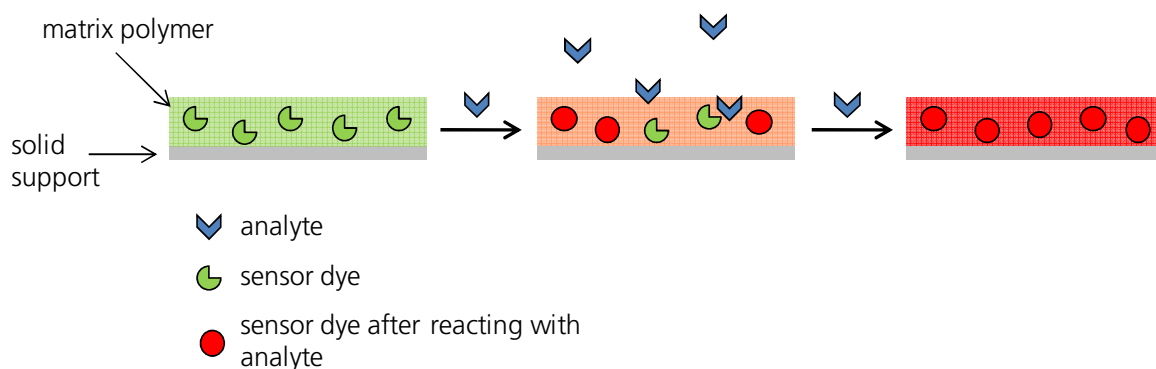


**Figure A2.** Principle of sensors consisting of reagents immobilized in e.g. polymer matrices. The optical properties of the dye are modified after reaction with an analyte.

Structural characteristics of matrix materials strongly influence reagent immobilization, stability, and permeability to the analyte.<sup>41</sup> Herein only polymer materials will be discussed, which generally have a distinct effect on the sensor performance. Response time and selectivity, for instance, are greatly dependent on the diffusion properties of the respective analyte through the matrix material.<sup>14,37</sup> Furthermore, the thickness of polymer films is generally a compromise between sensitivity and response time of the sensing system. While thicker films provide higher sensitivity, the response time of the sensor increases. Additionally, the polymer material acts as a support for the active chemical reagent (sensor dye) and can provide a protective covering. Furthermore, a certain degree of analyte selectivity can be achieved which is attributed to the structural features of the polymer material.<sup>43</sup> Possible polymeric supports include polyester, polyamide, or similar polymers used in textile fabrication.

Optical chemical sensors have already been developed for gaseous analytes such as  $O_2$ ,  $SO_2$ ,  $SH_2$ , and  $CO_2$ .<sup>22,24,37,43–47</sup> An example of a commercially available oxygen sensor, manufactured by PreSens Precision Sensing (Regensburg, Germany) sketched in Figure A3. The sensor combines several techniques which were previously explained. The oxygen sensing spots consist of a reagent immobilized in a polymer matrix which is fixed on the tip of an optical fiber. These fibers transmit light to the sensor spot and back to the analyzer indicating the local oxygen

concentration. Figure A3 shows this optical measuring principle and the sensor foil fixed on the fiber's tip. In the presence of oxygen the optical properties of the sensor foil is changed which can be detected by a modified signal transported via the fiber. <sup>48</sup> Even non-invasive oxygen sensing is possible using these sensor spots by simply applying them inside glass bottles containing any liquid samples. Thus, detection of both, dissolved and gaseous oxygen is feasible from the outside of a vessel by simply monitoring the partial pressure. <sup>49</sup>

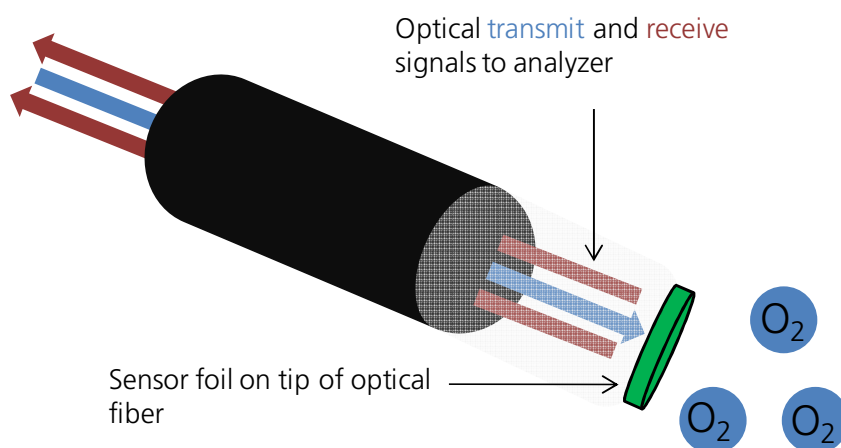


**Figure A3.** Optical measuring principle of oxygen sensing by PreSens Precision Sensing, Regensburg. <sup>48</sup>

Many of the early chemical sensor techniques were based on colorimetric methods, i.e. applying a color change of colorimetric sensor dyes in the presence of particular analytes. <sup>19</sup> A big advantage of colorimetric sensors is their visibility by the naked eye which allows a qualitative evaluation even without power consuming electronic devices. By combining them with compact, portable photometers, conversion of the analyte concentration into an electrical signal is also possible, and thus, the generation of a sensor according to the Cambridge definition. <sup>1,18</sup> The probably best-known colorimetric sensor dyes are pH-dependent dyes like bromothymol blue, cresol red, or methyl red. <sup>16,50–52</sup>

Irreversible colorimetric indicators, however, are not considered as sensors according to the Cambridge definition, as they do not show a reversible response and thus do not allow real-time monitoring of analyte concentration. As a result these irreversible indicators can only be used as single-shot probes and are restricted to applications which do not require a continuous detection of analytes. <sup>18</sup>

In the present thesis irreversible, colorimetric indicator dyes were applied e.g. for the detection of decomposition products of fat-containing foods. The indicators were directly incorporated into food packaging for detecting gaseous analytes generated by oxidation processes. For this purpose

an irreversible color change is advantageous to avoid false-negative results caused by leakage of volatile analytes from opened or resealed (e.g. for oil bottles) food packages.

Although colorimetric changes of either reversible or irreversible colorimetric indicator dyes can be detected by the naked eye, it can still be difficult to quantify the analyte concentration. For this purpose suitable video cameras, digital color analyzers, scanners or custom portable readers have already been employed.<sup>53–56</sup>

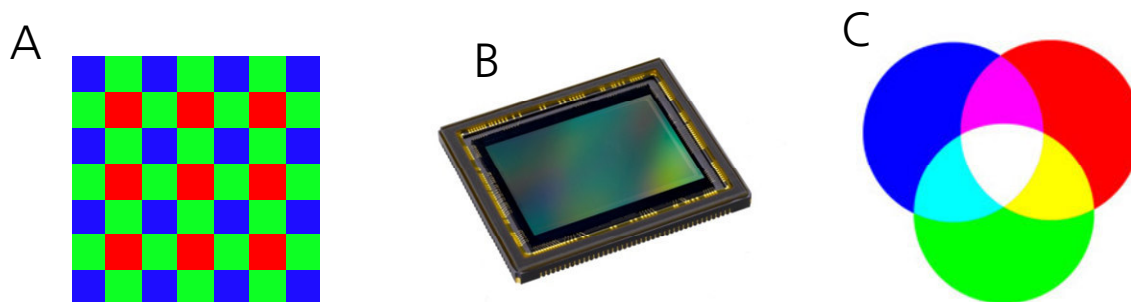


**Figure A4.** **A:** Bayer color filter; **B:** CMOS sensor;<sup>57</sup> **C:** Schematic of the additive RGB color space.<sup>58</sup>

In the present thesis digital color cameras were applied to quantify the color change of amine sensors for work safety applications and aldehyde indicators for food safety applications. In digital color cameras color filters (e.g. Bayer filter, see Figure A4, A) in combination with CCD- or CMOS camera sensors (Figure A4, B) are integrated for the generation of electrical signals.<sup>59,60</sup> The working principle of those image sensors is explained in detail in part B (chapter 1). Digital color cameras generally use the RGB color space (Figure A4, C) for image recording since the color filter consists of red, green, and blue single filters. Besides the RGB color space various other color spaces exist<sup>51,53</sup> which is intensely discussed in part B (chapter 2).

## References

- (1) McDonagh, C.; Burke, C. S.; MacCraith, B. D. *Chem. Rev.* **2008**, *108* (2), 400–422.
- (2) Chabukswar, V.; Pethkar, S.; Athawale, A. A. *Sens. Actuators, B* **2001**, *77* (3), 657–663.
- (3) Dai, C.-L.; Lu, P.-W.; Chang, C.; Liu, C.-Y. *Sensors* **2009**, *9* (12), 10158–10170.
- (4) Gu, L.; Huang, Q.-A.; Qin, M. *Sens. Actuators, B* **2004**, *99* (2-3), 491–498.
- (5) Matsuguchi, M. *J. Electrochem. Soc.* **1991**, *138* (6), 1862.
- (6) Liang, R.-N.; Song, D.-A.; Zhang, R.-M.; Qin, W. *Angew. Chem.* **2010**, *122* (14), 2610–2613.
- (7) Liang, R.; Zhang, R.; Qin, W. *Sens. Actuators, B* **2009**, *141* (2), 544–550.
- (8) Prasad, K.; Prathish, K. P.; Gladis, J. M.; Naidu, G.; Rao, T. P. *Sens. Actuators, B* **2007**, *123* (1), 65–70.
- (9) Wang G.-F., Li M.-G., Gao Y.-C., Fang B. *Sensors* **2004**, *4* (9), 147–155.
- (10) Saleh Ahammad, A. J.; Lee, J.-J.; Rahman, M. A. *Sensors* **2009**, *9* (4), 2289–2319.
- (11) Lawrence, N. S.; Davis, J.; Jiang, L.; Jones, Tim G. J.; Davies, S. N.; Compton, R. G. *Electroanalysis* **2000**, *12* (18), 1453–1460.
- (12) Pandey, S. K.; Kim, K.-H.; Tang, K.-T. *TrAC, Trends Anal. Chem.* **2012**, *32*, 87–99.
- (13) Hyakutake, T.; Taguchi, H.; Kato, J.; Nishide, H.; Watanabe, M. *Macromol. Chem. Phys.* **2009**, *210* (15), 1230–1234.
- (14) Schäferling, M. *Angew. Chem. Int. Ed. Engl.* **2012**, *51* (15), 3532–3554.
- (15) Alves, F. L.; Raimundo, I. M.; Gimenez, I. F.; Alves, O. L. *Sens. Actuators, B* **2005**, *107* (1), 47–52.
- (16) Nakamura, N.; Amao, Y. *Sens. Actuators, B* **2003**, *92* (1-2), 98–101.
- (17) Janata J.; Josowicz M.; Vanysek P.; DeVaney D.M. *Anal. Chem.* **1998**, *70* (12), 179R–208R.
- (18) Stich, M. I. J.; Fischer, L. H.; Wolfbeis, O. S. *Chem. Soc. Rev.* **2010**, *39* (8), 3102–3114.
- (19) Newman, J.; Bogue, R. *Sens. Rev.* **2007**, *27* (2), 86–90.
- (20) Hradil, J.; Davis, C.; Mongey, K.; McDonagh, C.; MacCraith, B. D. *Meas. Sci. Technol.* **2002**, *13* (10), 1552–1557.
- (21) Borisov, S. M.; Wolfbeis, O. S. *Anal. Chem.* **2006**, *78* (14), 5094–5101.
- (22) Stich, M. I. J.; Nagl, S.; Wolfbeis, O. S.; Henne, U.; Schaeferling, M. *Adv. Funct. Mater.* **2008**, *18* (9), 1399–1406.
- (23) He, C.-L.; Ren, F.-L.; Zhang, X.-B.; Han, Z.-X. *Talanta* **2006**, *70* (2), 364–369.
- (24) Razek, T. *Talanta* **1999**, *50* (3), 491–498.
- (25) McDonagh, C.; Kolle, C.; McEvoy, A. K.; Dowling, D. L.; Cafolla, A. A.; Cullen, S. J.; MacCraith, B. D. *Sens. Actuators, B* **2001**, *74* (1–3), 124–130.
- (26) Ali, R.; Lang, T.; Saleh, S. M.; Meier, R. J.; Wolfbeis, O. S. *Anal. Chem.* **2011**, *83* (8), 2846–2851.



- (27) Nakamura, N.; Amao, Y. *Anal. Bioanal. Chem.* **2003**, 376 (5), 642–646.
- (28) Zhang, C.; Bailey, D. P.; Suslick, K. S. *J. Agric. Food Chem.* **2006**, 54 (14), 4925–4931.
- (29) Timmer, B.; Olthuis, W.; van Berg, A. d. *Sens. Actuators, B* **2005**, 107 (2), 666–677.
- (30) Sazhin, S. G.; Soborover, E. I.; Tokarev, S. V. *Russ. J. Nondestr. Test.* **2003**, 39 (10), 791–806.
- (31) Kim, H. N.; Guo, Z.; Zhu, W.; Yoon, J.; Tian, H. *Chem. Soc. Rev.* **2011**, 40 (1), 79–93.
- (32) Kim, H. N.; Ren, W. X.; Kim, J. S.; Yoon, J. *Chem. Soc. Rev.* **2012**, 41 (8), 3210–3244.
- (33) Vo, E.; Zhuang, Z. *Arch. Environ. Contam. Toxicol.* **2009**, 57 (1), 185–192.
- (34) Abel, T.; Ungerböck, B.; Klimant, I.; Mayr, T. *Chem. Cent. J.* **2012**, 6 (1), 124.
- (35) Lobnik, A.; Wolfbeis, O. S. *Sens. Actuators, B* **1998**, 51 (1-3), 203–207.
- (36) Quaranta, M.; Borisov, S. M.; Klimant, I. *Bioanal. Rev.* **2012**, 4 (2-4), 115–157.
- (37) Amao, Y. *Microchim. Acta* **2003**, 143 (1), 1–12.
- (38) Borisov, S. M.; Klimant, I. *Anal. Chem.* **2007**, 79 (19), 7501–7509.
- (39) Fercher, A.; Borisov, S. M.; Zhdanov, A. V.; Klimant, I.; Papkovsky, D. B. *ACS Nano* **2011**, 5 (7), 5499–5508.
- (40) Barbe, J.-M.; Canard, G.; Brandès, S.; Guillard, R. *Chem. Eur. J.* **2007**, 13 (7), 2118–2129.
- (41) Harsányi, G. *Sens. Rev.* **2000**, 20 (2), 98–105.
- (42) Dickert, F. L. *Adv. Mater.* **1997**, 9 (9), 762.
- (43) Brook, T. E.; Narayanaswamy, R. *Sens. Actuators, B* **1998**, 51 (1-3), 77–83.
- (44) Borisov, S. M.; Waldhier, M. C.; Klimant, I.; Wolfbeis, O. S. *Chem. Mater.* **2007**, 19 (25), 6187–6194.
- (45) Hodgkinson, J.; Tatam, R. P. *Meas. Sci. Technol.* **2013**, 24 (1), 1–59.
- (46) Aydogdu, S.; Ertekin, K.; Suslu, A.; Ozdemir, M.; Celik, E.; Cocen, U. *J. Fluoresc.* **2011**, 21 (2), 607–613.
- (47) Chen, B.; Li, W.; Lv, C.; Zhao, M.; Jin, H.; Jin, H.; Du, J.; Zhang, L.; Tang, X. *Analyst* **2013**, 138 (3), 946–951.
- (48) PreSens Precision Sensing. *Oxygen Probes*. 2015 [cited: 2015 october 11]; available from: <http://www.presens.de/products/brochures/category/sensor-probes/brochure/oxygen-probes.html>.
- (49) PreSens Precision Sensing. *Non-Invasive Optical Oxygen Sensors*. 2015 [cited: 2015 october 11]; available from: <http://www.presens.de/products/brochures/category/sensor-probes/brochure/non-invasive-oxygen-sensors.html>.
- (50) McMurray, H. N. *J. Mater. Chem.* **1992**, 2 (4), 401.
- (51) Shen, L.; Hagen, J. A.; Papautsky, I. *Lab Chip* **2012**, 12 (21), 4240–4243.
- (52) Rodríguez, A. J.; Zamarreño, C. R.; Matías, I. R.; Arregui, F. J.; Cruz, R. F. D.; May-Arrioja, D. A. *Sensors* **2014**, 14 (3), 4060–4073.
- (53) Steiner, M.-S.; Meier, R. J.; Duerkop, A.; Wolfbeis, O. S. *Anal. Chem.* **2010**, 82 (20), 8402–8405.

- (54) Feng, L.; Musto, C. J.; Suslick, K. S. *J. Am. Chem. Soc.* **2010**, *132* (12), 4046–4047.
- (55) Meier, R. J.; Schreml, S.; Wang, X.-d.; Landthaler, M.; Babilas, P.; Wolfbeis, O. S. *Angew. Chem. Int. Ed.* **2011**, *50* (46), 10893–10896.
- (56) Sen, A.; Albarella, J.; Carey, J.; Kim, P.; McNamara III, W. B. *Sens. Actuators, B* **2008**, *134* (1), 234–237.
- (57) Moore M. *How does a DSLR work?* 2012 [cited: 2015 october 11]; available from: <https://martinmoorephotography.wordpress.com/2012/04/04/how-does-a-dslr-work/>.
- (58) Corel Center. *Additive Farbmischung*. 2015 [cited: 2015 october 11]; available from: <http://www.corelcenter.de/knowledgebase/farbmodelle.html>.
- (59) Marczewska, B. *Radiat. Prot. Dosim.* **2006**, *120* (1-4), 129–132.
- (60) Stich, M. I. J.; Borisov, S. M.; Henne, U.; Schäferling, M. *Sens. Actuators, B* **2009**, *139* (1), 204–207.

## B Theoretical background

### 1 Sensors in digital cameras

The color change of indicators used in this thesis is quantified by a digital color camera. Photos are taken during the reaction with diverse analytes and evaluated by splitting into the red, green, and blue color channels. In digital single lens reflex cameras (DSLR-cameras) the most commonly used sensor is the so-called CMOS (Complementary Metal-Oxide Semiconductor) sensor. Another one is CCD (Charge Coupled Device) sensor which is less often used. The difference of both sensors is simply the control and readout of the individual photosites. Figure B1 shows the schematic set-up of an image sensor as well as the working principle which are nearly identical for both sensors.<sup>1</sup>

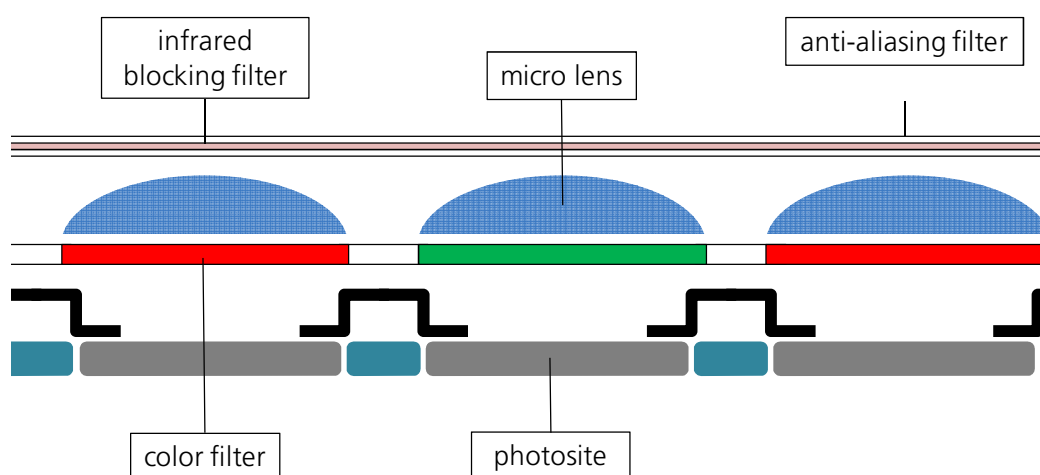


**Figure B1.** Schematic set-up of an image sensor integrated in digital color cameras.<sup>2</sup>

An object is projected onto the surface of the sensor when the camera is taking a picture. The sensor consists of numerous photosites (or photodiodes) collecting photons as long as the shutter speed allows to.<sup>3</sup> The more photons are collected by the individual photosite, the higher is the brightness of the related pixel in the picture. The light collection is supported by micro lenses which are arranged on top of each photosite and bundle the incoming light in the light-sensitive areas. Before the light is collected by these micro lenses it first has to pass two filters. The anti-aliasing filter smooths the incoming light to prevent the Moiré effect. The infrared blocking filter avoids infrared contamination of the sensor which would lead to off-color of the received images.<sup>2</sup>

In their native state image sensors are color blind and can only detect brightness values.<sup>4,5</sup> To enable color capture, color filters are placed between each photosite and the related micro lens. These color filters are arranged as array above the photosites and are red, green or blue colored. The most commonly applied color patterns derive in some way from the Bayer pattern.<sup>6</sup> Here, red, green, and blue pixels are arranged next to each other in a plain. Thus, each photosite becomes sensitive for one of the primary colors (Figure B2).<sup>2-5</sup>

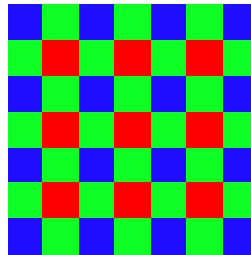


**Figure B2.** Typical Bayer pattern applied in color filter arrays. Red, green, and blue filters alternate in plain.

The human eye is most sensitive to green light, thus, twice as much green filters are arranged in the Bayer pattern as red and blue ones.<sup>5</sup> Since each photosite is only sensitive for one color, the signal processor in the camera needs to calculate the other colors. Via interpolation the missing colors are calculated based on the information received from surrounding pixels.<sup>2,5</sup> This process is also called color reconstruction or demosaicing and generates three different color channels for each pixel.

All digital pixels (picture-elements) have the same size and form. The only difference is their brightness and coloring. Since the photosites in image sensors are arranged in columns and rows, the pixels in digital pictures also have this layout. The pixel number of a photo depends on the number of photosites in the sensor of the camera.<sup>2,4</sup> Thus, the number of pixels can vary from 4288 x 2848 in amateur cameras to 7360 x 4912 (wide x height) pixels in a professional camera. An increasing density of photosites results in higher resolution of the generated picture.<sup>4</sup>

In digital cameras the image quality can be influenced by diverse camera settings. These are the ISO value, shutter speed (exposure time), and aperture size which are described in more detail below.

### **Sensor sensitivity (ISO value)**

Increasing the sensor sensitivity implies an intensification of the electrical signal which one photon produces when hitting a photosite. This becomes important at poor lighting conditions. However, an increase of the camera's gain can result into a high noise.<sup>7</sup> The adjusted sensitivity of the sensor is specified in ISO values, e.g. with ISO 800 the sensor is twice as sensitive as with ISO 400.

**Shutter speed**

The shutter regulates the time that the sensor captures incoming light (exposure time). The shutter can operate either mechanically or electrically by activating the sensor for a certain period of time. Professional DSLR cameras often hold both types whereby the mechanical one is used for longer and the electrical ones for shorter shutter speeds.<sup>2,8</sup> However, when setting the exposure time too high, motion blur can be caused by scene motion or slightly moving the camera.<sup>7</sup>

**F-Stop**

The f-Stop describes the aperture size. When opening the aperture more photons can pass in the same time as it is the case for a smaller one. Consequently, opening the aperture causes an increased brightness of the received image. The f-stops are specified in values like  $f/2$ ,  $f/4$ , or  $f/16$  with two times more light passing the aperture at  $f/2$  than  $f/4$ .<sup>8</sup> However, opening the aperture can cause a reduction in the depth of field and the aperture is highly limited by the type of lens.<sup>7</sup>

**White Balance**

White balance means the adjustment of digital cameras to different color temperatures of surrounding light. Light consists of electromagnetic radiation which includes a broad wavelength range. While in the morning ambient light includes more of the blue part, light in the evening includes more of the red part of the electromagnetic spectrum. Moreover, artificial light often consists of a very high amount of blue light. Hence, for avoiding color fault in digital images, a white balance has to be performed either by the automatic white balance function of the camera or by doing manual white balance.

## 2 Multivariate analysis - Principal Component Analysis

The Principal Component Analysis (PCA) is a method of multivariate analysis for the reduction of complex raw data. PCA is a descriptive-exploratory technique and identifies structures or relationships in large sets of variables. It separates highly correlated variables from less correlated ones which are summarized in groups, named as components. The general principle of PCA is shown in Figure B3. In this example three different objects are characterized regarding five different variables. PCA identifies a high correlation between variables 1-3 and between variables 4 and 5. Hence, these groups of variables are summarized to components 1 and 2.<sup>9,10</sup>

Additionally, the correlation of variables to components can also be shown quantitatively by calculating so-called component-values. These component-values for each variable can then be used instead of the original data and represented graphically.<sup>9</sup>

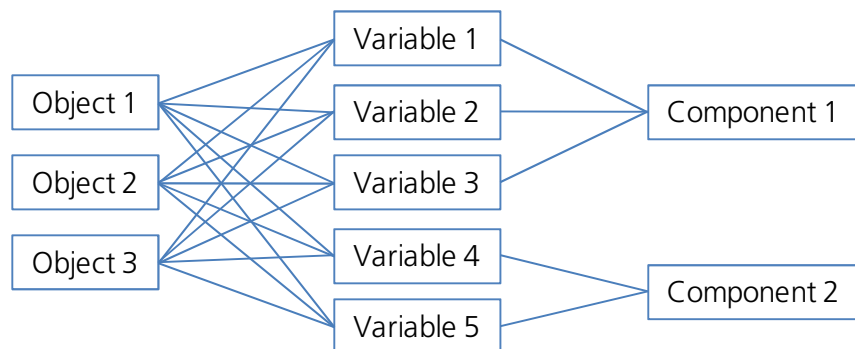


**Figure B3.** Schematic representation of principle component analysis (PCA). Correlated variables determined for diverse objects are summarized to components.

Before determining these component-values a statistical analysis needs to be applied for quantifying relations between individual variables. This relation is described by correlation coefficients easily summarized in correlation matrices. Afterwards, the number of extracted components is set by the user. Here, a compromise between data reduction and information loss needs to be found.

In general, the process of principal component analysis can be divided into four steps. These are the determination of correlation matrix, extraction of components, and the assignment of component numbers and component-values. These five steps are described more precisely in the below.<sup>9</sup>

### Determining the correlation matrix

Correlations between variables have to be quantified by calculating the so-called correlation coefficients. Equation B1 shows the determination of the correlation coefficient  $r$  between two variables  $x_1$  and  $x_2$ .<sup>9,10</sup>

$$r_{x_1, x_2} = \frac{\sum_{k=1}^K (x_{k1} - \bar{x}_1) \cdot (x_{k2} - \bar{x}_2)}{\sqrt{\sum_{k=1}^K (x_{k1} - \bar{x}_1)^2 \cdot (x_{k2} - \bar{x}_2)^2}} \quad \text{Eq. B1}$$

$x_{k1}$  and  $x_{k2}$  value of variable 1 and variable 2 of object  $k$

$\bar{x}_1$  and  $\bar{x}_2$  means of variable 1 and 2 over all objects

$r_{x_1, x_2}$  correlation coefficient of variable 1 and variable 2

By calculating all correlation coefficients for the five variables (Figure B3) a correlation matrix is generated. A typical correlation matrix for five different variables is depicted in Table B1.

**Table B1.** Typical correlation matrix for five different variables.

	Variable 1	Variable 2	Variable 3	Variable 4	Variable 5
Variable 1	1.0				
Variable 2	0.3	1.0			
Variable 3	0.3	0.7	1.0		
Variable 4	0.04	0.9	0.2	1.0	
Variable 5	0.1	0.2	0.7	0.2	1.0

Before calculating the correlation matrix, the raw data is often standardized. This means, calculating the difference between the mean of a variable and the individual variable values of a specific object  $k$ . The result is then divided by the standard deviation generated by forming the mean value (Equation B2).

$$z_{kj} = \frac{x_{kj} - \bar{x}_j}{s_j} \quad \text{Eq. B2}$$

$z_{kj}$	standardized value of variable $j$ of object $k$
$x_{kj}$	value of variable $j$ for object $k$
$\bar{x}_j$	mean of variable $j$ over all objects
$s_j$	standard deviation of the mean of variable $j$ over all objects

After the correlation matrix has been established the matrix and thus, also the original data is suitable for principal component analysis. For this proof, there are some statistical methods available such as testing significance of the correlations, the inverse of the correlation matrix, the Bartlett-test (test of sphericity), the anti-image-covariance-matrix, and the Kaiser-Meyer-Olkin-criterion. However, these statistical methods are not further explained in this context. The software used in this thesis for PCA applies one of these methods automatically, or the user can select one based on his/her own preferences. <sup>9,10</sup>

### Extraction of components

By applying the fundamental theorem of PCA components can be calculated based on the correlation matrix. The basic assumption is that each original variable  $x_j$  (or its standardized variable  $z_j$ ) can be described by a linear combination of different (hypothetic) components. The mathematical relationship is shown by Equation B3. <sup>9</sup>

$$x_{kj} = a_{j1} \cdot p_{k1} + a_{j2} \cdot p_{k2} + \dots + a_{j0} \cdot p_{k0} \quad \text{Eq. B3}$$

In Equation B3 parameters  $p$  represent the components and parameters  $a$  the loadings of the components. Thereby, the loadings describe the relationship between a component and the variables. This relationship is named the correlation coefficients between components and variables. <sup>9</sup>

The correlation matrix can also be represented by a vector diagram (Figure B4). Each vector represents a variable ( $x_1$ - $x_5$ ) and the cosine of the angle between two vectors is a measure for the correlation coefficient of these two variables. The more variables are included, the more dimensions are necessary for positioning all vectors. The aim of PCA is representing all correlation coefficients in the smallest possible dimension. Thereby, the number of necessary axes reflects the number of components. <sup>9</sup>



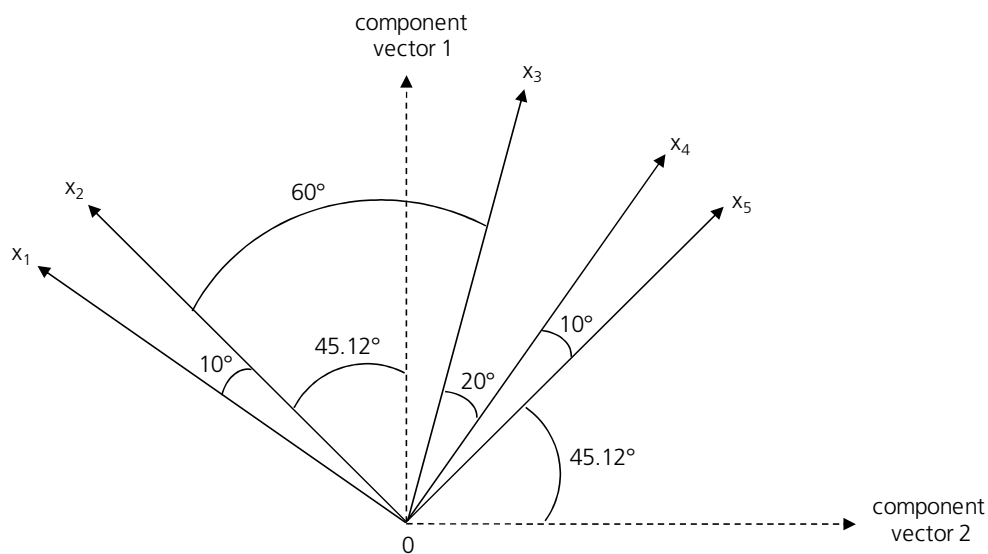


**Figure B4.** Vector diagram of five variables  $x_1$ - $x_5$  and resultant component vectors 1 and 2. Angles between the vectors represent the respective correlation coefficients.

In Figure B4 the resultante of all five vectors describes the first component. The second component which has to be independent from the first component is represented by the vector starting in the origin and being orthogonal to the vector of component 1.

Afterwards, the correlation of the variables to extracted components must be quantified. This correlation is reflected by component loadings. Those can be read out from the respective vector diagram as well since the angles between the vector of a variable and the component vector represent the respective component loading. E.g. in Figure B4, the component loading of variable  $x_2$  to component 1 is the cosine of  $45.12^\circ$ .

### Number of components

There is no unique regulation for determining the number of components, thus, the amount is regulated at the discretion of the user. However, some statistical methods can simplify the decision. The most frequently used methods are the Kaiser-Criterion and the Scree-Test whereby both procedures are very similar in its mathematical operations.

First of all, the Eigenvalues need to be calculated. The Eigenvalue of a component is the sum of the square component loadings of one component over all variables. The Kaiser-Criterion indicates that the number of components to be extracted is the same as the number of Eigenvalues with a value higher than 1. In Scree-tests all Eigenvalues are plotted in a coordinate system with decreasing value. Connecting the points a kink occurs at the point with the highest difference between two neighbored Eigenvalues. The first point left of this kink describes the number of components to be extracted.<sup>9,10</sup>

### Determination of component values

Component values need to be determined in order to quantify the correlation of objects to extracted components. The component values are calculated by complex matrix transformations which are not explained within the scope of this thesis.

The determined values can be represented graphically via a PCA bi-plot. In Figure B5 component values for two components of seven objects  $x_1$ - $x_7$  are plotted as well as the vector loadings of the original variables  $x_1$ - $x_5$ .<sup>9</sup>

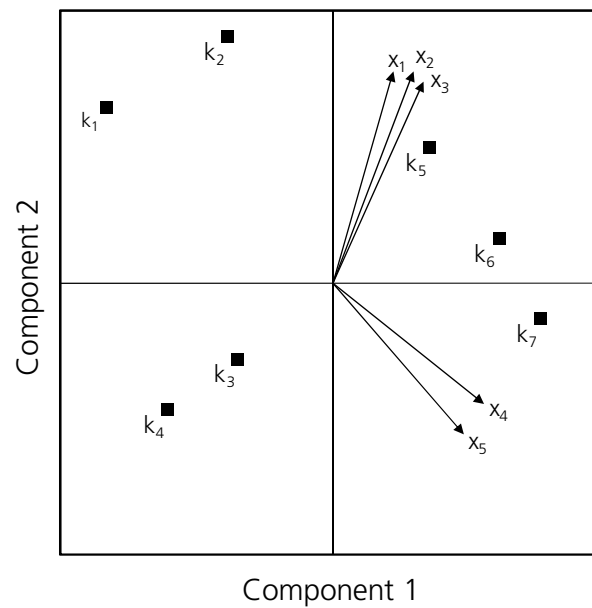


**Figure B5.** Typical PCA bi-plot showing the component values for two components of objects  $k$  and the variable vectors  $x$ .

### 3 Color spaces

A color space is a scientific way to organize colors in a three-dimensional representation. The human visual system (HVS) is able to sense a part of the electromagnetic spectrum between wavelengths of 300 and 830 nm. The HVS cannot detect all possible parts of the visible spectrum, however, is able to group various wavelength into colors. Via defined color spaces it is possible to describe different colors as perceived and processed by people, machines, and programs.<sup>11,12</sup>

A color itself is just the brains reaction to a specific stimulus. Although we can precisely describe colors by measuring its wavelength, recognizing colors by human eyes leads to redundancies since the eye is just sensitive to brightness and the three colors red, green, and blue. Thus, diverse color spaces were developed for specifying, visualizing, and describing color information.<sup>12</sup> In general, these can be categorized into three different groups.<sup>11,13</sup> The first group is formed by the color spaces based on the properties of the HVS. These are the RGB color spaces and spaces based on the opponent color theory. The second group are application specific color spaces adopted from television (TV) systems (YUV and YIQ color space), photo systems (Kodak PhotoYCC color space) and printing systems (CMYK color space). The last group includes the color spaces CIE XYZ, proposed by the International Commission on Illumination (CIE) as the first defined and device-independent color spaces.<sup>11</sup>

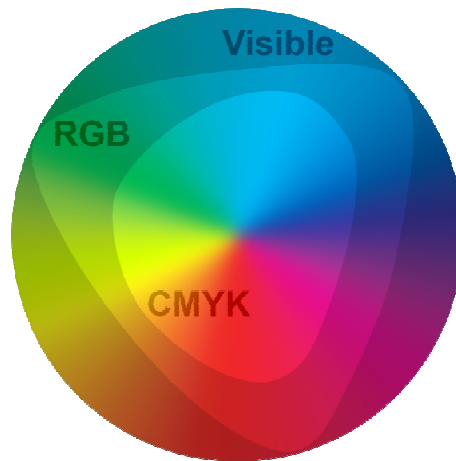


**Figure B6.** Whole color gamut of a person with normal vision (Visible). Additionally, CMYK and RGB color spaces are marked.<sup>14</sup>

The basis where photography and printing operates (RGB and CMYK color spaces) cannot reproduce the whole color gamut.<sup>12</sup> This fact is schematically represented by Figure B6. Here, CMYK and RGB color spaces are marked in the whole, visible, three-dimensional color space. The following sections describe the three groups of color spaces (HVS based, application specific, and CIE XYZ) in more detail.

### Color spaces based on the human visual system (HVS)

The main idea for the development of the RGB color space was simulating the human visual system. In the middle 19<sup>th</sup> century Maxwell, Young, and Helmholtz postulated the tri-chromatic theory. According to this theory, three types of photoreceptors are present in the HVS which are sensitive either to the red, green, or blue region of the electromagnetic spectrum. In fact, human eyes have three cones, one for long (L), middle (M), and short (S) wavelength sensitivity.<sup>11,15</sup>

Based on this, image capturing devices have an LMS-fashion light detector binning the captured light in the three components red (R), green (G), and blue (B). However, the R, G, and B values highly dependent on the individual sensitivities of the respective capturing device. Therefore, RGB is a device-dependent color space.<sup>11</sup> Furthermore, RGB is an additive color space and is mainly used throughout computer graphics as color displays usually apply red, green, and blue to create desired colors.<sup>12</sup> Additive means that colors are generated by adding specific colors, thus, a mixture of red, green, and blue with specific brightness forms the color white. Figure B7 shows the three-dimensional coordinate system of the RGB color space.<sup>13</sup>

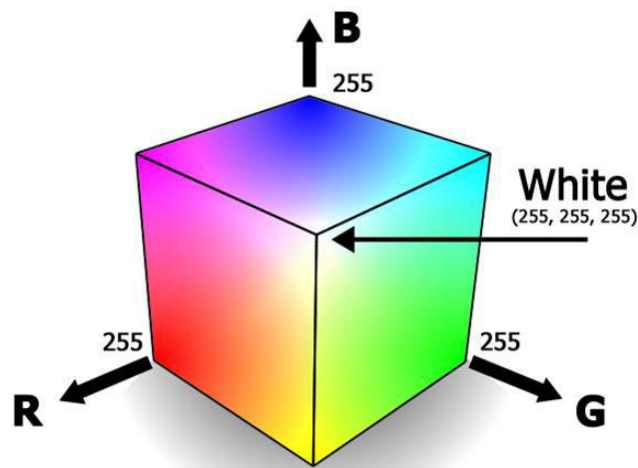


**Figure B7.** Illustration of the additive RGB color space.<sup>16</sup>

In the late 19<sup>th</sup> century Ewald Hering noted that certain hues are never used for describing colors (e.g. reddish-green, yellowish-blue). The LMS information recorded from cones in the eyes are processed by the HVS into an opponent color vector. This vector has an achromatic component (white-black) and two chromatic components (red-green) and (yellow-blue).<sup>11</sup>

Isaac Newton was the first to arrange colors in a circle called the Newton's color circle. Later Goethe and Schiffmann advanced this presentation of colors. The circle is widely used today and neglects the brightness property of colors using the attributes of hue, saturation and intensity.

This is the most natural way for humans to describe colors. Figure B8 shows the color wheel extended to 3-dimensions showing also the intensity.

In general, opponent color spaces present colors as being linear transformations of the RGB color space. Many of such HSV (hue, saturation, value) color spaces are defined in literature,<sup>11,13</sup> e.g. HSI (hue, saturation, intensity) or HCI (hue, chroma, intensity). All of them display linear transformations from RGB, thus being device-dependent as well.<sup>12</sup>

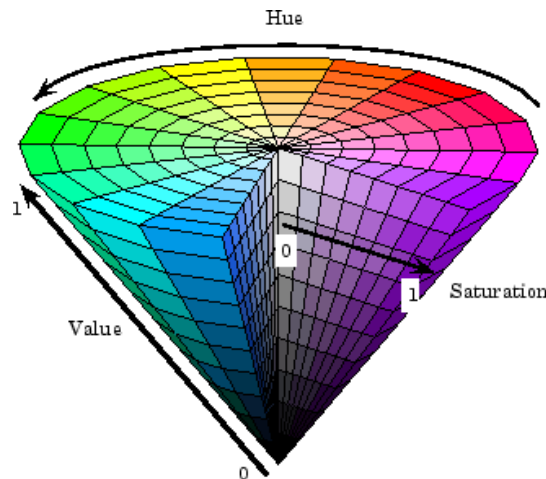


**Figure B8.** Illustration of the HSV (hue, saturation, value) color space.<sup>17</sup>

### Application-specific color spaces

For printing applications the most commonly used color space is the CMY(K) (cyan-magenta-yellow(-black)).<sup>15</sup> This is a subtractive color space (in contrast to RGB which is an additive color space) meaning the generation of colors by selectively removing a portion of the visual spectrum.<sup>11,12</sup> CMY(K) is easy to implement, however, proper transfer from RGB to CMY(K) is rather difficult.<sup>12</sup>

In television (TV) technique and computer monitors the luminescence signal was simply transmitted in early years. As the need for color TV was growing researchers developed a system encoding the RGB information in a TV-compatible system. If RGB would be used here, all three color components need to be of equal bandwidth to generate any color of the RGB color tube.<sup>13</sup> Thus, RGB wasn't used for color TV but two chrominance components were added to the luminescence signal. It is known that the human visual system is more sensitive to luminescence than to chrominance. Hence, for reducing the transfer signals size the bandwidth of the two chrominance components was reduced. In the European PAL standard RGB information was encoded in the YUV space while in American NTSC encoding was performed by calculating YIQ. In both spaces Y reflects the luminescence value. The only difference between YUV and YIQ is the

transformation process for calculating the two required chrominance components (U and V or rather I and Q).<sup>11,12</sup>

Furthermore, Eastman Kodak defined the Kodak PhotoYCC color space in 1992. Reason for this was the storage of digital color images on Photo CDs. By gamma correction, linear transformations and quantization of RGB components can be transformed into the corresponding YCC data.<sup>11,13</sup> Advantage of storing the images in separate intensity and color format, is the faster processing of images in this color space.<sup>13</sup>

### **CIE color spaces**

The International Commission on Illumination (Commission Internationale de l'Eclairage, CIE) laid down the CIE 1931 color space as the first defined relationship between colors visualized by the human eye and the electromagnetic spectrum. CIE standardized the XYZ values as tristimulus values able to describe any color that can be perceived by an average human observer.<sup>11–13,15</sup> The resulting CIE XYZ color space is device independent and is usually used as a reference color space.<sup>11</sup>

In 1976 the CIE proposed two further color spaces  $CIE_{Luv}$  and  $CIE_{Lab}$  for providing a device-independent color repetition. These color spaces show strong correlation of the euclidean distance between two colors in the  $CIE_{Luv}$  or  $CIE_{Lab}$  and the human visual perception.<sup>12</sup> The main difference between the two color spaces is implemented in the chromatic adaptation model. While  $CIE_{Lab}$  color space normalizes its values by division with the white parameters the  $CIE_{Luv}$  value is normalized by the subtraction of the white point.<sup>11</sup>

## 4 References

- (1) Popescu, A. C.; Farid, H. *IEEE Trans. Signal Process.* **2005**, *53* (10), 3948–3959.
- (2) Busch, D. D. *Digitale Spiegelreflex-Fotografie*, 3rd edn.; Wiley-VCH-Verl.: Weinheim, 2013.
- (3) Bengel, W. M. *J. Esthet. Restor. Dent.* **2003**, *15*, S21–S32.
- (4) Ratner, D.; Thomas, C. O.; Bickers, D. *J. Am. Acad. Dermatol.* **1999**, *41* (5), 749–756.
- (5) Hubel, P. M.; Liu, J.; Guttosch, R. J., Spatial Frequency Response of Color Image Sensors: Bayer Color Filters and Foveon X3. In *Electronic Imaging 2004*.
- (6) Adams, J.; Parulski, K.; Spaulding, K. *IEEE Micro* **1998**, *18* (6), 20–30.
- (7) Petschnigg, G.; Szeliski, R.; Agrawala, M.; Cohen, M.; Hoppe, H.; Toyama, K. *ACM Trans. Graph.* **2004**, *23* (3), 664.
- (8) Stevens, M.; Parraga, C. A.; Cuthill, I. C.; Partridge, J. C.; Troscianko, T. S. *Biol. J. Linn. Soc.* **2007**, *90* (2), 211–237.
- (9) Backhaus, K. *Multivariate Analysemethoden*, 13th edn.; Springer: Berlin, 2011.
- (10) Otto, M. *Chemometrie*; VCH: Weinheim, 1997.
- (11) Tkalcic, M.; Tasic, J. F., Colour spaces: perceptual, historical and applicational background. In *IEEE Region 8 EUROCON 2003*.
- (12) Ford, A.; Roberts, A. *Color Space Conversions*. 1998 [cited: 2015 october 27]; available from: <http://www.poynton.com/PDFs/coloureq.pdf>.
- (13) Jack, K. *Video demystified*, 4th edn.; Elsevier: Amsterdam, Boston, 2005.
- (14) *Showing > RGB CMCK Color Space*. 2015 [cited: 2015 october 20]; available from: <http://alfa-img.com/show/rgb-cmyk-color-space.html>.
- (15) Pascale, D. *Babel Color, A review of RGB color spaces*. 2002-2003 [cited: 2015 october 27]; available from: <http://www.babelcolor.com/download/A%20review%20of%20RGB%20color%20spaces.pdf>.
- (16) Kenneth Moreland. *Is Black a Color? - Trichromatic Theory and Color Spaces*. 2013 [cited: 2015 october 20]; available from: <http://www.drmoron.org/is-black-a-color/>.
- (17) *Convert from HSV to RGB Color Space*. 2015 [cited: 2015 october 20]; available from: <http://de.mathworks.com/help/images/convert-from-hsv-to-rgb-color-space.html>.





## C Detection of volatile aldehydes for food safety applications

### 1 Introduction

Fats and oils are among the most important ingredients in our foods. Their consumption increased significantly over the last years. While per head consumption of cooking oil in Germany was 6.6 kg in 1990, it increased to immense 11.2 kg in 2013.<sup>1</sup> The main reason for the importance of fats and oils is their impact on human physiology. They are able to deliver energy and contain crucial compounds, e.g. fat-soluble vitamins (A, D, E, K), carotenoids, and unsaturated fatty acids. Especially vegetable oils contain a high amount of unsaturated fatty acids, which are essential nutrients. During metabolism unsaturated fatty acids are integrated into the fundamental building blocks of plasma membranes, they are stored in form of triglycerides or metabolized to provide ATP.<sup>2,3</sup> Hence, unsaturated fatty acids may play a role in modulation and prevention of human diseases, e.g. coronary heart diseases, cancers of breast and colon, and rheumatoid arthritis.<sup>4,5</sup> Moreover, they are of particular importance for human development in utero and infancy.<sup>6</sup>

Vegetable oils can generally be separated into pulp and seed oils with olive and palm oil being examples for pulp oils. Sunflower and soy oil in contrast are the main representatives for seed oils. The group of seed oils also includes oils made from nuts, e.g. hazelnuts or peanuts.<sup>7,8</sup> Besides the importance of cooking oils and oil-containing food for human metabolism quality control of derived products is also a critical issue. Unsaturated fatty acids are very susceptible to oxidation which can result in the formation of harmful substances.<sup>9,10</sup> The oxidation of unsaturated fatty acids is in turn triggered by free radicals which can be generated by light, high temperature, enzymatic reactions, and heavy metal ions. Amongst other substances especially aldehydes are generated during such oxidation processes.<sup>3,11</sup> Hexanal and 2,4-decadienal for example are responsible for the typical rancid smell of deteriorated fatty food and thus for a decrease of organoleptic food properties.<sup>7,12</sup> One of the most frequent fatty acids in vegetable oils is linoleic acid. In sunflower oil the content of linoleic acid is about 62-70 wt%. Linoleic acid is a fatty acid with 18 carbon atoms and is twice unsaturated.

In general, the oxidation rate of fatty acids is enhanced with an increasing number of C-C double bonds in the molecule.<sup>7</sup> Hence, foods with a high amount of unsaturated fatty acids or

especially of linoleic acid have a reduced oxidation and storage stability. Hexanal is a major reaction product generated during oxidation of linoleic acid. The presence of high hexanal concentrations in oxidized fatty foods has been described in many publications so far.<sup>13,14</sup> Due to the good correlation between oxidation state and hexanal concentration, hexanal is often used as an indicator for the quality of vegetable oils. Moreover, hexanal has a relatively low boiling temperature of 130 °C and a high vapor pressure (13 hPa at 25 °C).<sup>15</sup> Therefore, it evaporates fast which enables a convenient detection in the gas phase of food packaging.

Monitoring the rancidity of fatty food before opening a food package is very difficult until now. Existing methods are all external and are only practicable in laboratories using special equipment. Colorimetric detection systems, however, provide a promising solution here. When oxidation products such as hexanal are present, they induce a color change of a special indicator dye which can be immobilized in the food packaging. Thus the oxidation state of fats is easily visualized by the naked eye and as a result consumers can control the food quality before purchasing a certain product.

## 1.1 Autoxidation of fatty acids

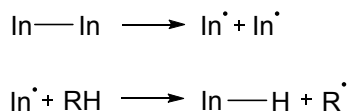
### Lipid peroxidation

The main components of vegetable oils and animal fats are triacylglycerides. Triacylglycerides contain of a glycerol backbone which is esterified by fatty acids.<sup>16</sup> In general it can be distinguished between saturated and unsaturated fatty acids.<sup>12</sup> Unsaturated fatty acids like linoleic acid contain one or more allylgroups in their acyl chain. The number of alternating allylgroups has a great effect on the oxidative fat stability as oxidation rate and induction period are highly dependent on the number of double bonds. More precisely, the relative oxidation rate becomes higher and in turn the induction period shorter with an increasing number of allyl groups.<sup>17</sup> In Table C1 relative oxidation rate and induction periods for autoxidation of stearic-, oleic-, linoleic-, and linolenic acid are shown. Linoleic acid shows a 1200 times higher relative oxidation rate than saturated stearic acid. Furthermore, the induction period decreases with an increasing number of double bonds in the alkyl chain of fatty acid. While the induction period of oleic acid is 82 h it is only 19 h for linoleic acid.

**Table C1.** Correlation between number of double bonds, oxidation rate and induction period of various fatty acids at 25 °C.<sup>7</sup>

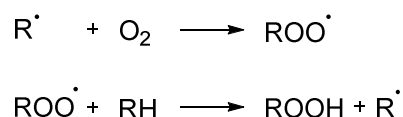
Fatty acid	Number of allyl groups	Relative oxidation rate	Induction period / h
Stearic acid - 18:0	0	1	n.d.
Oleic acid - 18:1 (9)	1	100	82
Linoleic acid - 18:2 (9, 12)	2	1200	19
Linolenic acid - 18:3 (9, 12, 15)	3	2500	1.34

Autoxidation is a spontaneous reaction of molecular, atmospheric oxygen with lipids. It is a radical chain reaction which includes the three steps initiation, propagation, and termination.<sup>3,7</sup> Formation of initiation radicals ( $\text{In}^{\bullet}$ ) is provoked by heat, irradiation, enzymatic reactions, or prooxidants like heavy metal ions (Scheme C1).  $\text{In}^{\bullet}$  can subsequently induce hydrogen abstraction from double bonds forming alkyl radicals ( $\text{R}^{\bullet}$ ).<sup>17,18</sup> The energy barrier for hydrogen abstraction is dependent on the H-atom's position in the molecule. Dissociation energy for allyl-H-atoms (e.g. in oleic acid) is 322 kJ/mol, whereas energy barrier for abstraction of biallyl-H-atoms (e.g. in linoleic acid) is only 272 kJ/mol.<sup>7,19,20</sup> Therefore, radical chain reaction is faster for linoleic acid compared to oleic acid which also implies a larger relative oxidation rate for linoleic acid in comparison to oleic acid (Table C1).



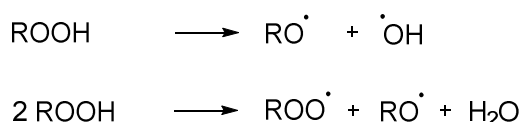
**Scheme C1.** Initiation of radical chain reaction by forming initiation radicals ( $\text{In}^\bullet$ ). By H-abstraction from alkyl chain, alkyl radicals ( $\text{R}^\bullet$ ) are generated.

After forming alkyl radicals by CH bond cleavage they further react with oxygen to generate peroxy-radicals ( $\text{ROO}^\bullet$ , Scheme C2). Peroxy-radicals can react to hydroperoxides ( $\text{ROOH}$ ) by subtraction of an allyl-hydrogen radical of an additional fatty acid (Scheme C2). As peroxy-radicals are relatively stable, generation of hydrogenperoxides is the rate limiting step of autoxidation reactions.<sup>21</sup>



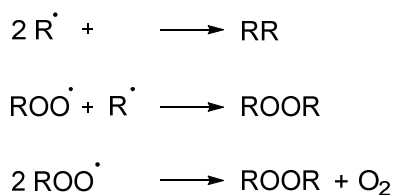
**Scheme C2.** Propagation step of radical chain reaction by generating peroxy-radicals ( $\text{ROO}^\bullet$ ) which subsequently react with unsaturated fatty acids to form hydroperoxides ( $\text{ROOH}$ ).

Along downstream reactions unstable hydrogen peroxides ( $\text{ROOH}$ ) are decomposed to alkoxy- ( $\text{RO}^\bullet$ ) and hydroxyl-radicals ( $\text{OH}^\bullet$ ). As a result lipid peroxidation is enhanced and the chain reaction is started (Scheme C3). During the reaction course hydroperoxides can accumulate and thus form dimers by hydrogen bonds. Decomposition of these dimers in turn causes the generation of a high amount of peroxy- ( $\text{ROO}^\bullet$ ) and alkoxy- ( $\text{RO}^\bullet$ ) radicals (Scheme C3).



**Scheme C3.** Decomposition of hydrogen peroxides causes a catalytically speed-up of radical chain reaction.

When oxygen is almost entirely consumed and, therefore, a high concentration of radicals is present, the probability of interaction between two radicals increase. By recombination of radicals to stable non-radical products the radical chain reaction becomes terminated (Scheme C4).<sup>18,22</sup>



**Scheme C4.** Termination of radical chain reaction by forming non-radical products via interaction of two radicals.

The hydroperoxides which are formed in the initial stage of autoxidation are non-volatile, odourless, and relatively unstable.<sup>19</sup> However, by further reaction secondary reaction products like aldehydes, ketones, or alcohols are generated. Especially the resulting carbonyl compounds have a very bad smelling and are therefore responsible for the oxidative or rancid flavor and taste.<sup>22</sup>

### Time-dependent generation of oxidation products

Autoxidation is a spontaneous process and includes an induction period which is dependent on the number of double bonds in the lipid as well as the atmospheric oxygen concentration. Furthermore, it is characteristic for the oxidation stability of fatty food. In Figure C1 a schematic time-dependent process of autoxidation is depicted. During the induction period hydroperoxides are generated and thus the oxygen uptake rate is slightly increased. After a certain period of time unstable hydroperoxides decompose to further radicals which results in an autocatalytic speeding up of the oxidation process. As a result the hydroperoxide formation rate decreases after reaching a maximum, whereby the secondary oxidation product and oxygen uptake rates both increase.<sup>22–</sup>

24

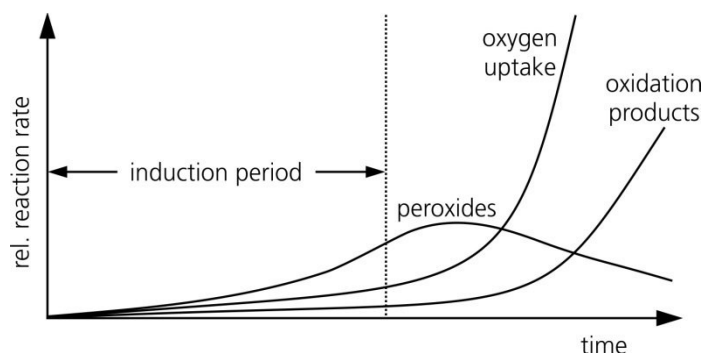
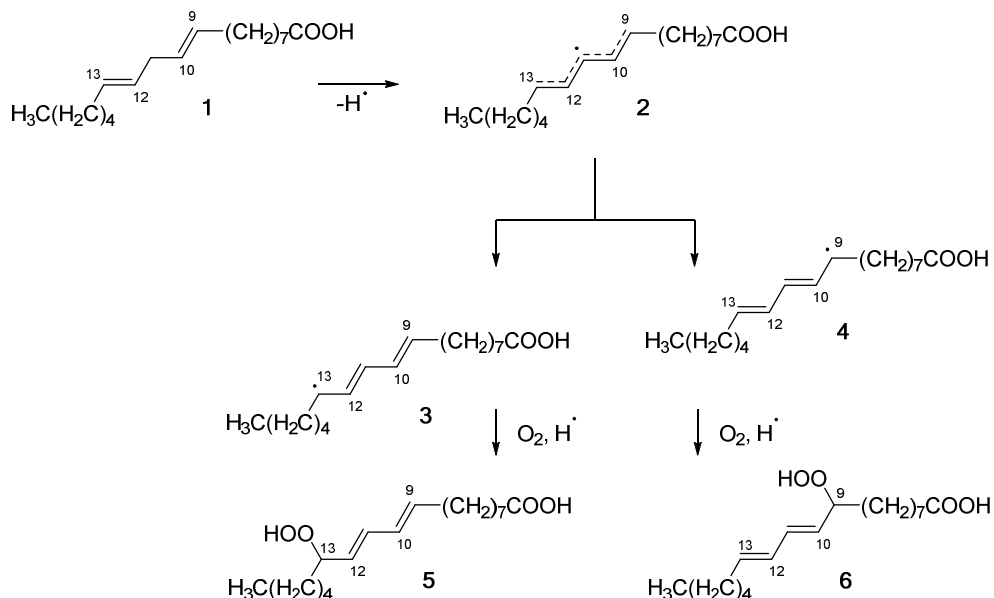


**Figure C1.** Time-dependent reaction rates of processes occurring during the autoxidation of fatty acids.<sup>25</sup>

### Autoxidation of linoleic acid

The relative oxidation rate of linoleic acid is 12 times faster than the oxidation rate of oleic acid (Table C1). This is due to the double-allylic methylen group of linoleic acid **1** at carbon atom 11 which is very reactive to hydrogen abstraction. By abstraction of an H-radical a pentadienyl radical **2** is formed which is especially stable due to resonance-stabilization over five carbon atoms (**3** and **4**). Therefore, oxygen can react with the radical positions 9 or 13 resulting in 9- and 13-

hydroperoxides **5** and **6** which both contain a conjugated diene-system (Scheme C5).<sup>9,18</sup> In addition, side reactions result also in 8-, 10-, 11-, 12-, and 14-hydroperoxides with an overall yield of 4%.<sup>7,26</sup>



**Scheme C5.** Generation of 9- and 13-hydroperoxides **5** and **6** during autoxidation of linoleic acid **1**.

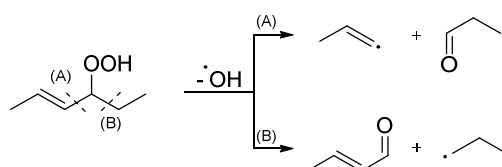
After further reaction steps secondary oxidation products are generated. Table C2 shows their corresponding concentrations after oxidizing 1 g of linoleic acid.<sup>27</sup> The main oxidation product of linoleic acid is hexanal with a concentration of 5100  $\mu\text{g/g}$ . Besides hexanal highly aroma-active compounds like 2,4-decadienal and (E)-2-nonenal were detected in high concentrations as well.<sup>7</sup>

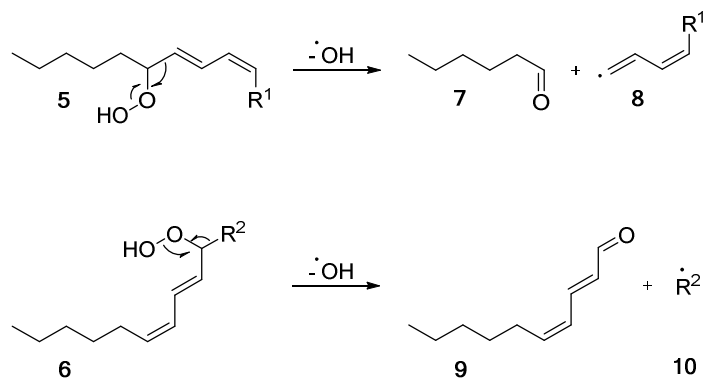
**Table C2.** Volatile compounds generated by autoxidation of 1 g linoleic acid at 20 °C up to an oxygen absorption of 0.5 mol per mol fatty acid. Values were detected using gas chromatography. <sup>7</sup>

Oxidation product	Concentration / $\mu\text{g/g}$	Oxidation product	Concentration / $\mu\text{g/g}$
Pentan	n.d.*	(Z)-3-Nonenal	30
Pentanal	55	(E)-3-Nonenal	30
Hexanal	5100	(Z)-2-Nonenal	n.d.
Heptanal	50	(E)-2-Nonenal	30
(E)-2-Heptenal	450	(Z)-2-Dezenal	20
Octenal	45	(E,E)-2,4-Nonadienal	30
1-Octen-3-on	2	(E,Z)-2,4-Decadienal	250
1-Octen-3-hydroperoxide	n.d.*	(E,E)-2,4-Decadienal	150
(Z)-2-Octenal	990	Trans-4,5-Epoxy-(E)-2-decenal	n.d.*
(E)-2-Octenal	420		

\*n.d.: not determined

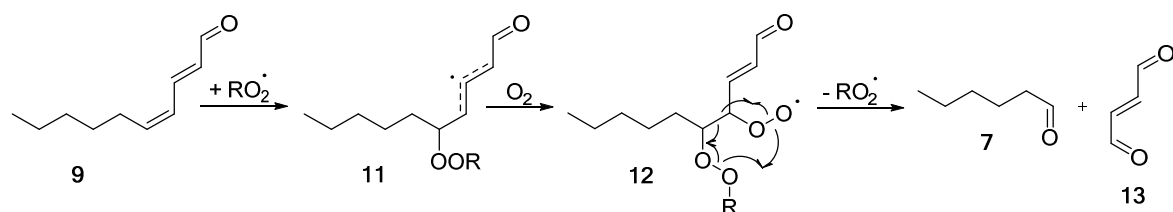
The reaction steps towards secondary oxidation products formation are shown in Schemes C6-C8. In water-free environment homolytic  $\beta$ -cleavage of monohydroperoxides is predominant. Here  $\beta$ -cleavage can take place in two different pathways A and B (Scheme C6). <sup>9</sup> Pathway A is energetically favored whereby hexanal **7** is generated from 13-hydroperoxide **5** (Scheme C7). Pathway B leads to the formation of pentan, 1-pentanol, and pentanal in this case. In contrast, 9-hydroperoxide **6** predominantly reacts to 2,4-decadienal **9** (pathway B, Scheme C8) besides 2-nonenal (pathway A). <sup>28 29 30</sup>

**Scheme C6.** Reaction pathways for the  $\beta$ -cleavage of monohydroperoxides whereby volatile secondary oxidation products are generated.



**Scheme C7.** Generation of the secondary oxidation products hexanal and 2,4-decadienal from 13- and 9-hydroperoxide.

Additionally, 2,4-decadienal **9** can be further oxidized to hexanal **7** and 2-octenal.<sup>30</sup> This proceeds by the reaction of peroxyradicals ( $\text{ROO}\cdot$ ) with **9**. Thereby, unstable 5- and 3-peroxylperoxides are generated during reaction with oxygen. 5-Peroxylperoxide **12** in turn can decomposes to hexanal whereas 3-peroxylperoxide leads to 2-octenal. The reaction pathway for hexanal formation is shown in Scheme C8.



**Scheme C8.** Reaction pathway for generation of hexanal from (E,Z)-2,4-decadienal.<sup>29</sup>

In summary the concentration of aldehydes and other oxidation products continuously increases during autoxidation of fatty acids for a certain period of time. Beyond a certain point of time, however, the concentration of aldehydes starts to decrease again due to further reaction processes like the oxidation to carboxylic acids.<sup>29,31</sup>



## 1.2 Measuring the autoxidation state of fatty food

For analyzing the oxidation state and the oxidation stability of fatty food many methods were developed in the past. In general these methods can be classified into four categories based on the measured analytes: oxygen absorption, reactant changes, formation of primary and secondary oxidation products, and free radical generation.<sup>30,32</sup> The mentioned methods are further explained in the following.

Since many fatty foods have long induction periods when stored under normal conditions, measuring the autoxidation state of fatty food would take very long. For reducing the analysis time many methods were developed speeding up the oxidation process. E.g. rise of temperature, supply of oxygen, light irradiation, and the addition of catalysts are procedures for activating or supporting the autoxidation process of fatty food.<sup>33</sup>

Commonly used testing procedures forecasting storage stabilities of foods include for example the Rancimate test which allows continuous measurement of the induction period.<sup>34</sup> Analyzing the concentration of secondary oxidation products is commonly performed by gas chromatography. Here volatile substances can be quantified by special head-space gas chromatography setups, optionally combined with mass spectrometry. Furthermore, determining of peroxide number, number of dienes, or carbonyl concentration are methods for analyzing the oxidation state of fats.<sup>9,35</sup> Additional, for food industry off-flavor detection by sensory evaluation is a crucial factor.<sup>19,36</sup>

The above mentioned methods can provide reasonable information about oxidation states but also suffer from a number of limitations. Autoxidation is a very complex process which can be influenced and changed by complex food matrices or extreme reaction conditions like sample heating for speeding up the oxidation process.<sup>28</sup> Moreover, especially the oxygen absorption rate can lead to wrong values since oxygen consumption is not only caused by fat oxidation but also by oxidation processes of proteins. This can lead to false conclusions about the oxidation state of investigated foods. Hence, for analyzing complex food samples any analysis method has to be selected quite carefully.<sup>36</sup>

### Measurement of oxygen absorption rate

The oxygen partial pressure has a direct influence on the oxidation stability of fats. Measuring the oxygen absorption rate of foods provides information about their sensitivity towards oxidation.<sup>37</sup> Furthermore, an estimation of the storage stability can be derived. During the induction period of autoxidation, no secondary reaction products can be measured yet, however, oxygen is already absorbed due to peroxides generation. As a consequence also the early period

of oxidation process becomes measurable by analyzing oxygen consumption. For a short storage stability of fats in fatty foods a fast increase in oxygen consumption is expected (Figure C2). In contrast, a better storage stability of fats leads to delayed oxygen absorption. Based on this information a comparison of shelf life for different food samples is possible.

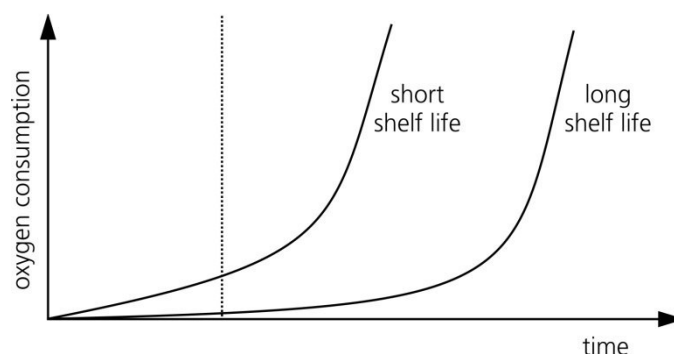


**Figure C2.** Time-depending oxygen consumption indicating the stability of fat-containing foods to oxidation. <sup>25</sup>

Oxygen absorption of an investigated fat or food sample can also be measured by mass increase due to oxygen consumption during autoxidation processes. For this purpose the oxidation can be speed up by heating the sample in an oven without air circulation. After certain time intervals the sample is cooled to room temperature and weighed whereby the obtained mass increase reflects the oxidation level of the food sample. The quite simple method can be extended to more sophisticated continuous monitoring of mass and energy changes as well by using thermogravimetry (TG) or differential scanning calorimetry (DSC).

Another method for quantifying oxygen uptakes is the headspace oxygen method which monitors the drop in oxygen pressure. For implementation a sample is placed in a closed vessel containing a certain concentration of oxygen at high temperature (usually around 100 °C). The drop of oxygen pressure is then continuously measured and recorded by an automatic detection unit (e.g. commercial Oxidograph by Mikrolab, Denmark). Pressure changes in the reaction vessel are electronically measured by pressure transducers here.

Alternatively oxygen reduction in the headspace of samples can be measured electrochemically using e.g. a Clark-electrode (galvanic sensor). The possibility of determining the oxidation process without any additional sample treatment like extraction or milling is considered as a big advantage for oxygen measurement methods.

### Measurement of reactant change

Unsaturated fatty acids are the main reactants of fat oxidation processes. As a consequence, changes in fatty acid composition provide indirect information about the stage of lipid oxidation. If necessary, lipids are extracted from food and subsequently converted into derivatives suitable for chromatographic analysis. Fatty acid methyl esters (FAME) are the derivatives most frequently used for determining fatty acid compositions and are usually quantified by gas chromatography techniques. Moreover, the iodine value can be used as an index for lipid oxidation which reflects the loss of unsaturation during oxidation processes. This method, however, is limited due to its inability of measuring the oxidation of saturated lipids.

### Measurement of primary oxidation products – peroxide value

As hydroperoxides are the main products generated during the induction period of autoxidation, the peroxide value serves as an important indicator for the oxidation stage of lipids. The peroxide value represents the total hydroperoxide content of investigated fat samples and is one of the most common quality indicators for fat production and storage. For determining the peroxide value a number of methods can be applied e.g. iodometric titration, analysis of ferric ion complexes (oxidation of  $\text{Fe}^{2+}$  to  $\text{Fe}^{3+}$ ), or infrared spectroscopy.<sup>19,38</sup> Detailed information about structure and amount of specific peroxides can be received by applying chromatographic techniques here.<sup>39</sup>

### Measurement of secondary oxidation products

Due to decomposition reactions of primary oxidation products volatile, non-volatile, and polymeric secondary oxidation products are generated. Those include aldehydes, ketones, alcohols, hydrocarbons, volatile organic acids, and epoxy compounds.<sup>27</sup> Various methods for assessing lipid oxidation are known e.g. thiobarbituric acid (TBA) test,<sup>19,39</sup> determination of *p*-anisidine value (*p*-AnV), or measurement of carbonyl compounds. For TBA tests thiobarbituric acid reacts with malonaldehyde forming a pink malonaldehyde-TBA complex with an absorption maximum at 530-535 nm. Malonaldehyde is a minor reaction product during lipid oxidation<sup>3,38</sup> and the TBA value is expressed finally as milligrams of malonaldehyde equivalents per kilogram sample. However, TBA is not very specific and sensitive<sup>30</sup> since various aldehydes react with TBA resulting in a yellow chromogen with an absorption maximum at 450 nm. This maximum overlaps with the malonaldehyde-TBA absorption band. Despite its limitations, however, the TBA test is one of the most extensively used methods for analyzing oxidative deterioration of fat-containing foods.<sup>36,40</sup>

Beside TBA test the *p*-anisidine test is often used for measuring the oxidation state of fats.<sup>3,19,38</sup> *p*-Methoxyaniline (*p*-anisidine) reacts with aldehydes under acidic conditions to give yellowish

products with an absorption maximum at 350 nm. The *p*-anisidine value (*p*-AnV) is defined as the absorbance of a solution resulting from the reaction of 1 g fat in isooxtane solution (100 mL) with *p*-anisidine reagent (0.25% in glacial acetic acid).<sup>36</sup>

Aldehydes and ketones are the major contributors to off-flavors associated with the rancidity of many fat-containing foods. Hence, analysis of total carbonyl compounds also provides useful information about the extent of lipid oxidation. For this purpose a colorimetric 2,4-dinitrophenylhydrazine procedure can be applied.<sup>41,42</sup> Here the carbonyl compounds generated during oxidation of lipids react with 2,4-dinitrophenylhydrazine (DNPH) followed by reaction of the resulting hydrazones with alkali. The products are then finally quantified by spectrophotometry.<sup>19,29,42</sup>

### Oil stability index (OSI)

During lipid oxidation volatile organic acids are formed by oxidation of alcohols and carbonyl compounds, e.g. formic and acetic acid.<sup>24,43</sup> The oil stability index (OSI) method measures the formation of volatile acids by monitoring the change in electrical conductivity. The OSI value is defined as the maximal change of oxidation rate. This method, however, requires a somewhat higher level of oxidation (peroxide value > 100) in order to obtain measurable results. The OSI method has already been automated within two commercially available instruments, the Rancimat (Metrohm Ltd., Switzerland) and the Oxidative stability instrument (Omnion Inc., USA).

The Rancimat assay enables continuous monitoring of the oxidation process and is a rapid automated measuring method. During Rancimat test the fat becomes highly oxidized due to continuous heating and high oxygen supply. Hence, primary oxidation products are generated which react further to secondary oxidation products such as formic acid. These compounds are collected in distilled water by air flow causing a conductivity increase of the solution.<sup>44</sup> The time period until the generation of carboxylic acid is generally referred to as induction period.<sup>45</sup>

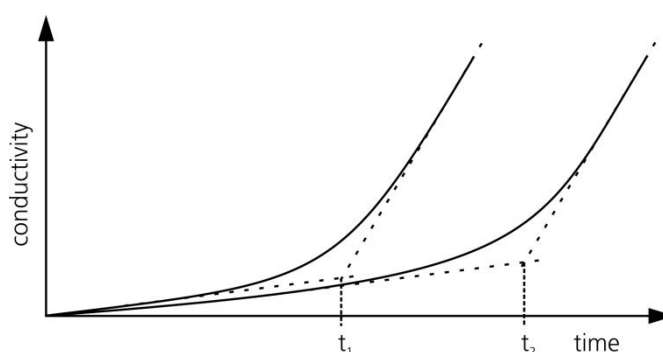


**Figure C3.** Schematic graph of a typical conductivity change during lipid oxidation. Determination of induction period can be performed applying the tangent method.<sup>35</sup>

The OSI is determined by recording conductivity as a function of time. The induction period is defined as distance between starting time and break-point of the conductivity curve here. The break-point can be identified by the tangent method in which the intersection of two tangents displays the end of induction period (Figure C3). A short induction period is represented by  $t_1$ , whereas the sample with induction period  $t_2$  shows higher oxidation stability. Oxidative Stability Instrument uses the same methods like Rancimat here. Furthermore, the volatiles collected by both methods can be further analyzed by headspace gaschromatography combined with FID (flame ionization detector) or MS (mass spectrometry) for quantifying individual volatiles.

### Measurement of free radicals

During autoxidation free radicals are present in the fat-containing sample. These radicals are short-lived intermediates which can be detected by electron spin resonance (ESR) spectroscopy. ESR is sensitive to the paramagnetic properties of unpaired electrons and measures the absorption of microwave energy when a sample is placed in the magnetic field. However, short life times and low steady-state concentration make radical detection rather difficult and limit detectable concentrations to around  $10^{-9}$  M. To overcome this problem, various approaches have been employed including pulse radiolysis, UV photolysis, continuous flow systems, and spin trapping as the most widely employed procedure. Spin trapping techniques allow the accumulation of longer-lived radicals by addition of a spin trapping agent. This agent reacts with free radicals to form more stable spin adducts. Nitroso compounds and nitrones are most commonly used spin traps, both leading to nitroxyl type spin adducts.<sup>36</sup>

### Sensory evaluation

For food industry the detection of volatile oxidation products (off-flavors) by taste or smell is the most important method for deciding about oxidation states and qualities of fat-containing products. Various methodologies have been developed for sensory evaluation of specific food products e.g. meat, peanuts, and vegetable oils. The American Oil Chemists' Society (AOCS) introduced a flavor quality scale which includes grading and flavor intensity description supporting the decision about lipid oxidation (Table C3). Descriptive analysis of a product includes detection and description of qualitative and quantitative sensory aspects and is generally performed by a trained panel, as the sensitivity to off-flavors varies strongly among different individuals.<sup>10,37,46</sup> If correctly performed, however, determining the induction period of fatty products becomes feasible.<sup>36,38</sup>

**Table C3.** Partial list of flavor- and process-related terms used to describe oxidized oil by sensory evaluation.

Flavor-related terms	Process-related terms
Buttery	Hydrogenated
Nuttery	Oxidized
Beany	Reverted
Grassy	Light-struck
Watermelon	Rancid
Painty	
Fishy	

### 1.3 Hexanal as indicator substance for rancidity of fats and oils

As already shown in Table C2 hexanal is one of the major secondary products generated during autoxidation of linoleic acid which represents a main component of natural fats. Hence, hexanal can serve as a reliable indicator of lipid oxidation in foods. A linear correlation between hexanal content, sensory scores, and TBA values was already reported.<sup>40</sup> In Table C4 linoleic acid content of some commonly consumed fat-containing food is shown.

**Table C4.** Linoleic acid content of hazelnuts, peanuts, and sunflower oil.<sup>25</sup>

	Total fat / wt%	Linoleic acid / wt%
Hazelnut	60-62	8-13
Peanut	50-55	3-27
Sunflower oil	~99.9	62-70

#### Flavor activity of volatile compounds

During lipid oxidation many volatile compounds are generated as previously demonstrated for the deterioration of linoleic acid (Table C2). Limited amounts of such volatiles are also important for the characteristic flavor of foods. In olive oil a hexanal concentration up to 0.3 mg/kg contributes to the natural flavor and, therefore, to a higher acceptance of consumers.<sup>47</sup> Beyond a certain concentration however volatile carbonyl compounds cause an oxidative false flavor and lead to a decrease of the organoleptic quality of food. Furthermore it has to be taken into account that flavor effectiveness is not just dependent on the substance concentration but also on recognition and smell thresholds.<sup>48</sup> Recognition thresholds describe the concentration being barely recognized without contributing to a clear decrease in flavor quality. Flavor thresholds in contrast are usually two to three times higher than recognition thresholds. The flavor threshold indicates the concentration being recognized by smell.<sup>7</sup> It was found that the flavor intensity of volatile compounds increases with enhanced non-saturation and is highly dependent on certain functional groups. Hence, furans, alkenes, and alcohols have a low correlation to the oxidative flavor of food since they have rather high threshold values. However, aldehydes and ketones have low flavor thresholds of about 0.002 to 2.5 mg/kg and thus a strong impact on the oxidative flavor of fatty foods.<sup>30</sup> Table 5 shows flavor thresholds for volatile substances being responsible for oxidative false flavor of food.

**Table C5.** Aroma potential of diverse aldehydes generated by peroxidation of linoleic acid.<sup>7</sup>

Aldehyde	Flavor threshold in oil / mg/kg		Odor quality
	Nasal	Retro-nasal	
Hexanal	0.32	0.075	tallow, green sheet
Heptanal	3.20	0.050	oily, fatty
2-E-Octenal	7.00	0.125	Fatty, nut-like
2-E-Nonenal	0.90	0.065	Tallow, cuke
2-E-Decenal	33.80	0.150	Tallow, orange
2,4-E,Z-Decadienal	0.18	0.040	Deep fry-aroma

Usually a combination of different components is responsible for oxidative false flavor (Table C5). Although hexanal has a non-rancid, but “green” smell<sup>27</sup> it contributes indirectly to the oxidative aroma due to its low odor threshold of about 0.3 mg/kg and its accumulation to rather high concentrations.<sup>11,30,40</sup> Moreover, it is highly volatile and can be quantified easily by headspace chromatography which greatly facilitated its use as indicator for lipid oxidation.<sup>37</sup> Ha et al. investigated hexanal as oxidative marker in vegetable oils by dynamic HS-GC/MS. Here a high correlation was demonstrated between hexanal concentrations and other markers for oxidation, e.g. acid value, peroxide number, or composition of fatty acids.<sup>13</sup> Sanches-Silva et al. determined the suitability of hexanal as indicator for the oxidation of potato chips applying GC and HPLC. With increasing storage time a loss in food quality was observed coming along with a simultaneous increase of hexanal concentration.<sup>14</sup> In comparison to hexanal 2,4-decadienal has a strong rancid flavor and is the most significant volatile substance appearing with deterioration of soy oil.<sup>28</sup> Min et al. investigated the generation of 2,4-decadienal from soy-, maize-, and cotton seed oil and found a high correlation ( $r > 0.95$ ) of 2,4-decadienal concentration and organoleptically observable rancidity.<sup>49</sup> Similar results were also demonstrated by Pokorný et al. for sunflower- and rape oil.<sup>48</sup> However, 2,4-decadienal is no suitable indicator substance since it is generated in much lower concentrations than hexanal.<sup>50</sup> 2,4-Decadienal is only produced via  $\beta$ -cleavage of 9-hydroperoxide and can afterwards be further oxidized to hexanal or other compounds (Scheme C8).<sup>29,51</sup>



### Critical value for hexanal concentration in foods

A relationship between the generation of volatile oxidation products and increasing deterioration of food has already been described in literature. For the successful development of a colorimetric detection system for the rancidity of fatty food determining the critical hexanal concentration is of fundamental importance. Rieblinger et al. have quantified the threshold for a noticeable oxidative flavor of hexanal to a concentration of 0.5 mg/kg for roasted hazelnuts <sup>25</sup> applying gaschromatographic and organoleptic analysis. Hazelnuts with a hexanal concentration beyond 1 mg/kg were classified to be highly rancid whereas for deep fried peanuts the threshold for consumer acceptance was set to 5.5 mg/kg hexanal. Hereby, hexanal concentrations were measured after 70 days of storage at 40 °C. <sup>52</sup> However, Ory et al. reported a much lower hexanal concentration of 2 mg/kg as threshold value for the noticeability of oxidative flavor by consumers. <sup>53</sup> For raw walnuts Mexis et al. have determined a hexanal threshold value of 1–2 mg/kg. <sup>54</sup> Decker et al. mentioned a hexanal concentration of 0.3 mg/kg for rape oil which was stored for 27 months and didn't show any false flavor yet. However, after additional 22 months a rancid flavor was finally detected which correlates well with an increase of hexanal concentration up to 2 mg/kg. <sup>55</sup> Azarabad et al. also analyzed sunflower oil which was stored in the fridge for four years. In fresh oil they quantified the hexanal concentration to be  $0.46 \pm 0.01$  mg/kg whereas the rancid oil exhibited  $8.9 \pm 0.1$  mg/kg. <sup>56</sup>

Based on these studies it becomes apparent that threshold values for hexanal vary strongly. It depends on many factors like the interaction with respective food matrices and changes of pressure due to temperature effects. <sup>7</sup> For this reason a correlation between hexanal concentration and perception by consumers should be determined particularly for each food product.

**Table C6.** Summary of critical hexanal concentrations for different fat-containing foods.

Food	Tolerance limit for hexanal / mg/kg
Roasted hazelnuts	0.5-1 <sup>25,52</sup>
Roasted peanuts	~2 <sup>53</sup>
Roasted peanuts	~5.5 <sup>52</sup>
Raw walnuts	1-2 <sup>54</sup>
Rape oil	~2 <sup>55</sup>

In this project published tolerance limits (summarized in Table C6) have been used for data evaluation of experiments with real food samples. For sunflower oil, however, no values have been reported so far, thus the threshold for rape oil was used due to their similar product matrices. In general, hexanal concentrations of 0.3 mg/kg are used as recognition threshold for tests on real food samples and concentrations of 1-2 mg/kg were classified to be barely recognizable but still acceptable. Additionally, hexanal concentrations above 2 mg/kg finally were assigned to clearly rancid food samples.

### **Influence of roasting processes on oxidative stability of nuts**

Often nuts are not consumed in their natural form but are roasted before. Roasting is an important process step in handling nuts, since roast flavor causes an intensification in taste. Moreover, color becomes more intensive and roasting causes a crispy texture.<sup>57</sup> During roasting processes non-enzymatic browning reactions take place. Additionally, at high temperatures enzymes become inactivated and microorganisms and allergens thus perish. Roasting profile and quality of nuts are highly dependent on the elected parameters of the roasting process. A disadvantage here is the decrease in oxidation stability which is dependent on the roasting temperature and time. For hazelnuts roasted at high temperatures an increased oxygen absorption rate and increased hexanal concentrations were measured which was correlated with a change in the hazelnut microstructure by Perren et al.<sup>58</sup> Due to the roasting process and the resulting loss in humidity the intracellular density of nuts decreases whereby extracellular pores are generated. As a result, oxygen transport into the matrix is faster and oxidation stability is lowered. By applying lower roasting temperatures these pore systems can be conserved.

## **1.4 Measuring methods for hexanal**

Free hexanal can easily be quantified by using common techniques like gas chromatography or NIR spectroscopy. However, these methods usually assume a complete volatilization of hexanal which is unlikely in real food samples. The "release" of hexanal can be hindered e.g. by covalent or non-covalent binding with the food matrices why this issue has to be addressed in the process of data evaluation. Haugen et al. performed investigations towards the rancidity of frozen turkey hen meat using gas-sensor arrays based on semiconductor metal oxides. They received a high correlation ( $r > 0.9$ ) between sensor signals and reference measurements like organoleptic tests and the generation rate of secondary oxidation products.<sup>59</sup> Additionally, Vinaixa et al. were able to distinguish between potato chips with different grade of rancidity. Their method, however, achieved only a success rate of 68% compared to measurements done by mass spectrometry.<sup>60</sup> Park et al. developed a biosensor which was claimed to be specific for hexanal. It consists of a chip with immobilized carbon-nanovesicles which carry a specific hexanal-receptor on their

surface. Hexanal binding induces a calcium flux into the vesicles and as a result a change in conductivity can be observed. Using this sensor it was possible to detect hexanal in milk directly without prior sample preparation. Sensor fabrication, however, is very expensive and time-consuming here. Therefore, a successful scale-up towards industrial application in the food packaging is rather unlikely.<sup>61</sup> Goodridge et al. instead developed a competitive indirect enzyme-linked immunosorbent assay (CI-ELISA) for monitoring lipid oxidation through quantification of hexanal-protein adducts. They compared their results with GC/MS-SPME and TBA test and found satisfactory correlations.<sup>62</sup> A general problem of such biosensors, however, remains the sensitivity for environmental conditions like temperature, humidity, and mechanical stress.<sup>63</sup>

Besides electronic noses or biosensors, colorimetric detection systems are suitable methods for measuring secondary oxidation products. Colorimetric detection systems generally consist of an indicator dye which changes its optical properties (absorbance) by reacting with a specific analyte like in this case hexanal or other aldehydes which are present in the headspace of food packaging. Mohr et al. showed a diazo-based indicator dye for the detection of aldehydes. The dye was immobilized in a polyvinylchloride (PVC) layer and used for the detection of formaldehyde.<sup>64</sup> Moreover, Vo et al. developed an indicator pad for aldehydes based on the indicator dye methyl red. Here the dye solution was applied on a cellulose pad and the color change was measured using a spectral photometer. The indicator pad showed a significant color change from yellow to red in the presence of 0.5  $\mu\text{L}$  of a 1% glutaraldehyde solution. A requirement for the reaction is the acidic  $\alpha$ -hydrogen atom of the carboxylic group of methyl red. Similar to glutaraldehyde, hexanal can also react with such pH-sensitive dye. For non-aliphatic aldehydes, however, the indicator was found to possess a low sensitivity.<sup>65</sup> Pararosaniline presents another indicator dye for aldehydes and was immobilized together with sulfuric acid or phosphoric acid in porous glass material by Maruo et al. Their indicator system showed a color change from yellow/orange to violet when formaldehyde is present in the gas phase. The reaction is reversible and a formaldehyde concentration between 10 ppb and 20 ppm has been measured successfully.<sup>66</sup>

## 1.5 Intelligent food packaging

Fat-containing foods are often exposed to oxidative conditions due to incorrect storage or damaged food packaging. This can result in shortened shelf life and premature loss in quality which in turn is usually not discovered until the product has been purchased by end-consumers. As a result consumers currently can estimate the quality of packed food only by best-before dates. These, however, just indicate the period in which the food is consumable at correct storage conditions.<sup>67</sup> Damaged packages, false transport- and storage conditions during trading, or wrong storage at home are not taken into account here. That means in all of these cases food can become deteriorated much earlier than it is indicated by the presented best-before date which is, however, often impossible to detect without opening the package. On the other hand foods are often still eatable at the end of best-before date but still disposed due to legal regulations or simple customer uncertainty. To avoid such kind of food wasting, fast and effective monitoring-systems are necessary for estimating food quality. Intelligent packaging could greatly contribute to this purpose when integrated sensors give additional and detailed information about food quality.<sup>63</sup> As a result intelligent and active packaging already mark a rapidly increasing sector in today's industry<sup>68</sup> with an expected increase in global sales from 31.4 billion \$ in 2011 up to 44.3 billion \$ in 2017.<sup>69</sup> This trend is also reflected by a rising number of national and international research projects and scientific publications. The number of publications about intelligent packaging raised from 22 in 2006 to 103 in 2014.

### Freshness and gas indicators

Deterioration of food can be caused by microbial, enzymatic, chemical, and physical effects. Therefore, the freshness of food can be evaluated on the basis of microbial growth, presence of degradation products, or product-specific metabolites.<sup>68</sup> Volatile oxidation products can for example be identified by gas detector systems based on indicator dyes changing their color in the presence of these substances.<sup>68</sup> Such colorimetric detectors can be integrated into food packaging for example and are willingly used in industry as they can be easily noticed and interpreted by consumers.<sup>70</sup> Freshness and gas indicator systems developed so far are able to indicate the presence of volatiles such as carbon dioxide,<sup>71–73</sup> oxygen,<sup>74–77</sup> sulfur dioxide,<sup>78–80</sup> amines including ammonia,<sup>81–86</sup> or hydrogen sulfide.<sup>87–89</sup> During deterioration of fish for example biogenic amines are formed primarily by microbial degradation. Kuswandi et al. successfully detected such amines using polyaniline (PANI) films. These films display a color change from green to blue with increasing amine concentration in the gas phase.<sup>90</sup> Applying calix[4]arene based indicator dyes, di- and trimethylamines could be detected in fish as well.<sup>91</sup> During deterioration of poultry instead hydrogen sulfide is formed which could also be detected in the headspace of food packaging. Through immobilization of myoglobin on agarose gel Smolander et al. developed a

colorimetric hydrogen sulfide indicator. Using this indicator they were able to detect the microbial and sensory quality of stored poultry samples.<sup>92</sup>

Many indicators for food quality control are already developed for their application on the market, e.g. Fresh Code®, Fresh Check®, or Ageless Eye®. Fresh Code® is based on a barcode indicating the storage time. More precisely, with proceeding time the barcode fades away and indicates the storage time to run off when it is not visible at all. Fresh Check® is a colorimetric time-temperature indicator which shows a time-depending color change. This change is faster at enhanced temperatures and FreshCheck® is therefore able to give qualitative information about storage conditions of the food. Additional, Ageless Eye® oxygen indicators are small tablets indicating the presence of oxygen by a color change. This colorimetric indicator system can be integrated into a food packaging containing anoxic atmosphere and thus indicates by a color change from pink to blue when oxygen got access.

All these indicators, however, are not able to directly detect deterioration products of foods. Thus they don't give information about the real food quality but only about storage time and temperatures. Since these factors are independent from food condition the food can still be eatable despite pasts its sell-by date. Hence, indication systems are required for deterioration products of foods and thus for directly displaying the quality of foods. Until now no colorimetric indicators are commercially available for signaling volatile deterioration products of fat-containing food and no aldehyde sensor materials for food safety control applications are known in literature.<sup>66</sup>

As previously discussed, many analytical methods are present for measuring the oxidation state and stability of fatty foods. They are partially very precise, selective, and also able to quantify oxidation products.<sup>36</sup> However, many of these analytical methods are expensive, time consuming, or include complex sample preparation. Moreover, usual food packaging has to be destroyed before analyzing the oxidation state of packed foods.<sup>63</sup> Thus intelligent packaging solutions are desirable making use of integrated sensors or detection systems for non-invasive visualization of the oxidation state. The presence of specific substances can be optically monitored via color change by applying indicators directly into the food package. Using integrated indicators instead of complex invasive methods or sensor systems, immediate and clear information about actual product freshness can be obtained without sample preparation or use of power-consuming electronic components.<sup>63</sup>

### Requirements and design criteria for aldehyde-indicators

By integration of indicators into food packaging the indicator system is in direct contact with the respective food. Thus, the indicator system needs to consist of components that are compatible with food, which are non-toxic, and water insoluble. Specific requirements for intelligent packaging are defined in regulation 1935/2004/EC<sup>93</sup> and 450/2009/EC.<sup>94</sup> Moreover, an indicator for rancidity needs to provide clear information without employing complex analysis or special equipment. This can be achieved by a simple color change of the indicator if exposed to a defined concentration of quality-indicating analyte. For this all reaction products of oxidative food degradation need to be quantified in order to avoid false-positive response by other aldehydes or substances. Furthermore, an irreversible indicator reaction is preferred here to avoid false-negative results caused by opened or resealed (e.g. for oil bottles) food packages from which already formed hexanal may have escaped. Another important requirement is the storage stability of such colorimetric indicators. They have to be stable at special storage and atmospheric conditions in the packaging, i.e. against temperature fluctuations, direct light exposure, and mechanical stress. For fat-containing foods the critical parameters are low humidity, damage by volatile product-specific substances, and interaction with inert gases in the packaging.

The production of new intelligent packaging provides a number of challenges as well: technical feasibility, stability of the packaging, scale-up of production, and especially production costs. The immobilization of indicator dyes needs to be simple which can be realized e.g. by direct integration in the polymer material. Other possibilities are varnishing or using diverse printing techniques. Recent research focuses on techniques for printing chemical sensors in packaging materials.<sup>63</sup> Alternatively the indicator could also be implemented by using sachets or labels. The inner protection layer film also plays an important role as it has to guarantee migration stability of the indicator dye, but at the same time be permeable for the volatile analytes. For a successful commercial launch cost-effectiveness is particularly important (< 1 cent per cm<sup>2</sup>). Thus, the indicator must not increase the overall costs of the package significantly. Finally the production process of the intelligent packaging materials must provide the ability for easy scale up with conventional well-established methods.<sup>95,96</sup>

## 1.6 Reaction mechanism of Schiff's reagent with aldehydes

In 1866 Hugo Schiff first observed the discoloration of Fuchsin by sulfuric acid.<sup>97</sup> This observation provided what is known today as Schiff's reagent, an indicator for aldehydes by color change from colorless to magenta.<sup>98,99</sup> By adding sodium sulfite to a red colored pararosaniline hydrochloride aqueous solution **14** can be converted to Schiff's reagent **15** (Figure C4). The sulfite attacks at the central  $sp^2$  carbon atom of pararosaniline hydrochloride which causes a break in the conjugated  $\pi$ -system and therefore a discoloration of the solution.

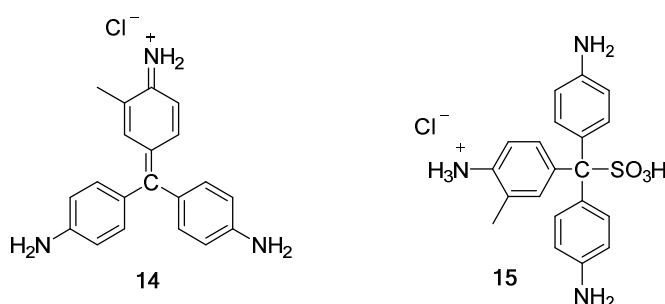
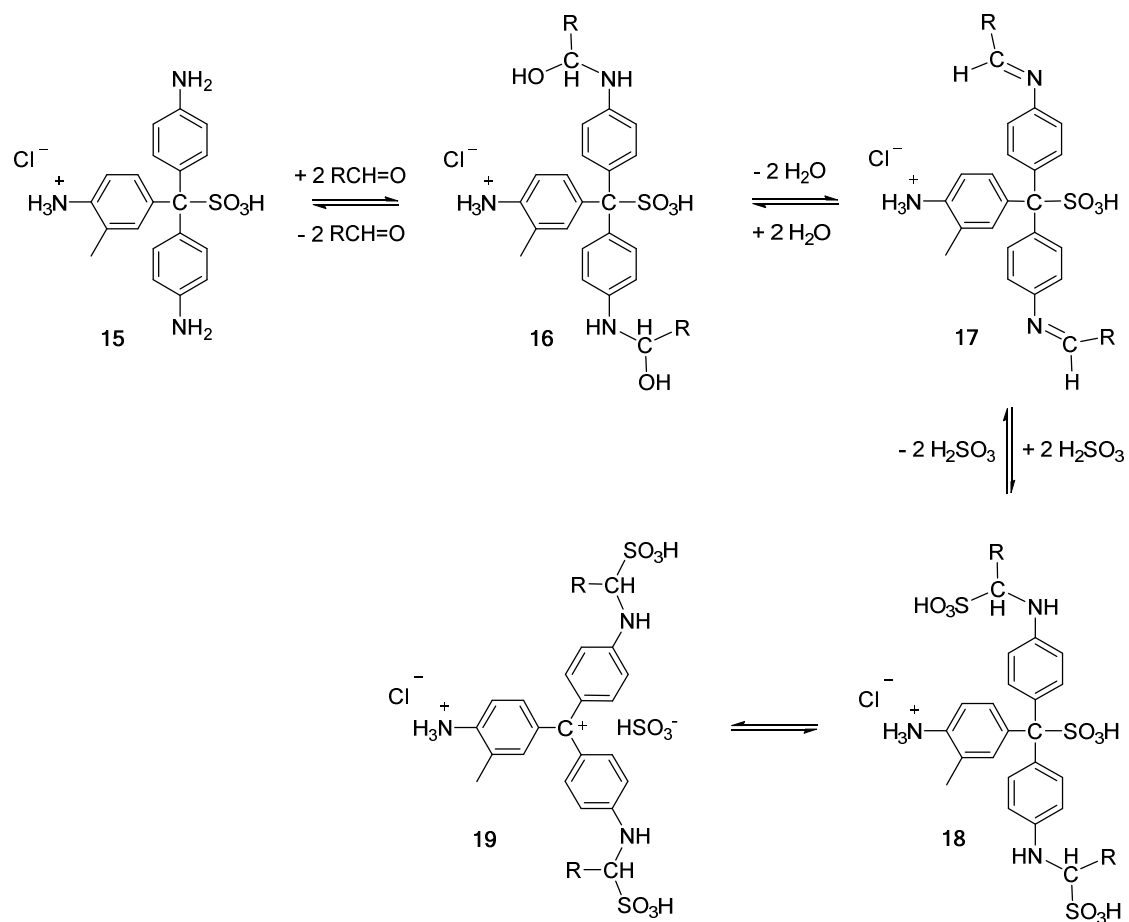


**Figure C4.** Pararosaniline hydrochloride **14** and Schiff's reagent **15**.

Several research groups suggested the presence of different molecular species after reaction of Schiff's reagent with aldehydes.<sup>100</sup> In 1979 Pincock et. al. performed NMR studies on the reaction of Schiff's reagent with acetaldehyde. They concluded that at low aldehyde concentrations complexes of acetaldehyde and Schiff's reagent with a stoichiometry of 1:1 and 2:1 are formed. For higher aldehyde concentrations they postulated an increase of the 2:1 complex at the cost of the 1:1. The reaction mechanism for the 2:1 complex in water is shown in Scheme C9. One equivalent of Schiff's reagent **15** here reacts with two equivalents of aldehyde to form the imine **17** via a carbinolamine intermediate although the equilibrium constant for imine formation from aromatic amines in water is very small.

This is the reason why an excess of sulfurous acid is required to shift the equilibrium towards **18**. This in turn reduces the concentration of sulfurous acid in solution finally enabling the formation of **19** (Scheme C9). As a result sulfurous acid concentration is a rather critical parameter since more than one equivalent is required for the reaction, but significantly higher concentrations also have a negative impact on the final equilibrium.<sup>101</sup>



**Scheme C9.** Reaction mechanism of Schiff's reagent **15** with aldehydes to form a complex of 2:1 stoichiometry.



## 2 Objective

Aim of this project was the development of a colorimetric detection system for food safety applications. For this, an indicator dye was to be implemented into food packaging in order to visualize the oxidation processes of fat-containing food without opening the package. The presence of hexanal in the packaging atmosphere induces a visible color change of this indicator and enables consumers to obtain information about the actual food quality.

A well-known indicator dye for aldehydes is Schiff's reagent which reacts with aldehydes forming a magenta-colored product in the presence of sulfuric acid. This indicator substance was to be immobilized on a suitable solid support and characterized regarding its response towards aldehydes, long-term stability, and cross sensitivities. For this purpose a suitable measurement setup had to be designed and data evaluation methods had to be developed and validated. Additionally integration of the indicator in food packaging models had to be performed for final testing with real food samples. This part was performed in collaboration with Fraunhofer IVV, Freising. Figure C gives an overview of the whole project.

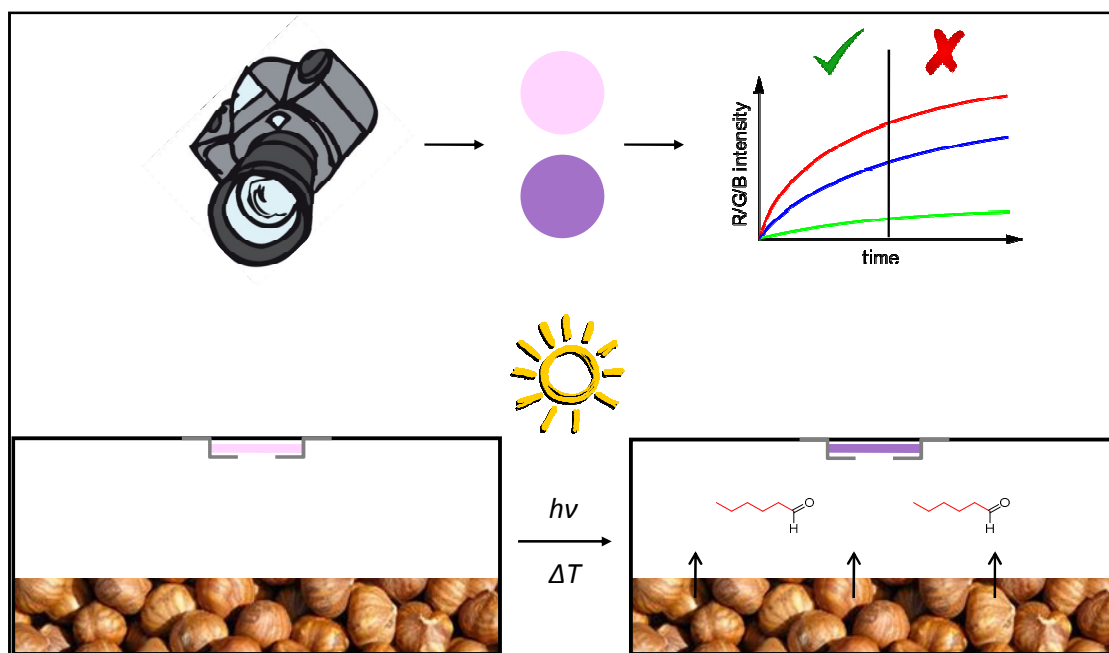


**Figure C.** Schematic illustration of the chapter's objective: an indicator dye is integrated into food packaging changing its color in the presence of hexanal in the headspace. Color change can be monitored by digital camera readout and R, G, B color splitting.

### 3 Materials and Methods

Hexanal (98%), propionaldehyde (97%), acetaldehyde (99%), and Schiff's reagent were purchased from Sigma Aldrich. Polyvinylacetate and silica particles (200-60  $\mu\text{m}$ ) were purchased from Carl Roth GmbH. All other chemicals not mentioned here were of analytical reagent grade (for details see Appendix, chapter 1). Glass vials and screw caps with hole and septum were purchased from Carl Roth GmbH and polyethyleneterephthalat (PET) foil (thickness 125  $\mu\text{m}$ ) from GoodFellow GmbH. PTFE tape was from Bauhaus with a width of 1 cm and thickness of 100  $\mu\text{m}$ .

#### 3.1 Preparation of indicator particles

Silica particles (30 g) were added to a 600 mL beaker and stirred in distilled water (60 mL). After 10 min an aqueous solution of Schiff's reagent was added and 10 min later water was evaporated in a drying oven at 80 °C. During the evaporation process the composition was mixed every 15 min. Indicator particles with different mass ratios of Schiff's reagent to silica were prepared: 75%, 50%, and 25%. That means for the preparation of 50% Schiff's reagent@silica (SR@Si) adding 15 mL Schiff's reagent to a batch of 30 g silica particles.

In the following chapters the different indicator particles are named as:

25% \* Schiff's reagent: SR@Si 1

50% \* Schiff's reagent: SR@Si 2

75% \* Schiff's reagent: SR@Si 3

\* mass ratio

Composition of aqueous Schiff's reagent:

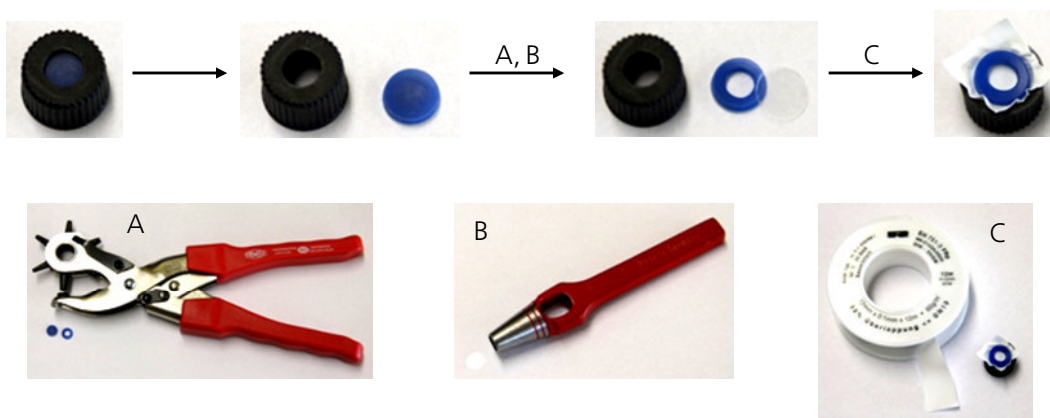
Pararosaniline	0.1 g
Sodium sulfite solution 10% (w/V)	10 mL
Hydrochlorid acid 35%	3 mL
Water	50 mL

As SR@Si 2 turned out to be the best composition for calibration measurements all measurements were performed utilizing these indicator particles except for experiments described in chapter 4.1.

#### 3.2 Preparation of measurement samples by applying PTFE tape as barrier

For quantifying aldehyde concentrations in the gas phase indicator particles were fixed in screw caps with a hole and septum. After removing the septum a hole was stamped in using punch

pliers (Scheme C10, A). Subsequently, a polyethyleneterephthalate (PET) foil was punched with a hollow punch (Scheme C10, B), generating a foil with 8 mm in diameter. The cap was turned over and after inserting the PET foil, 30 mg indicator particles were weighted directly into the cap. Finally, the indicator particles were fixed by placing a piece of PTFE tape (1x1 cm, thickness 100  $\mu\text{m}$ ) and the stamped septum (Scheme C10, C). After addition of hexanal solution the glass vials were sealed with the prepared screw caps. As a result direct contact between indicator particles and calibration solutions is avoided during measurements. Figure C5 shows the measuring sample setup.



**Scheme C10.** Preparation of measuring samples by immobilizing indicator particles in screw caps. PET foil was used as transparent replacement for the septum, whereas PTFE tape served as barrier.

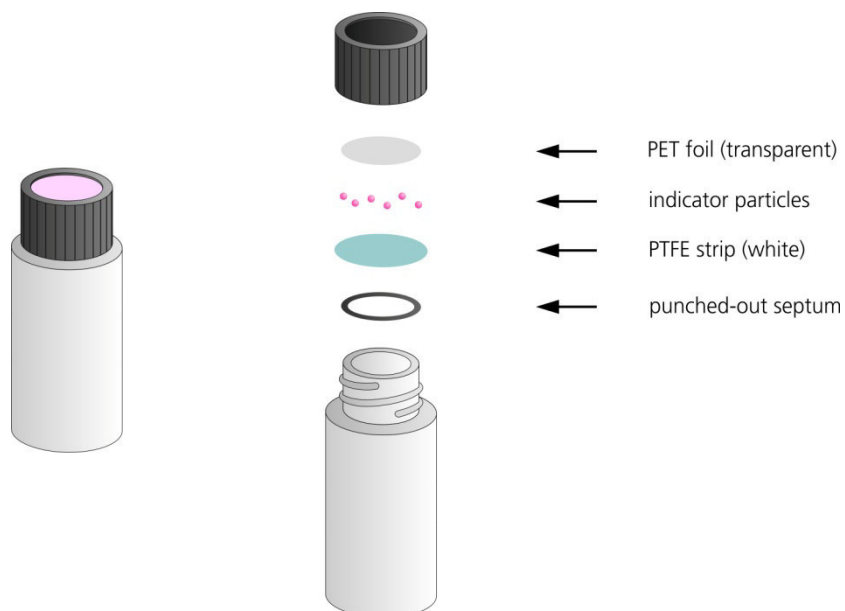


**Figure C5.** Exploded view drawing of sample vials.

### 3.3 Preparation of measurement samples by immobilizing indicator particles in a polyvinyl acetate matrix

An alternative method for preparing measurement samples was investigated by embedding indicator particles into polyvinyl acetate (PVA) as polymer matrix. For this purpose two different concentrations of PVA solutions were prepared whereat PVA ( $M_w = 55000\text{--}70000\text{ g/mol}$ ) was dissolved in ethyl acetate under stirring at room temperature.

*Composition of PVA-solutions:*

- 1) 10% \* PVA in ethyl acetate
  - 2) 20% \* PVA in ethyl acetate
- \* mass ratio

Based on the PVA-solutions two different kinds of indicator particles-PVA-mixtures were prepared. For this SR@Si 2 was mixed with PVA-solution and stirred for 30 minutes using a tube rotator.

Composition of indicator particle-PVA mixtures:

- 1) 20% \* indicator particles in PVA solution (10%)
  - 2) 20% \* indicator particles in PVA solution (20%)
- \* mass ratio of SR@Si 2 and PVA solution

Samples were prepared by adding 150  $\mu\text{L}$  of indicator particle-PVA-mixtures into a screw cap with hole whose septum was replaced by PET foil before. After evaporating ethyl acetate at room temperature the indicator layer looks pale rose (Figure C6, A and B). Afterwards caps were dried in a drying oven at 80  $^{\circ}\text{C}$  for 30 minutes. During drying process the indicator layer changes its color to yellowish (Figure C6, C and D) and after complete drying the layer finally looks magenta (Figure C6, E).

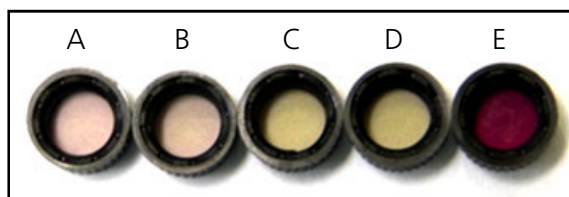


**Figure C6.** Color changes of indicator particle-PVA mixture (prepared with PVA solution (20%)) during drying process. The completely dry indicator layer is magenta colored (E).

30 mg of indicator particles were used for each screw cap no matter which immobilization method was used (see also chapter 3.2).

### 3.4 Measurement setup

A measurement setup was established for quantifying the color change of particles induced by reaction with aldehydes (Figure C7). The custom-made calibration chamber consists of a black box with dimensions of 27 x 37 x 21 cm (width x height x depth). The camera was mounted on the top of the chamber by cutting a hole into the chamber. A second hole was integrated for a light bulb to ensure defined lighting conditions. For this purpose an OSRAM LED STAR Classic P 25 (4 W; 250 lm; T = 2700 K; R<sub>a</sub> = 80) was applied.

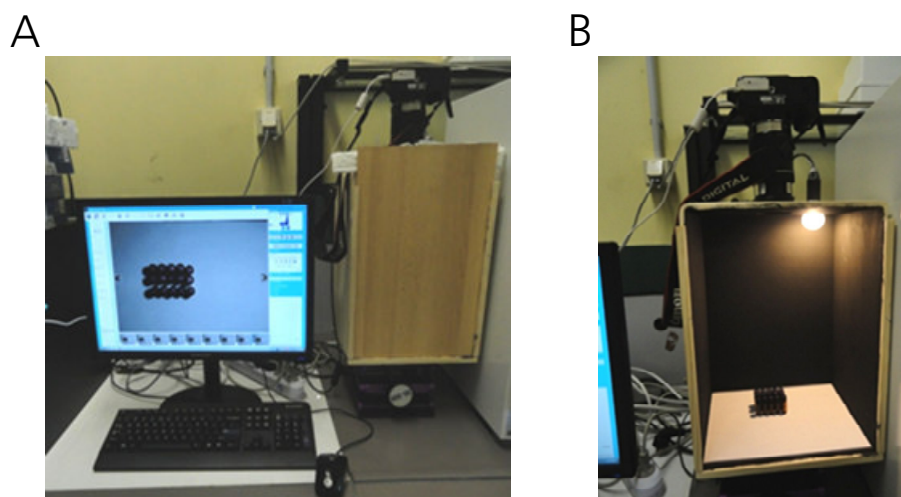


**Figure C7.** Pictures of custom-made calibration chamber. **A:** Complete measurement setup, calibration chamber is closed by a sliding door. **B:** Open calibration chamber showing integrated light bulb and measurement samples on a white paper sheet.

Imaging was performed using Canon EOS 550D SLR camera combined with Canon EF-S 18-135 mm lens. The calibration chamber can be closed by a sliding door to exclude ambient light. The camera was operated by digiCamControl software (for user interface see Figure C8). The integrated time-lapse function was used for image acquisition in defined time intervals of 300 s for a measurement period of three hours.

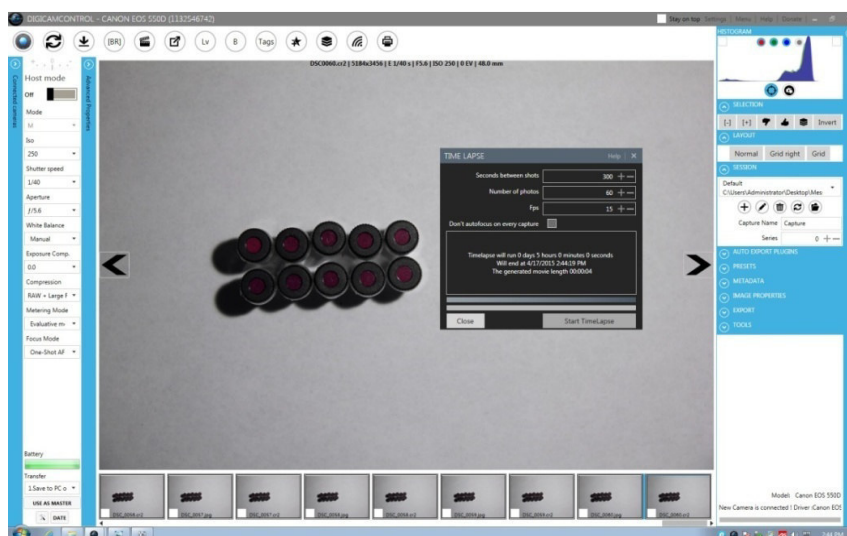
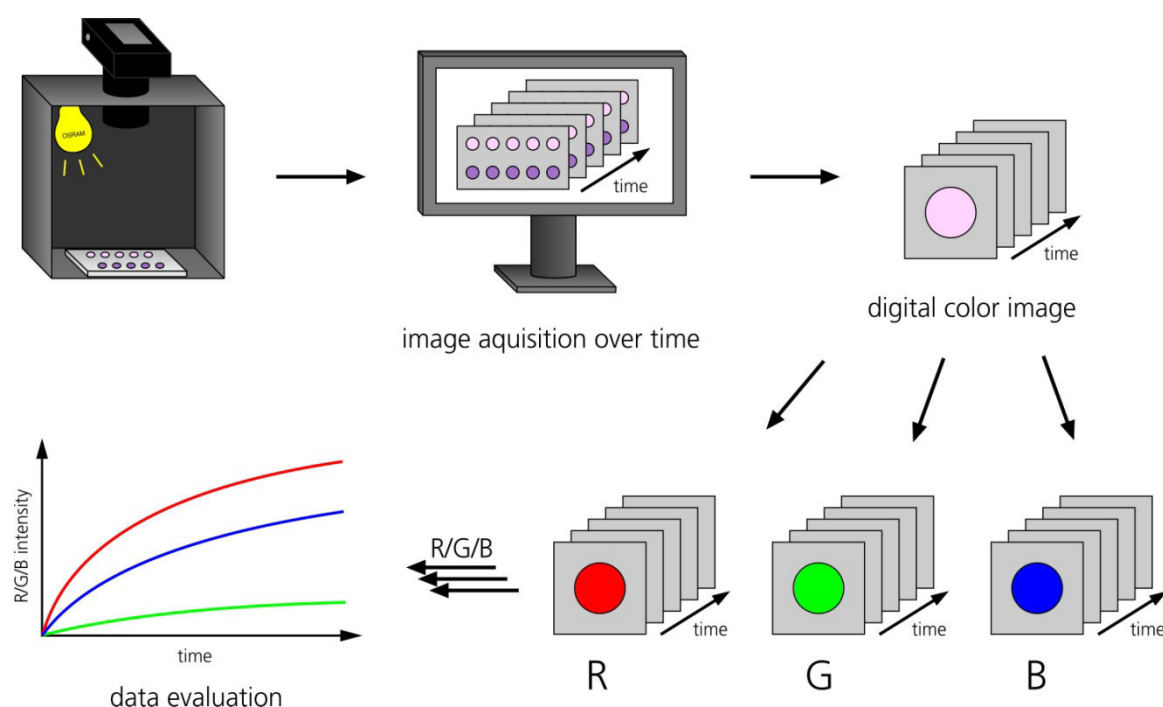


**Figure C8.** User interface of the free tethering software digiCamControl. Window for adjusting time-lapse is opened.

After image acquisition the pictures were converted into RBG (red, green, blue) color information (Scheme C11). The obtained color information was then further evaluated by mathematic transformations and plotting against the time (see chapter 3.7).



**Scheme C11.** Experimental setup for quantifying the color change of test samples during reaction with aldehydes.

Identical camera settings were used for all measurements to ensure identical illumination conditions. Photographs were taken via manual camera mode and white balance was performed using a white paper sheet in the calibration chamber (Figure C7).

**Camera settings** for particles fixed in screw caps with PTFE strip as barrier:

Exposure time: 1/50 s

F-stop: F/5.6

ISO Value: 200

**Camera settings** for indicator particles immobilized in polyvinyl acetate polymer:

Exposure time: 1/40 s

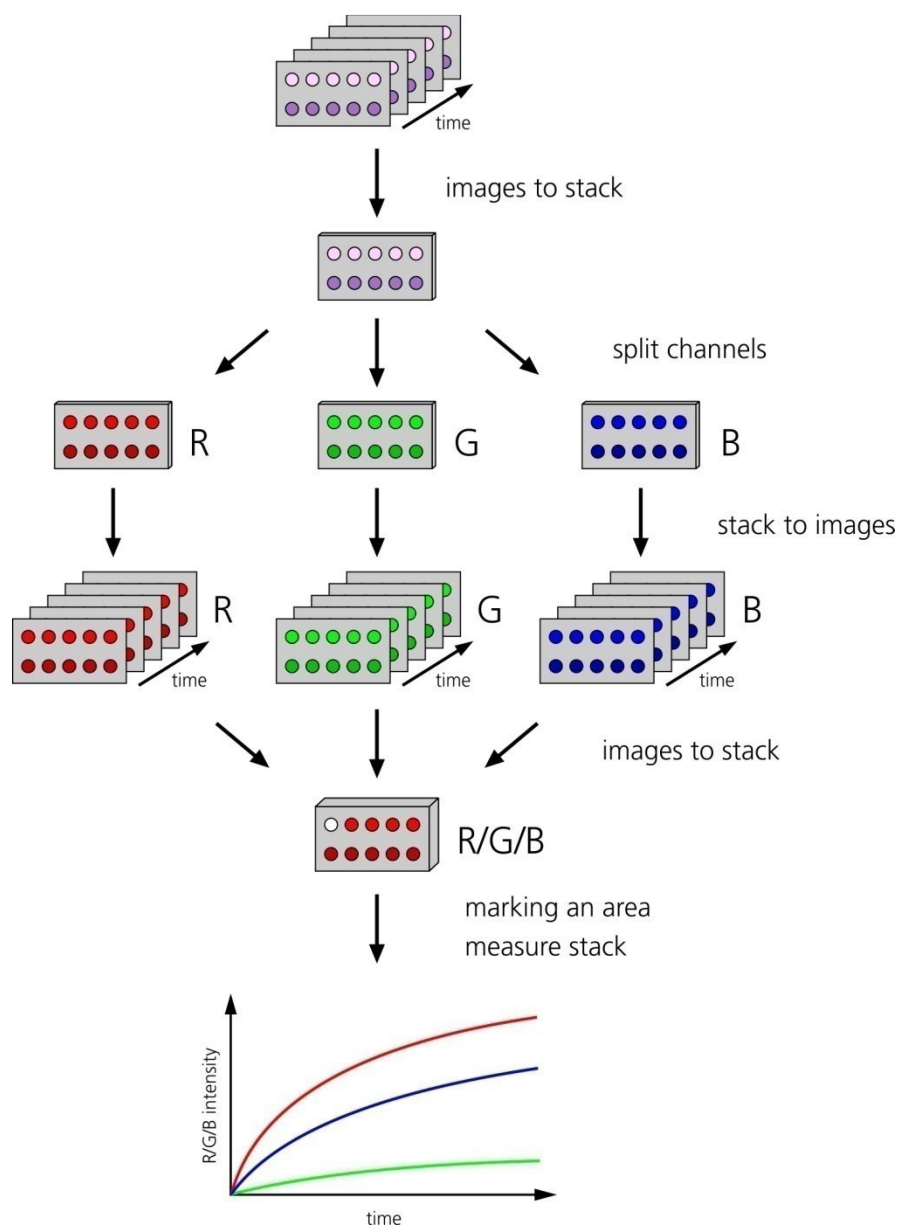
F-stop: F/5.6

ISO Value: 250

### 3.5 Data processing

Digital images were evaluated using the free Image J software by splitting the color channels of photographs to obtain the red, green, and blue color information (Scheme C12). Afterwards referenced signal changes were visualized in time course plots following the data processing described in chapter 3.7. The exact process of data evaluation applying Image J software is explained in the following paragraph.

After uploading all images a stack was created (Image → Stack → Images to Stack). The stack was split into red, green, and blue color channels (Image → Color → Split channels) which results in three single stacks (red, green, and blue color channel). Those were then split to their separate images again (Image → Stack → Stack to Images; 3x) in order to create one general stack out of all images (Image → Stack → Images to Stack). Afterwards, the first region of interest was marked and measured (Plugins → Stack → Measure Stack). The instruction “Measure Stack” generates a list of measured brightness values of all images in the stack which can be saved as XLS-file. Outlining the region of interest has to be repeated for each single screw cap. Finally, the files were opened in Origin Lab software for data processing and graph plotting.



**Scheme C12.** Overview of the steps of image evaluation using Image J software

### 3.6 Adjustment of aldehyde concentrations

For adjusting defined aldehyde concentrations in glass vials the total volume of the vials has to be determined first. For this purpose glass vials were weighed, completely filled with distilled water and reweighed since the mass of water is directly proportional to the vial volume ( $\rho_{\text{water}} = 1 \text{ g/mL}$ ). This procedure was performed for a total of five glass vials and repeated three times for each vial (Appendix, Table G1) resulting in the following value:

**Volume of glass vials:**  $1.82 \pm 0.02 \text{ mL}$  (mean  $\pm$  SD;  $N = 15$ )



Subsequently, aldehyde calibration solutions were prepared. The compositions were chosen to give aldehyde concentrations between 0 and 250 ppm inside the glass vials (see Table C7 for hexanal calibration solutions). For calibration measurements 10  $\mu\text{L}$  of the respective calibration solution were pipetted into a glass vial which was subsequently closed using a screw cap with integrated indicator particles. ppm-Values of the final aldehyde concentrations (Table C7, second column) were determined by dividing the volumes of hexanal by the vial volume of 1.82 mL.

**Table C7.** Pipette Scheme for the preparation of hexanal calibration solutions. Calibration solutions were prepared from respective stock solutions SLI, SLII, or SLIII and filled to their total volume with *n*-hexane. Hexanal concentrations in the second column represent the ppm-values (volume concentrations) of hexanal in the glass vials after adding and evaporating 10  $\mu\text{L}$  of respective calibration solutions.

	c(hexanal) / ppm	V(hexanal) / $\mu\text{L}$	V(SLI) / $\mu\text{L}$	V(SLII) / $\mu\text{L}$	V(SLIII) / $\mu\text{L}$	Total volume / mL *
<b>SLI</b>	250	1140	-	-	-	25
	200	-	4000	-	-	5
	150	-	3000	-	-	5
<b>SLII</b>	110	200	-	-	-	10
	55	-	-	2500	-	5
	44	-	-	2000	-	5
	33	-	-	1500	-	5
	23	-	-	1050	-	5
<b>SLIII</b>	14	25	-	-	-	10
	4	-	-	-	1500	5

\* samples were filled with *n*-hexane to their total volume

### 3.7 General procedure for data evaluation

During reaction with aldehydes the color of indicator particles changes from pale rose to violet (Figure C9).

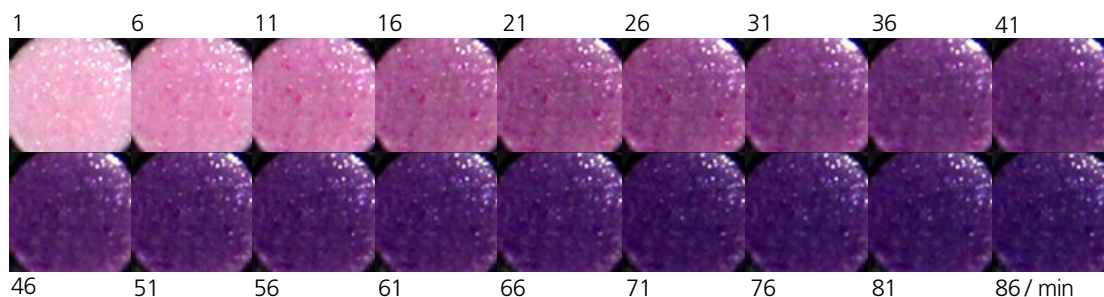


**Figure C9.** Color change of a measurement sample (SR@Si 2 immobilized in screw caps with PTFE strip as barrier) induced by 55 ppm hexanal during 86 minutes.

The reaction of indicator particles was quantified by taking digital color images of measurement samples (chapter 3.4 and 3.5). By splitting the RGB images into the corresponding color channels a time course of red, green, and blue color channel intensities became available (Figure C10) which was almost completed after about 60 minutes.

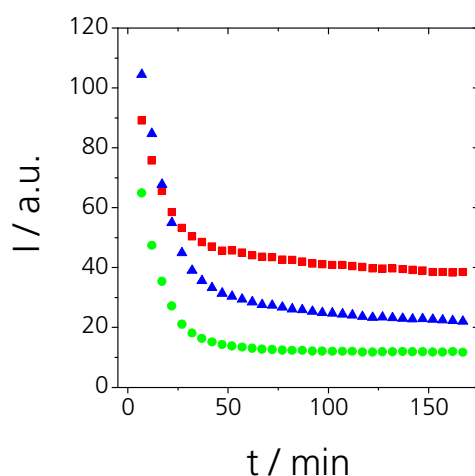


**Figure C10.** Typical time-dependent change of red (■), green (●), and blue (▲) color channel intensities in the presence of 55 ppm hexanal.

Data evaluation was performed by ratiometric analysis of two color channels. The ratios blue/red channel [B/R] (Equation C1) and blue/green channel [B/G] gave the best results here.  $B(t_1)$  and  $R(t_1)$  represent the intensities of blue and red color channel of first measurement point here,  $B(t_2)$  and  $R(t_2)$  the data for second measurement points.

$$\left[ \frac{B(t)}{R(t)} \right] = \left[ \frac{B(t_1)}{R(t_1)} \right], \left[ \frac{B(t_2)}{R(t_2)} \right], \left[ \frac{B(t_3)}{R(t_3)} \right], \dots \quad \text{Eq. C1}$$

An alternative evaluation method was performed by calculating euclidean distances [e.d.] of red, green, and blue color channel intensities in the three dimensional RGB color space (Equation C2).

$$f(R, G, B) = \sqrt{(R_0 - R_t)^2 + (G_0 - G_t)^2 + (B_0 - B_t)^2} \quad \text{Eq. C2}$$

$R_0$  represents the value of red color channel at time  $t = 0$  and  $R_t$  the values of red color channel at time  $t$ .  $G_0$  and  $G_t$  describe the values for green color channels and  $B_0$  and  $B_t$  the values for blue color channels (Equation C2). For determining  $R_0$ ,  $G_0$ , and  $B_0$  the saturation curves of control measurement (with pure *n*-hexane) were used. The mean of the last ten data points was calculated for red, green, and blue color channel.  $R_0$ ,  $G_0$ , and  $B_0$  were determined once in five replicates and used for data evaluation of all calibration measurements.

The error of the euclidean distance  $\Delta f(R, G, B)$  was calculated by error propagation according to Equations C3-C6. Here  $\Delta R_0$  describes the error of the blank of the red color channel and  $\Delta R_t$  represents the errors of the red color channel at time  $t$  (Equation C4). Those errors were determined as standard deviations from five replicate measurements. For green and blue color channels the calculations were performed accordingly (Equation C5 and C6).

$$\Delta f(R, G, B) = \sqrt{\left( \frac{\partial f(R, G, B)}{\partial R_0} \cdot \Delta R_0 \right)^2 + \left( \frac{\partial f(R, G, B)}{\partial R_t} \cdot \Delta R_t \right)^2 + \left( \frac{\partial f(R, G, B)}{\partial G_0} \cdot \Delta G_0 \right)^2 + \left( \frac{\partial f(R, G, B)}{\partial G_t} \cdot \Delta G_t \right)^2 + \left( \frac{\partial f(R, G, B)}{\partial B_0} \cdot \Delta B_0 \right)^2 + \left( \frac{\partial f(R, G, B)}{\partial B_t} \cdot \Delta B_t \right)^2} \quad \text{Eq. C3}$$

$$\frac{\partial f(R, G, B)}{\partial R_0} = \frac{1}{2 \cdot f(R, G, B)} \cdot (2R_0 - 2R_t); \quad \frac{\partial f(R, G, B)}{\partial R_t} = \frac{1}{2 \cdot f(R, G, B)} \cdot (-2R_0 + 2R_t) \quad \text{Eq. C4}$$

$$\frac{\partial f(R, G, B)}{\partial G_0} = \frac{1}{2 \cdot f(R, G, B)} \cdot (2G_0 - 2G_t); \quad \frac{\partial f(R, G, B)}{\partial G_t} = \frac{1}{2 \cdot f(R, G, B)} \cdot (-2G_0 + 2G_t) \quad \text{Eq. C5}$$

$$\frac{\partial f(R, G, B)}{\partial B_0} = \frac{1}{2 \cdot f(R, G, B)} \cdot (2B_0 - 2B_t); \quad \frac{\partial f(R, G, B)}{\partial B_t} = \frac{1}{2 \cdot f(R, G, B)} \cdot (-2B_0 + 2B_t) \quad \text{Eq. C6}$$

After determining color changes of the indicator particles by one of the above mentioned evaluation methods the obtained data values were plotted against time. For all measurements a saturation curve was received which was then fitted by a logistic function (Equation C7).

$$y = \frac{A2 + (A1 - A2)}{1 + \left(\frac{x}{x_0}\right)^p} \quad \text{Eq. C7}$$

Afterwards the saturation values of time-dependent curves had to be determined for the generation of calibration plots. These values represent the signal change of indicator particles after complete reaction with the present aldehyde. For this purpose two different methods were applied. The first was calculating the mean of the last ten data points, respectively. As second method the parameters of the logistic fit functions were used. Parameter A2 here describes the end point of the fit function and, therefore, the saturation value (Equation C7).

Finally, obtained values were plotted against the aldehyde concentration for generating calibration plots. Calibration curves were then fitted with an exponential association (Equation C8).

$$y = y_{\infty} - (y_{\infty} - y_0) \cdot e^{-k \cdot \frac{x}{x_0}} \quad \text{Eq. C8}$$

$y_{\infty}$       y-value for an infinite value of x

$y_0$       y-value for x = 0

$x_0$       constant (= 1 ppm)

### Determination of limits of detection (LOD)

For small aldehyde concentrations linear signal responses were observed for all calibration measurements. Those were fitted with linear fit functions to determine the limits of detection (LODs). For this purpose the blank value method was used which is described in DIN 32 436 for linear calibrations.<sup>102</sup> Limit of detection (LOD), limit of identification (LOI), and limit of quantification (LOQ) are also defined therein. For a practical application it proved useful to perform some simplifications resulting in Equation C9 for calculation of the LOD value ( $x_{\text{LOD}}$ ).

$$x_{\text{LOD}} = \frac{s_{y_0}}{m} \cdot t \cdot \left[ \frac{1}{\tilde{N}} + \frac{1}{N} \right]^{1/2} \quad \text{Eq. C9}$$

$s_{y_0}$       standard deviation of N blank value measurements

N      number of blank value measurements

$\tilde{N}$       number of parallel measurements

t      t-value (f = N-1, P = 95% or 99%)

m      slope of linear fit function

The error propagation for LOD calculation was performed according to Equation C10 and C11.

$$s_{x_{LOD}} = \sqrt{\left(\frac{\partial x_{LOD}}{\partial m} \cdot s_m\right)^2} \quad \text{Eq. C10}$$

$$s_{x_{LOD}} = \sqrt{\left(-\frac{s_{y_0} \cdot t \cdot \left[\frac{1}{\tilde{N}} + \frac{1}{N}\right]^{1/2}}{m^2} \cdot s_m\right)^2} \quad \text{Eq. C11}$$

According to DIN 32 436 the limit of identification  $x_{LOI}$  and the limit of quantification  $x_{LOQ}$  are defined as multiples of  $x_{LOD}$  (Equation C12 and C13).

$$x_{LOI} = 2 \cdot x_{LOD} \quad \text{Eq. C12}$$

$$x_{LOQ} = 3 \cdot x_{LOD} \quad \text{Eq. C13}$$

For a certain concentration  $x_A$  its corresponding values  $x_{LOD}$ ,  $x_{LOI}$ , and  $x_{LOQ}$  have the following meanings assuming a quantification uncertainty of  $P = 95\%$ :

$x_A < x_{LOD}$	Detection successful in less than 50% *
$x_A \approx x_{LOD}$	Detection successful in 50% *
$x_{LOD} < x_A < x_{LOI}$	Detection successful in 50% to 95% *
$x_A \approx x_{LOI}$	Detection successful in 95% *
$x_{LOI} < x_A < x_{LOQ}$	Detection successful *; Quantification is uncertain with the statistical certainty P
$x_A \approx x_{LOQ}$	Detection successful *; Quantification is possible with the statistical certainty P

\* *Detection successful*: statement „analyte present“ is true.

Furthermore, an even more simplified Equation for LOD calculation is widely used in analytics. Triple standard deviation of blank value  $x_0$  is calculated and added to the original blank value  $y_0$  (Equation C14). Error propagation was then performed as described in Equation C15 and C16.

$$y = A + m \cdot x \rightarrow x_{\text{LOD}} = \frac{(y_0 + 3 \cdot s_{y_0}) - A}{m} \quad \text{Eq.14}$$

$$s_{x_{\text{LOD}}} = \sqrt{\left(\frac{\partial x_{\text{LOD}}}{\partial A} \times s_A\right)^2 + \left(\frac{\partial x_{\text{LOD}}}{\partial m} \times s_m\right)^2} \quad \text{Eq.15}$$

$$s_{x_{\text{LOD}}} = \sqrt{\left(-\frac{1}{m} \cdot s_A\right)^2 + \left(-\frac{y - A}{m^2} \cdot s_m\right)^2} \quad \text{Eq. 16}$$

A	intersection
$s_A$	error of intersection A
m	slope
$s_m$	error of slope m

Both methods for calculating the limits of detection were performed for the calibration of indicator particles with hexanal (see chapter 3.2.1). The obtained values were compared and additionally limits of identification and quantification were also determined. For the remaining calibration measurements using other analytes LODs were only calculated by the triple standard deviation method (Equation C14-C16).

### Sensitivity

The sensitivity is defined as slope of the linear calibration functions.

## 4 Results and Discussion

### 4.1 Determination of best composition for Schiff's reagent@silica

For identifying the optimal concentration ratio between Schiff's reagent and silica particles, three different indicator particles (SR@Si) with varying composition were prepared. Particles were of type SR@Si 1, SR@Si 2, and SR@Si 3 (for details see chapter 3.1).

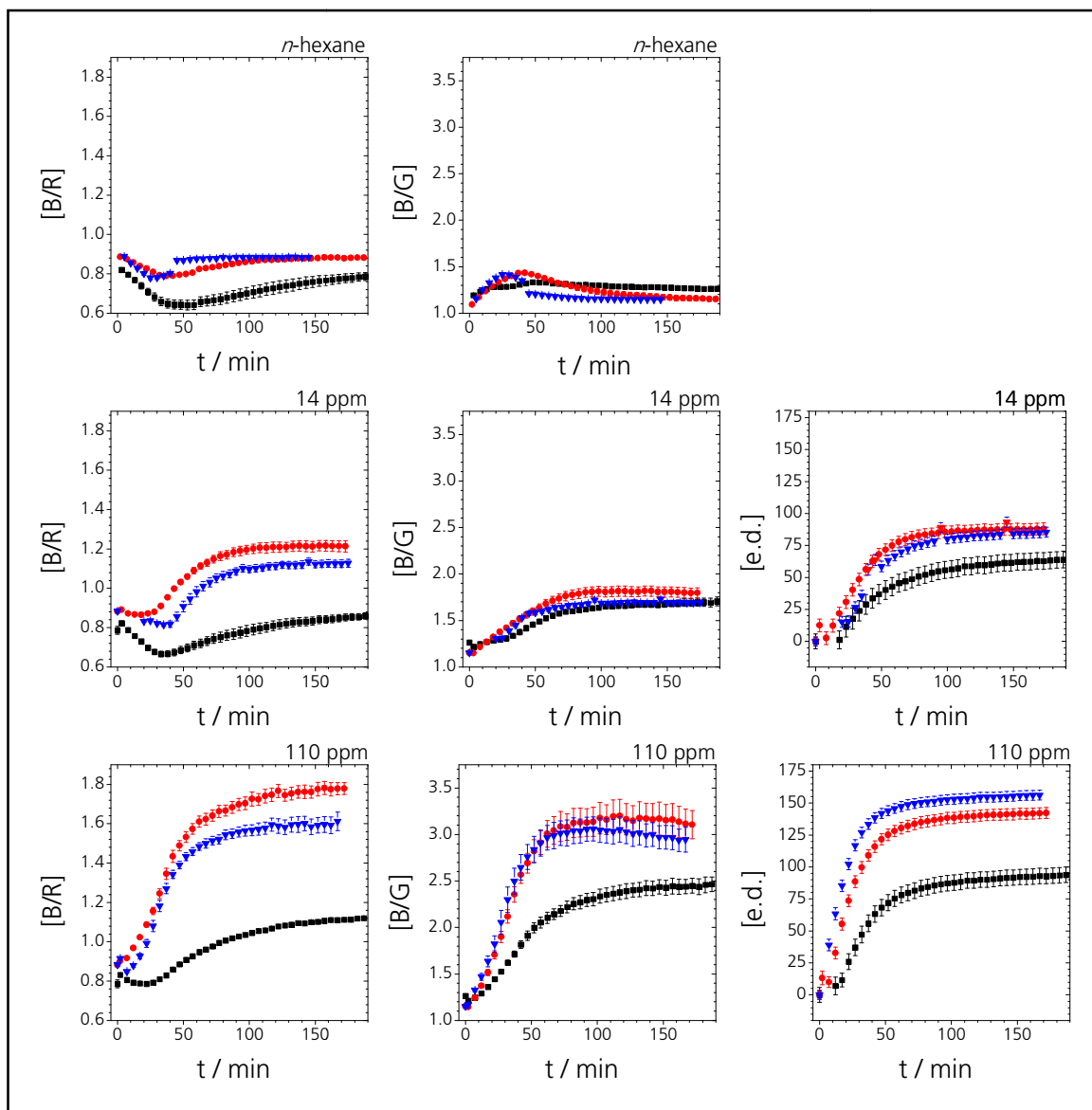


**Figure C11.** Response curves for SR@Si 1 (■, black), SR@Si 2 (▼, blue), and SR@Si 3 (●, red). Signal changes caused by pure *n*-hexane and hexanal in concentrations of 14 and 110 ppm are shown. Data evaluation was performed by calculating [B/R] (left), [B/G] (middle), and [e.d.] (right) (mean  $\pm$  SDM; N = 5).

The effect of pure *n*-hexane, 14 ppm, and 110 ppm hexanal on the three different types of SR@Si was investigated with *n*-hexane as control substance. Time-dependent curves were plotted from signals [B/R], [B/G], and [e.d.] (Figure C11). Saturation values were calculated as mean of the last ten data points (120-170 min) for each graph. Based on the obtained data the absolute signal changes for SR@Si 1, SR@Si 2, and SR@Si 3 were determined using *n*-hexane saturation value as blank (Table C8).

**Table C8.** Absolute signal changes  $\Delta$  of SR@Si 1, SR@Si 2, and SR@Si 3 after reaction with 14 ppm, and 110 ppm hexanal.

Particle type	c(hexanal) / ppm	$\Delta$ [B/R]	$\Delta$ [B/G]	$\Delta$ [e.d.]
SR@Si 1	14	0.07	0.44	64
	110	0.34	1.21	94
SR@Si 2	14	0.25	0.54	85
	110	0.73	1.79	156
SR@Si 3	14	0.33	0.65	88
	110	0.90	1.96	142

Signal changes for SR@Si 1 are smallest compared to SR@Si 2 and SR@Si 3 (Table C8). For SR@Si 1  $\Delta$  [B/R] is 0.07 for 14 ppm and 0.34 for 110 ppm hexanal. In contrast, for SR@Si 3 the values are 0.33 and 0.90. Particles of type SR@Si 2 also show higher values (0.25 and 0.73) compared to SR@Si 1. The same signal trends can be observed from [B/G] and from [e.d.] values. Therefore, particles SR@Si 1 are not applicable as indicator particles for low aldehyde concentrations as a high signal change is required for sensitive detection.

By comparing the curves of particle types SR@Si 1, SR@Si 2, and SR@Si 3 for pure *n*-hexane (Figure C11, first row), it is obvious that saturation is reached faster for SR@Si 2 than for SR@Si 3. Simultaneously, particles SR@Si 1 don't reach a saturation value at all during the whole measuring time also eliminating them from application.

Signal changes caused by hexanal are similar for SR@Si 2 and SR@Si 3. E.g. for 14 ppm hexanal  $\Delta$  [B/R] is 0.25 for SR@Si 2 and 0.33 for SR@Si 3. For 110 ppm hexanal the values are 0.73 for SR@Si 2 and 0.90 for SR@Si 3. As a result all further experiments were performed applying SR@Si 2 as they more rapidly reach the blank saturation value (with *n*-hexane), provide a similar analytical performance at lower manufacturing cost compared to SR@Si 3.



## 4.2 Calibration measurements

Calibration measurements were performed for determining the response behavior of indicator particles towards hexanal. As comparison propionaldehyde and acetaldehyde were investigated as well.

For calibration measurements SR@Si 2 was used and fixed in screw caps using PTFE tape as barrier (for details see chapter 3.2). Calibration solutions for hexanal, propionaldehyde, and acetaldehyde in hexane were prepared to reach aldehyde concentrations in the headspace of the measurement chamber between 0 and 250 ppm (for details see chapter 3.6). All calibration measurements were performed in five replicates determination. After preparation of all vials they were placed in the calibration chamber and time lapse was started. Time elapsed until the first picture was also measured here and included in final data evaluation. All control measurements for calibration experiments were performed using pure *n*-hexane. The obtained saturation values were applied as blank for calibration plots.



**Figure C12.** Color change of indicator particles after reaction with different concentrations of hexanal. A color change from pale rose to violet is clearly observable here.

Settings for SLR camera (manual mode) were as following: F-stop F/5.6, exposure time 1/50 seconds, ISO 200 and furthermore, manual white balance was performed with a white paper sheet (for details see chapter 3.4). These camera adjustments were identical for calibration measurements with hexanal, propionaldehyde, and acetaldehyde.

Measurements were evaluated by three different methods: ratio of blue and red color channel [B/R], ratio of blue and green color channel [B/G], and euclidean distance [e.d.] (for details see chapter 3.7). For all aldehydes under study and for different concentrations as well, time-dependent signal increase and saturation curves were obtained. Due to the irreversibility of the detection reaction a complete consumption of present aldehyde in reaction vessels is assured which enables the plotting of calibration curves from saturation values. For this purpose two different determination methods were applied (for details see chapter 3.7) and the resulting data (time-dependent and calibration plots) is shown below for the aldehydes under study. Fits were performed here by logistic (for time course data), exponential (for dose-response data), or linear fit functions (for dose-response data) whereas limits of detection (LOD) were finally calculated by using the linear calibration curves (for details see chapter 3.7). Fitting of controls (measurements with *n*-hexane) by logistic fit function, however, was not practicable so that blank of calibration plots was only determined as mean of the last ten data points.

### 4.2.1 Calibration with hexanal

#### Data evaluation by [B/R]

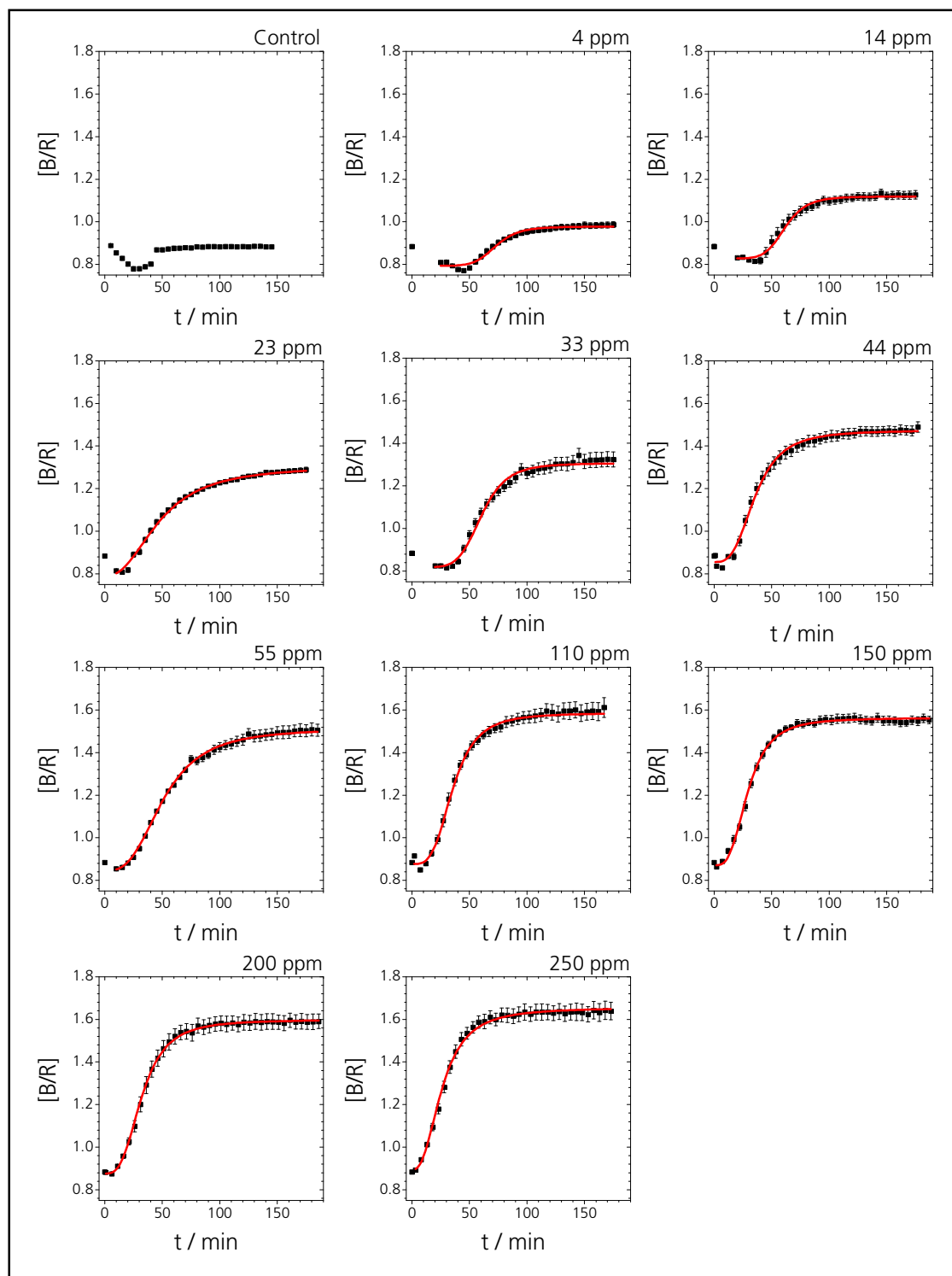


**Figure C13.** Time-dependent increase of signal [B/R] during reaction of indicator particles with different concentrations of hexanal. Indicator particles were of type SR@Si 2 and fixed in screw caps using PTFE tape as barrier. Data was fitted with logistic fit functions (except control). Fit parameters are described in Appendix (Table G2) (mean  $\pm$  SDM; N = 5).

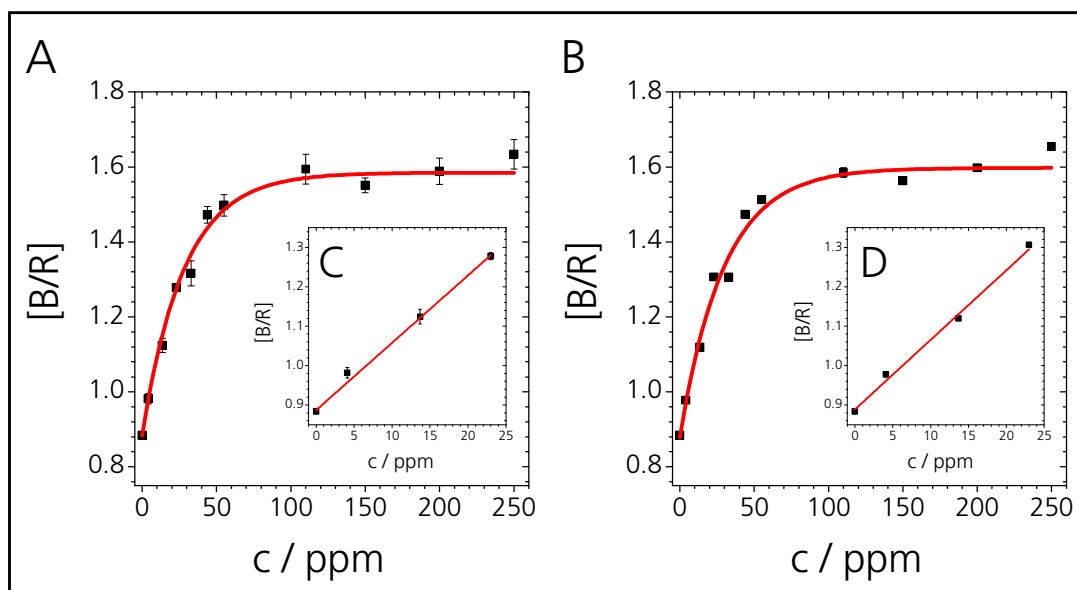


**Figure C14.** Hexanal calibration plots for calculated ratios of blue and red color channel [B/R]. Data was derived from time-dependent curves (Figure C13). Saturation values for each concentration were calculated by the mean of the last ten data points (130-180 min) for **A**. For **B** end points were determined from fit parameters of logistic fit functions. Calibration plots **A** and **B** were fitted with an exponential association. Small graphs **C** and **D** show linear response for small hexanal concentrations (mean  $\pm$  SDM;  $N = 5$ ).

Time-dependent signal increase of [B/R] could be described by saturation processes for all hexanal concentrations (Figure C13) and were fitted using a logistic fit function (Equation C7). Saturation values were determined by two different methods (see chapter 3.7) and plotted against the respective hexanal concentrations (Figure 14, A and B). The resulting calibration curves were both be described by an exponential association ( $R^2 = 0.99$  for A,  $R^2 = 0.98$  for B). For small hexanal concentrations a linear signal response was observed (Figure C14, C and D) here. Corresponding parameters for the linear fit functions of graphs C ( $R^2 = 0.99$ ) and D ( $R^2 = 0.98$ ) are summarized in Table C9.

**Table C9.** Parameters of linear fits (Figure C14, C and D).

	Slope $\pm$ error / ppm <sup>-1</sup>	Intercept $\pm$ error
Fig. C14, C	$0.0171 \pm 0.0006$	$0.887 \pm 0.007$
Fig. C14, D	$0.018 \pm 0.001$	$0.89 \pm 0.01$

## Data evaluation by [B/G]

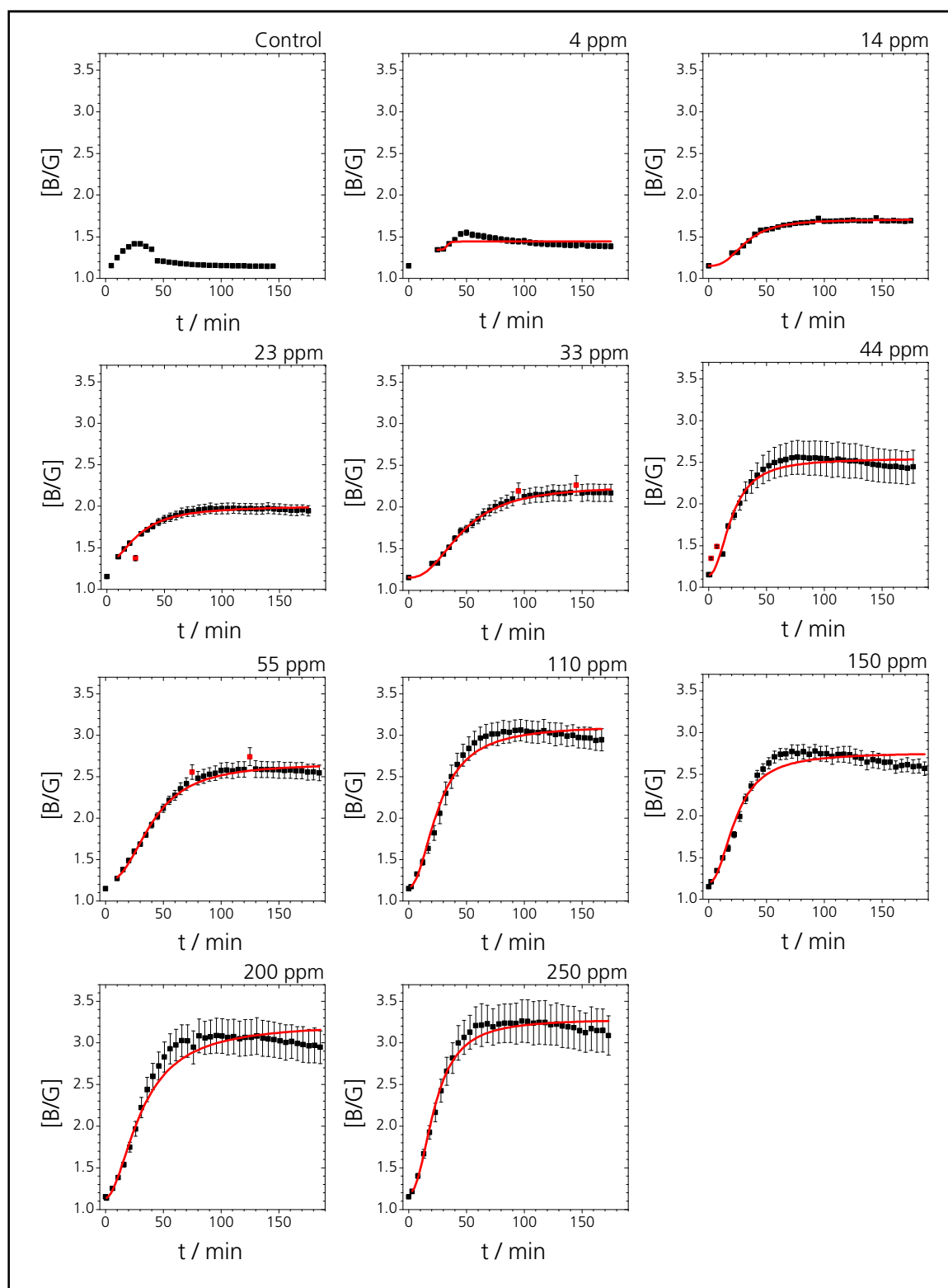


**Figure C15.** Time-dependent increase of signal [B/G] during reaction of indicator particles with different concentrations of hexanal. Indicator particles were of type SR@Si 2 and were fixed in screw caps using PTFE tape as barrier. Data was fitted with a logistic fit function and fit parameters are summarized in Appendix (Table G3) (mean  $\pm$  SDM;  $N = 5$ ).

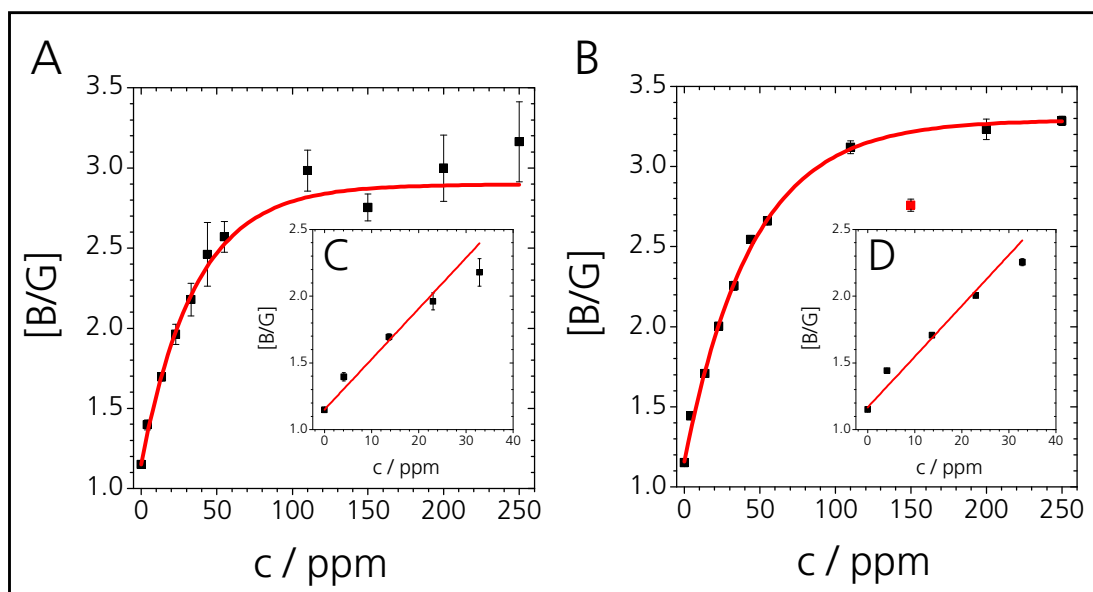


**Figure C16.** Hexanal calibration plot for calculated ratios of blue and green color channel [B/G]. The data is derived from time-dependent curves (Figure C15). Saturation values for each concentration were calculated by the mean of the last ten data points (130-180 min) for **A**. For **B** end points were determined from fit parameters of logistic fit functions (excluding the value for 150 ppm hexanal as an outlier). Calibration plots **A** and **B** were fitted with an exponential association. Small graphs **C** and **D** show a linear response for small hexanal concentrations (mean  $\pm$  SDM; N = 5).

Time-dependent signal changes of [B/G] have been successfully described by a saturation process for all hexanal concentrations (Figure C15). The resulting saturation curves were fitted using a logistic fit function (Equation C7). Based on the data saturation values were determined by two different methods (see chapter 3.7) and plotted against the respective hexanal concentrations (Figure C16, A and B). The resulting calibration curves could be fitted by an exponential association showing excellent accuracy ( $R^2 = 0.99$  for A and  $R^2 = 0.99$  for B). For small hexanal concentrations signal increase has been described by a linear response (Figure C16, C and D). Parameters of the corresponding linear fit functions of graphs C ( $R^2 = 0.98$ ) and D ( $R^2 = 0.97$ ) are summarized in Table C10.

**Table C10.** Parameters of linear fits (Figure C16, C and D).

	Slope $\pm$ error / ppm <sup>-1</sup>	Intercept $\pm$ error
Fig. C16, C	$0.038 \pm 0.002$	$1.150 \pm 0.006$
Fig. C16, D	$0.038 \pm 0.003$	$1.17 \pm 0.03$

## Data evaluation by [e.d.]

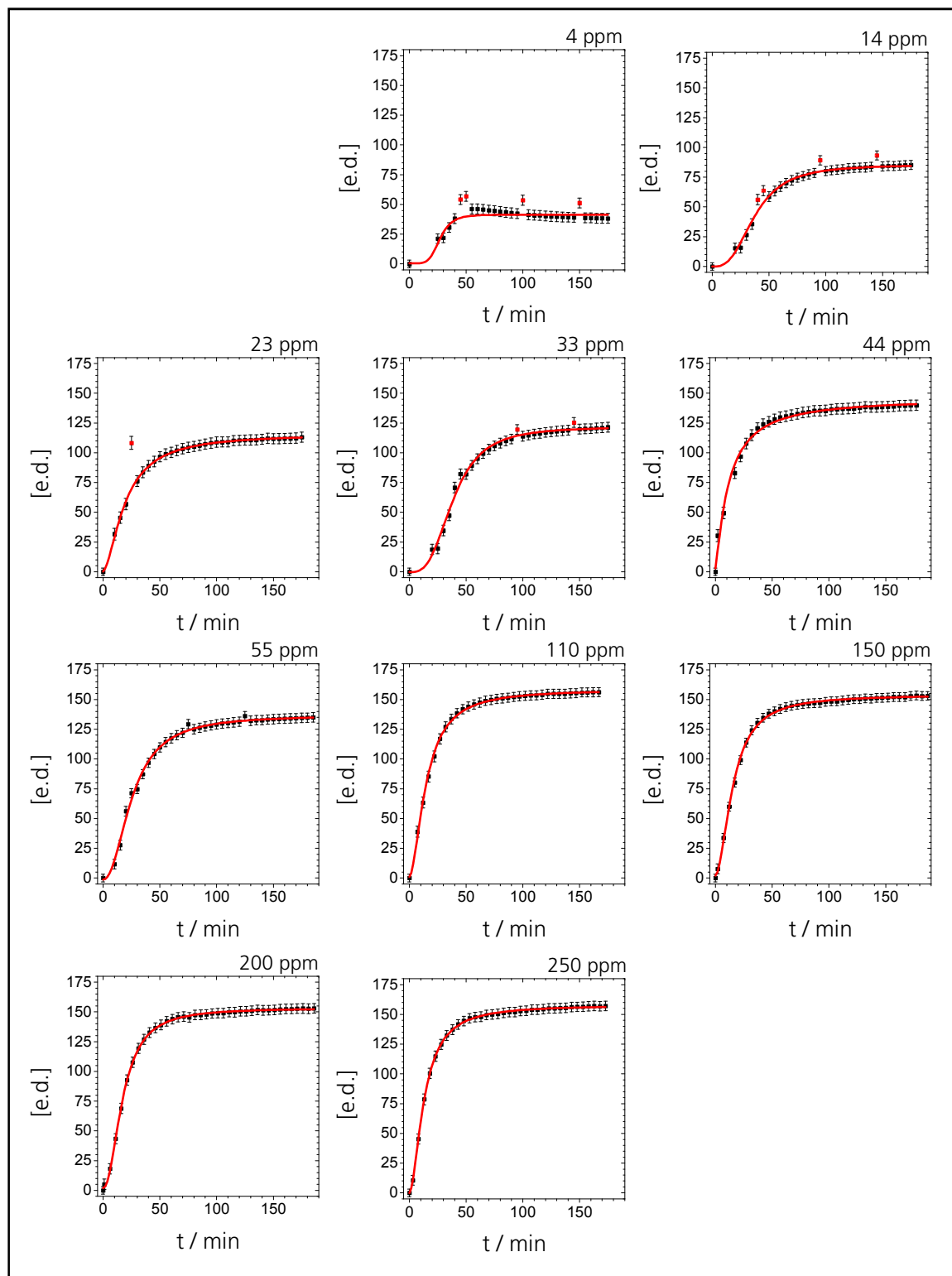


**Figure C17.** Time-dependent increase of [e.d.] during reaction of indicator particles with different concentrations of hexanal. Indicator particles were of type SR@Si 2 and fixed in screw caps using PTFE tape as barrier. Data was fitted with logistic fit functions. Corresponding fit parameters are summarized in Appendix (Table G4) (mean  $\pm$  SDM; N = 5).

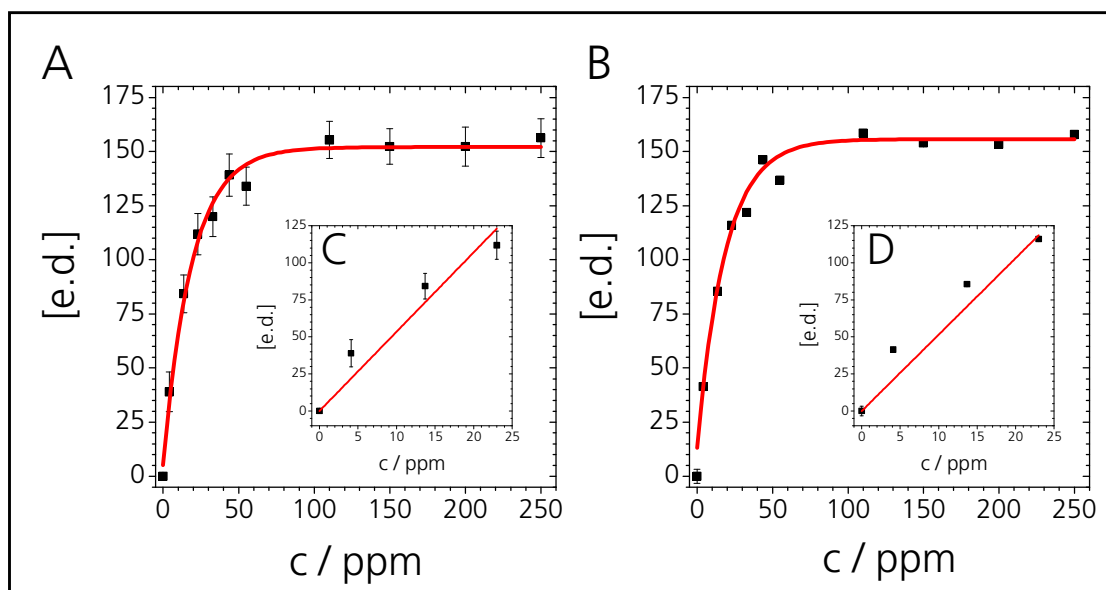


**Figure C18.** Hexanal calibration plot using [e.d.] calculated for the observed color change. The data is derived from time-dependent curves (Figure C17). Saturation values for each concentration were calculated by the mean of the last ten data points (130-180 min) for **A**. For **B** end points were determined from fit parameters of logistic fit functions Calibration plots **A** and **B** were fitted with an exponential association. Small graphs **C** and **D** show a linear response for small hexanal concentrations (mean  $\pm$  SDM; N = 5).

Time-dependent increase of [e.d.] can be described by saturation processes for all hexanal concentrations (Figure C17). The saturation curves were fitted using a logistic fit function (Equation C7). Based on the data corresponding saturation values were determined applying two different calculation methods (see chapter 3.7) and plotted against the respective hexanal concentrations shown in Figure C18, graph A and B. The resulting calibration curves were fitted by an exponential association ( $R^2 = 0.98$  for A and B) whereas for small hexanal concentrations (0-25 ppm) a linear signal response was observed (Figure C18, C and D). Parameters of the linear fit functions of graphs C ( $R^2 = 0.96$ ) and D ( $R^2 = 0.96$ ) are summarized in Table C11. For fitting these linear calibration curves the intercept was fixed to 0 here.

**Table C11.** Parameters of linear fits (Figure C18, C and D).

	Slope / $\pm$ error ppm <sup>-1</sup>	Intercept
Fig. C18, C	$5.4 \pm 0.5$	0
Fig. C18, D	$5.2 \pm 0.3$	0

### Calculation of limits of detection, identification, and determination

Limits of detection (LOD) and associated errors  $s_{x_{\text{LOD}}}$  were determined in this chapter by applying two different calculation methods (Equations C9-C11 and C14-C16, for details see chapter 3.7). Application of Equations C14 and C16 provides a more simplified method compared to Equations C9 and C11. Here  $x_{\text{LOD}}$  represents the limit of detection value which is just referred to as LOD in the explaining text and tables. The calculated LODs for both determination methods are shown in Table C12.

$$x_{\text{LOD}} = \frac{s_y}{m} \cdot t \cdot \left[ \frac{1}{\tilde{N}} + \frac{1}{N} \right]^{1/2}, \quad s_{x_{\text{LOD}}} = \sqrt{\left( -\frac{s_y \cdot t \cdot \left[ \frac{1}{\tilde{N}} + \frac{1}{N} \right]^{1/2}}{m^2} \cdot s_m \right)^2} \quad \text{Eq. C9 and C11}$$

$$N = 5$$

$$\tilde{N} = 1$$

$$t = 2.13 \text{ (one-sided question } P = 95\%)$$

$$y = A + m \cdot x \rightarrow x_{\text{LOD}} = \frac{(y_0 + 3 \cdot s_{y_0}) - A}{m}, \quad s_{x_{\text{LOD}}} = \sqrt{\left( -\frac{1}{m} \cdot s_A \right)^2 + \left( -\frac{y - A}{m^2} \cdot s_m \right)^2} \quad \text{Eq. C14 and C16}$$

**Table C12.** LODs determined by two different calculation methods (Equations C9-C11 and C14-C16) for the calibration data of hexanal. LODs were calculated for three different methods of data evaluation [B/R], [B/G], and [e.d.] and different kinds of end-point determination (Fig. 14, 16, and 18; C and D, respectively).

		LOD* <sup>1</sup> ± error / ppm	LOD* <sup>2</sup> ± error / ppm
[B/R]	Fig. 14, C	0.7 ± 0.4	0.65 ± 0.02
	Fig. 14, D	0.5 ± 0.7	0.62 ± 0.03
[B/G]	Fig. 16, C	0.3 ± 0.2	0.20 ± 0.01
	Fig. 16, D	0.1 ± 0.7	0.20 ± 0.02
[e.d.]	Fig. 18, C	1.8 ± 0.2	1.4 ± 0.1
	Fig. 18, D	1.9 ± 0.1	1.4 ± 0.1

\*<sup>1</sup> LOD determined by Equations C14 and C16, \*<sup>2</sup> LOD determined by Equations C9 and C11

LOD values of individual data evaluation methods ([B/R], [B/R], and [e.d.]) are all in the same range regardless of which calculation method was applied. Nevertheless, values vary slightly with higher errors for the more simplified method using Equations C14 and C16. Exemplary, LODs



from [B/R] are  $0.7 \pm 0.4$  ppm and  $0.5 \pm 0.7$  ppm for simplified method whereas values of  $0.65 \pm 0.02$  ppm and  $0.62 \pm 0.03$  ppm are obtained from Equations 9 and 11. Hence, LOD calculation is feasible by both calculations if the used method is just clearly indicated. The LOD values for hexanal shown here are discussed in more detail in chapter 4.3.

Furthermore, values for LOI and LOQ were determined by applying Equations C12 and C13. These were calculated based on LOD values calculated by simplified method (Equations C14 and C16, Table C13).  $x_{LOI}$  and  $x_{LOQ}$  here present the limit of identification and quantification values in the Equations. In the text and in tables  $x_{LOI}$  is simply referred to as LOI and  $x_{LOQ}$  as LOQ.

$$x_{LOI} = 2 \cdot x_{LOD} \quad \text{Eq. C12}$$

$$x_{LOQ} = 3 \cdot x_{LOD} \quad \text{Eq. C13}$$

**Table C13.** LODs determined by Equations C14-C16. Based on the LODs, LOI and LOQ were calculated by Equations C12 and C13. Errors of  $x_{LOI}$  and  $x_{LOQ}$  were determined by error propagation.

		LOD* $\pm$ error / ppm	LOI $\pm$ error / ppm	LOQ $\pm$ error / ppm
[B/R]	Fig. 14, C	$0.7 \pm 0.4$	$1.4 \pm 0.8$	$2 \pm 1$
	Fig. 14, D	$0.5 \pm 0.7$	$1 \pm 1$	$2 \pm 2$
[B/G]	Fig. 16, C	$0.3 \pm 0.2$	$0.6 \pm 0.4$	$0.9 \pm 0.6$
	Fig. 16, D	$0.1 \pm 0.7$	$0 \pm 1$	$0 \pm 2$
[e.d.]	Fig. 18, C	$1.8 \pm 0.2$	$3.6 \pm 0.4$	$5.4 \pm 0.6$
	Fig. 18, D	$1.9 \pm 0.1$	$3.8 \pm 0.2$	$5.7 \pm 0.3$

\* LOD determined by Equations C14 and C16

For the following calibration measurements with propionaldehyde and acetaldehyde only LODs were only determined by the simplified calculation method applying Equations C14 and C16.

### 4.2.2 Calibration with propionaldehyde

#### Data evaluation by [B/R]

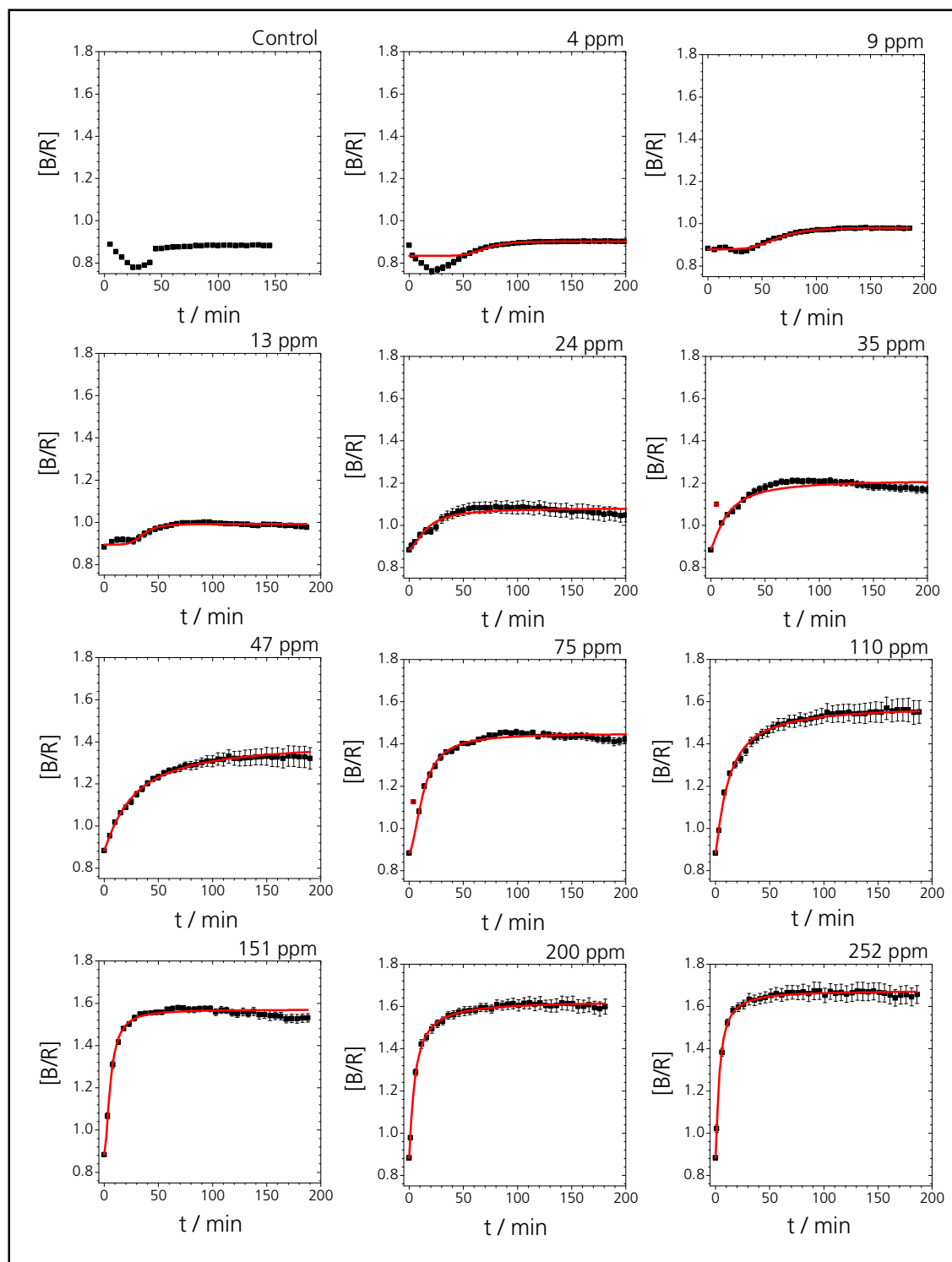


**Figure C19.** Increase of [B/R] during reaction of indicator particles with different concentrations of propionaldehyde. Indicator particles were of type SR@Si 2 and were fixed in screw caps using PTFE tape as barrier. Data shown here was fitted with logistic fit functions. Corresponding fit parameters are summarized in Appendix (Table G5) (mean  $\pm$  SDM; N = 5).

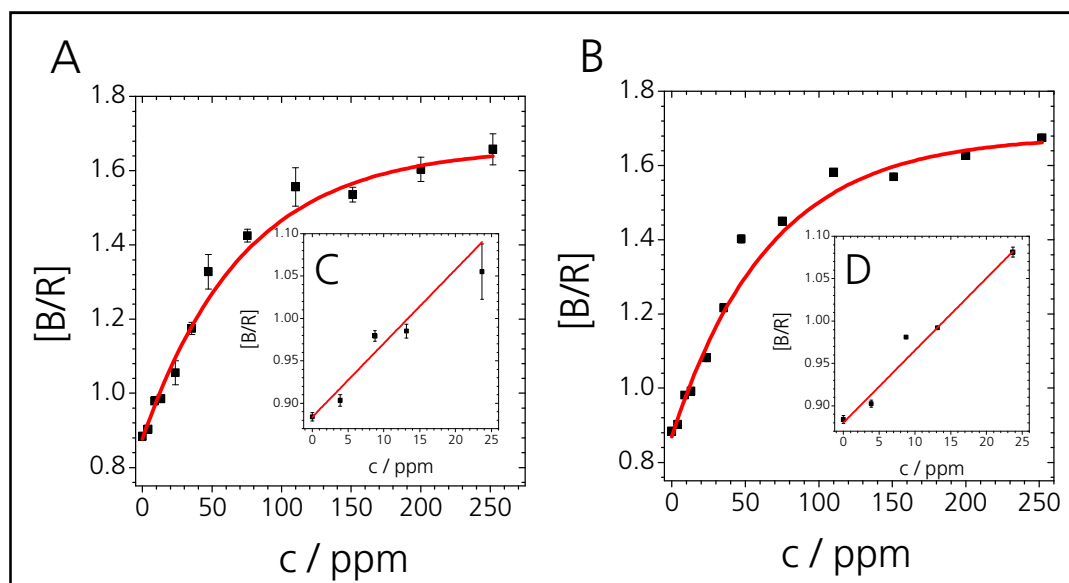


**Figure C20.** Propionaldehyde calibration plots for signal [B/R] derived from time-dependent curves (Figure C19). Saturation values for each concentration were calculated by the mean of the last ten data points (130-180 min) for **A**. For **B** end points were determined by fit parameters of logistic fit functions. Calibration plots **A** and **B** were fitted with an exponential association. Small graphs **C** and **D** show the linear response of small propionaldehyde concentrations (0-25 ppm) (mean  $\pm$  SDM; N = 5).

The time-dependent signal changes of [B/R] shown in Figure C19 has been successfully described by saturation processes for all propionaldehyde concentrations so that saturation curves were fitted using a logistic fit function (Equation C7). Saturation values derived from two different determination methods were plotted against the respective propionaldehyde concentrations (Figure C20, A and B). The calibration curves have been fitted with an exponential association showing excellent accuracy ( $R^2 = 0.98$  for A and  $R^2 = 0.99$  for B). For small hexanal concentrations (0-25 ppm) a linear signal response was observed (Figure C20, C and D). Parameters for the linear fit functions of graphs C ( $R^2 = 0.89$ ) and D ( $R^2 = 0.98$ ) are summarized in Table C14. LODs depicted here were calculated by three times standard deviation (for details see chapter 3.7) and error propagation was performed using the parameters of linear fits.

**Table C14.** Fit parameters and calculated LODs for linear fits of Figure C20, graphs C and D.

	Slope $\pm$ error / ppm <sup>-1</sup>	Intercept $\pm$ error	LOD $\pm$ error / ppm
Fig. 20, C	0.009 $\pm$ 0.001	0.88 $\pm$ 0.01	2 $\pm$ 1
Fig. 20, D	0.0085 $\pm$ 0.0005	0.880 $\pm$ 0.008	2.1 $\pm$ 0.9

## Data evaluation by [B/G]

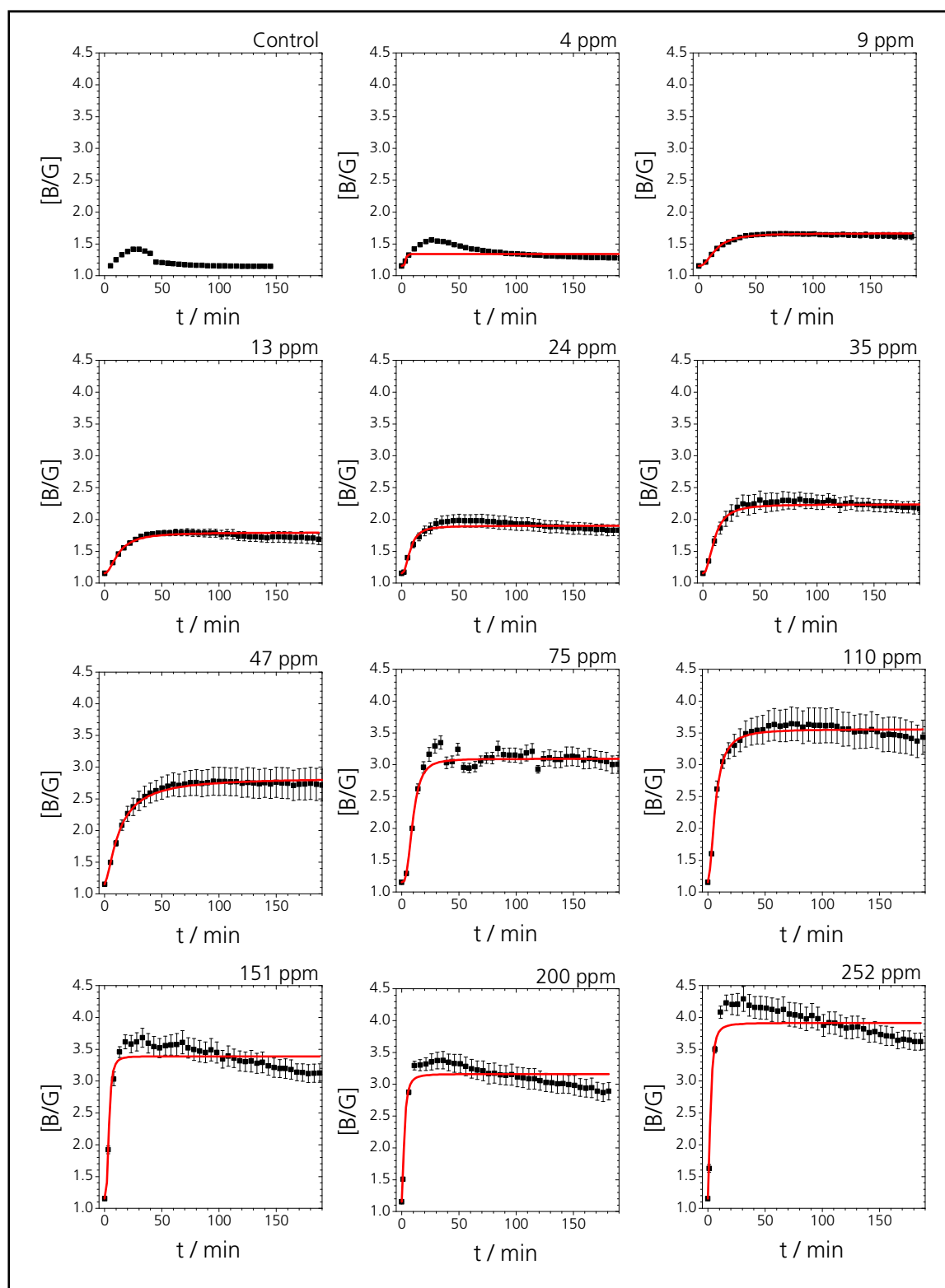


**Figure C21.** Increase of [B/G] during reaction of indicator particles with different concentrations of propionaldehyde. Indicator particles were of type SR@Si 2 and were fixed in screw caps using PTFE tape as barrier. Data was fitted with a logistic fit function and the fit parameters are summarized in Appendix (Table G6) (mean  $\pm$  SDM; N = 5).

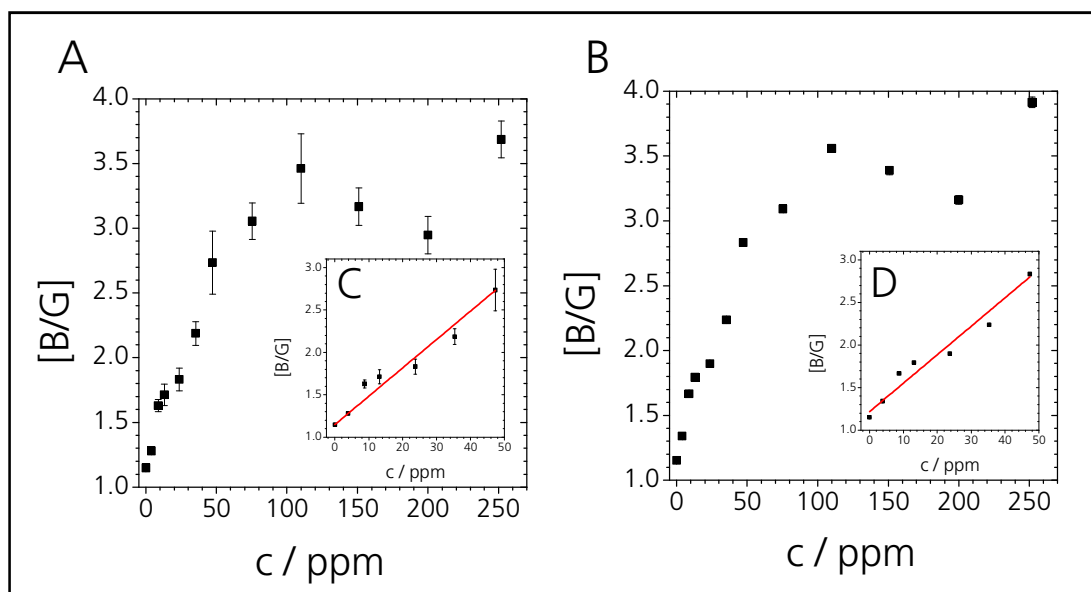


**Figure C22.** Propionaldehyde calibration plot of signal [B/G] were derived from time-dependent curves (Figure C15). Saturation values for each concentration were calculated by the mean of the last ten data points (130–180 min) for **A**. For **B** end points were determined by fit parameters of logistic fit functions. Small graphs **C** and **D** show a linear response for small propionaldehyde concentrations (0–50 ppm) (mean  $\pm$  SDM; N = 5).

Time-dependent signal increase of [B/G] shown in Figure C21 has been successfully described by saturation processes for all propionaldehyde concentrations. All saturation curves were fitted using a logistic fit function (Equation C7). Based on this data saturation values were determined by two different methods (see chapter 3.7) and values were plotted against the respective propionaldehyde concentrations (Figure C22, A and B). The resulting calibration curves have not been fitted due to high fluctuations for high aldehyde concentrations. For small concentrations, however, a linear signal response between 0 and 50 ppm propionaldehyde was observed (Figure C22, C and D). Parameters of corresponding linear fit functions of graphs C ( $R^2 = 0.94$ ) and D ( $R^2 = 0.91$ ) are summarized in Table C15. LODs were calculated by three times standard deviation (for details see chapter 3.7) and error propagation was performed using the received parameters of linear fits (Table C15).

**Table C15.** Fit parameters and calculated LODs for linear fits of Figure C22, graphs C and D.

	Slope $\pm$ error / ppm <sup>-1</sup>	Intercept $\pm$ error	LOD $\pm$ error / ppm
Fig. 22, C	0.033 $\pm$ 0.003	1.149 $\pm$ 0.006	0.4 $\pm$ 0.2
Fig. 22, D	0.033 $\pm$ 0.004	1.22 $\pm$ 0.06	2 $\pm$ 2

## Data evaluation by [e.d.]

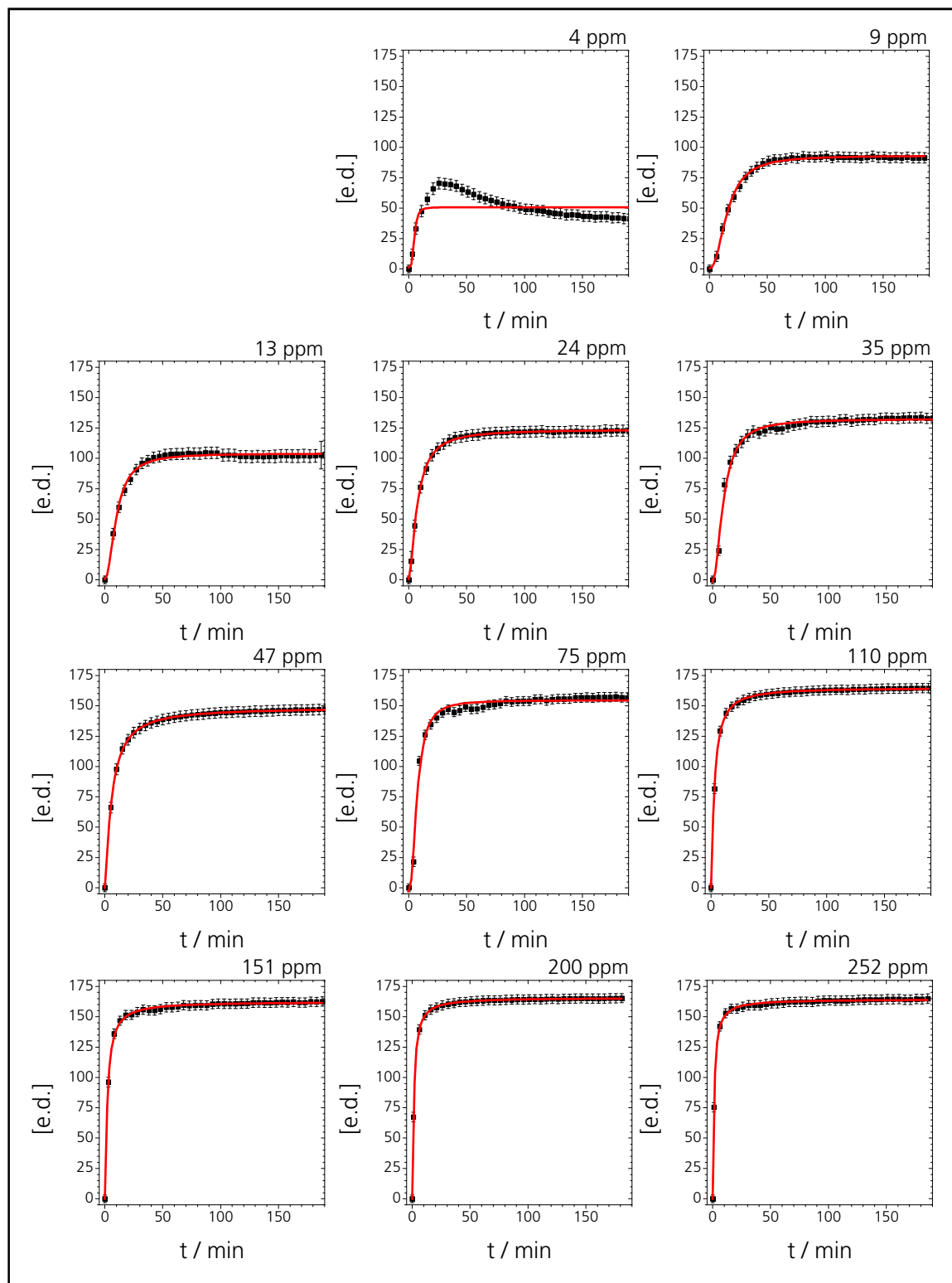


**Figure C23.** Increase of [e.d.] during reaction of indicator particles SR@Si 2 with different concentrations of propionaldehyde. Indicator particles were fixed in screw caps using PTFE tape as barrier. Data shown here was fitted with logistic fit functions whereat fit parameters are summarized in Appendix (Table G7) (mean  $\pm$  SDM; N = 5).

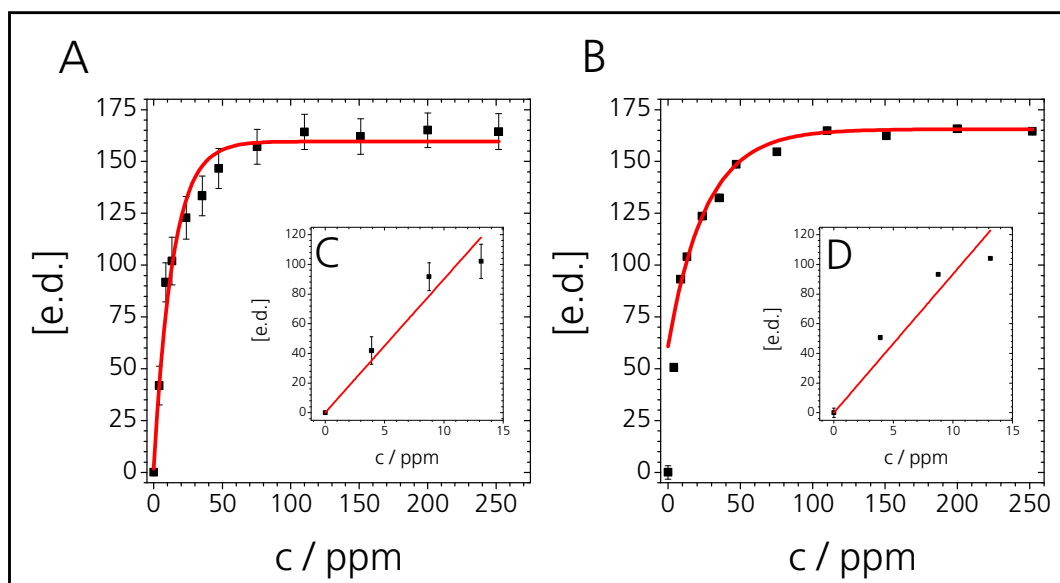


**Figure C24.** Propionaldehyde calibration plot for calculated [e.d.] of color change. The data is derived from time-dependent curves (Figure C23). Saturation values for each concentration were calculated by the mean of the last ten data points (130–180 min) for **A**. For **B** values received from logistic fit functions were used. Calibration plots **A** and **B** were fitted with an exponential association. Small graphs **C** and **D** show the linear response for small propionaldehyde concentrations (mean  $\pm$  SDM; N = 5).

Time-dependent signal increase of [e.d.] was described by saturation processes for all propionaldehyde concentrations (Figure C23). Saturation curves were fitted using a logistic fit function (Equation C7). Determination of saturation values was performed by applying two different calculation methods (see chapter 3.7): Afterwards data was plotted against respective propionaldehyde concentrations (Figure C24, A and B). The resulting calibration curves were fitted by an exponential association ( $R^2 = 0.97$  for A and  $R^2 = 0.99$  for B). For small propionaldehyde concentrations (0–13 ppm) a linear signal response was observed (Figure C24, C and D) whereas the fitting was performed by fixing the intercept to 0. Parameters of linear fit functions of graphs C ( $R^2 = 0.96$ ) and D ( $R^2 = 0.97$ ) are summarized in Table C16. The presented LODs were calculated by three times standard deviation (for details see chapter 3.7) and error propagation was performed using parameters of linear fits.

**Table C16.** Fit parameters and calculated LODs for linear fits of Figure C24, C and D.

	Slope $\pm$ error / ppm <sup>-1</sup>	Intercept	LOD $\pm$ error / ppm
Fig. 24, C	9.0 $\pm$ 0.8	0	1.07 $\pm$ 0.09
Fig. 24, D	9.3 $\pm$ 0.8	0	1.03 $\pm$ 0.09

### 4.2.3 Calibration with acetaldehyde

#### Data evaluation by [B/R]

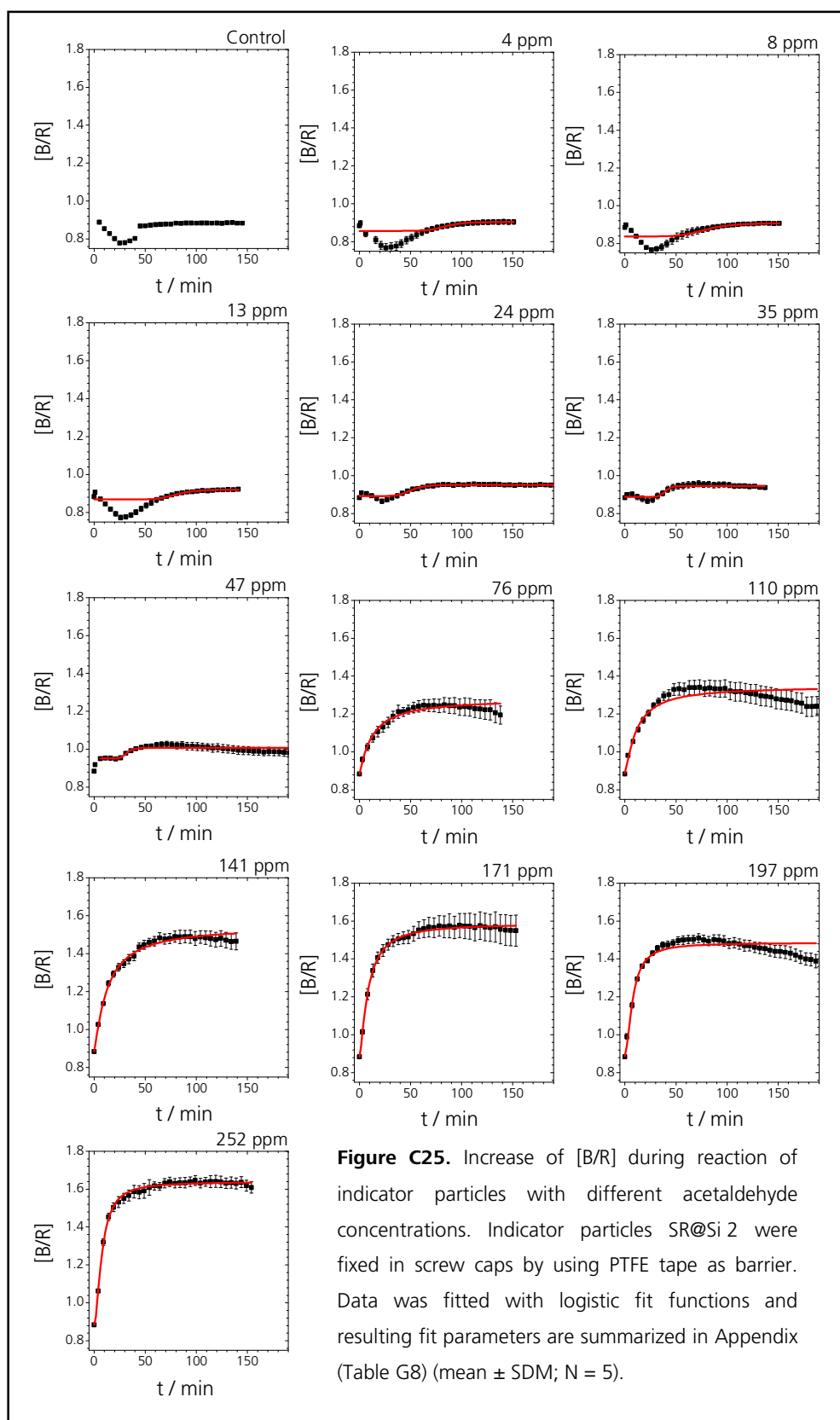


**Figure C25.** Increase of  $[B/R]$  during reaction of indicator particles with different acetaldehyde concentrations. Indicator particles SR@Si 2 were fixed in screw caps by using PTFE tape as barrier. Data was fitted with logistic fit functions and resulting fit parameters are summarized in Appendix (Table G8) (mean  $\pm$  SDM;  $N = 5$ ).



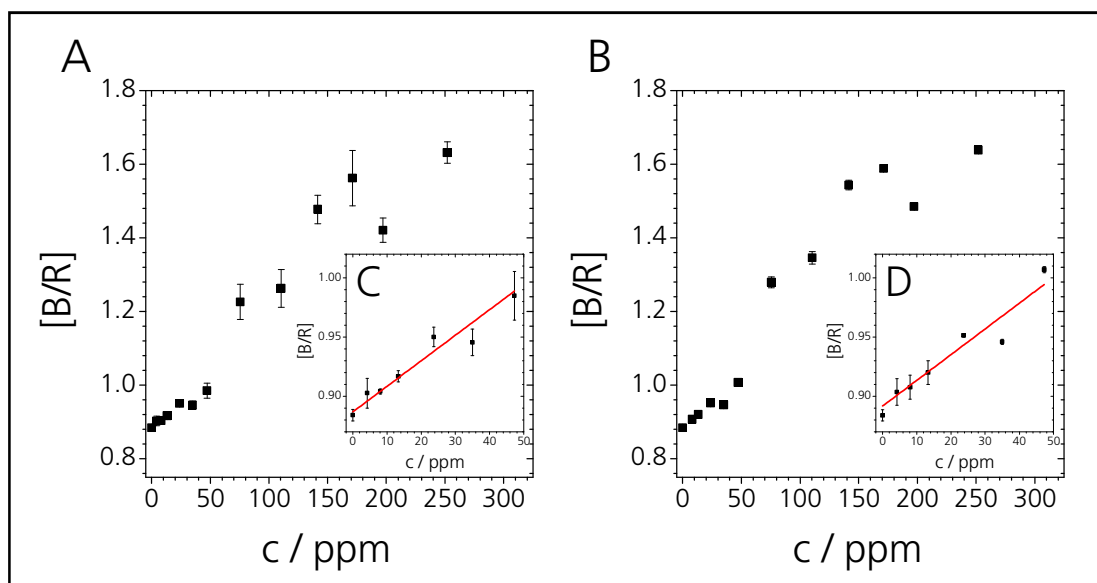


**Figure C26.** Acetaldehyde calibration plots for calculated ratios of blue and red color channel [B/R]. The data is derived from time-dependent curves (Figure C25). Saturation values for each concentration were calculated by the mean of the last ten data points (130-180 min) for **A**. For **B** end points were determined from fit parameters of logistic fit functions. Small graphs **C** and **D** show a linear response for small acetaldehyde concentrations (mean  $\pm$  SDM; N = 5).

Time-dependent signal increase of [B/R] has been successfully described by saturation processes for all acetaldehyde concentrations (Figure C25) so that the curves were fitted using a logistic fit function (Equation C7). The corresponding saturation values were determined by two different calculation methods and data was plotted against the respective acetaldehyde concentrations resulting in Figure C26, graphs A and B. The resulting curves have not been fitted, however, for small acetaldehyde concentrations a linear signal response was observed (Figure C27, C and D). The parameters from linear fit functions of graphs C ( $R^2 = 0.95$ ) and D ( $R^2 = 0.95$ ) are summarized in Table C17. LODs were calculated here by three times standard deviation (for details see chapter 3.7) and error propagation was performed using the parameters of linear fits.

**Table C17.** Fit parameters and calculated LODs for linear fits of Figure C26, graphs C and D.

	Slope $\pm$ error / ppm <sup>-1</sup>	Intercept $\pm$ error	LOD $\pm$ error / ppm
Fig. 26, C	0.0022 $\pm$ 0.0003	0.887 $\pm$ 0.003	5 $\pm$ 2
Fig. 26, D	0.0022 $\pm$ 0.0005	0.89 $\pm$ 0.028	3 $\pm$ 8

## Data evaluation by [B/G]

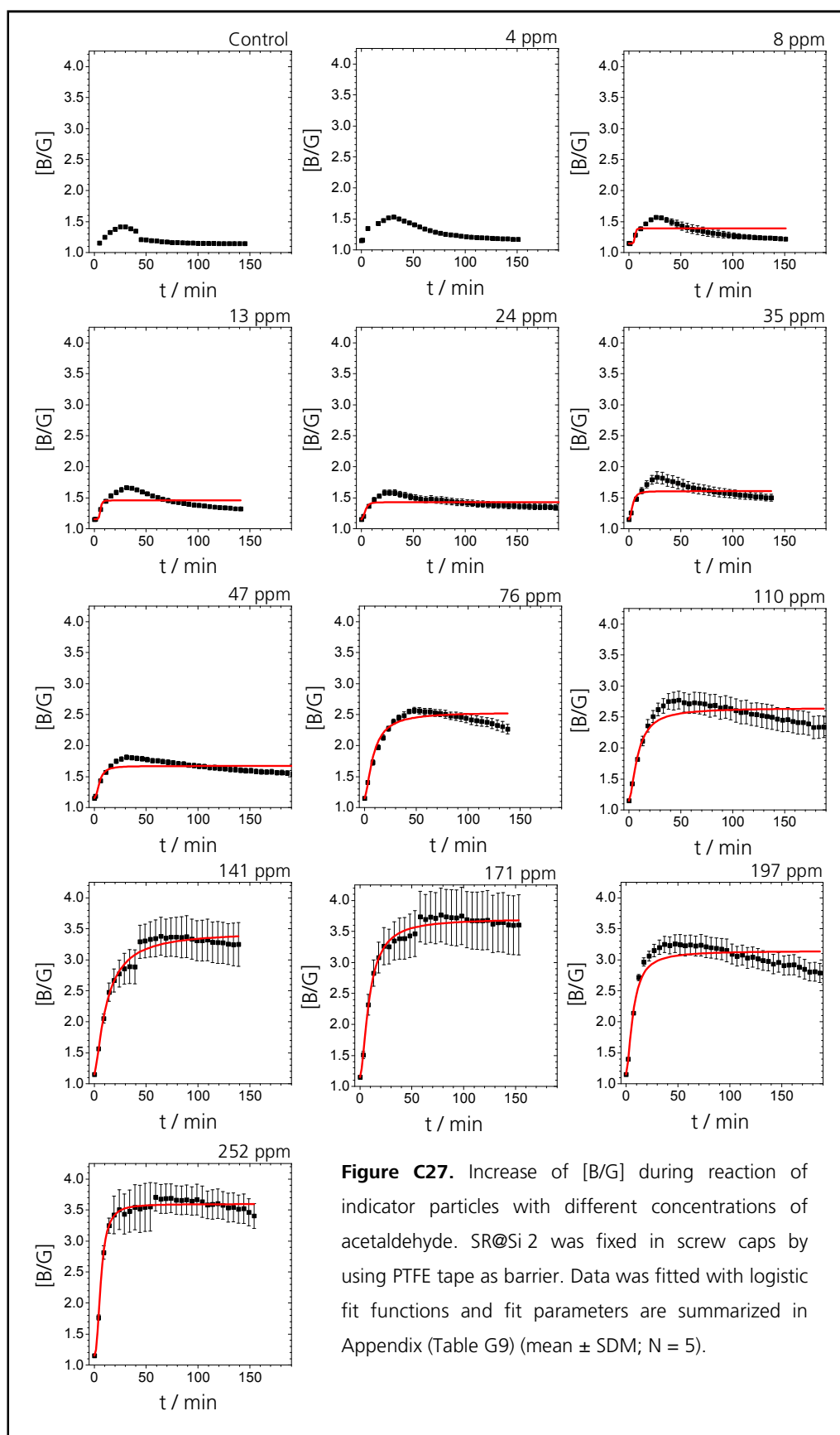


**Figure C27.** Increase of [B/G] during reaction of indicator particles with different concentrations of acetaldehyde. SR@Si 2 was fixed in screw caps by using PTFE tape as barrier. Data was fitted with logistic fit functions and fit parameters are summarized in Appendix (Table G9) (mean  $\pm$  SDM; N = 5).

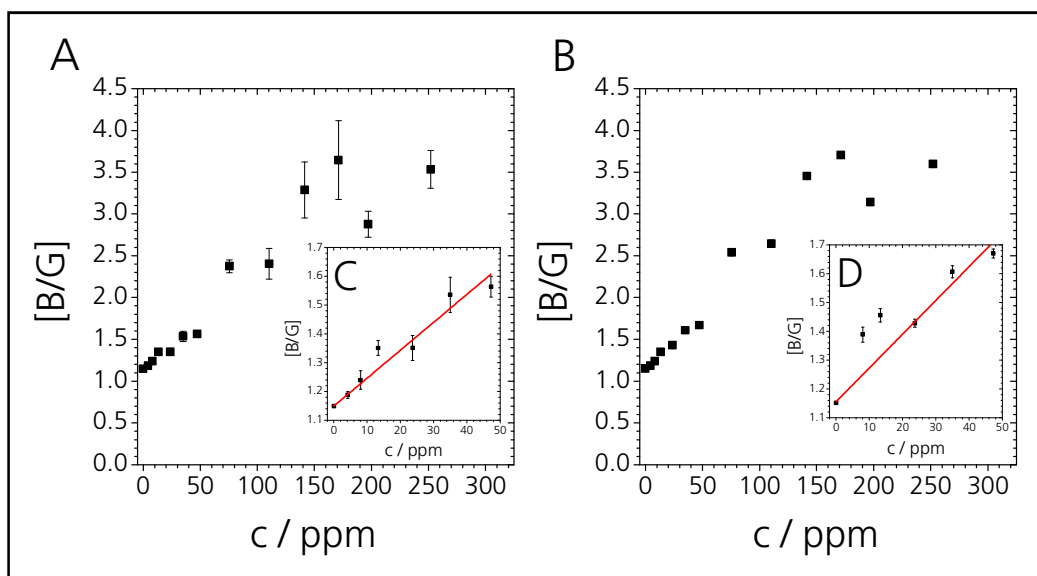


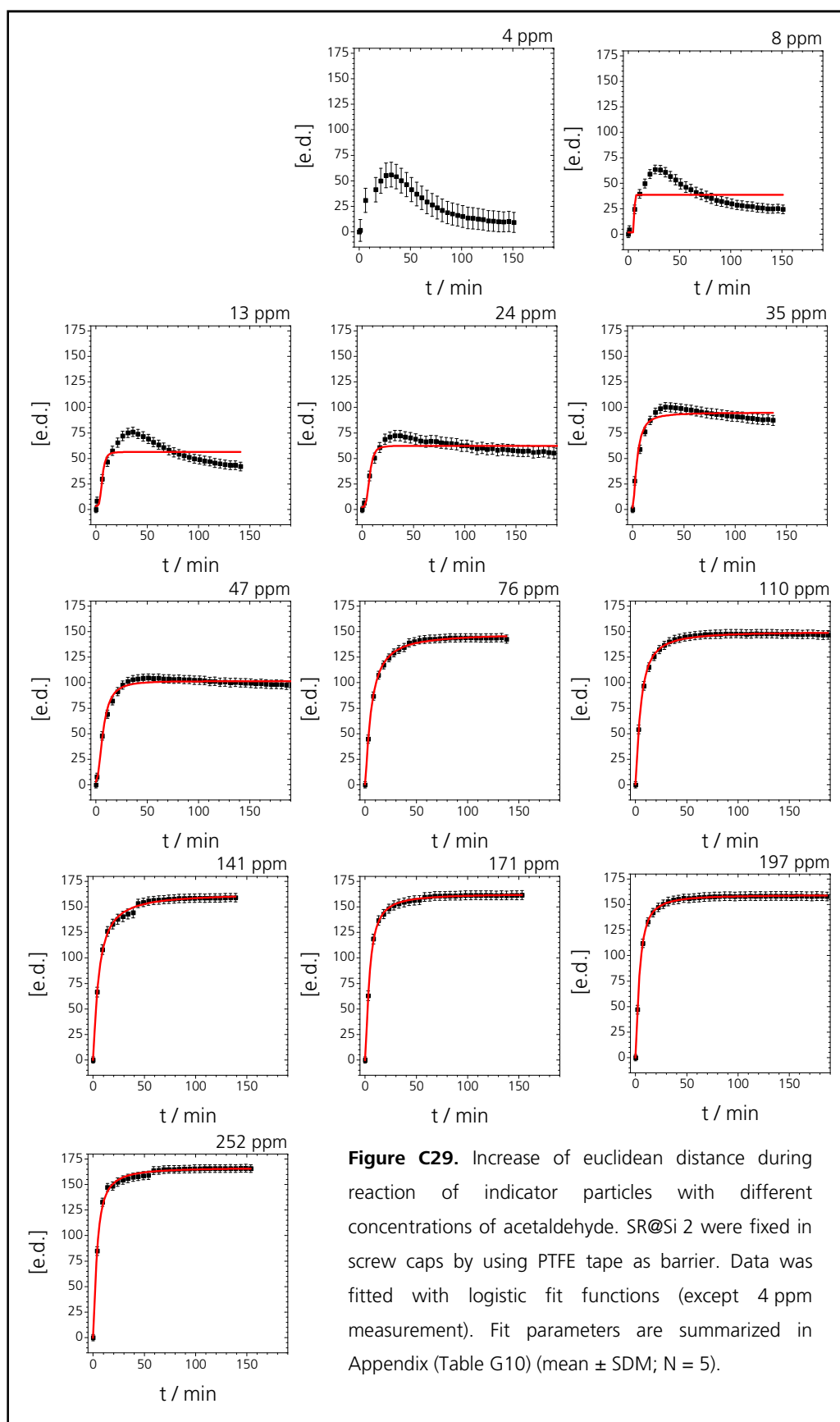
**Figure C28.** Acetaldehyde calibration plots for ratios of blue and green color channel [B/G]. The data is derived from time-dependent curves (Figure C27). Saturation values for each concentration were calculated by the mean of the last ten data points (130-180 min) for **A**. For **B** end points were determined from fit parameters of logistic fit functions. Small graphs **C** and **D** show a linear response for small acetaldehyde concentrations (mean  $\pm$  SDM; N = 5).

Time-dependent signal increases of [B/G] have been successfully described by saturation processes for all acetaldehyde concentrations except for 4 ppm (Figure C27). These saturation curves were fitted with a logistic fit function (Equation C7). Based on the data saturation values were calculated by two different methods (see chapter 3.7) and plotted against the respective aldehyde concentrations (Figure C28, A and B). The resulting plot could not be fitted, however, for small hexanal concentrations a linear signal response was observed (Figure C28, C and D). Parameters of linear fit functions for graphs C ( $R^2 = 0.95$ ) and D ( $R^2 = 0.95$ ) are summarized in Table C18. LODs were calculated by three times standard deviation (for details see chapter 3.7) and error propagation was performed using the received parameters of linear fits (Table C18).

**Table C18.** Fit parameters and calculated LODs for linear fits of Figure C28, graphs C and D.

	Slope $\pm$ error / ppm <sup>-1</sup>	Intercept $\pm$ error	LOD $\pm$ error / ppm
Fig. 28, C	$0.0097 \pm 0.0009$	$1.150 \pm 0.004$	$1.2 \pm 0.4$
Fig. 28, D	$0.012 \pm 0.001$	$1.16 \pm 0.01$	$1 \pm 1$

## Data evaluation by [e.d.]



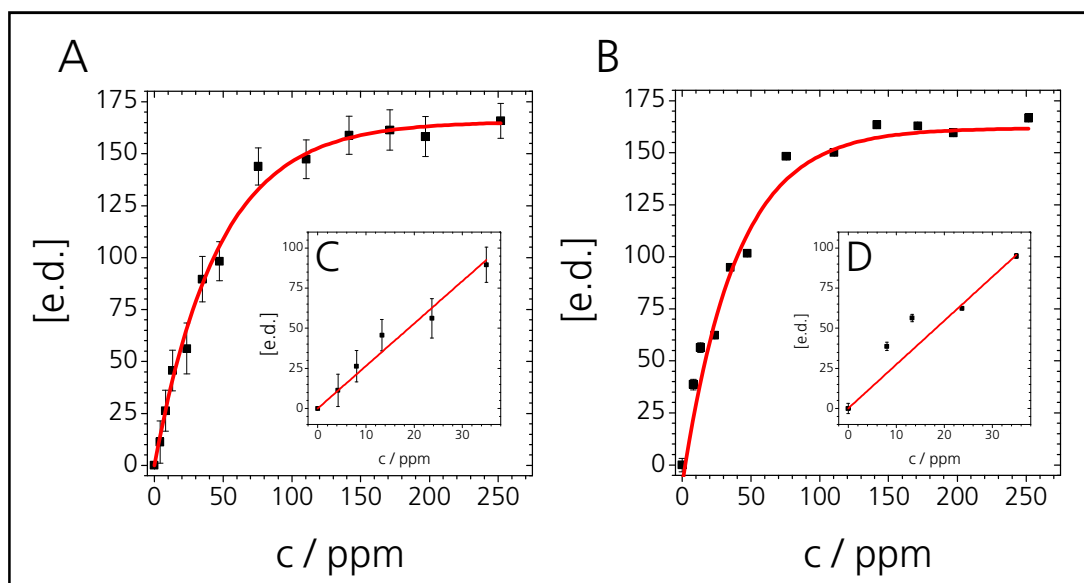


**Figure C30.** Acetaldehyde calibration plot for signals [e.d.] of color change. The data is derived from time-dependent curves (Figure C29) here. Saturation values were calculated by the mean of the last ten data points (130-180 min) for **A**. For **B** end points were determined from fit parameters of logistic fit functions, however, determination of 4 ppm was not practicable. Calibration plots **A** and **B** were fitted with an exponential association whereas small graphs **C** and **D** show a linear response for small acetaldehyde concentrations (mean  $\pm$  SDM; N = 5).

Time-dependent signal changes of [e.d.] have been successfully described by saturation processes for all acetaldehyde concentrations except for 4 ppm (Figure C29). Saturation curves were fitted using a logistic fit function (Equation C7). Saturation values were determined by two different methods and data was plotted against the respective acetaldehyde concentrations (Figure C30, A and B). Afterwards the resulting calibration curves were fitted by an exponential association with excellent accuracy ( $R^2 = 0.99$  for A and  $R^2 = 0.95$  for B). For small acetaldehyde concentrations a linear signal response was observed (Figure C30, graphs C and D) whereat fitting was performed fixing the intercept to zero. The parameters of linear fit functions for graphs C ( $R^2 = 0.98$ ) and D ( $R^2 = 0.98$ ) are summarized in Table C19. LODs calculation was performed by three times standard deviation method (for details see chapter 3.7) and error propagation was carried out based on the parameters of linear fits (Table C19).

**Table C19.** Fit parameters and resulting LODs for linear fits of Figure C30, graphs C and D.

	Slope $\pm$ error / ppm <sup>-1</sup>	Intercept	LOD $\pm$ error / ppm
Fig. 30, C	$2.6 \pm 0.1$	0	$3.6 \pm 0.2$
Fig. 30, D	$2.7 \pm 0.2$	0	$3.5 \pm 0.2$

### 4.3 Comparison of limits of detection (LOD) and sensitivities

Calculated limits of detection (LOD) derived from calibration measurements are summarized in Table C20. All LOD values shown here were determined by simplified calculation methods applying Equations C14-C16 (for details see chapter 3.7).

LODs derived from two different methods of end-point determination were all found to have the same dimension which is true for all three aldehydes under study as well as all methods of data evaluation. For example LODs for hexanal calculated by [B/R] are  $0.7 \pm 0.4$  ppm for end point determination by the last ten data points and  $0.5 \pm 0.7$  ppm for end point determination by logistic fit functions.

Regarding single aldehydes the lowest LODs have been obtained for each using data from [B/G]. The LOD for hexanal for example was  $0.3 \pm 0.2$  ppm using the data of [B/G] while [B/R] gave a value of  $0.7 \pm 0.4$  ppm and the [e.d.]  $1.8 \pm 0.2$  ppm, respectively.

**Table C20.** Overview of calculated LODs for hexanal, propionaldehyde, and acetaldehyde. For each aldehyde three different methods of data evaluation were performed ([B/R], [B/G], and [e.d.]). Furthermore, two different methods of end point determination for the time-dependent concentration plots were applied.

		LOD $\pm$ error / ppm	
	Method of data evaluation	End point determination by the mean of the last ten data points	End point determination by logistic fit function
Hexanal	[B/R]	$0.7 \pm 0.4$	$0.5 \pm 0.7$
	[B/G]	$0.3 \pm 0.2$	$0.1 \pm 0.7$
	[e.d.]	$1.8 \pm 0.2$	$1.9 \pm 0.1$
Propion-aldehyde	[B/R]	$2 \pm 1$	$2.1 \pm 0.9$
	[B/G]	$0.4 \pm 0.2$	$2 \pm 2$
	[e.d.]	$1.07 \pm 0.09$	$1.03 \pm 0.09$
Acetaldehyde	[B/R]	$5 \pm 2$	$3 \pm 8$
	[B/G]	$1.2 \pm 0.4$	$1 \pm 1$
	[e.d.]	$3.6 \pm 0.2$	$3.5 \pm 0.2$

By comparing LOD values of hexanal, propionaldehyde, and acetaldehyde it can be concluded that LODs for hexanal and propionaldehyde are in the same order of magnitude (about 0.5 - 2 ppm) whereas values for acetaldehyde are slightly higher (about 1 - 5 ppm). On the one hand this could be due to the lower reactivity of acetaldehyde in contrast to propionaldehyde and hexanal. Acetaldehyde has a very low boiling point (20 °C) which causes systematic errors during the preparation of calibration solutions and the measurement samples at room temperature. Hence, small errors in the calibration curve can have a significant effect on the final LOD values.

**Table C21.** Overview of sensitivities from linear fits of the three aldehydes under study. For each aldehyde three different methods of data evaluation were performed ([B/R], [B/G], and [e.d.]). Furthermore, two different methods for end point determination of time-dependent concentration plots were applied.

	Method of data evaluation	Sensitivity $\pm$ error / ppm <sup>-1</sup>	
		End point determination by the mean of the last ten data points	End point determination by logistic fit function
<b>Hexanal</b>	[B/R]	0.0171 $\pm$ 0.0006	0.017 $\pm$ 0.001
	[B/G]	0.038 $\pm$ 0.003	0.038 $\pm$ 0.003
	[e.d.]	5.4 $\pm$ 0.5	5.2 $\pm$ 0.3
<b>Propionaldehyde</b>	[B/R]	0.009 $\pm$ 0.001	0.0085 $\pm$ 0.0005
	[B/G]	0.033 $\pm$ 0.003	0.033 $\pm$ 0.004
	[e.d.]	9.0 $\pm$ 0.8	9.3 $\pm$ 0.8
<b>Acetaldehyde</b>	[B/R]	0.0022 $\pm$ 0.0003	0.0022 $\pm$ 0.0005
	[B/G]	0.0097 $\pm$ 0.0009	0.012 $\pm$ 0.001
	[e.d.]	2.6 $\pm$ 0.1	2.7 $\pm$ 0.2

In Table C21 sensitivities of all experiments and evaluation methods derived from calibration measurements with hexanal, propionaldehyde, and acetaldehyde are summarized. The sensitivity values here confirm the conclusions made from LODs in Table C20.

Comparing the values received by different methods of end point determination it can be stated that results are almost the same for both procedures. The sensitivity for the calibration of hexanal and data evaluation by [B/R] for example is 0.0171  $\pm$  0.0006 ppm using end point determination

by the mean of last ten data points. In comparison, the sensitivity for data evaluation by logistic fit function parameters was found to be  $0.017 \pm 0.001$  ppm.

Highest sensitivity values for individual aldehydes are obtained for data evaluation by [e.d.]. Furthermore, values for [B/G] are higher than values obtained from [B/R]. However, these sensitivity values strongly depend on the dimension of the signal values and of course the data evaluation method. Therefore, it is not reasonable to compare sensitivity values obtained by different methods.

For sensitivities derived from [B/R] acetaldehyde gave the worst results. Values are higher for propionaldehyde and the highest sensitivity is obtained from hexanal. The exact same is true for data evaluation by [B/G]. For data obtained from [e.d.] in contrast the highest values are observed for calibration of propionaldehyde followed by hexanal and finally acetaldehyde.

The sensitivities reflect the LOD values since calibration curves with a high sensitivity show lower limits of detection. For data evaluation by [B/R] the sensitivity decreases from hexanal to propionaldehyde and acetaldehyde (Table C21) and the same trend is also reflected by the calculated LODs (Table C20). The lowest LOD is obtained for hexanal with  $0.7 \pm 0.4$  ppm. It increases to  $2 \pm 1$  ppm for propionaldehyde and  $5 \pm 2$  ppm for acetaldehyde. Furthermore, the same is obtained from data evaluation by [B/G] and [e.d.].

In summary the calibration measurements show that indicator particles provide a very good response towards hexanal, propionaldehyde, and acetaldehyde. For all aldehydes under study a linear signal response is obtained for small aldehyde concentrations (0-30 ppm for hexanal or 0-40 ppm for propionaldehyde and acetaldehyde). Highest sensitivity values were obtained for hexanal, followed by propionaldehyde and acetaldehyde. Moreover, LODs of about 1 ppm for hexanal and propionaldehyde and a slightly higher LOD of 3 ppm for acetaldehyde were achieved. As a consequence, data evaluation by [B/G] provides the best method here since lowest LODs are obtained compared to [B/R] and [e.d.].



#### 4.4 Assessment of cross sensitivities

In order to study cross sensitivities of SR@Si 2 for other substances, samples with PTFE strip as barrier were prepared as described in chapter 3.2. A qualitative screening was performed with the following twelve substances: acetone, acetonitrile, formic acid, butan-2-one, chloroform, acetic acid, ethylacetate, ethanol, water, methanol, ammonia (33-35% (w/v) in water), and toluene. Measurements were performed by pipetting 10  $\mu$ L of substance in glass vials and subsequently closing the vials with prepared screw caps. Experiments were carried out here in triplicate for each substance. Data evaluation was performed by calculating [B/R], [B/G], and [e.d.]. Moreover, end-points were determined by calculating the mean of last ten data points for each substance after 150 min. Finally, image acquisition was performed each five minutes for a measuring period of three hours (for details see chapter 3.4) applying the same camera settings as for previous measurements.

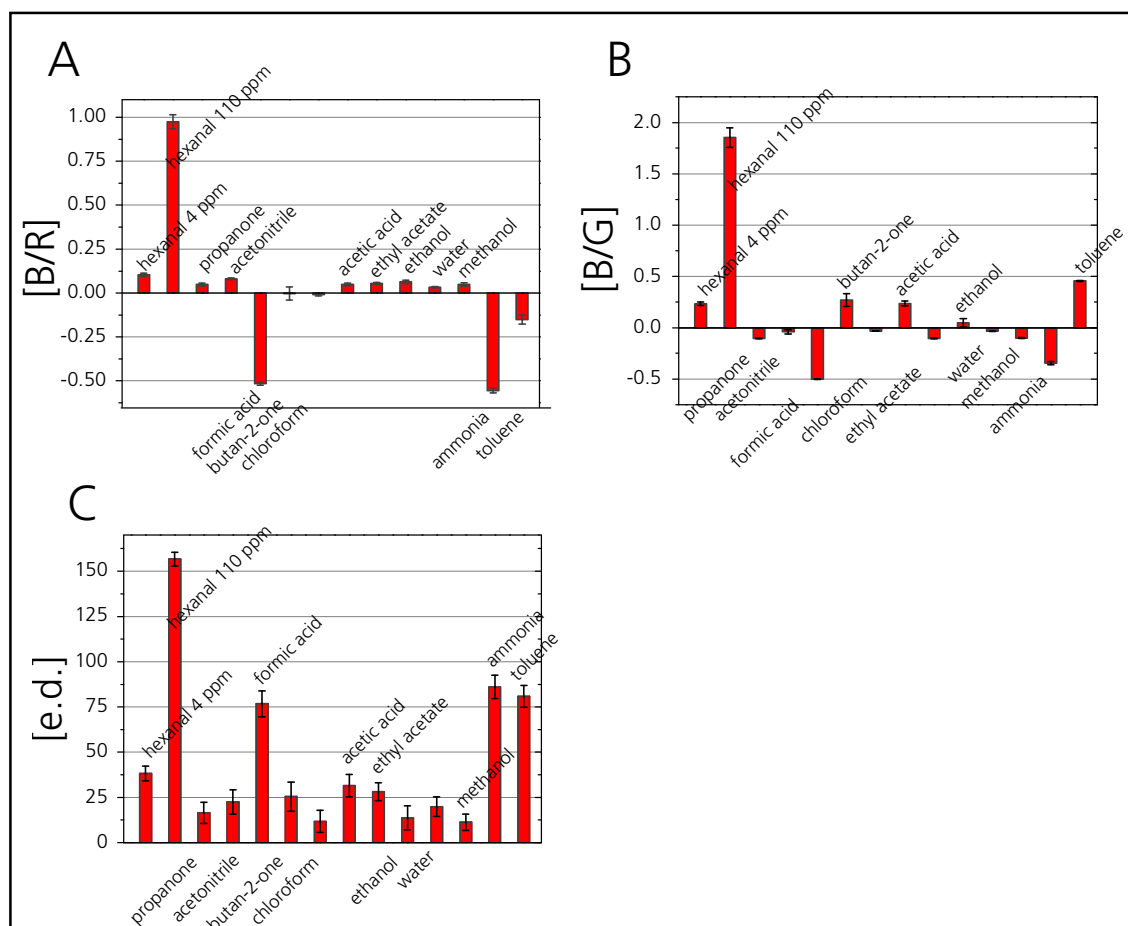


**Figure C31.** Signals of [B/R] (A), [B/G] (B), and [e.d.] (C) derived from end-point determination by mean of the last ten data points. Twelve substances and hexanal in a concentration of 4 and 110 ppm are plotted. For **A** and **B** the signals were normalized to the value of *n*-hexane by subtracting the *n*-hexane value. For **C** the value of *n*-hexane was used as reference point (mean  $\pm$  SDM; N = 3 for the 12 substances and N = 5 for hexanal values).

Signals of [B/R] (Figure C31, A), [B/G] (Figure C31, B), and [e.d.] (Figure C31, C) are shown as bar graphs. For comparison hexanal values for 4 and 110 ppm are plotted as well. For graphs A and B the signals were normalized to the value of *n*-hexane whereas for graph C the value of *n*-hexane was used as reference point for calculating [e.d.] (for details see chapter 3.7).

Negative values for [B/R] were obtained for formic acid, ammonia, and toluene (Figure C31, A) with ammonia and formic acid showing the greatest response. Values for butan-2-one and chloroform in contrast are close to zero. The signals for hexanal and all other substances are in the positive range and the intensities of all compounds lacking an aldehyde group are below the value for 4 ppm hexanal.

For [B/G] (Figure C31, B) formic acid and ammonia also give negative values, however, the signal for toluene is in the positive range. Small negative signals are also obtained for propanone, acetonitrile, chloroform, ethylacetate, water, and methanol here. Hexanal and all other compounds again give positive values including butan-2-one, acetic acid, and ethanol.

Due to the method of determination all [e.d.] are in the positive range. The highest values were obtained for 110 ppm hexanal here, followed by formic acid, ammonia and toluene. All remaining substances show signal intensities comparable to the response for 4 ppm hexanal.

Depending on the methods of data evaluation (Figure C31, bar graphs A, B, and C) different signal patterns for the individual substances were observed. Hexanal signals for example are positive in each graph whereas formic acid shows a negative signal for [B/R] as well as for [B/G]. In contrast, for [e.d.] a highly positive signal is received and the same is also true for ammonia. Toluene instead shows a slightly negative [B/R] but a highly positive [B/G] and [e.d.].

Finally, to combine the three different signals for each individual substance further multivariate statistics in form of principal component analysis (PCA). Score data forming the basis for the PCA plot shown in Figure C32 is presented in Appendix (Table G11). Additionally, correlation matrix, eigenvalues, and extracted eigenvalues calculated during the mathematical transformations are given in Appendix (Table G12-G14). Moreover, the theoretical background for principal component analysis is described in part B (chapter 2).

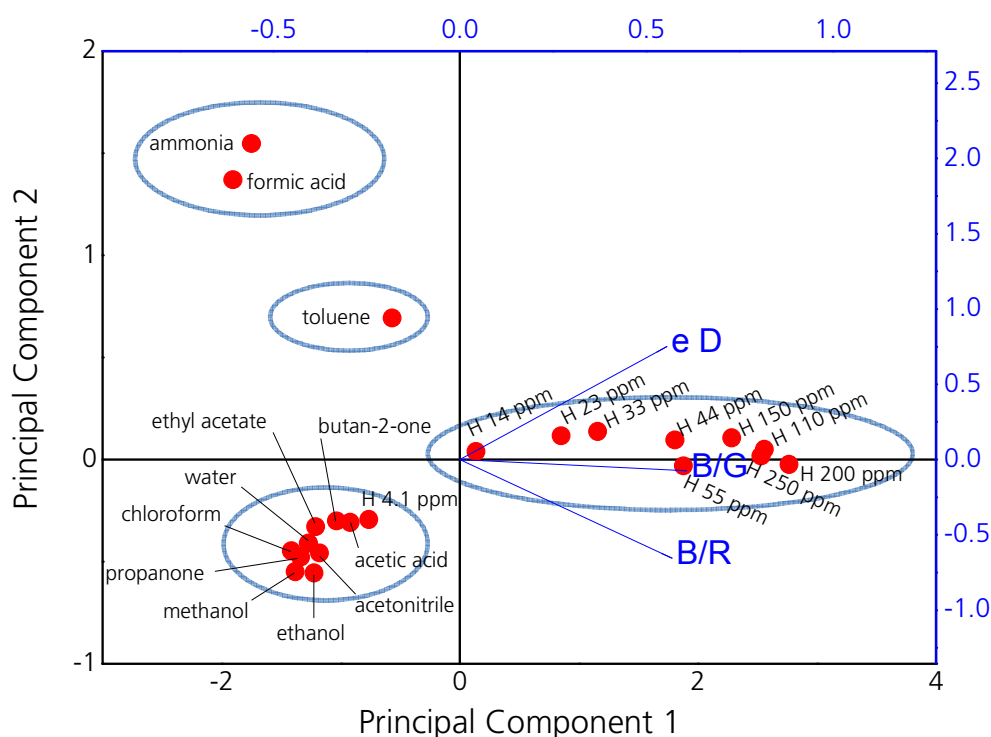


**Figure C32.** Principal component analysis for the twelve substances under study and hexanal in concentrations from 4 to 250 ppm (hexanal in different concentrations is named as H x ppm in the graph). B/R, B/G, and e.d. display the components of PCA (for details see part B, chapter 2.)

Figure C32 shows the plot obtained from principal component analysis for acetone, acetonitrile, formic acid, butan-2-one, chloroform, acetic acid, ethylacetate, ethanol, water, methanol, ammonia (33-35% (w/v) in water), and toluene. Hexanal values are shown for comparison. The signals can be classified into four groups. The first group is displayed by hexanal signals received for concentrations from 14 to 250 ppm. The second group consists of ammonia and formic acid whereas toluene represents the third group. Finally, all other substances are combined in the fourth group.

The significantly different signals for ammonia and formic acid can be explained by acid-base reactions with Schiff's reagent and thus the inactivation of the detection reagent. Ammonia is basic ( $pK_a = 9.2$ ) and can neutralize sulfonic acid groups of  $SR@Si$ . Formic acid in contrast is a strong acid ( $pK_a = 3.8$ ) which is known to deactivate Schiff's reagent by protonation of amino groups.<sup>101</sup> Hence, nucleophiles become inactivated and cannot react with aldehydes anymore. Acetic acid in contrast is not strong enough ( $pK_a = 4.75$ ) to protonate nitrogen atoms of Schiff's reagent. As a result the signal for acetic acid is found in the group of substances which do not interact with  $SR@Si$ .

Furthermore, toluene also seems to react with the indicator particles similar to formic acid and ammonia. A possible explanation can be strong  $\pi$ - $\pi$ -interactions between toluene and the aromatic backbone of Schiff's reagent which might hinder the reaction with aldehydes and thus change the signal pattern of SR@Si 2.

In general principal component analysis as a method of multivariate analysis provides a great tool for data simplification and thus gives access to signal patterns which are too complex to be observed without these mathematical transformations. The obtained PCA plot (Figure C32) in this case allows for an easy differentiation of signals for hexanal and all other tested substances.

#### 4.5 Investigating long-term stability of indicator particles

Sufficient long-term stability is essential for the successful application of indicator particles for food packaging. Most fat-containing foods have a shelf life of six to nine months. Thus, indicator particles have to be stable for at least six months.

SR@Si 2 was used for long-term stability measurements and stored in a glass with screw cap under ambient temperature, air and light. In time intervals of about one month particles were immobilized into screw caps with PTFE as barrier (see chapter 3.2) and the color change for three different concentrations of hexanal was determined. Chosen concentrations were 14 ppm, 33 ppm, and 110 ppm hexanal here. All measurements were performed in five replicates evaluated by plotting [B/G] as already described before (Figure C33). Additional plots for [B/R] and [e.d.] are given in Appendix (Figure G1 and G2).

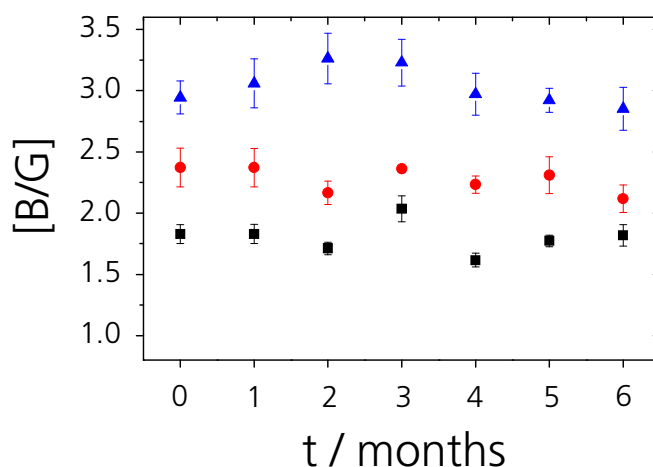


**Figure C33.** Long-term stability of SR@Si 2 evaluated by [B/G]. Three different hexanal concentrations were measured (14 ppm, ■, black; 33 ppm, ●, red; 110 ppm, ▲, blue) over 6 months (mean  $\pm$  SDM; N = 5).

As shown in Figure C33 signals provide good stability over six months. Small alterations in signal intensities are likely due to errors originating from preparing and pipetting calibration solutions. However, for each hexanal concentration a stable signal was obtained and no significant degradation of the indicator was observable. This observation, however, was further proofed statistically by performing a Neumann's trend test.

### Trend-test by Neumann

The stability of particles can be verified statistically by applying Neumann's trend-test (Equations C17-C19). If a calculated test value (TV) is higher than the corresponding tabular value (W) the trend is excluded by this method.<sup>103,104</sup>

$$TV = \frac{\Delta^2}{s^2} \quad \text{Eq. C17}$$

$$\Delta^2 = \frac{1}{n-1} \sum_{i=1}^{n-1} (x_i - x_{i+1})^2 \quad \text{Eq. C18}$$

$$s^2 = \frac{1}{n-1} \sum (x_i - \bar{x})^2 \quad \text{Eq. C19}$$

$\Delta^2$       scattering square of the differences

$s^2$       variance

$n$       number of measuring values

$x_i$       measuring value  $i$

$\bar{x}$       mean value of test series

For a plausibility of 99% and for  $N = 7$  the tabular value is:  $W = 0.6140$ .<sup>105</sup>

For a plausibility of 95% and for  $N = 7$  the tabular value is:  $W = 0.9359$ .<sup>105</sup>

Tabular values  $W$  are given in Appendix (Table G15).

A trend test was performed using the [B/G] data obtained for the reaction with 110 ppm hexanal. The resulting TV was calculated to be 0.8710. Since  $W$  equals 0.6140 (plausibility 99%) and 0.9359 (plausibility 95%) a trend can be excluded with a plausibility of 99%.

#### 4.6 Immobilization of particles in a polyvinyl acetate matrix

For application of indicator particles in food packaging systems direct immobilization in a polymer matrix was also investigated to avoid loose particles inside the packaging materials and enable convenient integration techniques like printing. For this polyvinyl acetate (PVA) was used as polymer matrix as it is already licensed for food compatibility.<sup>106</sup> PVA is used in food industry even for the manufacturing of chewing gums.<sup>107</sup>

First of all, a suitable solvent had to be found to dissolve the polymer, but not the Schiff's reagent from the silica particles. Hence, the influence of the following solvents towards SR@Si 2 was investigated: THF, toluene, acetone, water, petrolether, *n*-hexane, ethyl acetate, ethanol, chloroform, and methanol. For this purpose 20 mg of indicator particles were mixed with 2 mL of each solvent (Figure C34). THF and especially all polar protic solvents (water, ethanol, and methanol) readily dissolve the Schiff's reagent and wash it off the silica particles as shown in Figure C34.

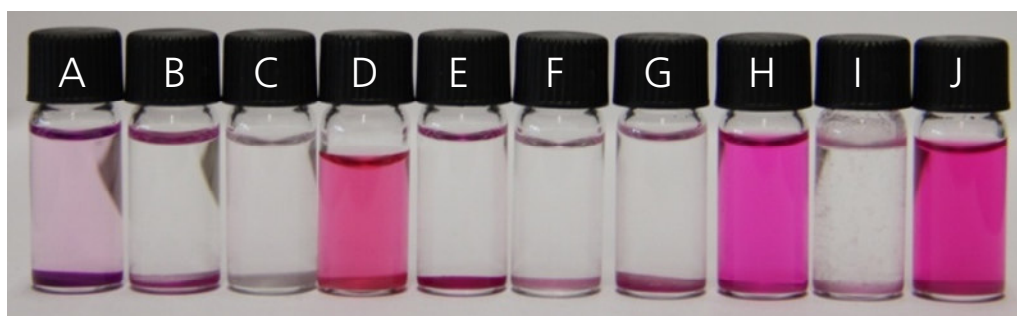


**Figure C34.** 20 mg of SR@Si 2 in 2 mL THF (A), toluene (B), acetone (C), water (D), petroleum ether (E), *n*-hexane (F), ethylacetate (G), ethanol (H), chloroform (I), and methanol (J).

As a result ethyl acetate was used as a solvent for the experiments as polyvinyl acetate also shows a very good solubility in this solvent. Detailed instructions for the preparation are described in chapter 3.3. Particles were immobilized in PVA solutions of two different concentrations (10% and 20%, mass ratio). These mixtures were pipetted into screw caps with integrated PET foils (8 mm in diameter). A total amount of 30 mg indicator particles per sample was used to allow a comparison with previously obtained data from the calibration measurements with loose particles. The same amount of particles was also used for samples prepared with PTFE strips as barrier layer.

For quantifying the color change of prepared particle-polymer layers two different concentrations of hexanal were investigated (33 and 110 ppm). The following camera settings were used for these measurements: exposure time 1/40 s, F-stop F/5.6, and ISO 250. Measurements were performed in five replicates with 10  $\mu$ L of respective calibration solution (for details see chapter 3.6). Thus, two different particle-PVA layers using 10% and 20% (mass ratio) PVA were tested with two different hexanal concentrations each.

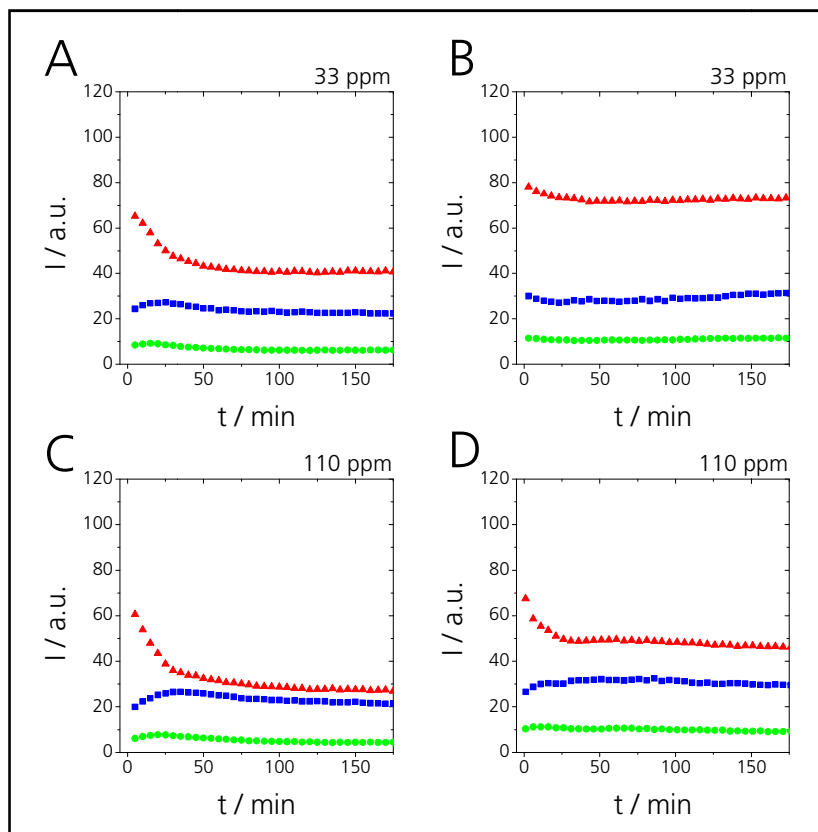


**Figure C35.** Time-dependent intensity changes of red ( $\blacktriangle$ ), green ( $\bullet$ ), and blue ( $\blacksquare$ ) color channels for concentrations of 33 ppm and 110 ppm hexanal. SR@Si 2 in 10% polyvinyl acetate (**A** and **C**) and SR@Si 2 in 20% polyvinyl acetate (**B** and **D**) were investigated (mean  $\pm$  SDM;  $N = 5$ ).

Changes of red, green, and blue color channel intensities in the presence of 33 and 110 ppm hexanal were again plotted against time (Figure C35). Graphs A and C show changes for particles immobilized in PVA solution (10%) while B and D indicate the signal changes in PVA solution (20%) here. For all graphs a decrease was observed for the red channel intensity. For graphs A, C, and D signals of blue color channel increase whereas graph B shows a slight decrease during the first 20 minutes. The green color channel instead shows a slight increase during the first few minutes but remains nearly constant for the remaining time of the measurements (Figure C35, A-D). For a quantitative evaluation of the data  $[B/R]$  and  $[e.d.]$  were calculated.  $[B/G]$  didn't give useful results here, due to poor intensity changes of the green color channel. Time-dependent changes of  $[B/R]$  and changes in  $[e.d.]$  were plotted for particles immobilized in 10% PVA solution (Figure C36) and 20% PVA solution (Figure C37). Changes were plotted for 33 ppm and for 110 ppm hexanal for each particle-polymer layer and starting values were determined by measuring the color intensity of the respective layers in the presence of 10  $\mu$ L pure *n*-hexane (for details see chapter 3.7).

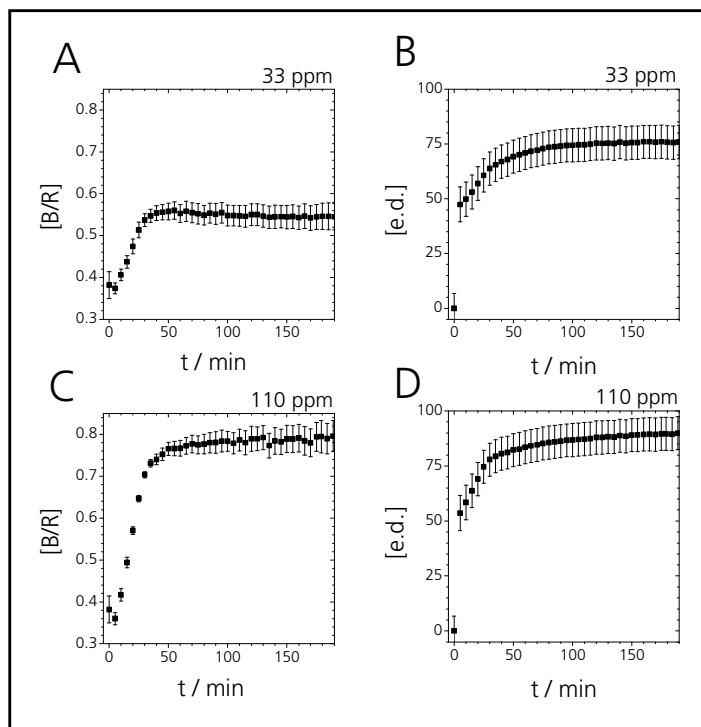


**Figure C36.** Measurements with SR@Si 2 immobilized in PVA solution (10%). Hexanal concentrations of 33 and 110 ppm were investigated. Starting value was determined by measuring pure *n*-hexane as blank, data evaluation was performed by [B/R] (graphs **A** and **C**) and calculating [e.d.] (graphs **B** and **D**) (mean  $\pm$  SDM; N = 5).

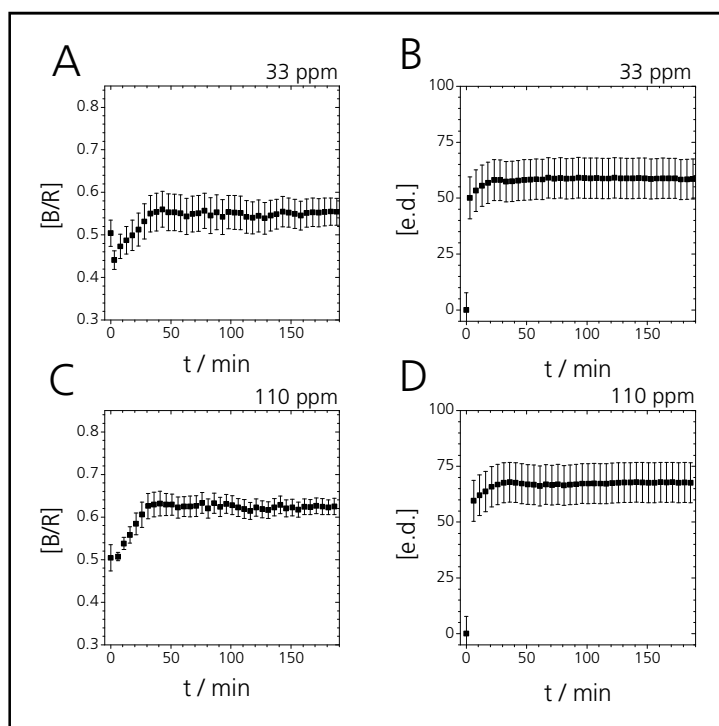


**Figure C37.** Measurements with SR@Si 2 immobilized in PVA solution (20%). Hexanal concentrations of 33 and 110 ppm were investigated. Starting value was determined by measuring pure *n*-hexane as blank, data evaluation was performed by [B/R] (graphs **A** and **C**) and calculating [e.d.] (graphs **B** and **D**) (mean  $\pm$  SDM; N = 5).



All curves reach signal saturation after about 50 minutes (Figure C36 and C37). Overall signal changes (from blank to saturation) of SR@Si 2 immobilized in 10% and 20% PVA solutions were calculated and are shown in Table C22 for reaction with 33 ppm and 110 ppm hexanal.

**Table C22.** Signal changes ( $\Delta$ ) for SR@Si 2 immobilized in 10% and 20% PVA solution for measurement of 33 and 110 ppm hexanal. Signal changes are depicted for data evaluation by [B/R] and [e.d.].

c(hexanal) / ppm	Particles in 10% PVA matrix		Particles in 20% PVA matrix	
	$\Delta$ [B/R]	$\Delta$ [e.d.]	$\Delta$ [B/R]	$\Delta$ [e.d.]
33	$0.16 \pm 0.03$	$76 \pm 7$	$0.05 \pm 0.03$	$59 \pm 9$
110	$0.79 \pm 0.03$	$90 \pm 7$	$0.12 \pm 0.02$	$68 \pm 9$

Particles immobilized in 10% PVA solution were found to show higher signal changes than particles in 20% PVA solution for 33 ppm as well as 110 ppm. The obtained values for [B/R] are  $0.16 \pm 0.03$  for 33 ppm hexanal and 10% PVA solution but only  $0.05 \pm 0.03$  for particles in 20% PVA solution. For 110 ppm hexanal the signal change obtained by particles in 10% PVA solution is  $0.79 \pm 0.03$  and  $0.12 \pm 0.02$  for 20% PVA solution. Similar results were obtained by comparing values of [e.d.].

Based on the experiments shown in this chapter it can be concluded that the concentration of polyvinyl acetate has a high influence on the performance of SR@Si 2 regarding its reaction with hexanal. By reducing the amount of polymer from 20% to 10% signal changes induced by the reaction with hexanal increase significantly. A threefold increase for example is observed for [B/R] obtained for reaction with 33 ppm hexanal by reducing the polymer by 50%. For 110 ppm hexanal the value even showed 6.5-fold enhancement.

## 4.7 Application to real food samples

Results which are described and discussed in the following chapter were obtained in cooperation with Fraunhofer IVV, Freising. The applied indicator particles were prepared in Regensburg while experiments on real food samples were performed by Fraunhofer IVV. Aim of this work was the integration of indicator particles into food packaging and its application for real food samples (Figure C38).<sup>25</sup>

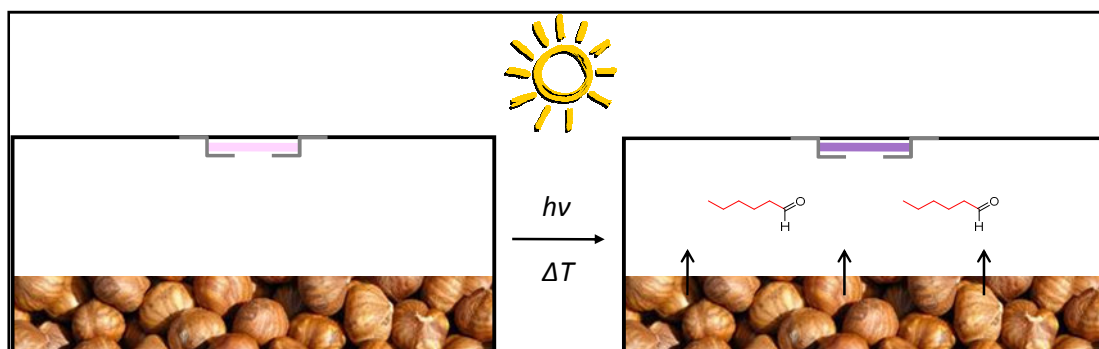


**Figure C38.** Working principle of colorimetric indicator system in food packaging. Due to deterioration of fatty food hexanal is produced which causes a color change of the detection system. Color change can be analyzed by consumers without manipulation of the packaging.

For testing the colorimetric indicator system on real food samples, fatty foods with high content of linoleic acid were chosen. Linoleic acid is a fatty acid which represents a main component in natural fats and is very prone to oxidation due to its unsaturated molecule structure. By deterioration diverse volatile substances are generated, with hexanal as the main reaction product (Table C2). Since they are widely consumed, hazelnuts, peanuts, and sunflower oil were selected as food samples. The content of linoleic acid for the three food products is shown in Table C4.

**Table C4.** Linoleic acid content in hazelnuts, peanuts, and sunflower oil.

	Total fat / wt%	Linoleic acid / wt%
Hazelnut	60-62	8-13
Peanut	50-55	3-27
Sunflower oil	~99.9	62-70

### Preparation of indicator-polymer layer and measurement samples

First of all an indicator particle-polymer mixture was prepared by applying 66 wt% ethylacetate, 20 wt% indicator particles, and 14 wt% polyvinyl acetate (Vinnapas®). The mixture was coated on a LDPE (low-density polyethylene)-foil (thickness 30 µm) using a semi-automatic varnishing machine (Coating Unit CUF5, Sumet Messtechnik, Denklingen). After drying at 80 °C the layers were laminated with a PET-foil (thickness 23 µm) using a 20 wt% PVA-ethylacetate solution as adhesion promoter (Figure C39). LDPE is often used as inner sealable coating and is very suitable for this application due to its high permeability for hexanal.<sup>108</sup> PET-foil was used as outer layer due to its good barrier properties and its high transparency.

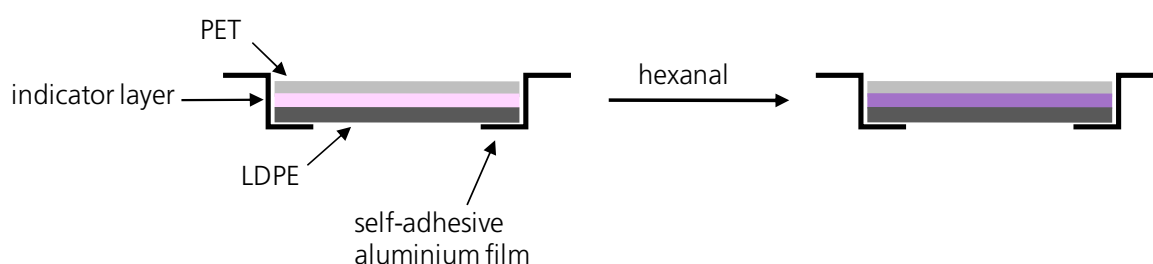


**Figure C39.** Setup of indicator layer for integration in food packaging. Mixture of indicator particles in ethyl acetate and polyvinyl acetate polymer was coated on a LDPE foil using a semi-automatic varnishing machine. Afterwards, the indicator layer was laminated by a PET foil.

For preparing measurement samples the prepared foil was punched by a hollow punch with a diameter of 20 mm. The received spots were either integrated in caps of glass vials or in PA/PE (polyamide/polyethylene) packaging pouch. Integration in glass vials is quite easy by simply replacing the included septum by the indicator spot.

PA/PE pouch consists of polyethylene as inner polymer layer and polyamide as outer layer. Indicator spots were fixed onto the inner layer of pouch using a self-adhesive aluminium film (Figure C39). Thereby, the hexanal-permeable LDPE film is pointed towards the inside. The applied aluminium-film prevents diffusion of hexanal into the indicator layer from the cutting edge and thus diffusion of hexanal through the LDPE layer resulting in a non-uniform color change. Fat-containing food like hazelnuts was filled into the obtained pouch with the integrated indicator spot and the vial was closed by heat-sealing (Figure C40).



**Figure C40.** Indicator spot integrated in the inner packaging pouch using a self-adhesive aluminium film. The presented indicator spot has already changed its color due to hexanal produced by deterioration of hazelnuts (Fraunhofer IVV).

### Measurement of color changes

By applying indicator spots either fixed with self-adhesive aluminium film in a pouch or fixed in caps of glass vials a color change from pink to violet can be monitored in the presence of hexanal in the gas phase of the measurement sample (see Figure C39 and C40). Color changes of indicator spots were documented by a Konica hand-spectral photometer which illuminates at 380-700 nm and measures the light reflected by the corresponding sample. The spectrometer automatically calculates and displays  $\Delta E$  which reflects the (Equation C20).

The noticeability of color changes by the human eye has already been described in a number of different studies.<sup>25</sup> Values for distances between two colors which can be clearly distinguished by a viewer, however, differ widely in the present literature. Due to Neubauer a clear color change is observable from a  $\Delta E$  value of 5-10 (Table C23).<sup>25</sup>  $\Delta E$  can be calculated from  $L^*a^*b$  values received from color measurements (Equation C20). Detailed information about various color spaces is given in part B (chapter 3).

$$\Delta E = \sqrt{(\Delta L^*)^2 + (\Delta a^*)^2 + (\Delta b^*)^2} \quad \text{Eq. C20}$$

$\Delta E$	color difference
$L$	lightness
$a^*$	color opponent dimensions (green – magenta)
$b^*$	color opponent dimensions (blue – yellow)

**Table C23.** Overview of noticeability of color differences  $\Delta E$ .<sup>25</sup>

$\Delta E$	Noticeability
<1	Not noticeable
1-2	Very low, nearly not noticeable
2-3	Low, limited noticeable
3-5	Noticeable
5-10	Clearly
>10	Intensely, difference noticeable as another color

### Results by testing real food samples

Peanuts, hazelnuts, and sunflower oil were freshly bought briefly before starting storage experiments. Two different types of hazelnuts were used. The first type was treated by long-time roasting (soft roasting method) for 30 minutes at 142 °C and the second type was short-time roasted (hard roasting method) for 9.5 minutes at 200 °C. Peanuts were roasted in vegetable oil and without addition of salt. Sunflower oil was refined and stored in a 1 L PET bottle.

These foods were stored for four months at different temperatures. Peanuts were stored at 20 °C, 30 °C, and 40 °C. In contrast hazelnuts roasted at 142 °C were stored at 20 °C and 30 °C and hazelnuts roasted at 200 °C were stored at 20 °C. Finally, sunflower oil was stored at 20 °C, 40 °C, and 60 °C. After 4 months of storage 100 g of nuts were repacked in a PA/PE pouch with integrated indicator spot and closed by heat-sealing. Additionally, sunflower oil was filled in glass bottles and sensor spots were fixed in its screw caps.

Afterwards, nuts and sunflower oil were stored at the respective storage temperatures for 30 days. After this time hexanal concentration in the head spaces of packaging were measured by head-space gas chromatography (HS-GC). For this purpose a gastight syringe was used for taking a 10 mL gas sample from the head space and injecting it into a GC glass vial. Color changes of integrated indicator spots were measured with Konica hand-spectral photometer. Results obtained by gas chromatography and color measurements are summarized in Table C24 for peanuts and hazelnuts.

**Table C24.** Summary of results obtained from application of indicator system on real food samples.

Sample	c(Hexanal) / mg/kg	$\Delta E$	Sample rancid?	Clear color change ( $\geq 5$ )?
Peanut 20 °C	0.93	2.54	No	No
Peanut 30 °C	2.95	6.89	✓	✓
Peanut 40 °C	9.53	17.75	✓	✓
Hazelnut (roasted at 142 °C) 20 °C	2.92	4.77	✓	✓
Hazelnut (roasted at 142 °C) 30 °C	6.86	13.96	✓	✓
Hazelnut (roasted at 200 °C) 20 °C	40.74	21.18	✓	✓

For peanuts the concentration of hexanal in the package increases with increasing storage temperature (Table C24). The same is observed for hazelnuts roasted at 142 °C. The hexanal concentration found for hazelnuts stored at 20 °C was 2.92 mg/kg whereas samples stored at 30 °C already showed a hexanal concentration of 6.86 mg/kg.

Comparing soft-roasted and hard-roasted hazelnuts the hard roasted ones showed much higher hexanal concentrations. Hard-roasted hazelnuts stored at 20 °C gave a value of 40.74 mg/kg hexanal whereas the hexanal concentration of soft-roasted hazelnuts at 20 °C was just 2.92 mg/kg.

Using data from Table C6 (chapter 1.3) for critical hexanal concentrations peanuts were considered rancid beyond 2 mg/kg hexanal, whereas roasted hazelnuts were considered rancid beyond 1 mg/kg hexanal. For sunflower oil the literature value reported for rape oil was used (2 mg/kg). In summary, all food samples under study were found rancid except peanuts stored at 20 °C.

By applying the noticeability values for color distance  $\Delta E$  of Neubauer a clear color change was observed for values between five and ten. Hence, all indicator spots showed a clear color change except those which were integrated in food packaging of peanuts stored at 20 °C. Those peanuts were not indicated as rancid due to the low hexanal concentration in the corresponding gas phase of 0.9 mg/kg. All remaining food packaging contained clearly rancid food samples which were successfully indicated by a distinctly observable color change of the indicator spots. Furthermore, no false positive results were observed in these experiments.

Critical hexanal concentration for rape seed oil (and as assumed also for sunflower oil) starts from 2 mg/kg (Table C6, chapter 1.3). Indicator spots integrated into screw caps of sunflower oil packaging, however, didn't show any color change as the measured hexanal concentration in gas phase of such bottles was very low. However, high hexanal concentrations were detected in the oil itself which can be explained by the high solubility of hexanal in sunflower oil. Hexanal thus doesn't evaporate into the gas phase and as a result cannot react with the indicator spot which was integrated in screw cap of the bottle.

In conclusion all rancid food samples were correctly identified by integrated indicator spots. Hence, this developed indicator system is suitable for application in packaging for peanuts and hazelnuts. However, an application for sunflower oil was not possible due to the high solubility of hexanal in this sample and thus insufficient volatilization into the gas phase where the reaction with the indicator spot takes place.

The integration of the hexanal indicator spot into food packaging can be achieved by printing techniques for example. The addition of reference colors around the indicator spot can facilitate the evaluation by the customer here. Prototypes of such indicator spots are shown in Figure C35.



**Figure C35.** Prototypes of indicator spots for the integration into food packaging. Reference colors are arranged around the indicator spot.

## 5 Summary and conclusion

A colorimetric indicator system based on the well-known Schiff's reagent and silica particles as solid support was successfully prepared. For quantifying the reaction of aldehydes in the gas phase indicator particles were immobilized into screw caps of glass vials. The design of an experimental setup to measure the color change and for the quantification of present aldehydes was employed. The setup consisted of a custom-made calibration chamber with an integrated light source and a SLR camera. By automatic control of the camera digital color images were taken after certain periods of time and RGB color information were evaluated. Using this setup, measuring the concentration of aldehydes is accessible. In the context of this work hexanal, propionaldehyde, and acetaldehyde were used and limits of detection of about 1 ppm were observed. Different methods for data evaluation were compared including ratiometric calculations of two color channel intensities and determination by [e.d.] in the three-dimensional RGB color space. As a result, evaluation by [B/G] provided the lowest LOD values. Furthermore, indicator particles were found to be stable for at least six months. Data for long-term stability can be analyzed by performing a trend-test by Neumann. Additionally, qualitative studies about the cross sensitivity towards substances without aldehyde groups were carried out. In this work it was shown that data evaluation is feasible applying principal component analysis.

Finally, experiments on real food samples were performed including hazelnuts, peanuts, and sunflower oil in collaboration with Fraunhofer IVV, Freising. Reference measurements for quantifying hexanal concentrations were performed by head-space gas chromatography. The rancidity of hazelnuts and peanuts could be indicated successfully by aldehyde indicator spots which were integrated into the food packaging material. The rancidity of sunflower oil, however, is hard to detect due to insufficient volatilization of dissolved hexanal into the gas phase. In conclusion, the colorimetric indicator system developed here is not applicable to sunflower oil but shows an excellent performance for hazelnuts and peanuts. The color change of indicator, furthermore, can be enhanced (in this work up to 6.5 fold) by simply reducing the polymer content.

To date no colorimetric indicators are commercially available for signaling volatile deterioration products of fat-containing food and no aldehyde sensor materials for food safety control applications are known in literature.<sup>66</sup> The indicator shown in this work provides best requirements for its integration into packaging systems for fat-containing food. As a result of this, evaluating the food quality of fat-containing foods by consumers even before opening the package can become realizable the first time.



## 6 References

- (1) Bundesministerium für Ernährung und Landwirtschaft. *Statistisches Jahrbuch über Ernährung, Landwirtschaft und Forsten 2014*, 1st edn.; Landwirtschaftsvlg Münster: Münster, Westf, 2015.
- (2) Simopoulos, A. P. *Am. J. Clin. Nutr.* **1991**, *54* (3), 438–463.
- (3) Ayala, A.; Muñoz, M. F.; Argüelles, S. *Oxid. Med. Cell. Longevity* **2014**, 360438.
- (4) Bucher, H. C.; Hengstler, P.; Schindler, C.; Meier, G. *Am. J. Med.* **2002**, *112* (4), 298–304.
- (5) Kris-Etherton, P. M. *Arterioscler., Thromb., Vasc. Biol.* **2003**, *23* (2), 151–152.
- (6) Connor, W. E. *Am. J. Clin. Nutr.* **2000**, *71*, 171S–175S.
- (7) Belitz, H.-D.; Grosch, W.; Schieberle, P. *Lehrbuch der Lebensmittelchemie*, 6th edn.; Springer: Berlin, Heidelberg, 2008.
- (8) Krist, S. *Lexikon der pflanzlichen Fette und Öle*; Springer Vienna: Vienna, 2013.
- (9) Frankel, E. N. *Lipid oxidation*, 2nd edn.; Oily Press; Lipid Technology: Bridgwater, England, 2005.
- (10) Warner, K.; Nelsen, T. J. *Am. Oil Chem. Soc.* **1996**, *73* (2), 157–166.
- (11) Warner, K.; Dimick, P. S.; Ziegler, G. R.; Mumma, R. O.; Hollender, R. J. *Food Sci.* **1996**, *61* (2), 469–472.
- (12) Jeleń, H. H.; Obuchowska, M.; Zawirska-Wojtasiak, R.; Wąsowicz, E. *J. Agric. Food Chem.* **2000**, *48* (6), 2360–2367.
- (13) Ha, J.; Seo, D.-W.; Chen, X.; Hwang, J.-B.; Shim, Y.-S. *Anal. Sci.* **2011**, *27* (9), 873.
- (14) Sanches-Silva, A.; Rodríguez-Bernaldo de Quirós, A.; López-Hernández, J.; Paseiro-Losada, P. J. *Chromatogr. A* **2004**, *1046* (1-2), 75–81.
- (15) Sigma Aldrich. *MSDS Hexanal*. 2015 [cited: 2015 august 07]; available from: <http://www.sigmaaldrich.com/MSDS/MSDS/DisplayMSDSPage.do?country=DE&language=de&productNumber=115606&brand=ALDRICH&PageToGoToURL=http%3A%2F%2Fwww.sigmaaldrich.com%2Fcatalog%2Fproduct%2Faldrich%2F115606%3Flang%3Dde>.
- (16) Mattson, F. H.; Lutton, E. S. *J. Biol. Chem.* **1958**, *233* (4), 868–871.
- (17) Ho, C.-T.; Hartman, T. G., Eds. *Lipids in Food Flavors*; American Chemical Society: Washington, DC, 1994.
- (18) Grosch, W. *Chem. Unserer Zeit* **1970**, *4* (4), 121–126.
- (19) Wąsowicz, E.; Gramza, A.; Hęś, M.; Jeleń, H. H.; Korczak, J.; Małecka, M.; Mildner-Szkudlarz, S.; Rudzińska, M.; Samotyja, U.; Zawirska-Wojtasiak, R. *Pol. J. Food Nutr. Sci.* **2004**, *54* (13), 87–100.
- (20) Yin, H.; Xu, L.; Porter, N. A. *Chem. Rev.* **2011**, *111* (10), 5944–5972.
- (21) Choe, E.; Min, D. B. *Compr. Rev. Food Sci. Food Saf.* **2006**, *5* (4), 169–186.
- (22) Shahidi, F.; Bailey, A. E. *Bailey's industrial oil and fat products*, 6th edn.; Wiley: New York, Chichester, 2005.

- (23) Pokorný, J. *Nahrung* **1990**, 10 (34), 887–897.
- (24) St. Angelo, A. J. *Lipid oxidation in food*; American Chemical Society: Washington, DC, 1992.
- (25) Krisanova, K. Fraunhofer IVV, TU München, Ed. *Master Thesis: Hexanal-Indikator: Charakterisierung und verpackungstechnische Applikation eines Farbindikators zur Bestimmung des oxidativen Qualitätszustandes von fetthaltigen Lebensmitteln*: Freising, 2015.
- (26) Schneider, C. *Mol. Nutr. Food Res.* **2009**, 53 (3), 315–321.
- (27) Warner, K.; Evans, C. D.; List, G. R.; Dupuy, H. P.; Wadsworth, J. I.; Goheen, G. E. *J. Am. Oil Chem. Soc.* **1978**, 55 (2), 252–256.
- (28) Pokorný, J. *Nahrung* **1995**, 39 (5-6), 546–547.
- (29) Schieberle, P.; Grosch, W. *J. Am. Oil Chem. Soc.* **1981**, 58 (5), 602–607.
- (30) Ross, C. F.; Smith, D. M. *Compr. Rev. Food Sci. Food Saf.* **2006**, 5 (1), 18–25.
- (31) Palamand, S. R.; Dieckmann, R. H. *J. Agric. Food Chem.* **1974**, 22 (3), 503–506.
- (32) Gertz, C.; Klostermann, S.; Kochhar, S. P. *Eur. J. Lipid Sci. Technol.* **2000**, 102 (8-9), 543–551.
- (33) Matissek, R.; Steiner, G.; Fischer, M. *Lebensmittelanalytik*, 5th edn.; Imprint: Springer Spektrum: Berlin, Heidelberg, 2014.
- (34) Min, D. B.; Smouse, T. H. *Flavor chemistry of fats and oils*; American Oil Chemists' Society: Champaign, 1985.
- (35) Shahidi, F., Ed. *Bailey's Industrial Oil and Fat Products*; John Wiley & Sons, Inc: Hoboken, NJ, USA, 2005.
- (36) Shahidi, F.; Zhong, Y., Lipid Oxidation: Measurement Methods. In *Bailey's Industrial Oil and Fat Products*; Shahidi, Fereidoon, Ed.; John Wiley & Sons, Inc: Hoboken, NJ, USA, 2005.
- (37) Fritsch, C. W.; Gale, J. A. *J. Am. Oil Chem. Soc.* **1977**, 54 (6), 225–228.
- (38) Robards, K.; Kerr, A. F.; Patsalides, E. *Analyst* **1988**, 113 (2), 213.
- (39) Paquot, C. *Standard methods for the analysis of oils, fats and derivatives*, 6th edn.; Pergamon Press: Oxford, 1979.
- (40) Shahidi, F.; Pegg, R. B., Hexanal as an Indicator of the Flavor Deterioration of Meat and Meat Products. In *Lipids in Food Flavors*; Ho, Chi-Tang; Hartman, Thomas G., Eds.; American Chemical Society: Washington, DC, 1994.
- (41) Thomas, M. J.; Robison, T. W.; Samuel, M.; Forman, H. J. *Free Radical Biol. Med.* **1995**, 18 (3), 553–557.
- (42) Swoboda, P. A.; Lea, C. H. *J. Sci. Food Agric.* **1965**, 16 (11), 680–689.
- (43) Torres, M. M.; Martínez, M. L.; Maestri, D. M. *J. Am. Oil Chem. Soc.* **2005**, 82 (2), 105–110.
- (44) Gertz, C.; Kochhar, S., P. *Ol., Corps Gras, Lipides* **2001**, 8 (1), 82–88.
- (45) Läubli, M. W.; Bruttel, P. A. *J. Am. Oil Chem. Soc.* **1986**, 63 (6), 792–795.
- (46) Erickson, M. C.; Santerre, C. R.; Malingre, M. E. *J. Food Sci.* **1994**, 59 (6), 1234–1238.
- (47) Morales, M. T.; Rios, J. J.; Aparicio, R. *J. Agric. Food Chem.* **1997**, 45 (7), 2666–2673.

- (48) Pokorný, J. *Nahrung* **1990**, 34 (10), 887–897.
- (49) Min, D. B. *J. Am. Oil Chem. Soc.* **1983**, 60 (3), 544–545.
- (50) Ullrich, F.; Grosch, W. *Z. Lebensm.-Unters. Forsch.* **1987**, 184 (4), 277–282.
- (51) Shahidi, F. *Headspace Analysis of Foods and Flavors*; Springer: New York, 2001.
- (52) Grosso, N. R.; Resurreccion, A. *J. Food Sci.* **2002**, 67 (4), 1530–1537.
- (53) Ory, R. L.; Crippen, K. L.; Lovegren, N. V., Off-Flavors in Peanuts and Peanut Products. In *Off-Flavors in Foods and Beverages*; Elsevier, 1992.
- (54) Mexis, S. F.; Badeka, A. V.; Riganakos, K. A.; Karakostas, K. X.; Kontominas, M. G. *Food Control* **2009**, 20 (8), 743–751.
- (55) McClements, D. J.; Decker, E.; Elias, R. J. *Oxidation in foods and beverages and antioxidant applications*; Woodhead Pub.: Oxford, Philadelphia, 2010.
- (56) Azarbad, M. H.; Jeleń, H. *Food Anal.* **2015**, 8 (7), 1727–1733.
- (57) Ng, S.; Lasekan, O.; Muhammad, K.; Sulaiman, R.; Hussain, N. *Chem. Cent. J.* **2014**, 8 (1), 55.
- (58) Perren R. *Untersuchungen über das Rösten von Haselnüssen*: Eidgenössische Technische Hochschule Zürich, 1964.
- (59) Haugen, J.-E.; Lundby, F.; Wold, J. P.; Veberg, A. *Sens. Actuators, B* **2006**, 116 (1–2), 78–84.
- (60) Vinaixa, M.; Vergara, A.; Duran, C.; Llobet, E.; Badia, C.; Brezmes, J.; Vilanova, X.; Correig, X. *Sens. Actuators, B* **2005**, 106 (1), 67–75.
- (61) Park, J.; Lim, J. H.; Jin, H. J.; Namgung, S.; Lee, S. H.; Park, T. H.; Hong, S. *Analyst* **2012**, 137 (14), 3249–3254.
- (62) Goodridge, C. F.; Beaudry, R. M.; Pestka, J. J.; Smith, D. M. *J. Agric. Food Chem.* **2003**, 51 (26), 7533–7539.
- (63) Vanderroost, M.; Ragaert, P.; Devlieghere, F.; Meulenaer, B. de. *Trends Food Sci. Technol.* **2014**, 39 (1), 47–62.
- (64) Mohr, G. J. *Sens. Actuators, B* **2003**, 90 (1–3), 31–36.
- (65) Vo, E.; Murray, D. K.; Scott, T. L.; Attar, A. J. *Talanta* **2007**, 73 (1), 87–94.
- (66) Maruo, Y. Y.; Nakamura, J.; Uchiyama, M.; Higuchi, M.; Izumi, K. *Sens. Actuators, B* **2008**, 129 (2), 544–550.
- (67) Hamacher, S. G. *foodTECHNOLOGY* **2013** (2), 46–48.
- (68) Yam, K. L.; Takhistov, P. T.; Miltz, J. *J. Food Sci.* **2005**, 70 (1), R1.
- (69) Realini, C. E.; Marcos, B. *Meat science* **2014**, 98 (3), 404–419.
- (70) Bergmair, J.; Washüttl, M.; Wepner, B. *Prüfpraxis für Kunststoffverpackungen*, 2nd edn.; Behr: Hamburg, 2012.
- (71) Ali, R.; Lang, T.; Saleh, S. M.; Meier, R. J.; Wolfbeis, O. S. *Anal. Chem.* **2011**, 83 (8), 2846–2851.
- (72) Nakamura, N.; Amao, Y. *Anal. Bioanal. Chem.* **2003**, 376 (5), 642–646.

- (73) Schröder, C. R.; Klimant, I. *Sens. Actuators, B* **2005**, *107* (2), 572–579.
- (74) Amao, Y. *Microchim. Acta* **2003**, *143* (1), 1–12.
- (75) Borisov, S. M.; Papkovsky, D. B.; Ponomarev, G. V.; DeToma, A. S.; Saf, R.; Klimant, I. *J. Photochem. Photobiol., A* **2009**, *206* (1), 87–92.
- (76) Quaranta, M.; Borisov, S. M.; Klimant, I. *Bioanal. Rev.* **2012**, *4* (2-4), 115–157.
- (77) Stich, M. I. J.; Fischer, L. H.; Wolfbeis, O. S. *Chem. Soc. Rev.* **2010**, *39* (8), 3102–3114.
- (78) Alves, F. L.; Raimundo, I. M.; Gimenez, I. F.; Alves, O. L. *Sens. Actuators, B* **2005**, *107* (1), 47–52.
- (79) Das, S.; Chakraborty, S.; Parkash, O.; Kumar, D.; Bandyopadhyay, S.; Samudrala, S. K.; Sen, A.; Maiti, H. S. *Talanta* **2008**, *75* (2), 385–389.
- (80) Razek, T. *Talanta* **1999**, *50* (3), 491–498.
- (81) Delmarre, D.; Bied-Charreton, C. *Sens. Actuators, B* **2000**, *62* (2), 136–142.
- (82) Lee, B.; Scopelliti, R.; Severin, K. *Chem. Commun.* **2011**, *47* (34), 9639–9641.
- (83) Lobnik, A.; Wolfbeis, O. S. *Sens. Actuators, B* **1998**, *51* (1-3), 203–207.
- (84) Timmer, B.; Olthuis, W.; van Berg, A. d. *Sens. Actuators, B* **2005**, *107* (2), 666–677.
- (85) Trinkel, M.; Trettnak, W.; Reiningner, F.; Benes, R.; O'Leary, P.; Wolfbeis, O. S. *Anal. Chim. Acta* **1996**, *320* (2-3), 235–243.
- (86) Waich, K.; Borisov, S.; Mayr, T.; Klimant, I. *Sens. Actuators, B* **2009**, *139* (1), 132–138.
- (87) Kato, E. T.; Yoshida, C. M. P.; Reis, A. B.; Melo, I. S.; Franco, T. T. *Polym. Int.* **2011**, *60* (6), 951–956.
- (88) Wallace, K. J.; Cordero, S. R.; Tan, C. P.; Lynch, V. M.; Anslyn, E. V. *Sens. Actuators, B* **2007**, *120* (2), 362–367.
- (89) Xu, H.; Wu, J.; Chen, C.-H.; Zhang, L.; Yang, K.-L. *Sens. Actuators, B* **2010**, *143* (2), 535–538.
- (90) Kuswandi, B.; Jayus; Restyana, A.; Abdullah, A.; Heng, L. Y.; Ahmad, M. *Food Control* **2012**, *25* (1), 184–189.
- (91) Loughran, M.; Diamond, D. *Food Chem.* **2000**, *69* (1), 97–103.
- (92) Smolander, M.; Hurme, E.; Latva-Kala, K.; Luoma, T.; Alakomi, H.-L.; Ahvenainen, R. *Innovative Food Sci. Emerging Technol.* **2002**, *3* (3), 279–288.
- (93) Regulation (EC) No 1935/2004 of the european parliament and of the council of 27 October 2004 on materials and articles intended to come into contact with food and repealing directives 80/590/EEC and 89/109/EEC (Official Journal L 338), 4–17.
- (94) Commission Regulation (EC) No 450/2009 of 29 May 2009 on active and intelligent materials and articles intended to come into contact with food (Official Journal L 135), 3–11.
- (95) Mills, A. *Chem. Soc. Rev.* **2005**, *34* (12), 1003–1011.
- (96) Kerry, J. P.; O'Grady, M. N.; Hogan, S. A. *Meat Sci.* **2006**, *74* (1), 113–130.
- (97) Wieland H.; Scheuing G. *Ber. Dtsch. Chem. Ges.* **1921** (10), 2527–2555.

- (98) Baker, Mark E. J.; Narayanaswamy, R. *Analyst* **1994**, 119 (5), 959.
- (99) Elftman H. J. *Histochem. Cytochem.* **1959**, 7 (2), 93–97.
- (100) Robins, J. H.; Abrams, G. D.; Pincock, J. A. *Can. J. Chem.* **1980**, 58 (4), 339–347.
- (101) Robins, J. H.; G. D. Abrams, J. A. Pincock. *Can. J. Chem.* **1979**, 58, 339–347.
- (102) Müller W. *Kalibrierung nach DIN 32645 bzw. DIN 38402*. 2015 [cited: 07 october 2015]; available from: [http://www.ces.karlsruhe.de/culm/culm/culm2/th\\_themen/C06-kalibrierung/kalibrierung.pdf](http://www.ces.karlsruhe.de/culm/culm/culm2/th_themen/C06-kalibrierung/kalibrierung.pdf).
- (103) Kromidas, S. *Handbuch Validierung in der Analytik*, 2nd edn.; Wiley-VCH: Weinheim, 2011.
- (104) Funk, W.; Dammann, V.; Donnevert, G. *Qualitätssicherung in der analytischen Chemie*, 2nd edn.; Wiley-VCH: Weinheim, 2005.
- (105) Funk, W.; Dammann, V.; Donnevert, G. *Quality assurance in analytical chemistry*, 2nd edn.; Wiley-VCH: Weinheim, 2007.
- (106) DeMerlis, C.; Schoneker, D. *Food Chem. Toxicol.* **2003**, 41 (3), 319–326.
- (107) Wacker. *Info sheet Vinnapas*. 2015 [cited: 2015 october 06]; available from: [http://www.wacker.com/cms/media/publications/downloads/6766\\_EN.pdf](http://www.wacker.com/cms/media/publications/downloads/6766_EN.pdf).
- (108) Johansson, F.; Leufven, A. *J. Food Sci.* **1994**, 59 (6), 1328–1331.



## D Detection of carbon monoxide for work safety applications

### 1 Introduction

#### Toxic effect of carbon monoxide

Carbon monoxide (CO) is a colorless, tasteless, odorless, and nonirritating gas. These properties allow CO to rise undetected to toxic concentrations. Thus carbon monoxide has the reputation as a "silent killer".<sup>1-3</sup> The gas is responsible for a large number of poisonings and deaths due to its lethal force when inhaled.<sup>4</sup> Carbon monoxide is released when carbon-containing compounds are only partially oxidized e.g. in combustion engines.<sup>5,6</sup> Its threshold limit value is 30 ppm in Germany<sup>7</sup> and its primary toxic effect is through hypoxia.<sup>8,9</sup> Normally, respired oxygen is bound by hemoglobin in the blood. It is a metalloprotein in the red blood cells and is responsible for oxygen transport through the body. Human hemoglobin consists of four protein subunits. Since each subunit contains one prosthetic group (heme b complex, Figure D1, A) which can bind a single oxygen molecule one hemoglobin complex is able to bind four oxygen molecules.

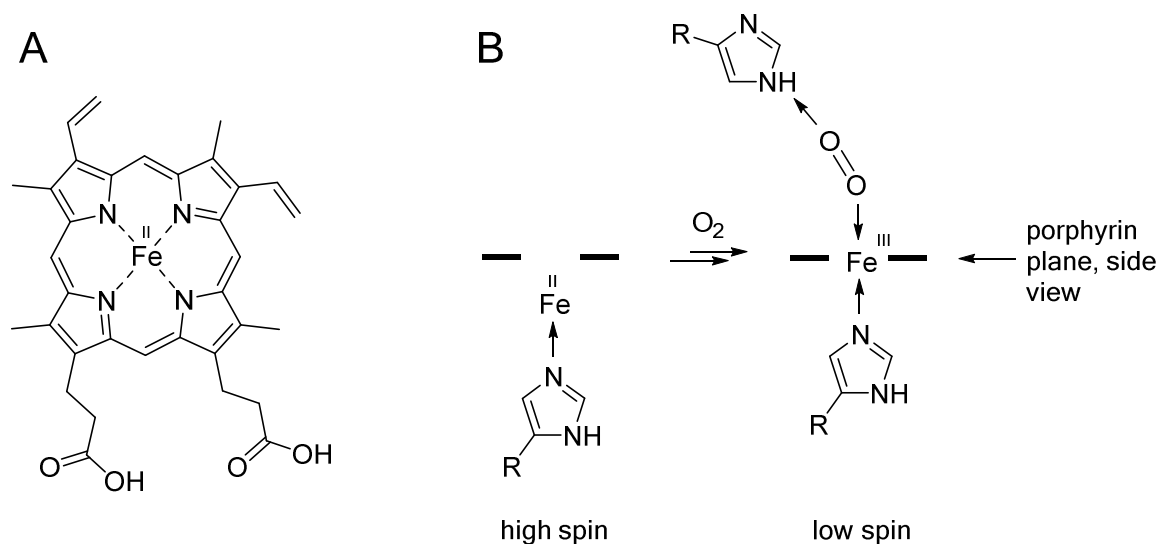


**Figure D1.** **A:** Heme b complex, **B:** High-spin heme b is bound by proximal histidin from the axial Fe(II) position below. After oxygen binding the Fe ion is brought in a low-spin state and fits in the porphyrin ring of heme b.

Free heme b are high spin complexes with iron ions in oxidation state two. Fe(II) is slightly too large to fit inside the cavity of its surrounding porphyrin ligand and is therefore positioned under the porphyrin plane. Heme b is coordinated within protein subunit by a proximal histidin in axial position (Figure D1, B). Provoked by oxygen binding at the second axial position of heme the

complex changes to its low-spin state and Fe(II) is oxidized to Fe(III). Due to size decrease the Fe ion now fits in the void of the porphyrin ring. Bound oxygen is stabilized via a hydrogen bond with distal histidin (Figure D1, B). <sup>5,10</sup>

When inhaled, carbon monoxide is taken up into the blood where it forms a slowly reversible complex with hemoglobin, known as carboxyhemoglobin. Hemoglobin exhibits an approximately 200 times higher affinity to carbon monoxide than to oxygen. <sup>6,11,12</sup> Therefore, oxygen binding of hemoglobin is hampered which causes systemic oxygen deprivation. <sup>5</sup> Especially organs with high oxygen consumption like brain and heart are affected. Carbon monoxide poisoning unfortunately is a quite common cause of death in modern society. <sup>12,13</sup> In Germany the number of deaths caused by CO was 582 in the year 2012. In 2013 the toll rate was 514 as the Statistisches Bundesamt Wiesbaden published in their statistics. <sup>14,15</sup>

Although CO-poisoning is a frequent hazard, it often is not diagnosed due to the nonspecificity of its clinical symptoms. <sup>1,16</sup> An exposure to CO-levels between 70 and 100 ppm over a few hours causes flu-like symptoms as headache, sore eyes, and a runny nose. A carbon monoxide concentration between 150 and 300 ppm leads to dizziness, drowsiness, and vomiting. Extreme exposure to CO-levels of 400 ppm and higher will result in unconsciousness, brain damage, coma, and death. Moreover, if more than 50% of the present hemoglobin is occupied by CO, a coma with often fatal consequences may result. <sup>5,11</sup> For children, the critical concentration levels are even lower due to their high metabolism and critical concentration levels for sick people and pregnant women are lowered as well. <sup>12</sup> Many people who are exposed to low concentrations of carbon monoxide are unaware of it making CO-poisoning so extremely dangerous. <sup>16</sup> The therapy for exposed persons consists of removing the persons from the toxic atmosphere and an immediate supply of 100% oxygen in order to expedite the elimination of carbon monoxide. However, many patients suffer from intellectual deterioration and memory impairment as long-time effects. <sup>1,4</sup>

Therefore, the detection of carbon monoxide emission is of uttermost importance, e.g. next to combustion engines, in underground parking lots, or heating installations as well as for work safety applications in industry. <sup>4</sup>



### Detection of carbon monoxide

Several methods for CO detection have been established so far e.g. gas chromatography,<sup>17</sup> laser infrared absorption,<sup>18</sup> and electrochemical measurements.<sup>5,19</sup> One type of currently available electrochemical sensors for carbon monoxide is based on semi-conducting metal oxides like SnO<sub>2</sub> or TiO<sub>2</sub>.<sup>19–21</sup> Upon exposure to molecular oxygen, negatively charged oxygen species like O<sub>2</sub><sup>•-</sup> or O<sup>•-</sup> accumulate on the surface of the metal oxide crystals and form less conductive zones. As carbon monoxide can act as reductant, it reacts with the surface oxygen species to form CO<sub>2</sub>. Therefore, the electrical conductance of the metal oxide film increases and generates a sensor response.<sup>19,22,23</sup> Another commercially available carbon monoxide sensor is based on catalytic combustion and amperometry. This type of sensor consists of a platinum wire along with a constant external voltage applied. The resistance of the wire changes with the heat evolving upon catalytic oxidation of CO to CO<sub>2</sub>, thus giving information about carbon monoxide concentration in the ambient air.<sup>22</sup>

As an alternative to electrochemical sensors, optical chemical sensors have received increasing attention during the last decade in many application fields.<sup>24–30</sup> They change their optical properties (e.g. absorbance, emission wavelength, luminescence intensity or lifetime)<sup>31,32</sup> when exposed to the respective analyte.<sup>32</sup> A standard test for monitoring CO is the carboxy-myoglobin (Mb-CO) assay. Here, the binding of CO by myoglobin is quantified via absorbance spectroscopy.<sup>33</sup> Moreover, a biosensor was developed based on the selective CO binding of a dimeric heme protein from *Rhodospirillum rubrum*. This protein is a homodimer which contains heme complexes and it is able to bind CO selectively, which induces a conformational change of the heme protein. Yellow fluorescent protein (YFP) served as fluorescent reporter being highly sensitive to changes in the protein conformation. Accordingly, CO binding initiates an increase of YFP fluorescence intensity.<sup>34,35</sup> Another method for optical CO detection was recently reported by Esteban et al. They applied a binuclear rhodium complex turning out to be highly selective and sensitive for carbon monoxide.<sup>36</sup> It contains two cyclometalated phosphine ligands which bind CO and thereby induce a color change from violet to yellow. The complex has a detection limit in the ppm-level, however, its regeneration time is approximately 15 h.<sup>21,37</sup>

The strong binding affinity of CO to transition metal ions is exploited in another approach applying palladium.<sup>38</sup> This probe is able to monitor carbon monoxide in living cells based on metal-mediated carbonylation chemistry. A cyclo-palladated species quenches the fluorescence of a borondipyrromethene difluoride (BODIPY) core via heavy-atom electronic effects. After CO binding a carbonylation reaction releases Pd(0) and a BODIPY dye with high fluorescence intensity. The increase in fluorescence intensity is concentration dependent with a detection limit

of 1  $\mu\text{M}$  CO. Since the palladium-based probe is nontoxic and biocompatible it enables CO monitoring in living cells. However, a drawback is its long response time of about an hour.<sup>5,38</sup>

Optical chemical sensor systems enable remote and on-line sensing and are easy to handle.<sup>39</sup> Moreover, they can simply be miniaturized and integrated in measuring devices.<sup>40,41</sup> However, more robust, sensitive, fast, reversible, scalable and non-invasive sensor dyes enabling for multiplexing are still needed for the development of optical gas sensors for carbon monoxide.

## Corroles

Corroles are tetrapyrrolic 18  $\pi$ -electron Hückel aromatic macrocycles which are closely related to porphyrins. In contrast to porphyrins corroles are contracted by one methidine bridge and have one direct pyrrole-pyrrole linkage (Figure D2).<sup>42,43</sup> The first corrole was reported by Johnson et al. in 1964 who synthesized it as a part of their work on synthetic models of vitamin B12.<sup>44,45</sup> In 1999 Gross et. al published the first direct synthesis of meso-substituted corroles and pioneered the corrole chemistry.<sup>42</sup> Since then, the number of publications on corroles increased very fast.<sup>43</sup> The field of corrole chemistry is rapidly growing with new corrole ligands, new metallocorrole complexes, and new synthetic methodologies and variants. E.g. synthesis pathways for corroles with meso-substituents either symmetric or unsymmetric and various beta-substituents were recently developed.<sup>46</sup>

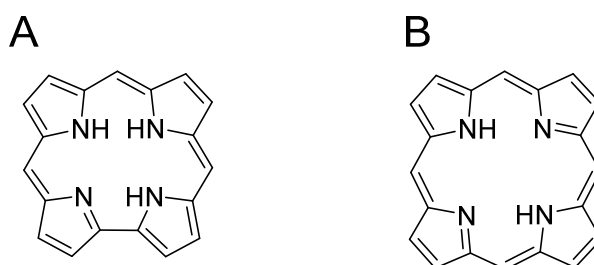


**Figure D2.** **A:** Corrole backbone, **B:** Porphyrin backbone.

In contrast to porphyrins which are diprotonic and can act as tetradentate dianionic ligands, corroles act as tetradentate trianionic ligands for metal ions.<sup>42</sup> Hence, complexes of corroles with trivalent metal ions like cobalt(III) are neutral and have, in the absence of other ligands, a coordination number of four.<sup>45</sup> Much progress in corrole chemistry was achieved with respect to metallation of the corrole macrocycles. As a result, several unregarded regions of the periodic table have recently become subjects of great interest since alkali metals, early transition metals, lanthanides, and actinides were unknown in the corrole literature until 2012. In addition, heavy elements including third row transition metals and heavy main group species had very limited representation in organometallic literature.<sup>46</sup>

Compared to porphyrins and most other ligands, corroles are able to stabilize unusually high oxidation states, e.g. Fe(IV), Co(IV) and Co(V).<sup>47</sup> Thus the exploration of metallocorroles in oxidative catalysis, group transfer catalysis, and reduction catalysis was enhanced intensely. Apart from this, metallocorroles have demonstrated potential application in the field of photochemical sensors, artificial photosynthesis, and biomedical applications during the last two decades.<sup>48</sup> Low-valent metallocorroles should be very reactive and might therefore be expected to show unique properties regarding the activation of small molecules. Co(III)-corroles are known for their ability to coordinate donor-ligands, derived from the Lewis acidic character of the central Co(III)-ion.<sup>45</sup> As Co(III)-corroles are able to coordinate CO they might be suitable as sensing probe for carbon monoxide.<sup>20,49</sup>

Recently much effort has been spent on the implementation of corroles in optical sensing components. Sankar et al. applied Cu(III)-corroles in selective colorimetric sensors for iodide in dichloromethane solution. A color change from yellow to green is caused by electron transfer from iodide to Cu(III) whereby Cu(III) is reduced and iodine is generated. High selectivity for iodide over bromide, chloride, and fluoride has been observed and a detection limit of 7  $\mu$ M iodide is achieved.<sup>50</sup> Furthermore, Zhang et al. established a sensor for mercury ions. By immobilizing free-base corrole in polyvinylchloride (PVC) the detection of Hg(II) by means of changes in fluorescence intensity was made possible. Hg(II) is complexed by the corrole macrocycle causing changes in the electronic structure of the system. As a result, the fluorescence intensity is decreased.<sup>51</sup> In addition, Bandyopadhyay et al. investigated the sensing properties of free-base corroles for mercury ions in toluene solution by fluorescence and absorption measurements.<sup>52</sup>

Barbe et al. showed the potential of Co(III)-corroles for application in gas sensing systems. They investigated different cobalt(III)-corroles and studied their adsorption properties for CO, O<sub>2</sub> and N<sub>2</sub>. The CO affinity of Co(III)-corroles is dependent on the Lewis-acid character of the Co(III)-core. A high electron density on the metal enhances the binding affinity for carbon monoxide. Additionally, the results show that there is no adsorption of O<sub>2</sub> and N<sub>2</sub>.<sup>20</sup>

### **Immobilization of indicator dyes in polymers**

By immobilizing indicator dyes in polymers, inexpensive and easy fabricable sensor systems might be prepared. Monitoring of analytes in gaseous phase becomes feasible when applying these sensors.<sup>53</sup> This approach is widely used for e.g. oxygen<sup>41,54,55</sup> and carbon dioxide<sup>26,32</sup> sensing.

The sensors described in this work consist of two different polymer layers. The bottom layer is an inert polymer sheet and is used as a solid support for the sensing layer. Indicator probes for the respective sensor application are embedded in a polymer matrix and are coated on the solid

support in a certain thickness. In principle there are different coating techniques possible for depositing sensing layers, e.g. screen printing,<sup>56</sup> ink jet methods,<sup>57</sup> spraying techniques,<sup>58</sup> or the use of knife-coating devices.<sup>32</sup> For each specific sensor application, indicator dye and coating technique different requirements of the polymer have to be complied. Crucial properties of polymers are e.g. hydrophilicity, permeability for the analyte, solubility of the indicator dye, and mechanical and chemical stability. One big advantage of such sensor foils and paints are their transparency and flexibility. Furthermore, the sensor might be cut into any desired shape by the simple use of a scalpel, scissors, or cutting dies, just to mention a few. In addition, the indicator-polymer-blend might be deposited on any object (e.g. aircraft models for pressure sensing). Another unique advantage is the possibility of optical multiplexing, which means that two or more different kinds of probes are incorporated in the matrix, thus enabling for sensing of two or more analytes simultaneously with high spatial resolution.<sup>53</sup> For this reasons the application field of sensor foils became very broad during the last decades.

## 2 Objective

The aim of this part of the thesis was the development of a fast and reversible optical sensor system for carbon monoxide. Therefore, different Co(III)-corrole based sensor dyes had to be synthesized and characterized with respect to their suitability for monitoring CO. For sensor preparation, the dyes had to be immobilized in an appropriate matrix polymer on a solid support. The performance of the sensor systems had to be characterized and evaluated. Therefore, a measurement setup had to be established which enables on-line monitoring of changes in absorbance. Based on the findings of the master thesis "Synthesis of indicator dyes and development of new sensor systems for carbon monoxide sensing" from 2012, the syntheses of 5,10,15-[tris(2,3,4,5,6-pentafluorophenyl)corrole] cobalt(III) and 5,10,15-[tris(2,6-dichlorophenyl)corrole] cobalt(III) had to be carried out. After characterization of the dyes with respect to their photophysical properties, the corroles had to be embedded in an appropriate matrix polymer. The optical CO-sensors had to be characterized and their features like response time, selectivity, sensitivity, and reversibility had to be determined. This was accomplished via custom-built, tailor-made measurement setups. These consist of a reflectance or absorbance spectrometer, respectively, and a flow-through cell connected to mass flow controllers for the calibration gases as key components. Figure D gives an overview of the project.

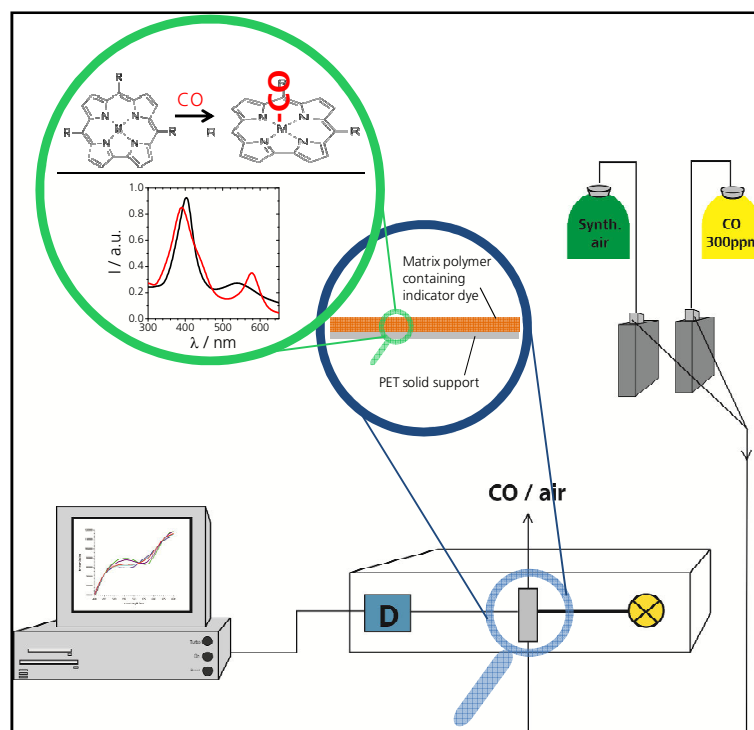


**Figure D.** Schematic illustration of the chapter's objective: indicator dye is integrated into matrix polymer changing its absorbance properties in the presence of carbon monoxide. Absorbance changes are monitored via a custom-made measuring setup.

### 3 Materials and Methods

Commercially available reagents and solvents were of analytical grade and were used as received if not mentioned otherwise (for details see Appendix, chapter 1). Pyrrole was distilled prior to use. Polystyrene (granulated) was obtained from Carl Roth GmbH and ethylcellulose (49% ethoxy content) from Fluka AG. The PET-foil (Mylar®, 125  $\mu\text{m}$  thickness) was purchased from GoodFellow GmbH.

**Thin layer chromatography (TLC)** was performed with TLC aluminum sheets ALUGRAM R SIL G/UV 254 (Macherey-Nagel GmbH). Visualization was accomplished using UV lamp or vanillin solution and subsequent heating.

**Flash chromatography** was performed using silica gel 60 (0.06 mm - 0.2 mm) (Carl Roth GmbH).

**Absorption measurements** were recorded on a Perkin Elmer Lambda 35 UV-Vis spectrometer. All spectra were acquired using 10 mm Hellma Quarzglass SUPRASIL® cuvettes.

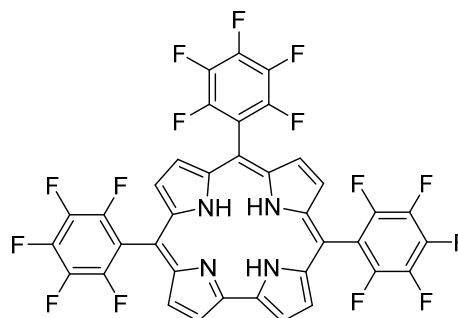
#### **NMR spectroscopy**

$^1\text{H}$ -NMR spectra were recorded on a Bruker Avance 400 spectrometer (400 MHz). All measurements were performed at ambient temperature. Chemical shifts  $\delta$  are displayed in parts per million [ppm] relative to the solvent signal as internal standard, coupling constants  $J$  are given in Hertz [Hz].  $^1\text{H}$  NMR splitting patterns are designated as doublet (d) or doublet of doublets (dd). Splitting patterns that could not be interpreted are designated as multiplet (m).

**Centrifugation** was performed using a Hettich Universal 320 centrifuge.

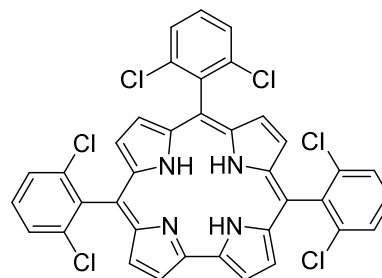
### 3.1 Synthesis of indicator dyes

#### 5,10,15-Tris(2,3,4,5,6-pentafluorophenyl)corrole <sup>43</sup> (TPFPC)



2,3,4,5,6-Pentafluorobenzaldehyde (196 mg, 1.0 mmol, 1.0 equiv.) was dissolved in pyrrole (105  $\mu$ L, 1.5 mmol, 1.5 equiv.) and a 10% trifluoroacetic acid (TFA) solution in dichloromethane (DCM) (10  $\mu$ L, 12  $\mu$ mol, 0.012 equiv.) was added while stirring. After 10 min at r.t. the reaction mixture was diluted with 10 mL DCM. A solution of 2,3-dichloro-5,6-dicyano-1,4-benzoquinone (DDQ) (273 mg, 1.20 mmol, 1.2 equiv.) in 2 mL toluene/tetrahydrofuran (THF) (1:1) was added and stirred at r.t. for additional 5 min. The reaction mixture was concentrated under reduced pressure and purified by flash chromatography ( $R_f$  (hexanes/DCM 7:1) = 0.2) to obtain the product as a purple solid (21 mg, 8%). <sup>1</sup>H-NMR (400 MHz; CDCl<sub>3</sub>):  $\delta$  = 9.11 (d,  $J$  = 4.2 Hz, 2H), 8.78 (d,  $J$  = 4.5 Hz, 2H), 8.67-8.45 (m, 4H). UV-Vis (CHCl<sub>3</sub>):  $\lambda_{max}/nm$  = 407, 562, 605.

#### 5,10,15-Tris(2,6-dichlorophenyl)corrole <sup>43</sup> (TDCPC)

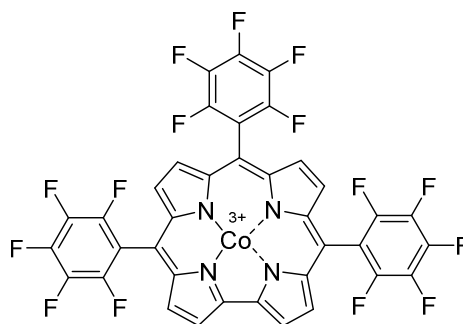


2,6-Dichlorobenzaldehyde (175 mg, 1.0 mmol, 1.0 equiv.) was dissolved in pyrrole (350  $\mu$ L, 5.0 mmol, 5.0 equiv.) and TFA (16  $\mu$ L, 0.21 mmol, 0.21 equiv.) was added while stirring. After 16 h at r.t. the reaction mixture was diluted with DCM, neutralized with triethylamine (NEt<sub>3</sub>) (29  $\mu$ L, 0.21 mmol, 0.21 equiv.) and added to 40 mL of stirred DCM simultaneously with a solution of DDQ (227 mg, 1.0 mmol, 1.0 equiv.) in 10 mL THF over 10 min. The reaction mixture was stirred for additional 5 min, concentrated and purified by flash chromatography ( $R_f$  (hexanes/DCM 10:1) = 0.3) to obtain the product as a purple solid (18.6 mg, 9%). <sup>1</sup>H-NMR (400 MHz; CDCl<sub>3</sub>):  $\delta$  = 8.94 (d,  $J$  = 3.8 Hz, 2H), 8.52 (d,  $J$  = 4.5 Hz, 2H), 8.35 (m, 4H), 7.76 (dd,  $J$  = 8.1, 3.2 Hz, 6H), 7.70-7.57 (m, 3H). UV-Vis (CHCl<sub>3</sub>):  $\lambda_{max}/nm$  = 410, 566, 605.

### General procedure for the insertion of cobalt in free-base corroles.<sup>20</sup>

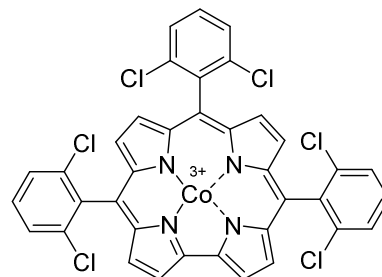
The respective free-base corrole (1.0 mmol, 1.0 equiv.) was dissolved in  $\text{CHCl}_3$ /methanol (MeOH) (7:3), then cobalt(II)acetate ( $\text{Co}(\text{OAc})_2$ ) (5 mmol, 5.0 equiv.) was added and the reaction mixture was refluxed, monitoring the reaction progress via UV-Vis spectroscopy. After full conversion the solvent was evaporated, the mixture was dissolved in DCM, washed with water, and dried over  $\text{MgSO}_4$ . After evaporating the solvent the products were obtained as red-brown solid.

### [5,10,15-Tris(2,3,4,5,6-pentafluorophenyl)corrole] cobalt(III) (CoTPFPc)



CoTPFPc was prepared according to the general procedure and obtained as a red-brown solid (20.3 mg, 90%). UV-Vis ( $\text{CHCl}_3$ ):  $\lambda_{\text{max}}/\text{nm} = 401, 538$ .

### [5,10,15-Tris(2,6-dichlorophenyl)corrole] cobalt(III) (CoTDCPC)



CoTDCPC was prepared according to the general procedure and obtained as a red-brown solid (19 mg, 95%). UV-Vis ( $\text{CHCl}_3$ ):  $\lambda_{\text{max}}/\text{nm} = 393, 525$ .

### Poly[1-(trimethylsilyl)-1-propyne]<sup>59</sup> (polyTMSP)

$\text{TaCl}_5$  (64.5 mg, 0.18 mmol, 1 equiv.) was dissolved in toluene (8 mL) and stirred for 30 min at 80 °C. Afterwards 1-(trimethylsilyl)-1-propyne (1.32 mL, 8.9 mmol, 49.4 equiv.) was added to the reaction mixture and stirred for 24 h at 80 °C. Then MeOH (50 mL) was added for precipitating the polymer. After complete precipitation the mixture was centrifuged (20 min, 3000 rpm) and the supernatant decanted. Then the polymer was dissolved in toluene again, precipitated into MeOH (50 mL) and centrifuged. After repeating the procedure three times the polymer was dried in an exsiccator for 24 h. (0.81 g, 79%)



### 3.2 Sensor fabrication

The sensor foils described in this work consist of two different polymer layers. The bottom layer is an inert, highly transparent polymer sheet (PET, Mylar®, thickness 125  $\mu\text{m}$ ) and is used as solid support for the sensing layer. 5,10,15-[tris(2,3,4,5,6-pentafluorophenyl)corrole] cobalt(III) (CoTPFPC) and 5,10,15-[tris(2,6-dichlorophenyl)corrole] cobalt(III) (CoTDCPC) were applied as indicator dyes (Figure D10). The sensing layer is composed of CoTPFPC and CoTDCPC embedded in a polymer matrix. This blend (referred to as “cocktail”) is cast on the solid support. Figure D3 shows a schematic of the sensor setup.

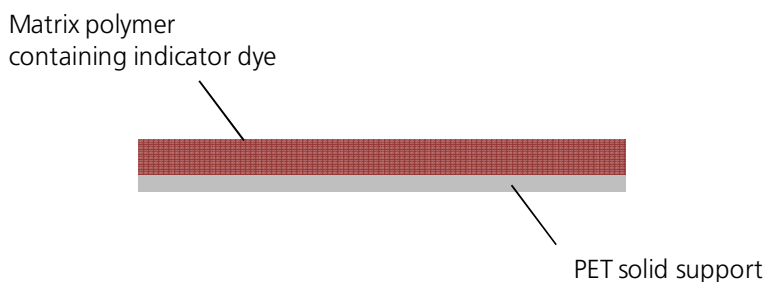


**Figure D3.** Schematic presentation of sensor foil setup (not to scale).

In this work three different polymers were investigated for their application as a matrix. Those were dissolved in chloroform in the following concentrations:

polystyrene	10 wt%
ethylcellulose	10 wt%
poly[1-(trimethylsilyl)-1-propyne]	5 wt%

Subsequently, the indicator dyes were dissolved in these polymer solutions with a concentration of 1 wt% (for reflection measurements) or 2 wt% (for absorbance measurements), respectively. The polymer/indicator blends were cast onto a Mylar® support (thickness of 125  $\mu\text{m}$ ) using a knife-coating device mounted with 60  $\mu\text{m}$  spacers (Figure D4). Afterwards the sensing layers were dried at room temperature for 30 minutes before further application.

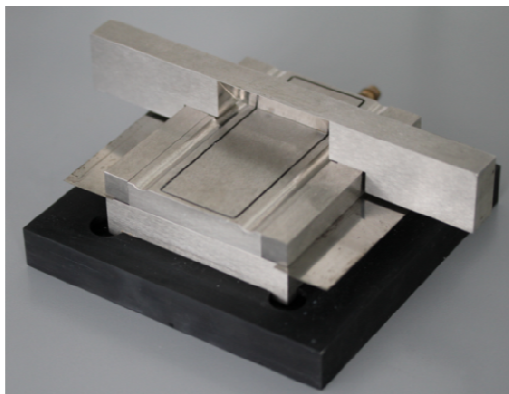


**Figure D4.** Home-made knife coating device for the preparation of homogeneous sensor films. PET foil is placed on the planar surface of the device where it is adhered by vacuum and a thin water film. On both sides of the surface variable spacer bars are mounted for adjusting the coating thickness of the sensor film. The above resting knife has a sharp edge which is moved along the foil for homogeneously spreading the polymer/indicator blends on the solid support.

### 3.3 Experimental setup for reflection measurements

The setup for performing reflection measurements is composed of following components (Figure D5):

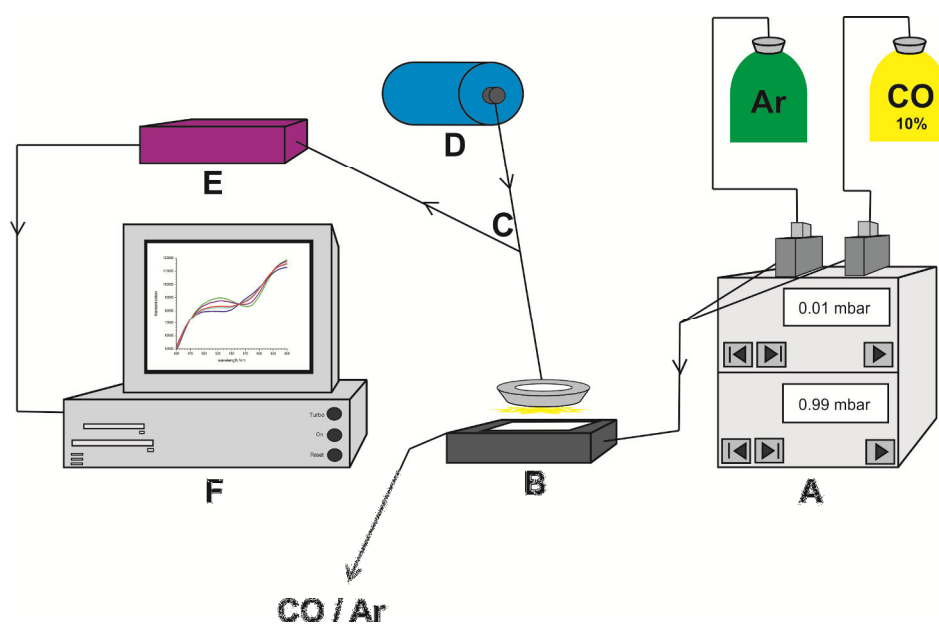


**Figure D5.** Experimental setup for sensor calibration by means of reflection measurements. **A:** Mass flow controllers and digital power supply with display, **B:** Measuring cell, **C:** Y-shaped fiber combining illumination and reading, **D:** Halogen light source, **E:** Spectrometer, **F:** Computer.

The mass-flow controllers were connected to inert argon which was used as carrier gas for adjusting CO-concentrations, as well as to carbon monoxide (10% in nitrogen) gas bottles. Two

mass-flow controllers from MKS instruments (type GVS-44) were regulated by a MKS instruments PR4000 digital power supply and display (Figure D5, A). The gas mixture was pumped into a home-made measuring cell (Figure D5, B) containing the sensor foil (1 cm x 1 cm) placed on a white ceramic pad (Figure D6). The sensor foil was illuminated by a halogen light source from Mikropack (type HL-2000-FHSA) via illumination fiber (Figure D5, C and D) through a transparent acrylic glass cover on top of the measuring cell. Detection of absorbance change was accomplished from above. Measuring 0 ppm CO implies the application of pure argon gas.

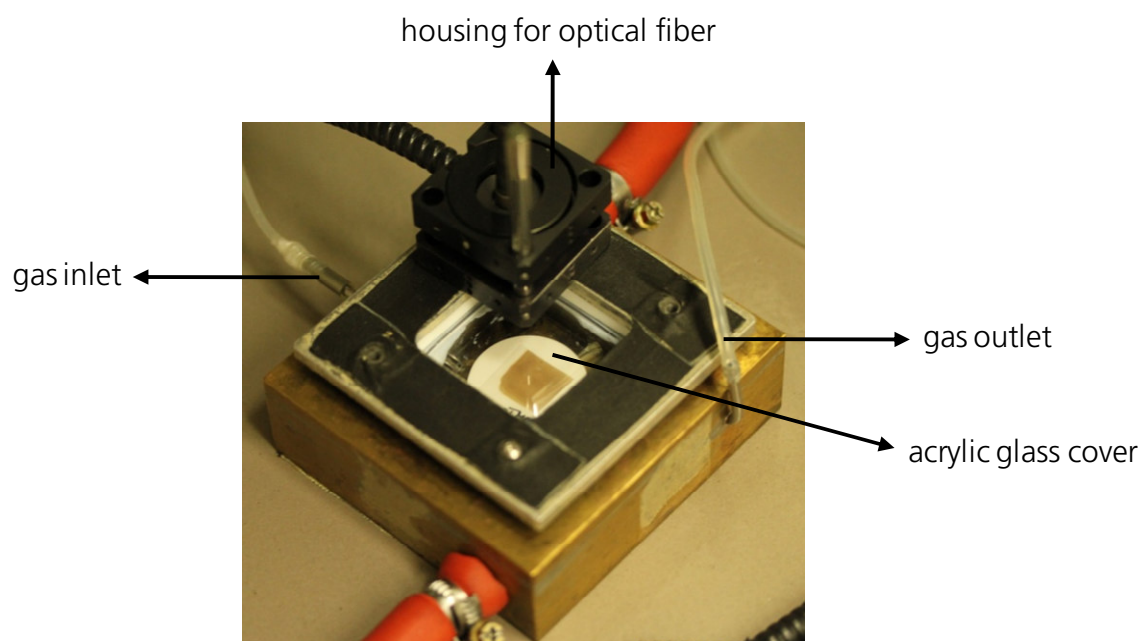


**Figure D6.** Measuring cell (B, Figure D5) for reflection measurements. Sensor foil was placed inside the cell onto a ceramic pad. By an acrylic glass cover the cell was closed and gas was pumped through. Reflection changes were measured from above by one Y-shaped optical fiber for illumination and reading.

### 3.4 Experimental setup for absorbance measurements

The setup for performing absorbance measurements is composed of following components (Figure D7):

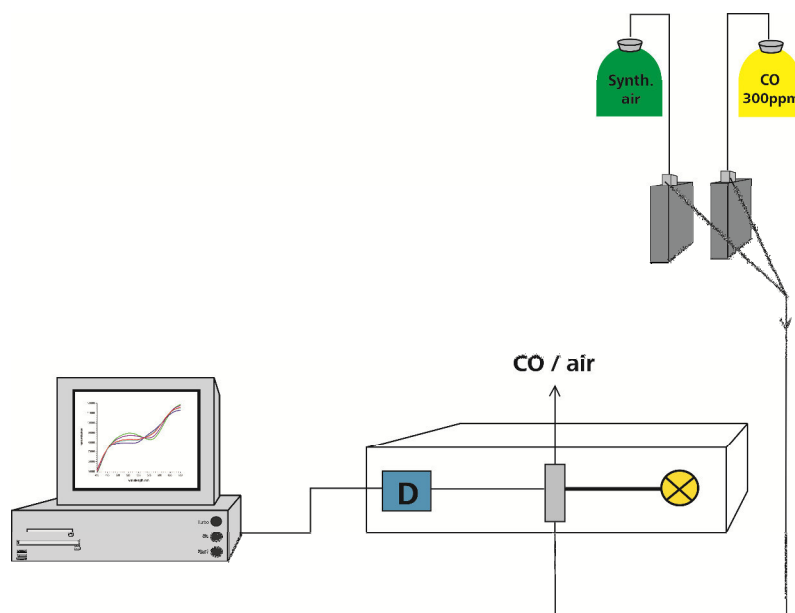


**Figure D7.** Experimental setup for sensor calibration by absorbance measurements.

The experimental setup for absorbance measurements consisted of a gas mixing device which were composed of mass flow controllers from Unit Instrument Inc. (UFC-8160A and UFC-1660) being controlled via a computer and custom-made software. The flow controllers were connected to synthetic air as inert carrier gas to adjust concentration of analyte gas and to CO, CO<sub>2</sub>, or NO<sub>2</sub> gas bottles as analytes (Figure D7).

The following reference gases were applied:

- 300 ppm CO diluted in synthetic air
- 3000 ppm CO<sub>2</sub> diluted in synthetic air
- 10 ppm NO<sub>2</sub> diluted in synthetic air

An overall gas flow of 100 sccm (standard cubic centimeter per minute) was applied and the gas mixtures were pumped into a home-made flow-through cell (Figure D8). After mounting a piece of sensor foil into the cell it was fixed in a Perkin Elmer Lambda 35 absorbance spectrometer replacing the cuvette holder. The flow-through cell was connected to the flow controllers by PTFE tubes which were mounted below (gas inlet) and above (gas outlet) the measuring chamber. Hence, gas mixtures were pumped through the cell, forming a defined atmosphere around the foil (Figure D8). For online-sensing the absorbance spectra were recorded every 24 s as this was

the fastest data acquisition rate. Measuring 0 ppm CO implies the application of pure synthetic air.

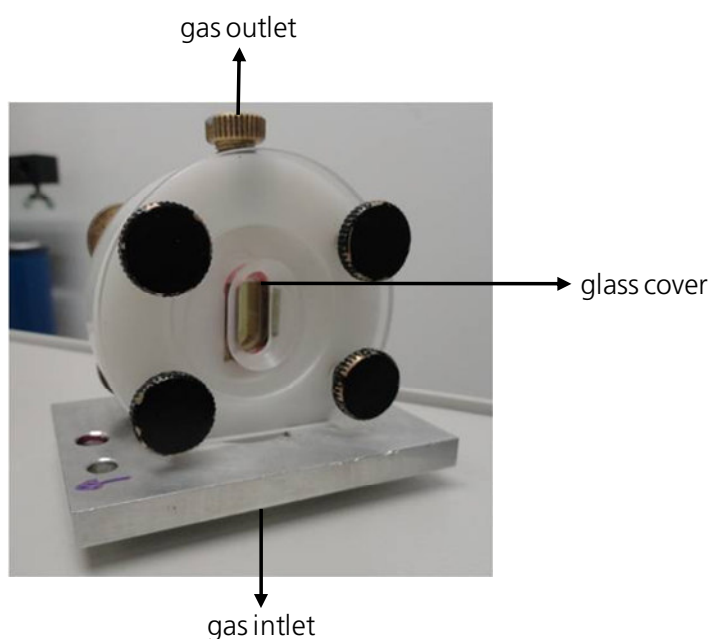


**Figure D8.** Measuring cell for absorbance measurements. PTFE tubes were mounted below (gas inlet) and above (gas outlet) the flow-through cell for pumping gas mixtures over the sensor foil.

### 3.5 Determination of absorption coefficients

According to Lambert-Beer law (Equation D1) the absorbance of a substance in dilute solutions depends on its molar absorption coefficient  $\varepsilon$ , its concentration  $c$ , and the light pathlength  $l$  through the sample.

$$A = \varepsilon * c * l \quad \text{Eq. D1}$$

In this work  $\varepsilon$  was calculated from triple determination for TPFPC, TDCPC, CoTPFPC, and CoTDCPC, respectively. For this purpose a dye solution in chloroform was prepared and diluted to obtain a linear relationship between absorbance intensities towards its dye concentrations. Afterwards the measured absorbance signals were plotted against the concentrations and plots were fitted with linear fit functions by adjusting the intercept to  $x = 0$  ppm;  $y = 0$ . As the light pathway  $l$  is 1 cm the absorption coefficients are represented by the slope of the linear fit functions. Absorption coefficient values were calculated as mean of three independent measurements and errors were determined as standard deviation. In the Appendix (Figure G3-G6) represent the linear curves for all dyes.

### 3.6 Determination of limits of detection (LOD) and sensitivity

When calibrating sensor foils with carbon monoxide gas linear signal responses were observed for small CO concentrations. Based on the parameters obtained from curve fitting the determination of limits of detection (LODs) became accessible. The quantification of LOD was performed by applying the blank value method described in DIN 32 436.<sup>60</sup> For practical application, however, it is useful to perform some simplifications which results in Equation D2 where  $x_{\text{LOD}}$  represents the LOD value and  $y_0$  the blank value with corresponding error  $s_{y_0}$ . Additional,  $A$  reflects the intersection of linear fit curves with the y axis and  $m$  the slope. Error propagation for LOD calculation was performed as shown by Equation D3 and D4 where  $s_A$  represents the error of intersection  $A$ ,  $s_m$  the error of slope  $m$ , and  $s_{x_{\text{LOD}}}$  the calculated error of LOD  $x_{\text{LOD}}$ .

$$y = A + m \cdot x \rightarrow x_{\text{LOD}} = \frac{(y_0 + 3 \cdot s_{y_0}) - A}{m} \quad \text{Eq. D2}$$

$$s_{x_{\text{LOD}}} = \sqrt{\left(\frac{\partial x_{\text{LOD}}}{\partial A} \cdot s_A\right)^2 + \left(\frac{\partial x_{\text{LOD}}}{\partial m} \cdot s_m\right)^2} \quad \text{Eq. D3}$$

$$s_{x_{\text{LOD}}} = \sqrt{\left(-\frac{1}{m} \cdot s_A\right)^2 + \left(-\frac{y - A}{m^2} \cdot s_m\right)^2} \quad \text{Eq. D4}$$

#### Sensitivity

For small carbon monoxide concentrations a linear signal response was observed. The sensitivities of sensor foils for carbon monoxide are here defined as the slope of corresponding linear calibration functions.

### 3.7 Data evaluation

The exposure of the sensor foils to carbon monoxide has an effect on reflectance and absorbance spectra of the indicator dye, respectively. Increasing the carbon monoxide concentration results in a signal increase of reflectance spectra at 530 nm and a decrease at 580 nm (Figure D9). For absorbance spectra the changes are reversed.

For generating calibration curves and time course data, the raw data evaluation was processed by calculating the ratio of signal intensities at 580 and 530 nm. The calculated values were plotted against the time to obtain time course data or against the carbon monoxide concentration for receiving calibration plots.

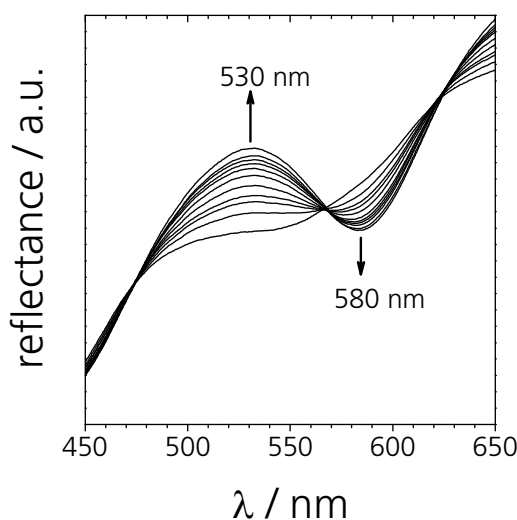


**Figure D9.** Spectral changes of reflected light intensity of the sensor system CoTPFPC/polyTMSP upon increasing the CO concentration from 0% to 10% carbon monoxide. Spectra plotted here were recorded after 15 min equilibration time with the respective CO concentrations.

## 4 Results and Discussion

### 4.1 Photophysical properties of indicator dyes

In this work two indicator dyes, namely 5,10,15-[tris(2,3,4,5,6-pentafluorophenyl)corrole] cobalt(III) (CoTPFPC) and 5,10,15-[tris(2,6-dichlorophenyl)corrole] cobalt(III) (CoTDCPC), were investigated for their applicability for carbon monoxide sensing (Figure D10). Both indicator dyes are metallocorroles with a cobalt(III) central ion and they only differ in their *meso*-substituents. While CoTDFPC (Figure D10, A) has bound three dichlorophenyl substituents, CoTPFPC (Figure D10, B) contains three pentafluorophenyl substituents (Figure D10, B).

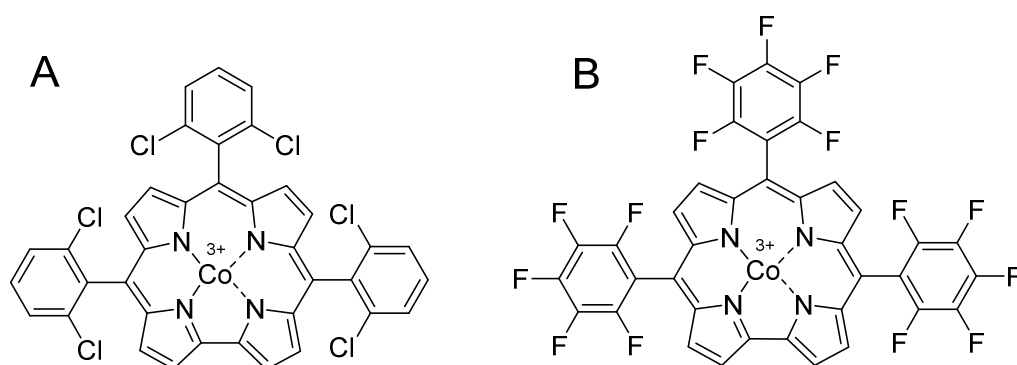


**Figure D10.** Chemical structure of indicator dyes. **A:** 5,10,15-Tris(2,6-dichlorophenyl)corrole] cobalt(III) (CoTDCPC), and **B:** 5,10,15-[Tris(2,3,4,5,6-penta-fluorophenyl)corrole] cobalt(III) (CoTPFPC).

The absorbance spectra of both indicator dyes in chloroform are depicted in Figure D11. Both possess high-intensity Soret bands at around 400 nm. Additionally, the spectra exhibit a weaker band (Q band) at around 550 nm whereas CoTPFPC shows a higher intensity compared to the spectrum of CoTDCPC.

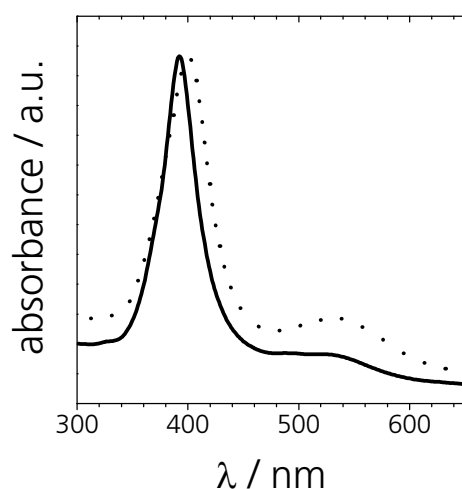


**Figure D11.** Absorbance spectra of CoTPFPC (dotted line) and CoTDCPC (solid line) in chloroform.



Precursors of CoTPFPC and CoTDCPC synthesis are the free-base corroles, namely 5,10,15-[tris(2,6-dichlorophenyl)corrole] cobalt(III) (TDCPC) and 5,10,15-[tris(2,3,4,5,6-pentafluorophenyl)corrole] cobalt(III) (TPFPC). Those are metalized with  $\text{Co}(\text{OAc})_2$  to generate the corresponding Co(III)-corroles, respectively. Absorption coefficients  $\epsilon$  were determined for the free-base corroles as well as for Co(III)-corroles (for details see chapter 3.5). The  $\epsilon$  values together with the corresponding standard deviation for each absorption band ( $\lambda_{\text{abs}}(\text{max})$ ) are depicted in Table D1.

**Table D1.** Absorption maxima ( $\lambda_{\text{max}}$ ) and molar absorption coefficients  $\epsilon$  with corresponding errors for free-base corroles TPFPC and TDCPC and for Co(III) corroles CoTPFPC and CoTDCPC in chloroform (mean  $\pm$  SD; N = 3).

Dye	$\lambda_{\text{max}} / \text{nm}$	$\epsilon \pm \text{SD} \times 10^{-3} / \text{M}^{-1} \text{cm}^{-1}$
TPFPC	407	$153 \pm 2$
	562	$25.3 \pm 0.5$
	605	$14.1 \pm 0.4$
TDCPC	410	$104 \pm 4$
	566	$15.9 \pm 0.9$
	605	$9.1 \pm 0.8$
CoTPFPC	401	$55 \pm 3$
	538	$16.5 \pm 0.9$
CoTDCPC	393	$68 \pm 3$
	525	$8.4 \pm 0.4$

Compared to TDCPC the  $\epsilon$  values of TPFPC are generally higher. For the respective Soret bands an  $\epsilon$  value of  $(153 \pm 2) \times 10^3 / \text{M}^{-1} \text{cm}^{-1}$  was determined for TPFPC, whereas TDCPC has a decreased value of  $(104 \pm 4) \times 10^3 / \text{M}^{-1} \text{cm}^{-1}$ . The same observation is reflected by the residual absorption coefficients as TPFPC has higher values at 562 and 605 nm than TDCPC at corresponding wavelengths 566 and 605 nm. Another observation from Table D1 is the blue shifted Soret band of TPFPC (407 nm) in contrast to TDCPC which has its maximum wavelength at 410 nm.

The Co(III)-corroles behave slightly different as CoTPFPC exhibits a lower  $\epsilon$  value at 401 nm ( $(55 \pm 3) \times 10^3 / \text{M}^{-1} \text{cm}^{-1}$ ) than CoTDCPC at 393 nm which is  $(68 \pm 3) \times 10^3 / \text{M}^{-1} \text{cm}^{-1}$ . Moreover,

the Q absorption bands at around 530 nm show a reverse effect than the Soret bands. Here the  $\epsilon$  value is higher for CoTPFPC ( $(16.5 \pm 0.9) \times 10^3 / \text{M}^{-1} \text{cm}^{-1}$ ) than for CoTDCPC ( $(8.4 \pm 0.4) \times 10^3 / \text{M}^{-1} \text{cm}^{-1}$ ). Furthermore, while the free-base corrole TPFPC showed a blue shifted Soret band in comparison to TDCPC the Co(III)-corrole CoTPFPC has a higher maximum wavelength at 401 nm than CoTDPC (393 nm).

Generally, Gouterman's four-orbital model is applied for the explanation of UV-Vis properties of symmetrical porphyrinoids. However, corroles have a direct pyrrol-pyrrol linkage and therefore, possess a lower symmetry. Nevertheless, the four orbital model was also confirmed to be valid for corroles. Hence, the absorption bands at around 400 nm are assigned to be Soret bands (B bands) and the absorptions between 500 and 700 nm are Q bands.<sup>61</sup> Absorption spectra of corroles are controlled by  $\pi$ - $\pi^*$  transitions similar to those of porphyrins which exhibit a more intense and broader Soret band and lower intensity Q-bands.<sup>62</sup>

Zhang et al. investigated the photophysical properties of electron-deficient free-base corroles containing *meso*-fluorophenyl substituents. They observed a blue-shift of Soret bands by enhancing the number of fluoride groups. The results indicate that an electron-withdrawing effect together with a heavy atom effect noticeably influences the photophysical properties of corroles.<sup>61</sup> Furthermore, Ding et al. investigated the effect of electron-withdrawing and -donating groups on the *meso*-phenyl rings of corroles. Similar to Zhang et al. they could demonstrate a blue shift of the Soret bands with enhanced electron withdrawing groups. Hence, as CoTPFPC has bound three pentafluorophenyl substituents on its corrole backbone its *meso*-substituents have an higher withdrawing effect than those of CoTDCPC. Consequently, the Soret band of CoTPFPC is blue shifted compared to the band of CoTDCPC.<sup>62</sup>

Comparing *meso*-substituted corroles with analogous porphyrins, a blue shift in Soret band and lower  $\epsilon$  values are observed for corroles. The blue-shift occurs since the symmetry of the corrole ring is reduced. Similar to porphyrins corroles have an 18- electron  $\pi$ -system, however, the reduced symmetry of corroles induces a splitting of the lowest unoccupied molecular orbitals ( $e_g$ ). This change in orbital energy results in lower-energy transitions for some of the Q-bands and a higher-energy transition for the Soret band. The reduction in alternancy symmetry simultaneously causes an increase of extinction coefficients of the corroles Q-bands (and lowers the  $\epsilon$  of Soret bands). In porphyrin molecules the Q-band transition dipole vectors are nearly the same in magnitude and have both a parallel orientation leading to a pseudo-parity forbidden transition. The opposite is true for the Soret band which increases in intensity. This effect is partially turned off by the changes in symmetry of the corrole ring, resulting in a Soret/Q-band ratio closer to unity.<sup>62</sup>

## 4.2 Choice of matrix polymers

Polymers for embedding CO sensing dyes need to fulfill various requirements. For the coating technique used in this work (for details see chapter 3.2) the polymer and the dye need to be soluble in the same solvent. Moreover, the sensor dye also needs to stay dissolved in the solid polymer when the solvent has evaporated, since absorbance or fluorescence cannot be measured in the case of precipitation. Furthermore, the polymer must be mechanically stable and highly permeable for carbon monoxide whereat less is known, however, about polymer permeabilities for carbon monoxide.

Gas adsorption and permeation in one special polymeric material is amongst other factors mainly dependent on the size of a gas. Gas sizes have been determined empirically by Hirschfelder, Curtiss and Bird.<sup>63</sup> For their work they presumed the intermolecular interaction of gases to follow the Lennard-Jones-(12,6)-potential (Equation D5).<sup>64</sup>

$$\Phi(r) = 4\varepsilon \left[ \left( \frac{\sigma}{r} \right)^{12} - \left( \frac{\sigma}{r} \right)^6 \right] \quad \text{Eq. D5}$$

$\Phi(r)$	potential
$\varepsilon$	potential depths
$\sigma$	particle distance for $\Phi(r) = 0$
$r$	particle distance

In his work Breck named the particle distance  $\sigma$  in Equation D5 as the kinetic diameter.<sup>64</sup> Today, kinetic diameters are widely used in discussing gas permeability of porous and polymeric materials. Carbon monoxide presumably exhibits diffusion properties similar to oxygen due to the small dipole moment of carbon monoxide ( $\mu_{\text{CO}} = 0.10980 \text{ D}$ )<sup>65</sup> and the similar kinetic diameters of the two gases ( $\sigma_{\text{CO}} = 3.76 \text{ \AA}$  and  $\sigma_{\text{O}_2} = 3.46 \text{ \AA}$ ).<sup>64</sup>

In this work it is assumed that carbon monoxide exhibits good permeability in oxygen-permeable polymers due to previously discussed reasons. Thus, we decided to investigate the highly oxygen permeable polymers polystyrene (PS), ethylcellulose (EC),<sup>66</sup> and poly[1-(trimethylsilyl)-1-propyne] (polyTMSP) as matrix polymers for carbon monoxide sensor fabrication.

<sup>67</sup> Figure D12 shows the chemical structures of the applied polymers.

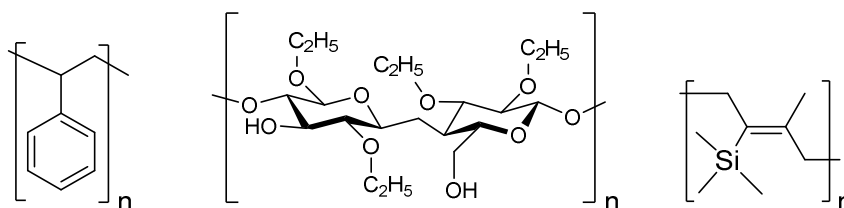


**Figure D12.** Chemical structures of the oxygen-permeable matrix polymers under study. **A:** polystyrene (PS), **B:** ethylcellulose (EC), and **C:** poly[1-(trimethylsilyl)-1-propyne] (polyTMSP).

The three polymers are widely used for gas sensing applications. Polystyrene and ethylcellulose are especially known for the application in optical oxygen sensing.<sup>40,68</sup> In addition, poly[1-(trimethylsilyl)-1-propyne] is established for embedding pressure-sensitive dyes being used in aerodynamic research<sup>39</sup> since polyTMSP is a glassy polymer with an extremely high oxygen permeability.<sup>59</sup>

In general permeability of different polymers depends on several factors and is not directly a function of the kinetic diameter of gases or the polymer's chemical structure. It depends on the orientation and density of the macromolecules as well as the thickness of the coating. The most common parameter for quantifying the diffusion of gases through a polymer is the so-called permeability coefficient  $P$  (Equation D6).<sup>66</sup>

$$P = \frac{(\text{thickness of polymer film}) \times (\text{quantity of gas})}{(\text{area}) \times (\text{time}) \times (\text{pressure drop across the film})} \quad \text{Eq. D6}$$

The determination of  $P$  is expressed by Equation D6. Thus, the polymer film thickness, quantity of gas (which means the gas volume), area of polymer film, time, and the pressure drop across the film affect the permeation coefficient.

**Table D2.** Oxygen permeability coefficients for the polymers under study at standard conditions (273.15 K and  $1.013 \times 10^5$  Pa).

Polymer	Permeability coefficient / $\text{cm}^2 (\text{Pa s})^{-1}$
Polystyrene <sup>66</sup>	$1.9 \times 10^{-13}$
Ethylcellulose <sup>66</sup>	$11 \times 10^{-13}$
Poly[1-(trimethylsilyl)-1-propyne] <sup>67</sup>	$3000 \times 10^{-13}$

Oxygen permeability coefficients for the three polymers under study are presented in Table D2. Hence, poly[1-(trimethylsilyl)-1-propyne] shows the highest permeability coefficient ( $P = 3000 \times 10^{-13} \text{ cm}^2(\text{Pa s})^{-1}$ ) followed by ethylcellulose ( $P = 11 \times 10^{-13} \text{ cm}^2(\text{Pa s})^{-1}$ ), and polystyrene which exhibits an oxygen permeation coefficient of  $1.9 \times 10^{-13} \text{ cm}^2(\text{Pa s})^{-1}$ . As a result the best carbon monoxide permeability is expected for polyTMSP followed by ethylcellulose and polystyrene.

For the development of a sensor another crucial property is reversibility. If the analyte gas is very soluble in the applied matrix polymer this can result in a very poor reversibility of the sensor. Hence, the gas stays solved in the matrix and cannot diffuse out. Consequently, a compromise is needed between high permeability and solubility of an analyte gas in the polymer for achieving fast response and an acceptable reverse time.

### 4.3 Calibration by reflection measurements (0 - 10% CO)

Sensor foils were calibrated by reflection measurements applying carbon monoxide concentrations between 0 and 10% (0 - 10.000 ppm). Details about the measurement setup are explained in chapter 3.3. Primarily indicator dye CoTPFPC was immobilized in the polymers polystyrene (PS), ethylcellulose (EC), and poly[1-(trimethylsilyl)-1-propyne] (polyTMSP) and coated on PET as solid support (chapter 3.2). Thus, sensor foils exhibiting a thickness of 3 – 6  $\mu\text{m}$  were received. The gathered reflection data was analyzed by ratiometric evaluation (for details see chapter 3.7). The corresponding calibration curves were established by fitting the data (Figure D13, A-C) applying an exponential fit function (Equation D7).

$$y = y_{\infty} - (y_{\infty} - y_0) \cdot e^{-k \frac{x}{x_0}} \quad \text{Eq. D7}$$

$y_{\infty}$       y-value for an infinite value of x

$y_0$         y-value for x = 0

$x_0$         constant (= 1 ppm)

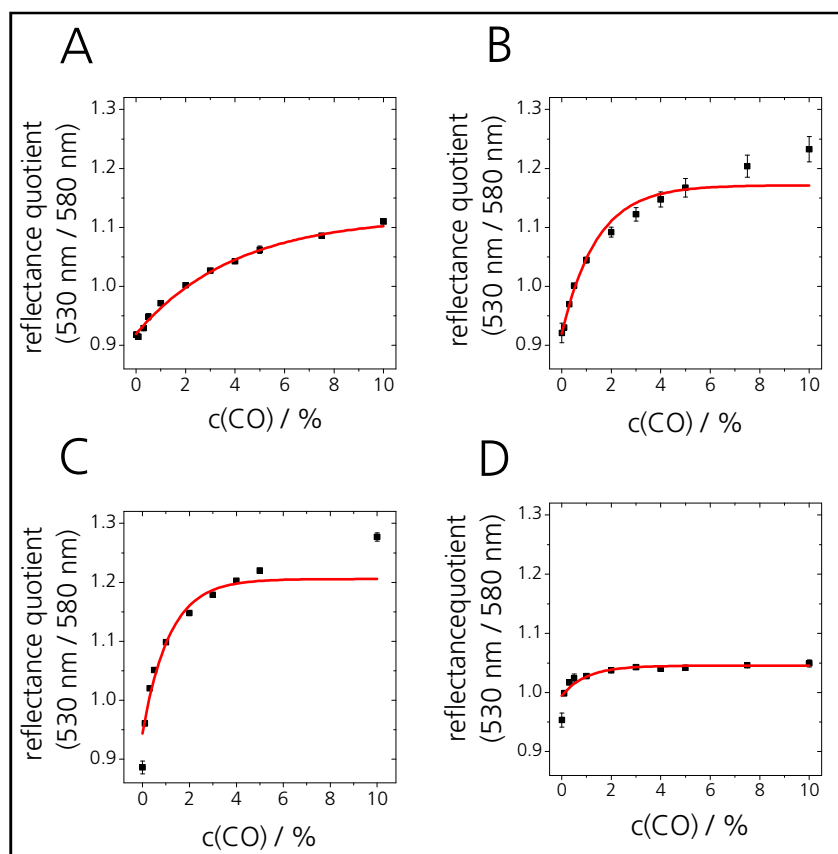


**Figure D13.** Calibration curves fitted by an exponential fit function of the following sensor systems **A:** CoTPFPC/PS ( $R^2 = 0.99$ ), **B:** CoTPFPC/EC ( $R^2 = 0.97$ ), **C:** CoTPFPC/polyTMSP ( $R^2 = 0.98$ ), and **D:** CoTDCPC/polyTMSP ( $R^2 = 0.97$ ), in a concentration range between 0 and 10% carbon monoxide (mean  $\pm$  SD,  $N = 3$ ).

All calibration curves with CoTPFPC as indicator dye show an increase of reflectance quotient (530 nm/580 nm) with increasing carbon monoxide concentration from 0 to 10% (Figure D13, A-C). Graph C, however, exhibits the highest overall signal increase of about 0.4 units followed by graph B (0.32 units), and A (0.2 units). Comparing the initial slope of the three curves graph B (CoTPFPC/EC) shows a steeper slope than graph A (CoTPFPC/PS). Curve C (CoTPFPC/polyTMSP), however, has the highest initial increase at low CO concentrations. As a result the polymer polyTMSP exhibits the highest carbon monoxide permeability followed by ethylcellulose and polystyrene. Additionally, it exhibits the highest sensitivity for low carbon monoxide concentrations due to its high initial slope. As polyTMSP turned out to be the most suitable matrix polymer it was used for both sensor dyes CoTPFPC and CoTDCPC. The calibration curve for CoTDCPC immobilized in polyTMSP was fitted with an exponential association as well and is depicted in Figure D13, D.

The calibration curve shows an increase with increasing carbon monoxide concentration however, at about 3% CO saturation is achieved and the signal remains constant despite further increase of the CO concentration. The overall signal change of sensor foil CoTDCPC/polyTMSP is just about 0.15 units. By comparing graph C and D it appears that CoTDCPC has a steeper initial slope than CoTPFPC/polyTMSP.

As a result CoTDCPC/polyTMSP should have the highest sensitivity for low carbon monoxide concentration and is not useful for concentrations higher than about 3% CO. In contrast, CoTPFPC/polyTMSP is less sensitive for low CO concentrations, however, it is applicable for concentrations up to 10%.

In order to obtain information about the response characteristics of the sensor systems, time course measurements were performed applying the two sensor systems CoTPFPC/polyTMSP and CoTDCPC/polyTMSP. For this purpose reflectance spectra were recorded every 15 seconds varying the concentration of carbon monoxide inside the measuring cell every 15 minutes. The plots in Figure D14 are derived from ratiometric evaluation of the received reflectance data (for details see chapter 3.7).

Graph A (CoTPFPC/polyTMSP) exhibits a signal increase by changing the CO concentration from 0 to 5%. After a few minutes saturation is achieved. After 15 min the concentration was increased from 5% to 10% CO resulting in a further increase of reflectance quotient. The overall signal change, however, is lower than for the concentration change from 0 to 5%. Reduction of the concentration to 0% caused a signal decrease to the initial value. With CoTDCPC/polyTMSP sensor foil the same experiment was performed whereat a signal increase was only observed for CO concentration changes between 0 and 5% CO. A further increase from 5% to 10% CO didn't affect the sensor signal which confirms the results received by calibration measurements (Figure D13).

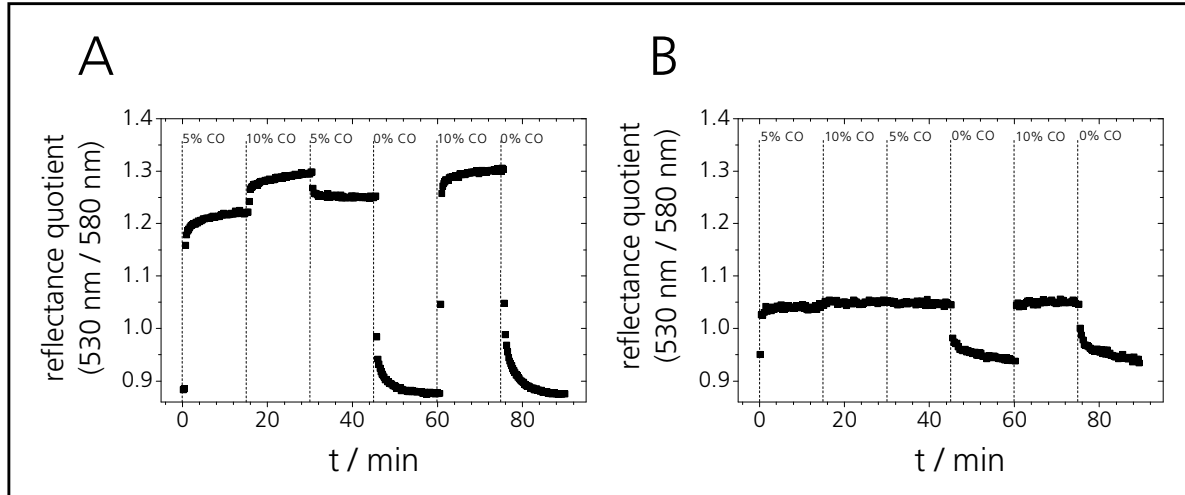


**Figure D14.** Time courses of the sensor systems **A:** CoTPFPC/polyTMSP and **B:** CoTDCPC/polyTMSP. Spectra were recorded every 15 seconds, varying the concentration of carbon monoxide inside the measuring cell every 15 minutes (5%, 10%, 5%, 0%, 10%, 0%).

Table D3 summarizes the calculated times until 90% of overall signal change ( $t_{90}$ ) is achieved for CO concentration changes from 0 to 10% and 10 to 0% carbon monoxide. Thereby, time for 0 to 10% is named as response and time for 10% to 0% as reverse time.  $T_{90}$  values were determined by fitting sectors of the time course measurements (Figure D14) with logistic fit functions (Equation D8). For this purpose sectors from 60-75 min were fitted for determining response times and sectors 75-90 min for reverse time calculation. A1 in Equation D8 represents the starting value of the fit curve whereas A2 marks the end point. By applying these parameters  $t_{90}$  were calculated.

$$y = \frac{A2 + (A1 - A2)}{1 + \left(\frac{x}{x_0}\right)^p} \quad \text{Eq. D8}$$

For both sensor foils the reverse times are higher than the response times (Table D3). Exemplary the response time of CoTPFPC/polyTMSP is 60 seconds while its reverse time is 165 seconds. Moreover, the response time of CoTPFPC/polyTMSP is higher compared to CoTDCPC/polyTMSP (45 seconds) whereas reverse times show an inverse behavior. The sensor system CoTPFPC/polyTMSP displays a reverse time of 165 seconds whereas it is 540 seconds for CoTDCPC/polyTMSP.

The determination of errors for response and reverse times was not reasonable due to limitations in the measurement setup. Connecting tubes between the gas mixing device and the measuring cell were about three meters and it was not possible to determine the exact time a



new gas mixture needs for arriving at the measuring cell. Thus, an indication of errors in the small size range of seconds is not meaningful and was therefore omitted.

**Table D3.**  $t_{90}$  values of the sensor systems CoTPFPC/polyTMSP and CoTDCPC/polyTMSP derived from time course measurements by changing CO concentration from 0 to 10% (response time) and from 10 to 0% (reverse time).

Sensor system	$t_{90} / s$	
	0 → 10% CO	10 → 0% CO
CoTPFPC/polyTMSP	60	165
CoTDCPC/polyTMSP	45	540

For determining limits of detections for the sensor foils lower carbon monoxide concentrations had to be investigated. Consequently, a new measurement setup was accomplished which is described in chapter 3.4. As polyTMSP turned out to be the most suitable polymer the measurements described in the following chapter were only carried out for the sensor systems CoTPFPC/polyTMSP and CoTDCPC/polyTMSP.

#### 4.4 Calibration by absorbance measurements (0 - 100 ppm CO)

Calibration measurements at lower carbon monoxide concentrations were performed for the sensor systems CoTPFPC/polyTMSP and CoTDCPC/polyTMSP. Therefore, a measurement setup was established as described in chapter 3.4 whereby an adjustment of CO concentrations between 0 and 100 ppm carbon monoxide became accessible. Calibration curves in Figure D15 result from ratiometric evaluation of the corresponding absorption spectra whereby the quotient of absorbance intensities at 580 nm/530 nm was determined. In order to achieve a direct comparability of calibration curves, the values were normalized to the blank value before plotting against the carbon monoxide concentration. The data sets were fitted using a linear fit function. The corresponding parameters are presented in Table D4.

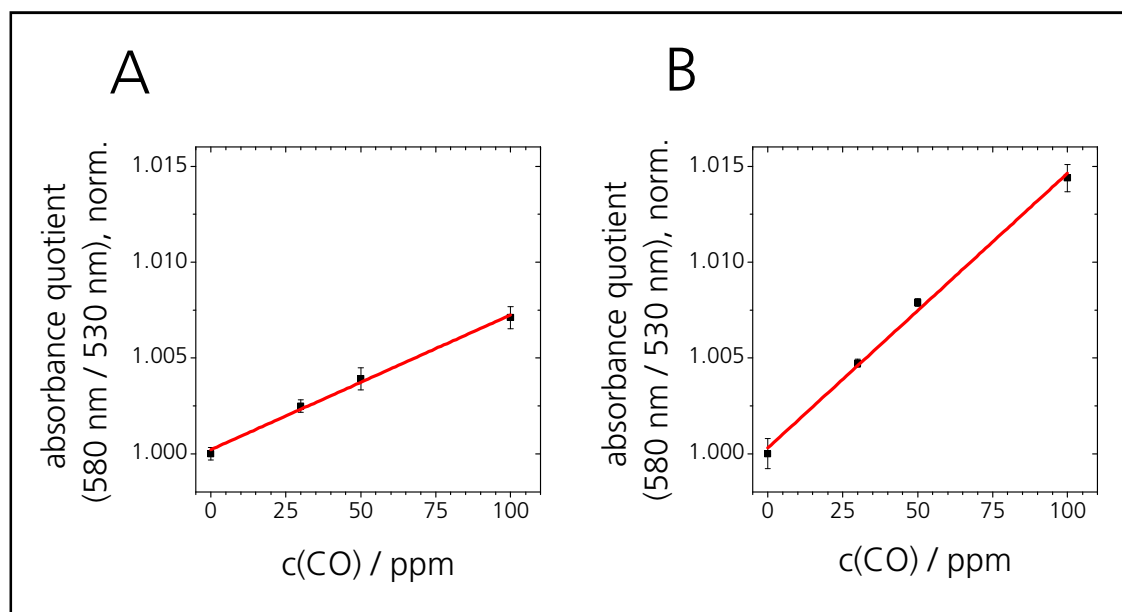


**Figure D15.** Normalized linear calibration curves of the sensor systems **A:** CoTPFPC/polyTMSP ( $R^2 = 0.99$ ) and **B:** CoTDCPC/polyTMSP ( $R^2 = 0.99$ ) in a concentration range between 0 and 100 ppm carbon monoxide (mean  $\pm$  SD,  $N = 3$ ).

As shown in Table D4 the calibration curve of sensor system CoTDCPC/polyTMSP exhibits a higher slope than CoTPFPC/polyTMSP. The slopes are  $1.43 \pm 0.06 \times 10^{-4}$  and  $7.0 \pm 0.3 \times 10^{-5}$  ppm $^{-1}$ , thus, the sensitivity of a carbon monoxide sensor is improved by applying CoTDCPC as indicator dye. This result was already expected by analyzing calibration plots received from reflectance measurements for CO concentrations between 0 and 10% (chapter 4.2.) and could now be verified definitely.

**Table D4.** Parameters of linear fit functions for sensor systems CoTPFPC/polyTMSP and CoTDCPC/polyTMSP. Errors derive from fitting.

Sensor system	Intercept	Slope / ppm $^{-1}$	Coefficient of determination $R^2$
CoTPFPC/polyTMSP	$1.0002 \pm 0.0002$	$7.0 \pm 0.3 \times 10^{-5}$	0.99
CoTDCPC/polyTMSP	$1.0003 \pm 0.0003$	$1.43 \times \pm 0.06 \times 10^{-4}$	0.99

Based on the parameters obtained from linear fit functions (Table D4) the limits of detection (LOD) were determined (for calculation procedure see chapter 3.6). While the sensor system CoTDCPC/polyTMSP exhibits a value of  $15 \pm 3$  ppm, the LOD is higher for the sensor system CoTPFPC/polyTMSP with  $23 \pm 3$  ppm (Table D5). With both sensor systems limits of detection lower than the threshold limit value were achieved which is 30 ppm in Germany. <sup>7</sup>

**Table D5.** Limits of detection of CoTPFPC and CoTDCPC immobilized in polyTMSP. Errors derive from error propagation (for details see chapter 3.6).

Sensor system	Limit of detection / ppm
CoTPFPC/polyTMSP	$23 \pm 3$
CoTDCPC/polyTMSP	$15 \pm 3$

The response time as well as the reverse time of both sensor systems was investigated. In this context time course measurements were performed by varying the carbon monoxide concentration every 10 min between 0 ppm and 100 ppm. Therefore, absorbance spectra were recorded every 24 seconds as this was the fastest data acquisition rate. The measurement cycles were repeated six times and data was evaluated by calculating the absorbance quotient of signals at 580 and 530 nm (for details see chapter 3.7). In order to achieve a direct comparability of time course values were normalized to the blank value before plotting against the time (Figure D16, A and B). During the measuring time no visible photodegradation or hysteresis of the sensor systems has been observed.

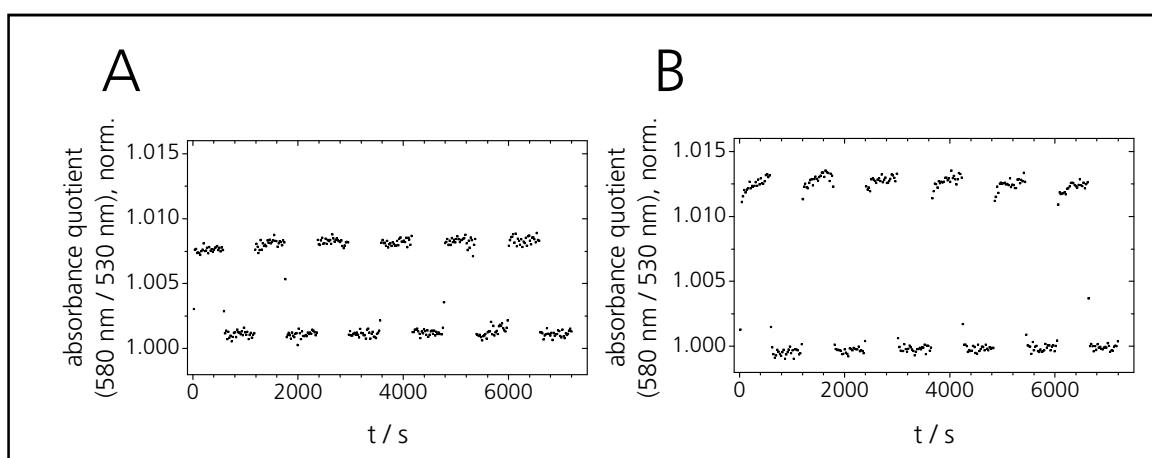
**Figure D16.** Representative, normalized time courses of the sensor systems **A:** CoTPFPC/polyTMSP and **B:** CoTDCPC/polyTMSP. The CO concentration was changed every 10 min between 0 and 100 ppm carbon monoxide whereby spectra were recorded every 24 seconds.

Table D6 displays the calculated rates for 90% overall signal change ( $t_{90}$ ), achieved for CO concentration changes from 0 to 100 ppm and from 100 to 0 ppm carbon monoxide. Thereby, time for 0 to 100 ppm is referred to as response and the time for 100 to 0 ppm as reverse time.  $T_{90}$  values were determined by fitting sectors of the time courses (Figure D16) by logistic fit functions (Equation D8).

For this purpose three different sectors (see Figure D16) which reflect a change from 0 to 100 ppm of one measurement were fitted with a logistic fit function. For the determination of response times this procedure was repeated for three individual measurements. For reverse time three different sectors belonging to a CO concentration change from 100 to 0 ppm of one measurement were fitted. This procedure was also repeated for overall three individual measurements. In Equation D8 parameter A1 represents the initial whereas A2 marks the saturation value. By applying these parameters  $t_{90}$  value calculation was performed. Values in Table D6 reflect the mean of the obtained response and reverse time. However, the obtained values are smaller than the fastest data acquisition rate of 24 seconds and, thus don't give a reasonable basis for comparison and discussion. Therefore, indication of errors was omitted.

**Table D6.** Response and reversibility times of CoTPFPC and CoTDCPC immobilized in polyTMSP (mean; N = 3).

Sensor system	Response time $t_{90}$ / s (N = 3)	Reverse time $t_{90}$ / s (N = 3)
CoTPFPC/polyTMSP	7	7
CoTDCPC/polyTMSP	20	20

For time course measurements with high carbon monoxide concentrations (0 to 10%, chapter 4.2) sensor system CoTPFPC/polyTMSP exhibited a  $t_{90}$  value of 165 seconds whereas it was 540 seconds for CoTDCPC/polyTMSP. However, the value for response time was higher for CoTPFPC/polyTMSP (60 seconds) than for CoTDCPC/polyTMSP (45 seconds). This effect might be attributed to the higher CO concentration investigated in chapter 4.2 since time course measurements were performed by varying carbon monoxide concentrations between 0 and 10%. While CoTPFPC/polyTMSP showed a signal increase for the whole concentration range of up to 10%, the CO sensor foil comprising CoTDCPC/polyTMSP exhibits no further change when increasing the CO content from 5% to 10%. Therefore, the lower response time of CoTDCPC/polyTMSP compared to CoTPFPC/polyTMSP might be attributed to reaching the maximum signal more rapidly due to a complement signal change already at about 3% CO.

#### 4.5 Assessment cross sensitivities

Carbon monoxide is generated during incomplete combustion processes of organic material. Therefore, installation of carbon monoxide sensors is reasonable next to combustion engines, in underground parking lots, or heating installations. Since nitrogen dioxide and carbon dioxide are generated during these combustion processes as well, cross sensitivities for these gases were investigated. For this purpose only sensor system CoTPFPC/polyTMSP was applied since it has a

higher indication range than CoTDCPC/polyTMSP. Moreover, it might be certainly assumed that CoTPFPC/polyTMSP and CoTDCPC/polyTMSP show similar results in qualitative analyzing their response to CO<sub>2</sub> and NO<sub>2</sub>.

Measurements were performed by changing concentrations every 10 minutes while absorbance spectra were recorded every 24 seconds. Thereby, concentration changes were chosen as follows:

CO<sub>2</sub>: 0 ppm – 2250 ppm – 0 ppm – 3000 ppm – 0 ppm

NO<sub>2</sub>: 0 ppm – 5 ppm – 0 ppm – 10 ppm – 0 ppm

The absorbance measurements were evaluated by calculating the absorbance quotients of signals at 580 and 530 nm. In order to achieve a direct comparability of both curves values were normalized to their respective blanks before plotting against the time (Figure D17, A and B). For CO<sub>2</sub> measurements no response of CoTPFPC/polyTMSP is observed up to 3000 ppm (Figure D17, A) as signals stay constant during the whole measuring time. In Figure D17, B signal fluctuations are realizable for NO<sub>2</sub>, however, those do not match to time intervals of concentration changing which was every 10 minutes. Furthermore, no signal drift is observed but rather signal peaks. Thus, signal fluctuations most probably appear from measurement noise and do not arise directly from a sensor response towards nitrogen dioxide.

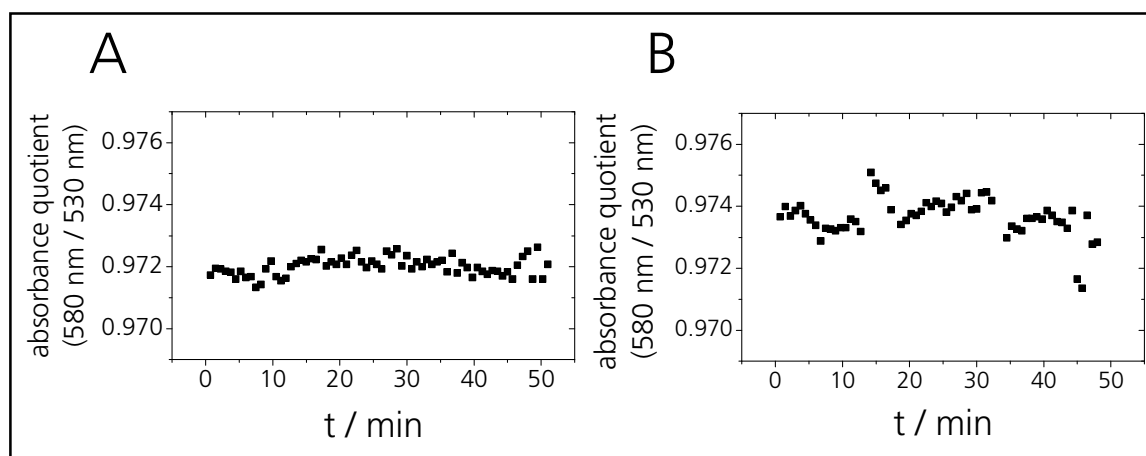


**Figure D17. A:** Cross sensitivity of CoTPFPC/polyTMSP towards **A:** CO<sub>2</sub> and **B:** NO<sub>2</sub>. Data is normalized to the starting value.

## 5 Summary and conclusion

A novel optical sensor system for carbon monoxide was developed applying two different Co(III)-corroles as indicator dyes. Those were 5,10,15-[tris(2,3,4,5,6-pentafluorophenyl)corrole] cobalt(III) (CoTPFPC) and 5,10,15-[tri(2,6-dichlorophenyl)corrole] cobalt(III) (CoTDCPC) which have slightly different photophysical properties due to their electronic structures. It is possible to incorporate the indicator dyes into polymers as solid support. In this work three different polymer matrices were used: polystyrene (PS), ethylcellulose (EC), and poly[1-(trimethylsilyl)-1-propyne] (polyTMSP). For the fabrication of sensor foils polymer-dye-blends were cast onto polyethyleneterephthalate (PET) as solid support. Those were calibrated by means of reflection and absorbance spectroscopy. Calibration by reflection measurements applying CO concentration between 0 and 10% carbon monoxide is possible and was already performed during a master thesis in 2012 ("Synthesis of indicator dyes and development of new sensor systems for carbon monoxide sensing") and results were reanalyzed in more detail and statistically evaluated in the context of this thesis. In conclusion, poly[1-(trimethylsilyl)-1-propyne] (polyTMSP) is the most suitable matrix polymer for fabricating optical carbon monoxide sensors.

Absorbance measurements at lower CO concentrations (0 - 100 ppm) with sensor foils CoTPFPC/polyTMSP and CoTDCPC/polyTMSP were performed. Both are stable over at least 120 min and do not undergo any photodegradation during this time. The Co(III)-corroles immobilized in polyTMSP might be applied for sensing carbon monoxide in ambient air, since sensor responses are fast and fully reversible. Response and reversibility times are lower than the fastest data acquisition rate of 24 seconds. Detection limits were calculated to be  $23 \pm 3$  ppm for CoTPFPC and  $15 \pm 3$  ppm for CoTDCPC and thus, are lower than the threshold limit value for CO in Germany of 30 ppm. From cross sensitivity experiments of CoTPFPC/polyTMSP towards CO<sub>2</sub> (up to 3000 ppm) and NO<sub>2</sub> (up to 10 ppm) a cross sensitivity for these gases is excluded.

In conclusion, for low carbon monoxide concentrations CoTDCPC shows the highest sensitivity and, thus, the lowest limit of detection. CoTPFPC has a faster response and reverse time and better response characteristics at high carbon monoxide concentrations. Hence, for the application of a CO sensor one can choose between these two systems depending on the use case requirements. E.g. if fast response and high reversibility are required, the CoTPFPC/polyTMSP system has to be preferred. If low carbon monoxide concentrations are of interest, however, CoTDCPC/polyTMSP is the system of choice.

## 6 References

- (1) Cevik, A. A.; Unluoglu, I.; Yanturali, S.; Kalkan, S.; Sahin, A. *Int. J. Clin. Pract.* **2006**, *60* (12), 1558–1564.
- (2) Nicholls J. C. *Med. Hypotheses* **2001**, *57* (5), 591–592.
- (3) Romão, C. C.; Blättler, W. A.; Seixas, J. D.; Bernardes, G. J. L. *Chem. Soc. Rev.* **2012**, *41* (9), 3571.
- (4) Raub, J. A.; Mathieu-Nolf, M.; Hampson, N. B.; Thom, S. R. *Toxicology* **2000**, *145* (1), 1–14.
- (5) Heinemann, S. H.; Hoshi, T.; Westerhausen, M.; Schiller, A. *Chem. Commun.* **2014**, *50* (28), 3644.
- (6) Omaye, S. T. *Toxicology* **2002**, *180* (2), 139–150.
- (7) Senatskommission zur Prüfung, DFG, Ed. *MAK- und BAT-Werte-Liste 2013*, 49th edn.; WILEY-VCH Verlag GmbH: Weinheim, 2013.
- (8) Des Gorman; Drewry, A.; Huang, Y. L.; Sames, C. *Toxicology* **2003**, *187* (1), 25–38.
- (9) Penney, D. G. *Toxicology* **1990**, *62* (2), 123–160.
- (10) Berg, J. M.; Stryer, L.; Tymoczko, J. L. *Biochemie*, 7th edn.; Springer Spektrum: Berlin, 2013.
- (11) Hartzell, G. E. *Toxicology* **1996**, *115* (1-3), 7–23.
- (12) Hampson, N. B.; Piantadosi, C. A.; Thom, S. R.; Weaver, L. K. *Am. J. Respir. Crit. Care Med.* **2012**, *186* (11), 1095–1101.
- (13) Sternbach, G. L.; Varon, J. *Resuscitation* **2003**, *58* (2), 127–130.
- (14) Statistisches Bundesamt (Destatis). *Gesundheit - Todesursachen in Deutschland - Fachserie 12 Reihe 4 - 2012*. 2013 [cited: 2015 september 16]; available from: <https://www.destatis.de/DE/Publikationen/Thematisch/Gesundheit/Todesursachen/Todesursachen2120400127004.html>.
- (15) Statistisches Bundesamt (Destatis). *Gesundheit - Todesursachen in Deutschland - Fachserie 12 Reihe 4 - 2013*. 2014 [cited: 2015 september 16]; available from: <https://www.destatis.de/DE/Publikationen/Thematisch/Gesundheit/Todesursachen/Todesursachen.html;jsessionid=EBA11A0543E96B2C3F2DBC49DB25DF69.cae2>.
- (16) Rajiah, K. *Afr. J. Pharm. Pharmacol.* **2011**, *5* (2), 259–263.
- (17) Marks, G. S.; Vreman, H. J.; McLaughlin, B. E.; Brien, J. F.; Nakatsu, K. *Antioxid. Redox Signaling* **2002**, *4* (2), 271–277.
- (18) Morimoto, Y.; Durante, W.; Lancaster, D. G.; Klattenhoff, J.; Tittel, F. K. *Am. J. Physiol.: Heart Circ. Physiol.* **2001**, *280* (1), H483–H488.
- (19) Fernández-Sánchez, J. F.; Fernández, I.; Steiger, R.; Beer, R.; Cannas, R.; Spichiger-Keller, U. E. *Adv. Funct. Mater.* **2007**, *17* (7), 1188–1198.

- (20) Barbe, J.-M.; Canard, G.; Brandès, S.; Jérôme, F.; Dubois, G.; Guillard, R. *Dalton Trans.* **2004** (8), 1208–1214.
- (21) Esteban, J.; Ros-Lis, J. V.; Martínez-Máñez, R.; Marcos, M. D.; Moragues, M.; Soto, J.; Sancenón, F. *Angew. Chem. Int. Ed. Engl.* **2010**, *49* (29), 4934–4937.
- (22) Heylen, S.; Martens, J. A. *Angew. Chem. Int. Ed. Engl.* **2010**, *49* (42), 7629–7630.
- (23) Fine, G. F.; Cavanagh, L. M.; Afonja, A.; Binions, R. *Sensors* **2010**, *10* (6), 5469–5502.
- (24) Borisov, S. M.; Klimant, I. *Anal. Chem.* **2007**, *79* (19), 7501–7509.
- (25) Borisov, S. M.; Wolfbeis, O. S. *Anal. Chem.* **2006**, *78* (14), 5094–5101.
- (26) Bültzingslöwen, C. v.; McEvoy, A. K.; McDonagh, C.; MacCraith, B. D.; Klimant, I.; Krause, C.; Wolfbeis, O. S. *Analyst* **2002**, *127* (11), 1478–1483.
- (27) Fercher, A.; Borisov, S. M.; Zhdanov, A. V.; Klimant, I.; Papkovsky, D. B. *ACS Nano* **2011**, *5* (7), 5499–5508.
- (28) Hradil, J.; Davis, C.; Mongey, K.; McDonagh, C.; MacCraith, B. D. *Meas. Sci. Technol.* **2002**, *13* (10), 1552–1557.
- (29) Hyakutake, T.; Taguchi, H.; Kato, J.; Nishide, H.; Watanabe, M. *Macromol. Chem. Phys.* **2009**, *210* (15), 1230–1234.
- (30) Stich, M. I. J.; Nagl, S.; Wolfbeis, O. S.; Henne, U.; Schaeferling, M. *Adv. Funct. Mater.* **2008**, *18* (9), 1399–1406.
- (31) Iijima, Y.; Sakaue, H. *Sens. Actuators, A* **2012**, *184*, 128–133.
- (32) Stich, M. I. J.; Borisov, S. M.; Henne, U.; Schäferling, M. *Sens. Actuators, B* **2009**, *139* (1), 204–207.
- (33) Davidge, K. S.; Sanguinetti, G.; Yee, C. H.; Cox, A. G.; McLeod, C. W.; Monk, C. E.; Mann, B. E.; Motterlini, R.; Poole, R. K. *J. Biol. Chem.* **2009**, *284* (7), 4516–4524.
- (34) Wang, J.; Karpus, J.; Zhao, B. S.; Luo, Z.; Chen, P. R.; He, C. *Angew. Chem. Int. Ed.* **2012**, *51* (38), 9652–9656.
- (35) Yuan, L.; Lin, W.; Tan, L.; Zheng, K.; Huang, W. *Angew. Chem. Int. Ed. Engl.* **2013**, *52* (6), 1628–1630.
- (36) Chakravarty, A. R.; Cotton, F. A.; Tocher, D. A.; Tocher, J. H. *Organometallics* **1985**, *4* (1), 8–13.
- (37) Moragues, M. E.; Esteban, J.; Ros-Lis, J. V.; Martínez-Máñez, R.; Marcos, M. D.; Martínez, M.; Soto, J.; Sancenón, F. *J. Am. Chem. Soc.* **2011**, *133* (39), 15762–15772.
- (38) Michel, B. W.; Lippert, A. R.; Chang, C. J. *J. Am. Chem. Soc.* **2012**, *134* (38), 15668–15671.
- (39) Schäferling, M. *Angew. Chem. Int. Ed. Engl.* **2012**, *51* (15), 3532–3554.
- (40) Amao, Y. *Microchim. Acta* **2003**, *143* (1), 1–12.
- (41) Borisov, S. M.; Papkovsky, D. B.; Ponomarev, G. V.; DeToma, A. S.; Saf, R.; Klimant, I. *J. Photochem. Photobiol., A* **2009**, *206* (1), 87–92.



- (42) Gross, Z.; Galili, N.; Saltsman, I. *Angew. Chem. Int. Ed.* **1999**, 38 (10), 1427–1429.
- (43) Gryko, D. T.; Koszarna, B. *Org. Biomol. Chem.* **2003**, 1 (2), 350–357.
- (44) Aviv, I.; Gross, Z. *Chem. Commun.* **2007** (20), 1987.
- (45) Aviv-Harel, I.; Gross, Z. *Chem. - Eur. J.* **2009**, 15 (34), 8382–8394.
- (46) Buckley, H. L.; Arnold, J. *Dalton Trans.* **2015**, 44 (1), 30–36.
- (47) Simkhovich, L.; Galili, N.; Saltsman, I.; Goldberg, I.; Gross, Z. *Inorg. Chem.* **2000**, 39 (13), 2704–2705.
- (48) Basumatary, B.; Raja Sekhar, A.; Ramana Reddy, R. V.; Sankar, J. *Inorg. Chem.* **2015**, 54 (9), 4257–4267.
- (49) Barbe, J.-M.; Canard, G.; Brandès, S.; Guillard, R. *Chem. Eur. J.* **2007**, 13 (7), 2118–2129.
- (50) Basumatary, B.; Ayoub Kaloo, M.; Kumar Singh, V.; Mishra, R.; Murugavel, M.; Sankar, J. *RSC Adv.* **2014**, 4 (54), 28417.
- (51) He, C.-L.; Ren, F.-L.; Zhang, X.-B.; Han, Z.-X. *Talanta* **2006**, 70 (2), 364–369.
- (52) Pariyar, A.; Bose, S.; Chhetri, S. S.; Biswas, A. N.; Bandyopadhyay, P. *Dalton Trans.* **2012**, 41 (13), 3826–3831.
- (53) Stich, M. I. J.; Fischer, L. H.; Wolfbeis, O. S. *Chem. Soc. Rev.* **2010**, 39 (8), 3102–3114.
- (54) McDonagh, C.; Kolle, C.; McEvoy, A. K.; Dowling, D. L.; Cafolla, A. A.; Cullen, S. J.; MacCraith, B. D. *Sens. Actuators, B* **2001**, 74 (1–3), 124–130.
- (55) Papkovsky, D. B.; Ponomarev, G. V.; Trettnak, W.; O'Leary, P. *Anal. Chem.* **1995**, 67 (22), 4112–4117.
- (56) Kurihara, K.; Takamatsua, S.; Kobayashi, T.; Takagi, H.; Maeda, R. *Procedia Eng.* **2011**, 25, 876–879.
- (57) Tekin, E.; Smith, P. J.; Schubert, U. S. *Soft Matter* **2008**, 4 (4), 703.
- (58) Bose, S.; Bogner, R. H. *Int. J. Pharm.* **2010**, 393 (1–2), 32–40.
- (59) Khotimsky, V. S.; Tchirkova, M. V.; Litvinova, E. G.; Rebrov, A. I.; Bondarenko, G. N. *J. Polym. Sci. A Polym. Chem.* **2003**, 41 (14), 2133–2155.
- (60) Müller W. *Kalibrierung nach DIN 32645 bzw. DIN 38402*. 2015 [cited: 07 october 2015]; available from: [http://www.ces.karlsruhe.de/culm/culm/culm2/th\\_themen/C06-kalibrierung/kalibrierung.pdf](http://www.ces.karlsruhe.de/culm/culm/culm2/th_themen/C06-kalibrierung/kalibrierung.pdf).
- (61) Zhang, L.; Liu, Z.-Y.; Zhan, X.; Wang, L.-L.; Wang, H.; Liu, H.-Y. *Photochem. Photobiol. Sci.* **2015**, 14 (5), 953–962.
- (62) Ding, T.; Alemán, E. A.; Modarelli, D. A.; Ziegler, C. J. *J. Phys. Chem. A* **2005**, 109 (33), 7411–7417.
- (63) Hirschfelder, J. O.; Curtiss C. F.; Bird R. B. *J. Polym. Sci.* **1955**, 17 (83), 116.
- (64) Mehio, N.; Dai, S.; Jiang, D.-e. *J. Phys. Chem. A* **2014**, 118 (6), 1150–1154.

- (65) Haynes, W. M. *CRC Handbook of Chemistry and Physics*, 93rd edn.; CRC; Taylor & Francis: Boca Raton, Fla., London, 2012.
- (66) Brandrup, J.; Immergut, E. H.; Grulke, E. A. *Polymer Handbook*, 4th edn.; Wiley: New York, 1999.
- (67) Masuda, T.; Isobe, E.; Higashimura, T. *Macromolecules* **1985**, *18* (5), 841–845.
- (68) McDonagh, C.; Burke, C. S.; MacCraith, B. D. *Chem. Rev.* **2008**, *108* (2), 400–422.

## E Detection of ammonia for work safety applications

### 1 Introduction

#### 1.1 Sources of ammonia and application fields for ammonia sensors

Ammonia is a neutral and colorless gas with pungent odor. It is incombustible and exhibits very high water solubility. <sup>1-3</sup> Due to its water solubility ammonia is highly corrosive and causes irritation of eyes, skin, and mucous membranes. The strong smell of the gas can be perceived at concentrations close to 50 ppm <sup>3</sup> whereas the work place limit is already at 20 ppm. <sup>1,2</sup>

Exposure to ammonia concentrations below 25 ppm has no significant influence on body functions. <sup>3</sup> Prolonged exposure to 25 - 100 ppm ammonia influences the generation of asthma and bronchitis, chronic eye irritation and may cause dermatitis. <sup>3</sup> Exposure to 500 ppm ammonia can cause an immediate and severe irritation of nose and throat, swollen eyelids, and even permanent blindness. <sup>3</sup> Even higher ammonia concentrations ( $\geq 1000$  ppm) can result in pulmonary oedema being mostly unperceived within the first 24 h after exposure. Difficulty with breathing and tightness in the chest are first symptoms of an oedema. Short-term exposure to such high ammonia concentrations can result in severe or even fatal long-term respiratory system disorders and liver failure. <sup>4</sup> Furthermore, extremely high concentrations ( $> 5000$  ppm) are suggested to be lethal within 5 - 10 min. <sup>2</sup>

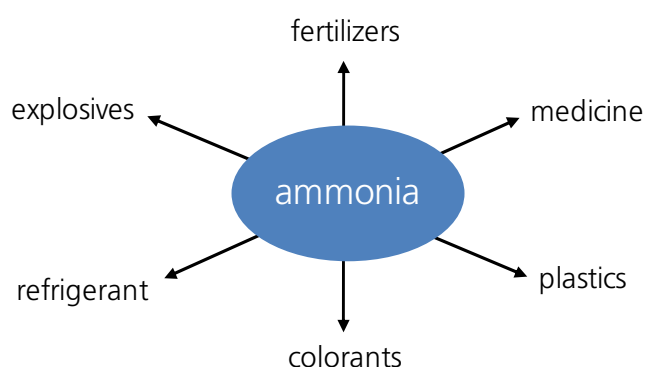


**Figure E1.** Overview of selected industrial products made from ammonia as basic substance. <sup>1</sup>

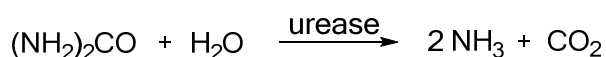
The major technique for the chemical production of ammonia is the Haber-Bosch process. Fritz Haber and Carl Bosch developed this production process during the period between 1909 and 1910. Based on Linde- and Ostwald-process they enabled ammonia generation from atmospheric

nitrogen and hydrogen. Ammonia production was initiated by the demand for an inexpensive supply of nitrogen for the generation of nitric acid and saltpeter as basic products for the production of explosives. Today, ammonia is a widely used chemical in industry.<sup>3</sup> An overview of selected products made from ammonia as key component is given in Figure E1.<sup>1,5</sup>

An important application of ammonia is the production of fertilizers for agriculture use.<sup>6,7</sup> These are, amongst others, ammonium nitrate ( $\text{NH}_4\text{NO}_3$ ), ammonium sulfate ( $(\text{NH}_4)_2\text{SO}_4$ ), and urea ( $\text{H}_2\text{N-CO-NH}_2$ ). In Germany about 1.6 million tons of nitrogen fertilizers are consumed in agriculture.<sup>1</sup> Furthermore, ammonia is used for the fabrication of plastics such as nylon, acrylonitrile, or polyamide and for sulfonamide generation used in medicine for inhibiting of bacterial growth.<sup>8</sup> Another substantial ammonia application field is the production of refrigerators. Almost all refrigeration systems for food processing and storage implement ammonia due to its ability of cooling below 0 °C by vapor compression.<sup>2</sup>

As shown in Figure E1 high amount of ammonia are used in the chemical industry.<sup>5,9,10</sup> Any defect in production plants or in production processes can cause a fatal ammonia emission into the environment. Unintended emission of ammonia from industrial facilities accounts for 3% of the total ammonia emission in Germany. Another 2% is caused by traffic mainly due to the application of ammonia in catalysts for  $\text{NO}_x$  reduction in diesel vehicles.<sup>2</sup> However, the main source of ammonia emission is agriculture (95%).<sup>1</sup> This is caused by spreading nitrogen fertilizers on farmland as well as by livestock farming.<sup>7,9,11,12</sup>

Decomposition of nitrogen containing material such as dead tissue of animals or plants and excrements results in a delivery of bound nitrogen in the form of ammonia.<sup>11,13</sup> Moreover, ammonia is also formed by digestion of protein-containing food. In this process ammonia is primarily generated by degradation of urea by the enzyme urease.<sup>12</sup> This enzyme widely appears in bacteria of soil and excrements and it catalyzes the reaction shown in Scheme E1.<sup>1</sup>



**Scheme E1.** Ammonia-forming reaction catalyzed by enzyme urease.

Besides the risk for human health ammonia is also very harmful to the environment.<sup>14</sup> High ammonia concentrations in the soil can cause acidification,<sup>12</sup> eutrophication, or an increase in atmospheric ammonia. This may result in a change for vegetation as many plants are highly sensitive to enhanced ammonia concentrations.<sup>9,13,15</sup> The process of acidification is caused by the high water solubility of ammonia. Thus, formed ammonium hydroxide can be further oxidized by

microorganisms generating nitrate ( $\text{NO}_3^-$ ). During this process of nitrification protons are formed resulting in the acidification of soil and water. <sup>1</sup>

Consequently, the prevention of ammonia emission is of uttermost importance for protecting human health and environment. Moreover, controlling of ammonia concentrations is necessary at places where prevention is not feasible, e.g. to protect working people from a toxic ammonia atmosphere in stables. Therefore, installing detection systems in all facilities using or generating ammonia exhibits a big step forward to the protection of human health and environment. <sup>5,16</sup>

## 1.2 Ammonia sensing principles

In literature many principles are described for measuring both, aqueous and gaseous ammonia. The most frequently used techniques for (commercial) ammonia detection are discussed below.

### Metal-oxide ammonia sensors

Metal-oxide gas sensors are based on semiconductor film materials like  $\text{SnO}_2$  and are widely used for ammonia sensing. <sup>3</sup> These materials are robust, inexpensive, and thus very promising for the development of gas sensors. It is well established by now that metal-oxide gas sensors vary their electrical conductivity caused by the adsorption of a present gas on the surface of the semiconductor material. <sup>5</sup> However, metal-oxide sensors are not selective to one particular gas which is a major drawback together with the energy-consuming operation at an elevated temperature of 100-400 °C. <sup>2,16</sup> These sensors are commercially available and already applied for ammonia leakage detection in refrigeration systems. Moreover, first air quality monitoring systems for regulating ventilation in cars are being implemented based on metal-oxide sensors. <sup>2</sup>

### Potentiometric ammonia sensors

Vast literature is present on the catalytic reactivity of metals in contact to specific gases, e.g. ammonia, hydrogen, and carbon monoxide. The working principle of potentiometric sensors is based on alteration of the charge carrier concentration in the presence of an analyte. The catalytic reaction proceeding at the sensing Pt-electrode causes a change in electrode potential. <sup>17</sup> The resulting potential difference between the electrode and a reference electrode is thereby directly dependent on the gas concentration. <sup>3</sup>

### Conducting polymer ammonia detectors

Another measuring principle for ammonia is based on conducting polymers. Different materials have been reported in this context, e.g. polypyrrole and polyaniline. <sup>10,18,19</sup> The sensing mechanism is caused by the reversible reduction of an oxidized conducting polymer through

ammonia. The reduction of the polymer film subsequently causes a conductivity change, allowing resistometric or amperometric ammonia detection.<sup>11</sup>

Furthermore, the reaction with ammonia results in a mass increase of the polymer film. Sensors have been described detecting ammonia by frequency changes of a resonator (piezoelectric crystals) coated with ammonia sensitive polymers.<sup>11,16</sup>

Furthermore, polyaniline films were also used for optical ammonia sensing.<sup>11,20</sup> Jin et al. treated a polyaniline film with hydrochloric acid. Ammonia then reacts with the formed imines to generate the deprotonated form of polyaniline, resulting in both, conductivity and electronic absorption spectrum alteration. With this method a detection limit of 1 ppm and response time of less than 15 seconds were achieved.<sup>10</sup>

### Optical gas analyzers

Two main optical principles exist for the detection of ammonia. The first is direct optical absorption detection by applying so-called laser-diode sensors of the gas. The second is based on changes of optical properties provoked by reaction of ammonia with a reagent.<sup>2,9,21</sup>

Direct optical absorption spectroscopy exhibits the most sensitive and selective way for ambient ammonia detection.<sup>3</sup> Systems with a detection limit of 1 ppb with response times in the range of seconds have been reported in this context. Such systems consist of a laser in combination with a spectrograph. Light travels through air with a long pathway whereby its spectrum is influenced by the gas composition being analyzed with a detector.<sup>16</sup> Optical absorbance analyzers are commercially available to measure even multiple gases. However, they cost thousands of dollars due to the need of expensive lasers. Furthermore, a large measurement system is necessary for a very accurate analysis. Thus, miniaturization always comes along with a downgrade in sensitivity why the principle is less suited for miniaturized ammonia sensors.

Optical chemical detection uses the change of optical properties (e.g. (NIR) absorbance, fluorescence) caused by the reaction of an analyte with a reagent.<sup>6,14,22–24</sup> Various colorimetric reactions are known for the detection of dissolved and gaseous ammonia. Best known is the Nessler's reaction which is e.g. applied for measuring the total ammonia concentration in aquaria.<sup>2,5,8</sup> Nessler reagent consists of dipotassium tetraiodomercurate(II) in a dilute alkaline solution (e.g. sodium hydroxide). This reagent, however, is toxic when inhaled, swallowed, or absorbed through the skin.<sup>3</sup>

The Berthelot reaction is another colorimetric method for ammonia in aqueous solution.<sup>5,8</sup> A combination of ammonia, phenol, and hypochlorite induces a blue color. One drawback is the rather slow kinetic of the reaction which was already improved by miniaturization in a flow-through analysis system. Furthermore, applications for water monitoring became feasible by such

microfluidic systems. However, drawbacks are still the consumption of reagents, the irreversibility of the sensor response, and the error prone nature of the microfluidic system. <sup>2,25</sup>

Lots of literature was published during recent years on applying commercially available indicator dyes for ammonia sensing. All examples use the deprotonation of a pH indicator and the resulting change of its optical properties. <sup>23,25</sup> Several approaches of optical ammonia sensor employing the principle of pH measurements have been reported. E.g. a pH-sensitive dye undergoes a suitable fluorescence or absorbance change when exposed to ammonia. This change is depending on the ammonia concentration and can be measured by feasible spectrometric techniques. <sup>3</sup>

For measuring gaseous ammonia the pH-sensitive dye has to be immobilized on solid phase using e.g. gas-permeable polymers or sol-gel matrices. <sup>26,27</sup> Afterwards, optical changes can be monitored by e.g. attaching the sensor films on the top of optical fibers. For this approach bromophenol blue was already used <sup>8,25</sup> immobilized in e.g. hydrogel as solid support. <sup>5</sup> Werner et al. dissolved bromocresol green and cetyltrimethylammonium bromide in silicone polymer layers for measuring gaseous ammonia. <sup>14</sup> Furthermore, bromocresol green was immobilized on the surface of an optical fiber via sol-gel. <sup>28</sup> Moreover, Xie et al. used erythrosin A as the fluorescent indicator for the determination of dissolved ammonia in aqueous solution. This dye was immobilized in plastics and used as fiber probe. <sup>6,28,29</sup> Bromothymol blue (BTB) was used for the detection of ammonia via acid-base reaction as well. Yimit et al. coated the surface of TiO<sub>2</sub> with a thin film of BTB by spin coating. The detection of gaseous ammonia was then accomplished by the optical waveguide method whereas a detection limit of 1 ppt ammonia was achieved. <sup>30 31</sup>

A new trend in sensory applications has been observed through the last years. This trend shows the implementation of various previously mentioned detection methods in textiles. The sensor textiles can measure and display various environmental and health parameters directly during wearing. In the following chapter, sensor textiles and precursors are described which are either in the development process or already commercially available.

### 1.3 Sensor systems in textiles

A great future potential is attributed to intelligent clothing ("smart clothes"). However, despite promising industrial applications, smart clothes are still not well established on the market. One of the great challenges is a reduction of costs. Customers want to buy cheap products which hinder an expansion of sensor textiles into the mass market. Consequently, a first entry for intelligent clothing would probably be in application fields where additional benefits are really needed e.g. in public health sector or safety clothing. Another challenge is the suitability of smart clothes for daily use. Intelligent clothing needs to be washed in the same way as normal clothing. However,

electronic components often don't survive 60 °C washing programs whereby skidding provides the biggest problem. <sup>32</sup>

Intelligent clothing can undertake various functions, e.g. positioning, entertainment, and information. In a glove for winter sports e.g. a phone is integrated able to connect with a smartphone via Bluetooth. Thus, calls can be accepted or declined directly by the glove (hi-Call Glove Handset from Hi-fun or SWANY G-Cell from Texsys). <sup>32–34</sup> In the public health sector textiles with integrated microsystem techniques offer new opportunities for diagnostics and therapy. Those are for example the monitoring of chronic illnesses and wounds. Moreover, physiological parameters like blood pressure, pulse, heart rate, rhythm of the heart, and breathing can be controlled. Smart clothes with integrated vital sensors, signal processing, and communication can enormously enhance the continuous monitoring of vitals. Particularly, for monitoring high-risk and high-maintenance patients, smart clothes might become a great benefit. Patients can be observed unremarkably and without any stress. <sup>35,36</sup> In the following part some applications of intelligent clothing and research areas are pointed out.

### **ECG-Measurements**

One of the most important methods in medical diagnosis is recording an electrocardiogram (ECG). Integration of an ECG-system in clothes enables long-term monitoring of high-risk patients. Moreover, athletes can benefit from continuous cardiovascular control as it might allow a more specific training. E.g. the ECG-Shirt from Falke KG <sup>37</sup> can be worn just like normal clothing. In combination with the special smartphone Vitaphone 1300 the shirt can be assistance for heart patients. A connection to a medical service-center has been established by pushing an emergency button or even automatically. Afterwards, the service center can precisely locate the wearer of the ECG-shirt to an accuracy of 15 meters and can send an ambulance. However, before washing the textile the integrated sensor module has to be removed.

In the Institute of textile- and process engineering in Denkendorf (Germany, Baden-Württemberg), researchers integrated sensors in romper suits for babies and in jackets for firefighters. The sensors monitor breathing, heartbeat, body temperature, and humidity of the skin. Generated data is transferred via radio communication and raise an alarm if required. <sup>35</sup>

### **Intelligent gloves for firefighters**

Data about vitals and environmental information can also be determined using the intelligent gloves for firefighters. Thereby, operation controllers receive additional information and are able to react immediately if dangerous situations are recognized. Moreover, firefighters can be precisely located with a positioning system incorporated in the gloves enabling for fast assistance. Important information can further be transferred via integrated intelligent gesture control either



in stress situations or in case of direct radio circuit overloading. If an insured person lies on the floor the firefighter can make a specific gesture which is evaluated automatically by the sensor system. Afterwards, concrete information is sent to the operation controllers enabling fast reaction. Moreover, the firefighter can receive important information by vibration signals. "Short-short" e.g. means a problem with temperature and "long-long" a too long distance between individual firefighters. Furthermore, individual glove pairs form an autonomous communication network with sensor- and radio-communication interface where they can also communicate among themselves.<sup>38</sup>

### Safety trousers for lumbermen

Researchers of the technology-center for informatics and information technology (TZI, University of Bremen, Germany) have developed intelligent safety trousers for lumbermen. Those can automatically switch off a chainsaw if dangerous machine and trousers come too close to each other. Radio communication sensors in trousers communicate via a small transmitter. The transmitter sends information to the receiver in the chain saw provoking the automatic switch off. Moreover, the trousers can be washed and ironed normally.<sup>39</sup>

### Hövding Airbag

Swedish researchers have developed Hövding for utilization on ski or bike. Instead of crash-helmet a broad collar protects the head. Hövding consists of an airbag with integrated gas cylinder and acceleration sensors. These sensors recognize accidents via special algorithms enabling a automated and fast inflating of the collar in the event of a collision or fall. Hövding Airbag already has a "CE"-license and is authorized officially as alternative to a classical bike helmet.<sup>32,39-41</sup> Figure E2 shows the closed collar on the left side and the inflated one on the right.



**Figure E2.** Hövding Airbag: closed collar on the left and inflated airbag for head protecting on the right side.<sup>42</sup>

### Pressure Sensor

Knitted fabrics made from conductive spun yarn can be used as distension or pressure sensors. Moreover, multifaceted applicable pressure sensors can be produced from a knitted fabric with two conductive sides. The two individual fabric zones are separated by an isolating yarn. With increasing pressure the two conductive sides of the “Spacer Fabrics” come in contact and produce a signal. Decreasing pressure causes a separation of the sides again. By varying electric contacting and evaluation of measured resistances, spacer fabrics are able to detect the position of a contact or the size of a touching area. These sensors might be applied e.g. in car seats for monitoring the presence of an assistant driver. The sensor can also be implemented in play rugs to give a signal when a baby is leaving the rug.<sup>36</sup>

### Temperature-regulating textiles

A wrapped yarn is used for temperature-regulating textiles. The yarn is made from a thin, conductive wire which is wrapped around a textile core. It can change its electric resistance by changing its temperature. Integrating the wrapped yarn in tight-fitting clothing enables measuring the body temperature of the wearer. Furthermore, textiles can be heated by applying a weak voltage. The yarn can be easily incorporated into textiles and does not disturb look or surface feel. Therefore, it can be used e.g. in temperature-regulating socks.<sup>36</sup>

### Technologies for integrating electronics in textiles

ECG-electrodes consist of textile conductors, e.g. wrapped yarns with a thin conductive wire, spun yarns with a small content of stainless steel, or yarn coated with a conductive layer. All these yarns can be handled as normal threads and the user doesn't notice the metal contents of the obtained fabric. Furthermore, the yarn might be used for weaving, embroidering, or knitting.

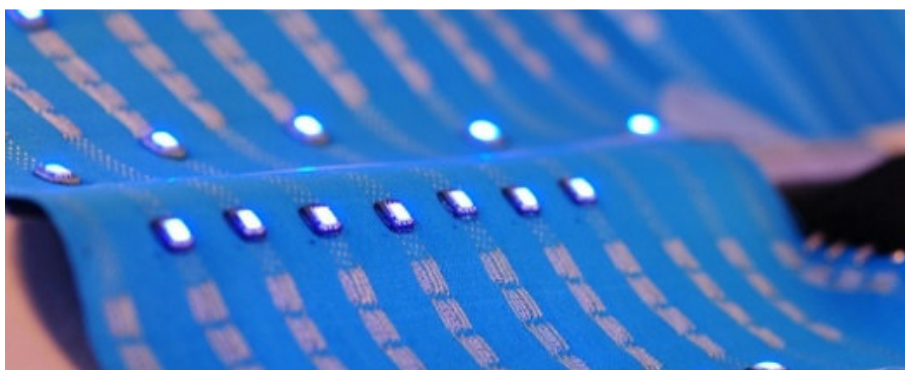


**Figure E3.** Textile conductive paths with bonded RGB-SmartPixel.<sup>43</sup>

Fraunhofer IZM developed an elastic interconnected device which can be laminated on textiles for the development of an interactive jacket for bikers. The device consists of thermoplastic

polyurethane enabling easy lamination on fabrics via standard manufacturing processes. In the interconnected device sensors, copper conductive paths and LEDs are integrated (Figure E3). Thus, also microelectronic techniques are used during the manufacturing process e.g. soldering at low temperature, sticking with conductive and non-conductive glues, and crimping. These electronic-textiles combinations are resistive against humidity and mechanical stress.<sup>32,43</sup> Figure E4 shows elastic conductive paths which were integrated in textiles.

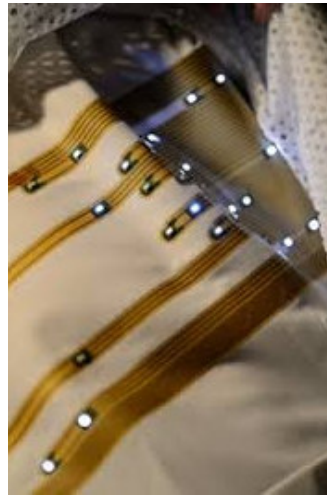


**Figure E4.** Elastic conductive paths integrated in fabrics.<sup>43</sup>

### Audio-Module

Infineon Technologies developed an audio-module directly incorporated in textiles (Figure E5). Thereby, chips and small sensors are integrated in special packages and are sew or weaved directly in the fabrics. Moreover, weaved conductive paths provide an electronic connection between individual parts of the audio-module. The flat keypad e.g. consists of metalized films fixed on a conductive fabric tape. The metalized films are fixed with adhesive glue which is commonly used in textile industries. Furthermore, headphone and microphone are connected with the audio-module as well by using a fabric tape. A critical part of the electronic-textile combination displays the connection of fabric with electronic components. These connections are often the most sensitive and, thus, the limiting part for suitability in daily use. Infineon applied two different methods: a technique similar to the wirebond-process and an elastic plastic tape with integrated connection pads conglutinated or brazed with textile structures. In both cases the whole module and the connection zones are packed hermetically.<sup>44</sup>



**Figure E5.** Audio Module from Infineon Technologies. <sup>45</sup>

In this chapter the principle of sensor textiles should be applied to colorimetric ammonia sensing. Dyeing of textiles with pH indicators can provide low-cost and sensitive monitoring of the toxic gas. Moreover, these sensor textiles are simple in both manufacturing and operation. Commercially available pH indicator dyes and polyamide fabric are used as basic components. Moreover, no special equipment is needed as the presence of ammonia is displayed by a color change of the textile being noticed by naked eye. These sensor textiles can be applied for the manufacturing of working clothes applied at places where ammonia is either processed or generated. Potential users are amongst others farmers, channel diggers, and workers in fertilizers industry or producer of refrigerators. <sup>44</sup>

## 2 Objective

Aim of this part of the thesis was the development of a fast and reversible colorimetric detection system for gaseous ammonia for work safety applications. The visualization of ammonia in working places had to be achieved by immobilizing an indicator dye directly into textile fibers of work clothes. If ammonia is present in the gas phase a color change of the sensor textile is provoked. Thus, workers are alerted and can leave the dangerous zone.

For this purpose different commonly available pH-indicator dyes were investigated for their dyeing ability of polyamide fabric. The sensor textiles had to be implemented in a suitable measuring chamber and characterized with respect to response time, selectivity, sensitivity, reversibility, and long-term stability. This was accomplished via a custom-built measurement setup for RGB color imaging. The design of this setup consists of a digital camera in combination with defined lighting conditions. The data had then to be analyzed by suitable data processing. Figure E gives an overview of the project.

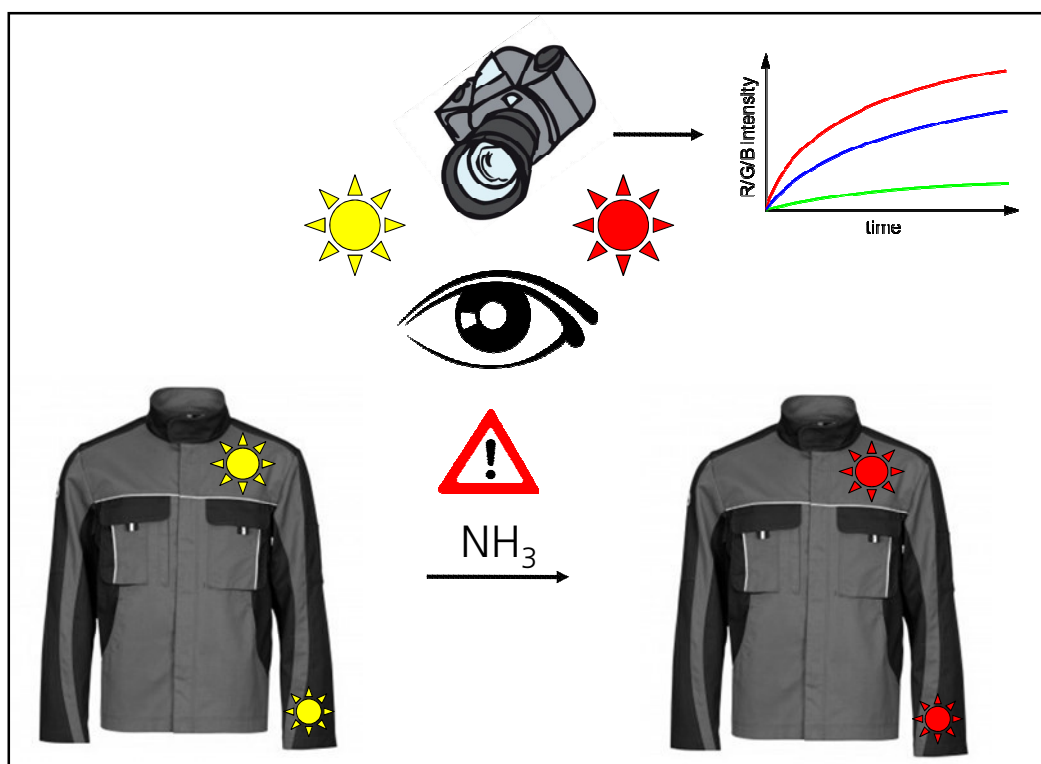


**Figure E.** Schematic illustration of the chapter's objective: an indicator dye is directly integrated into the textile fibers of working clothes. The color change provoked by gaseous ammonia can be identified either by naked eye or evaluated precisely by digital color images and subsequent data processing.

### 3 Materials and Methods

Ammonia (28-30% in water), ethylamine (70% in water), diethylamine (100%), triethylamine (100%), dimethylamine (40% in water), and trimethylamine (45% in water) were purchased from Sigma Aldrich. Polyamide fabric (200 g/m<sup>2</sup>), Lyogen NH, and Imacol PAM were obtained from co-operation partner J.G. Knopf's Sohn GmbH (Helmrechts, Germany). All remaining chemicals were of analytical reagent grade (see Appendix, chapter 1). Glass vials and screw caps with hole and septum were purchased from Carl Roth GmbH and polyethyleneterephthalat (PET) foil (thickness 125 µm) from GoodFellow GmbH.

#### 3.1 Dyeing with ammonia-sensitive probes

For fabricating sensing textiles for ammonia polyamide turned out to be the most suitable fabric due to its colorability with dyes containing acid moieties. Polyamide textile (200 g/m<sup>2</sup>) dyeing was successful applying three different commercially available pH-indicator dyes. These were bromothymol blue (BTB), cresol red (CR), and methyl red (MR). Table E1 shows all compounds applied for dye bath composition for polyamide dyeing.

**Table E1.** Bath composition for dyeing 13 g polyamide fabric (200 g/m<sup>2</sup>) by either indicator dye: bromothymol blue, cresol red, or methyl red.

Substance	Amount
Water	45 mL
Indicator dye	0.2 mmol
Lyogen NH <sup>*1</sup>	260 mg
Imacol PAM <sup>*2</sup>	150 mg
Phosphate buffer (100 mM, pH 6.5 <sup>*3</sup> )	30 mL

<sup>\*1</sup> anti-friction agent

<sup>\*2</sup> leveling additive

<sup>\*3</sup> phosphate buffer (100 mM) was set to pH 6.5 with sodium hydroxide solution (5 M)

All components were mixed and heated in an autoclave to 130°C for two hours. After cooling the fabrics were washed with cold water followed by laundering with Persil cleaning agent at

60°C for 30 min. Finally, the textiles were washed with Persil at 90°C for 30 min followed by pure water.

### 3.2 Preparation of measurement samples

Quantifying amine concentrations in the gas phase was accomplished by fixing sensor fabrics in screw caps with hole and septum. For this purpose sensor textiles were cut into circular pieces of 8 mm in diameter. Additionally, 8 mm PET-foil spots were generated by a hollow punch. After removing the septum the cap was turned around and the PET foil was inserted. Subsequently, the sensor textile sample was placed directly onto the foil. For measuring sensor response the analyte solutions were added to the glass vials which were sealed with the prepared screw caps immediately afterwards. Thus, a direct contact between sensor fabric and analyte solution is avoided. Figure E6 shows an exploded view drawing of the measurement sample setup.

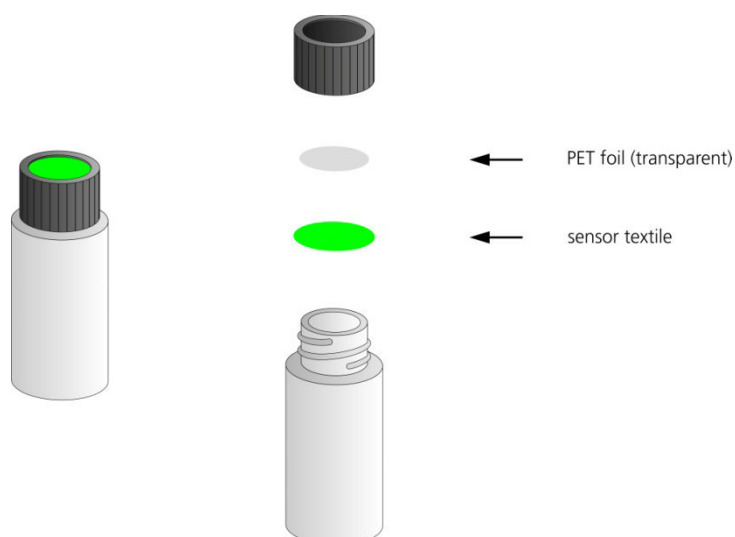


**Figure E6.** Exploded view drawing shows the setup of measurement samples.

### 3.3 Measurement setup and data processing

The applied measurement setup for quantifying color changes is identical to the setup described in part C, chapter 3.4. In this setup a Canon EOS 550D camera combined with Canon EF-S 18-135 mm lens was applied. **Camera settings** were as follows:

Exposure time: 1/40 s

F-stop: F/5.6

ISO Value: 400

Photographs were taken via manual camera mode and manual white balance was performed using a white paper sheet mounted in the calibration chamber. Image acquisition was performed in time intervals of 100 seconds for a measurement period of 65 min unless mentioned otherwise.

During the experiments identical camera settings were used for all measurements. Finally, the pictures were processed to their RGB color information using Image J software as previously described in part C (chapter 3.5).

### 3.4 Adjustment of amine concentrations

For adjusting defined amine concentrations the total volume of the glass vials was determined resulting in the following value (for detailed calculation see part C, chapter 3.6):

**Volume of glass vials:**  $1.82 \pm 0.02$  mL (mean  $\pm$  SD; N = 15)

Subsequently, amine calibration solutions were prepared. The compositions were chosen to give amine concentrations between 0 and 150 ppm inside the glass vials (see Table E2 for the preparation of ammonia calibration solutions). For calibration measurements 10  $\mu$ L of the respective stock solution were pipetted into a glass vial which was rapidly sealed using a screw cap with integrated sensor textile. ppm-Values of the final ammonia concentrations (Table E2, second column) were determined dividing the volumes of ammonia by the vial volume of  $1.82 \pm 0.02$  mL. The adjustment of other analyte concentrations was performed accordingly.

**Table E2.** Pipette scheme for the preparation of ammonia calibration solutions. Calibration solutions were prepared from respective stock solutions SLI, SLII, or SLIII and filled to their total volume with distilled water. Ammonia concentrations in the second column represent the ppm-values of ammonia in the glass vials after adding and evaporating 10  $\mu$ L of respective calibration solution.

	Concentration / ppm	Ammonia / $\mu$ L	SLI / mL	SLII / mL	SLIII / mL	Total volume* / mL
<b>SLI</b>	150	785	-	-	-	10
<b>SLII</b>	100	1300	-	-	-	25
	75	-	2.5	-	-	5
	50	-	-	5	-	10
<b>SLII</b>	36	475	-	-	-	25
<b>I</b>	22	-	-	-	3	5
	10	-	-	1.25	-	25

\* samples were filled with distilled water to their total volume



### 3.5 General procedure for data evaluation

Intensities of the red, green, and blue color channels received from data processing with Image J software (for details see chapter 3.3) were further analyzed by ratiometric evaluation of two color channels. Equation E1 indicates the ratio of blue and red color channels [B/R] whereby  $B(t_1)$  and  $R(t_1)$  represent the intensities of blue and red color channels of first measurement point,  $B(t_2)$  and  $R(t_2)$  the data of second measurement point. Based on the type of sensor fabric color channels were chosen by their signal response.

$$\left[ \frac{B(t)}{R(t)} \right] = \left[ \frac{B(t_1)}{R(t_1)} \right], \left[ \frac{B(t_2)}{R(t_2)} \right], \left[ \frac{B(t_3)}{R(t_3)} \right], \dots \quad \text{Eq. E1}$$

After quantifying the color changes by ratiometric evaluation, the obtained values were plotted against time. For all measurements a signal increase with an asymptotic saturation curve was received. These curves were fitted by a logistic function (Equation E2).

$$y = \frac{A2 + (A1 - A2)}{1 + \left( \frac{x}{x_0} \right)^p} \quad \text{Eq. E2}$$

Afterwards, the saturation values of time-dependent curves were determined in order to generate calibration plots. These values represent the signal change of sensor textiles in equilibrium with the analyte. For this purpose the mean of the last ten data points was calculated. Finally, values were plotted against the analyte concentration for generating calibration plots. The corresponding curves were fitted with an exponential association (Equation E3).

$$y = y_{\infty} - (y_{\infty} - y_0) \cdot e^{-k \cdot \frac{x}{x_0}} \quad \text{Eq. E3}$$

$y_{\infty}$       y-value for an infinite value of x

$y_0$       y-value for x = 0

$x_0$       constant (= 1 ppm)

### 3.5.1 Color change evaluation of bromothymol blue dyed polyamide fabric (BTB-PA)

Polyamide fabric dyed with bromothymol blue (BTB-PA) exhibits an increase of blue color channel intensity and a decrease of green and red color channel intensities. This is shown by Figure E7 for the example of 50 ppm ammonia. While the decrease of red color channel intensity is completed after almost five minutes, the saturation of green and blue color channel takes about 20 minutes. In general, red color channel exhibits a saturation intensity of about 30 a.u. followed by the green (70 a.u.) and blue (115 a.u.) color channel (Figure E7).

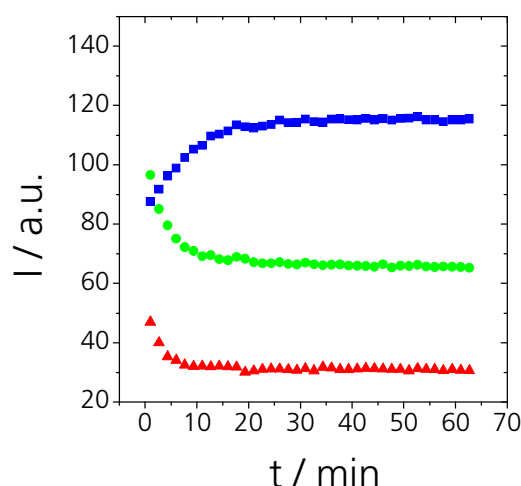


**Figure E7.** Typical time-dependent change of red ( $\blacktriangle$ ), green ( $\bullet$ ), and blue ( $\blacksquare$ ) color channel intensities of sensor fabric BTB-PA during reaction with 50 ppm ammonia.

Figure E8 shows a representative color response of BTB-PA in the presence of 50 ppm ammonia in this case. The original green-colored sensor fabric becomes turquoise after a few minutes and dark blue in the end. After about seven minutes no color change is observable anymore by naked eye. For evaluating the color change of sensor textile BTB-PA signals [B/R] and [B/G] gave the best results. Signals calculated from red and green color channels do not show a significant change.

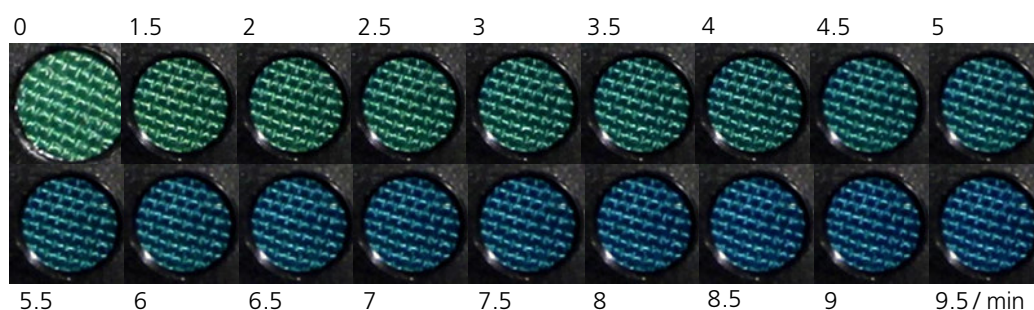


**Figure E8.** Typical time-dependent color change of polyamide fabric BTB-PA applying an ammonia concentration of 50 ppm.

### 3.5.2 Color change evaluation of cresol red dyed polyamide fabric (CR-PA)

Sensor textile dyed with cresol red (CR-PA) exhibits a decrease of red and green color channel intensities. Simultaneously, the blue channel intensity increases slightly. Figure E9 shows this RGB change for the example of 50 ppm ammonia. In this case, after the measuring time red color channel exhibits the highest intensity of about 140 a.u. followed by green (~75 a.u.) and blue (~70 a.u.) color channels (Figure E9).

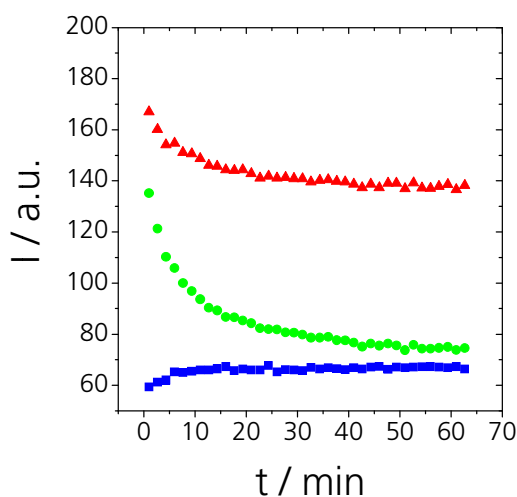


**Figure E9.** Typical time-dependent change of red (▲), green (●), and blue (■) color channel intensities of CR-PA during reaction with 50 ppm ammonia.

During reaction with ammonia the color of sensor fabric CR-PA changes from yellow to red-orange within the first ten minutes. Figure E10 shows a representative color change for 50 ppm ammonia. After about seven minutes no color change is observable anymore by naked eye. Since for CR-PA all calculated ratios show feasible responses data evaluation was performed by [B/R], [B/G], and [R/G].

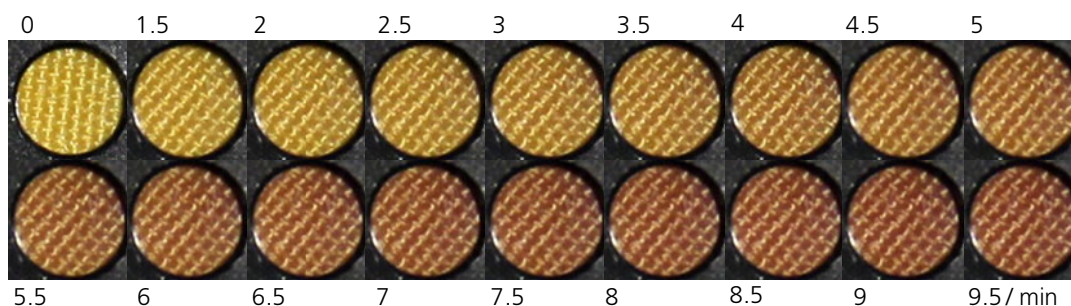


**Figure E10.** Typical time-dependent color change of polyamide fabric CR-PA applying an ammonia concentration of 50 ppm.

### 3.5.3 Color change evaluation of methyl red dyed polyamide fabric (MR-PA)

Polyamide fabric dyed with methyl red (PA-MR) exhibits only slight intensity changes in all three color channels (see Figure E11 for the experiment with 50 ppm ammonia). While an increase of green color channel signal is observed the red channel shows a slight decrease in intensity. The blue color channel doesn't show any change at all. After reaction with 50 ppm ammonia red color channel intensity possesses the highest intensity of about 200 a.u. followed by green (170 a.u.) and blue (55 a.u.) color channel intensities.

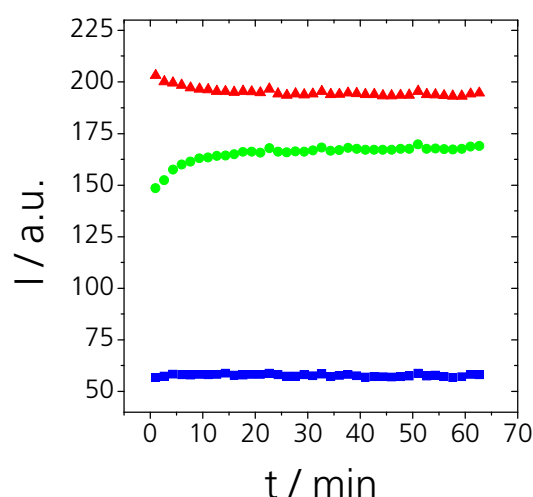


**Figure E11.** Typical time-dependent intensity changes of red ( $\blacktriangle$ ), green ( $\bullet$ ), and blue ( $\blacksquare$ ) color channels for polyamide fabric colored with methyl red. Here an ammonia concentration of 50 ppm was investigated.

Methyl red colored polyamide fabric is orange-colored before reacting with ammonia. During reaction it becomes brighter and finally yields a yellow color (see Figure E12 for the reaction with 50 ppm ammonia). After about 6 minutes no color change is observable anymore with naked eye. Since only signal [G/R] shows a suitable response this was the only feasible evaluation method for quantifying the color change of MR-PA sensor fabric.

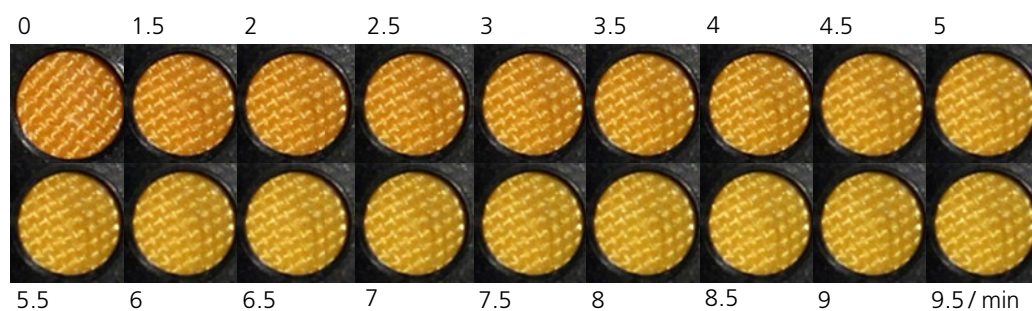


**Figure E12.** Typical time-dependent color change of polyamide fabric MR-PA applying an ammonia concentration of 50 ppm.

### 3.5.4 Determination of limits of detection (LOD) and sensitivities

For small ammonia concentrations linear signal responses were observed for all measurements performed on different sensor textiles. Those were fitted with linear fit functions to determine the limits of detection (LODs). For this purpose the blank value method was applied described in DIN 32 436 (for linear calibrations). For practical application it proved useful to perform some simplifications resulting in Equation E4 for the calculation of LOD value ( $x_{\text{LOD}}$ ). Error propagation was performed as shown by Equations E5 and E6.

$$y = A + m \cdot x \quad \rightarrow \quad x_{\text{LOD}} = \frac{(y_0 + 3 \cdot s_{y_0}) - A}{m} \quad \text{Eq. E4}$$

$$s_{x_{\text{LOD}}} = \sqrt{\left(\frac{\partial x_{\text{LOD}}}{\partial A} \cdot s_A\right)^2 + \left(\frac{\partial x_{\text{LOD}}}{\partial m} \cdot s_m\right)^2} \quad \text{Eq. E5}$$

$$s_{x_{\text{LOD}}} = \sqrt{\left(-\frac{1}{m} \cdot s_A\right)^2 + \left(-\frac{y - A}{m^2} \cdot s_m\right)^2} \quad \text{Eq. E6}$$

A	intersection
$s_A$	error of intersection A
m	slope
$s_m$	error of slope m

### Sensitivity

For all calibration measurements described in this chapter a linear signal response was observed for small analyte concentrations. The sensitivity is defined as slope of the linear calibration functions.

### 3.5.5 Determination of response and reverse times

Response and reverse times were determined for the reaction of sensor textiles with ammonia and several other amines. As all time-dependent measurements can be described as saturation curves they were fitted by logistic fit function Equation E2.

$$y = \frac{A_2 + (A_1 - A_2)}{1 + \left(\frac{x}{x_0}\right)^p} \quad \text{Eq. E2}$$

Based on the fit parameters A1 and A2 the total signal change was determined first. While parameter A1 indicates the starting value of the fit function, A2 reflects the saturation value. The time until 90% (ammonia calibrations) or respectively 80% (response towards diverse amines) of the total signal change was observed is named response time  $t_{90}$  or  $t_{80}$ . If applicable,  $t_{90}$  was calculated, however, for some experiments better comparability was achieved by  $t_{80}$ . Additionally, time until the starting value is reached after removing the ammonia atmosphere is referred to as reverse time.

For calibration experiments (chapter 4.1) the response times turned out to be rather independent from ammonia concentration. Thus, the mean value of determined response times (0-150 ppm ammonia) was calculated.

## 4 Results and Discussion

### 4.1 Calibration measurements with ammonia

Calibration measurements were performed for determining the response behavior of the three sensor textiles BTB-PA, MR-PA, and CR-PA to ammonia. For this purpose sensor textiles were fixed in screw caps (for details see chapter 3.2) and concentrations between 0 and 150 ppm ammonia were adjusted in the glass vials (chapter 3.5). All calibration measurements were performed in five replicates and controls were performed applying distilled water. Afterwards the values of control measurements were used as a blank value for time course plots. After preparation and addition of the calibration solution all vials were placed in the measuring chamber and time lapse was started.

Settings for SLR camera (manual mode) were as following: F-stop F/5.6, exposure time 1/40 seconds, and ISO 400. Additionally, manual white balance was performed with a white paper sheet (for details see chapter 3.3). The time elapsed until taking the first picture was also determined and included in final data evaluation. By means of ratiometric evaluation of color change and subsequent plotting the obtained values against time a signal increase with final saturation was obtained for all ammonia concentrations. After determination of the saturation values (see chapter 3.5) calibration plots were generated by plotting signals against analyte concentrations.

#### 4.1.1 Bromothymol blue dyed polyamide (BTB-PA)

As already mentioned in chapter 3.4.1 data evaluation for sensor textile BTB-PA is practicable by blue/red [B/R] and blue/green [B/G] color channels. Quantification of the response to ammonia was performed applying seven different ammonia concentrations between 0 and 150 ppm (see chapter 3.4). Saturation curves were obtained for both [B/R] and [B/G] independent of the applied ammonia concentrations. Therefore, all curves were fitted by a logistic fit function (Equation E2). The corresponding fit parameters are represented in the Appendix (Table G16 and G17).

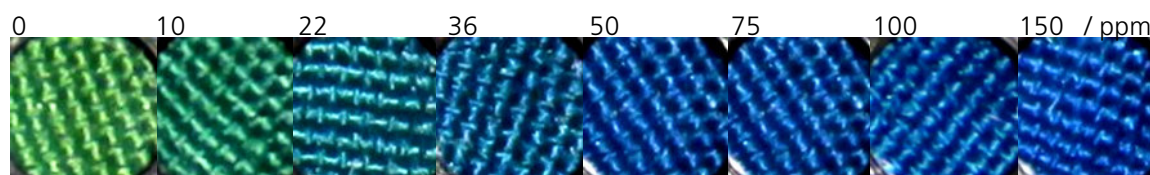


**Figure E13.** Color of sensor textile BTB-PA after reaction with different concentrations of ammonia. Images were taken after reaching the saturation values.

Figure E13 shows the colors of sensor textile BTB-PA after reaction with different ammonia concentrations. Images were taken after reaching the saturation value and show a color change from green to dark blue. Between 50 and 150 ppm ammonia no color change can be recognized by naked eye. Additionally, the equilibrium is reached after 20 minutes for all ammonia concentrations being visible by constant [B/R] and [B/G] signals (Figure E14 and E15).

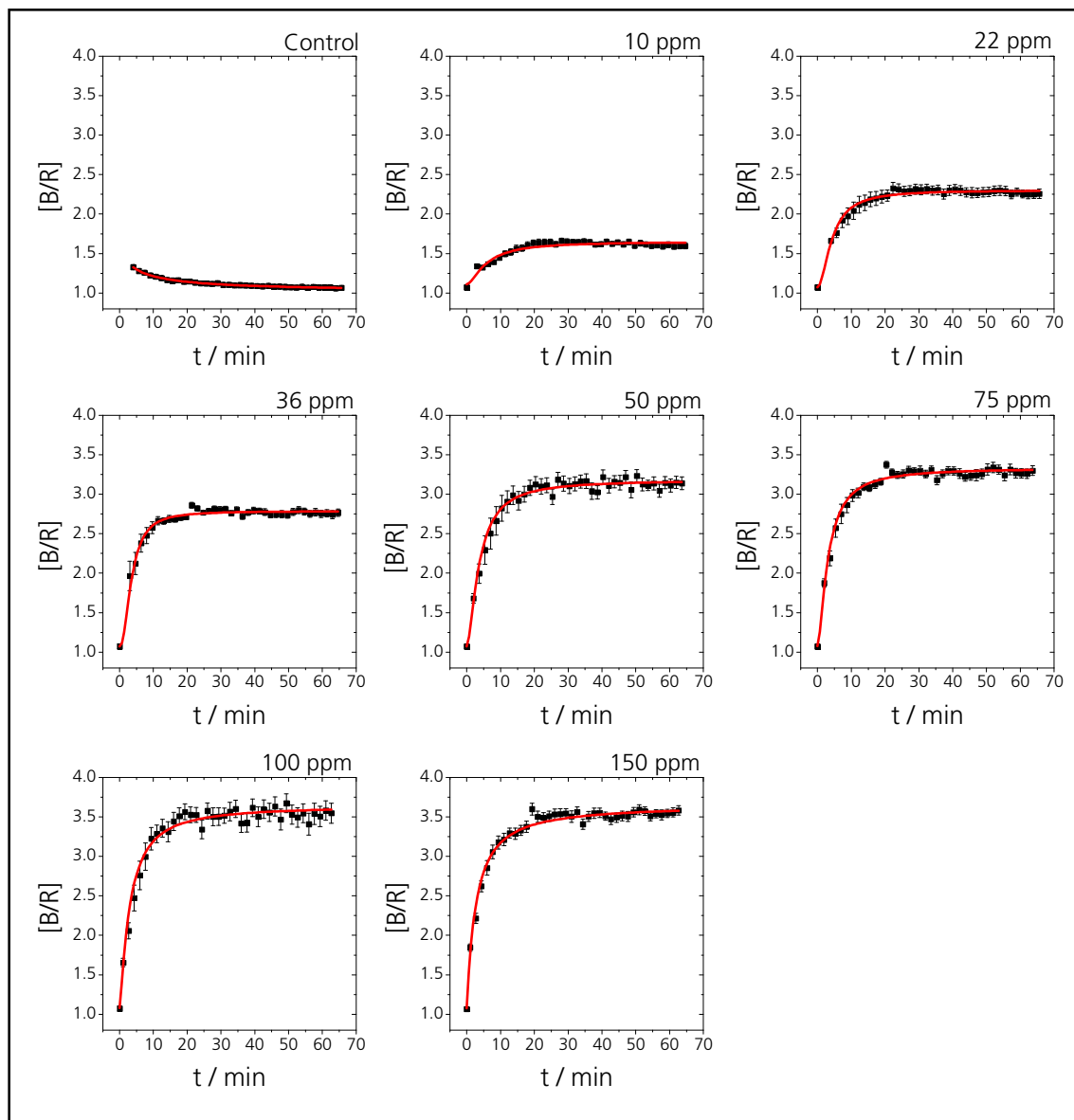


**Figure E14.** Time-dependent increase of [B/R] induced by reaction of BTB-PA with varying ammonia concentrations (0-150 ppm). Control was performed with 10  $\mu$ L distilled water and curves were fitted using a logistic fit function. Corresponding fit parameters are shown in the Appendix (Table G16) (mean  $\pm$  SDM; N = 5).

Figure E14 and E15 show the time-dependent increase of signals [B/R] and [B/G] during reaction of BTB-PA with varying concentrations of ammonia (0 - 150 ppm). Increasing the ammonia concentration causes an increase of the saturation value. However, beyond 100 ppm no further



increase was observed. This indicates a complete reaction of all bromothymol blue molecules being present in the textile.

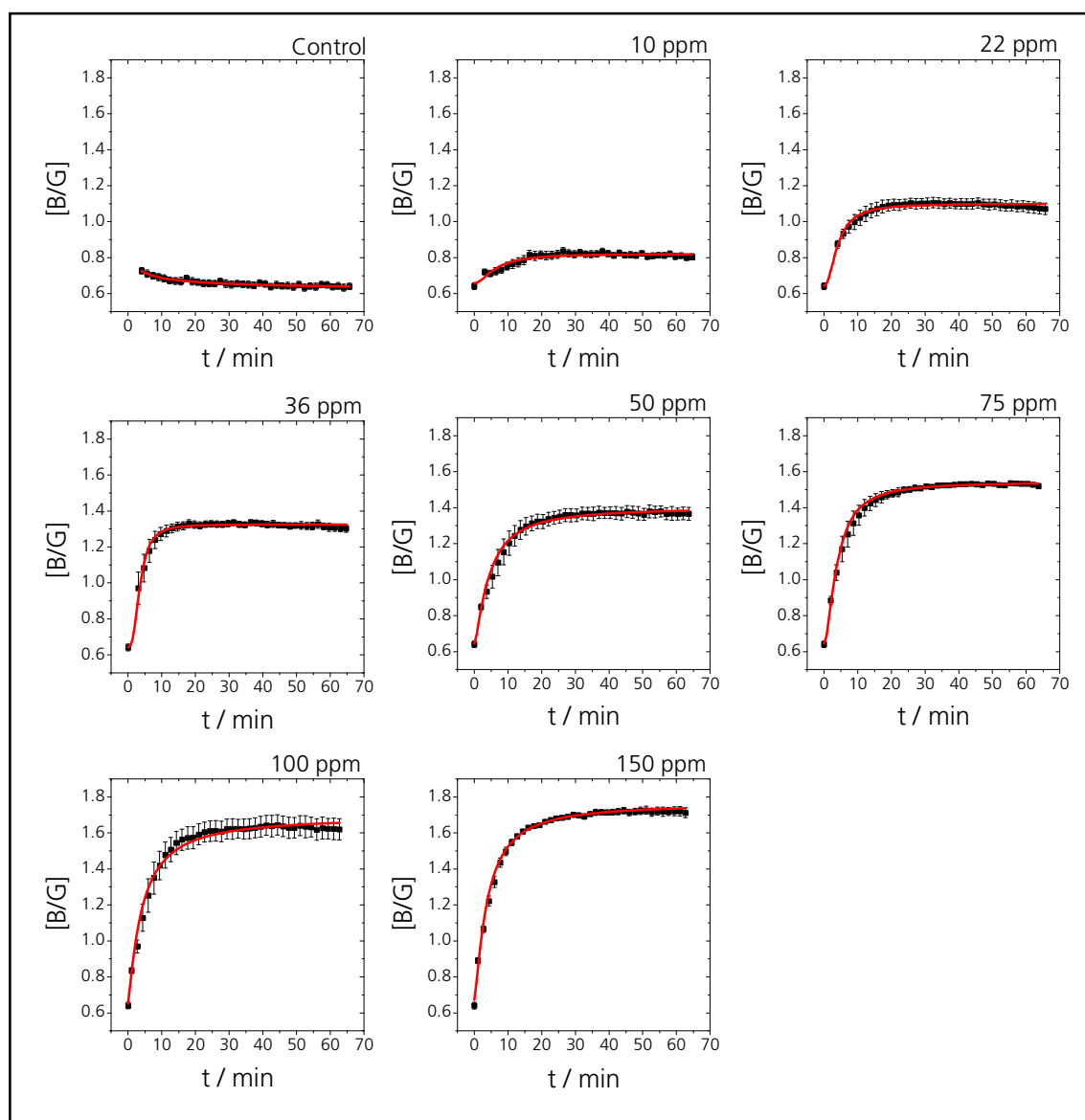


**Figure E15.** Time-dependent increase of [B/G] induced by reaction of BTB-PA with concentrations of ammonia between 0 and 150 ppm. Control was performed with 10  $\mu$ L distilled water and curves were fitted by a logistic fit function. Corresponding fit parameters are shown in the Appendix (Table G17) (mean  $\pm$  SDM; N = 5).

Based on the performed measurements applying various ammonia concentrations calibration curves were plotted. For this purpose the saturation value for each time-dependent plot was determined by calculating the mean of the last ten data points as described in chapter 3.5. Afterwards saturation values of [B/R] and [B/G] were plotted against the ammonia concentrations (Figure E16, A and B) and fitted with an exponential association ( $R^2 = 0.99$  for graph A and B). Small ammonia concentrations show a linear signal response (Figure E16, C and D) and were thus

fitted using a linear fit function. The parameters of linear fit functions of graph C ( $R^2 = 0.99$ ) and D ( $R^2 = 0.99$ ) are depicted in Table E3.

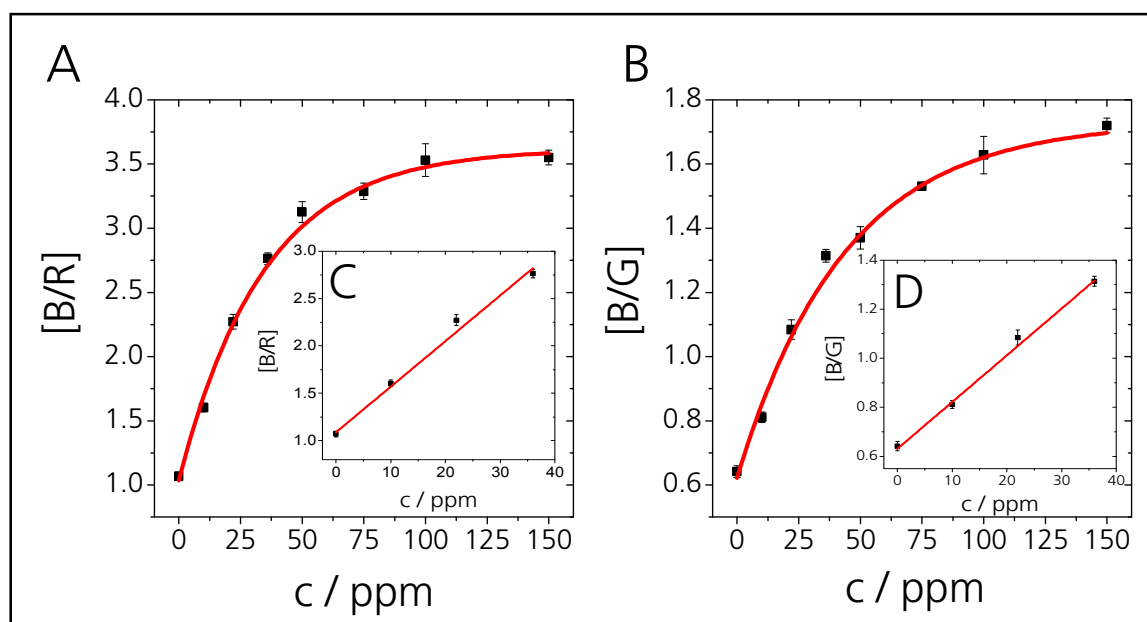


**Figure E16.** Ammonia calibration plots of sensor textile BTB-PA. **A:** calibration curve from data evaluation by the ratio [B/R], **B:** calibration plot from values [B/G]. The plotted data derive from calculating the mean of the last ten data points for each time-dependent saturation curve (Figure E14 and E15). The small graphs show the linear dependency of [B/R] (graph C) and [B/G] (graph D) to low ammonia concentrations (0-36 ppm) (mean  $\pm$  SDM; N = 5).

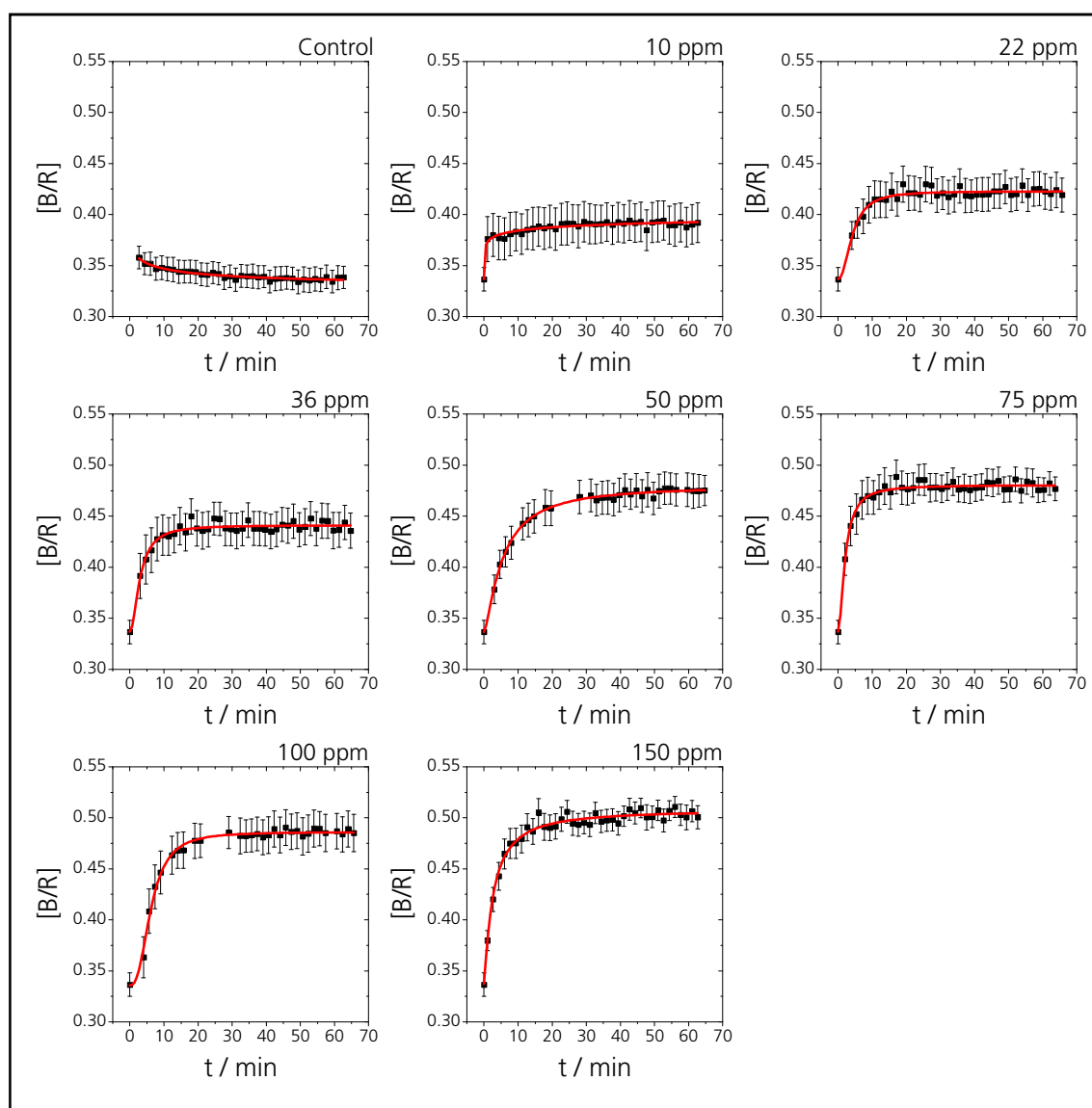
From Table E3 a higher slope of linear fit function can be recognized in case of data evaluation by rationing the blue and red color channels ( $0.048 \pm 0.003 \text{ ppm}^{-1}$ ) compared to [B/G] exhibiting a value of  $0.0190 \pm 0.0008 \text{ ppm}^{-1}$ .

**Table E3.** Parameters of linear fit functions received from Figure E16, graphs C and D.

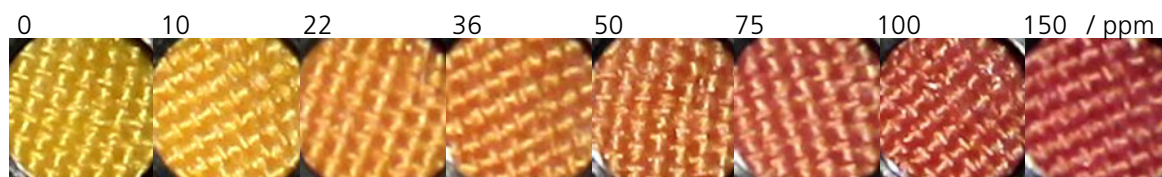
Graph	Slope $\pm$ error / $\text{ppm}^{-1}$	Intercept $\pm$ error
Fig. E16; C	$0.048 \pm 0.003$	$1.09 \pm 0.05$
Fig. E16; D	$0.0190 \pm 0.0008$	$0.63 \pm 0.02$

### 4.1.2 Cresol red dyed polyamide (CR-PA)

Calibration of sensor textile CR-PA was performed applying seven different concentrations of ammonia between 0 and 150 ppm (for details see chapter 3.4). Control was again accomplished with 10  $\mu$ L of distilled water. As already mentioned in chapter 3.4.2 color evaluation of CR-PA is accessible using the ratios [B/R], [B/G], and [R/G]. The values for [B/R], [B/G], and [R/G] were plotted against time. The curves (see Figure E17-E19) were fitted with a logistic fit function as all data shows saturation. (Equation E2) The corresponding parameters of logistic fit functions are depicted in the Appendix (Table G18 – G20).

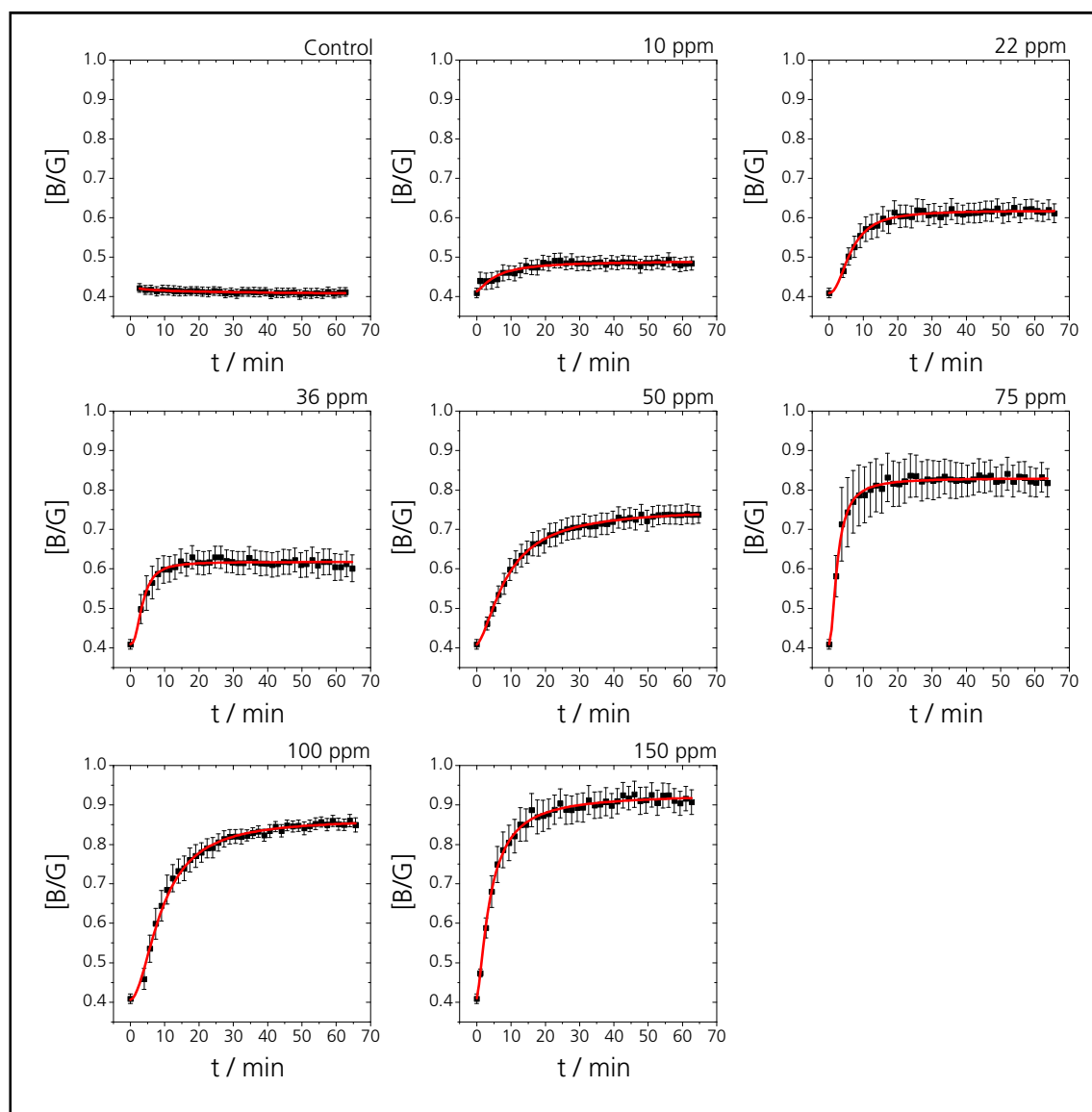


**Figure E17.** Time-dependent [B/R] increase of CR-PA induced by different concentrations of ammonia (0-150 ppm). Control was performed with 10  $\mu$ L distilled water. All curves were fitted using a logistic fit function and the calculated fit parameters are shown in Appendix (Table G18) (mean  $\pm$  SDM; N = 5).



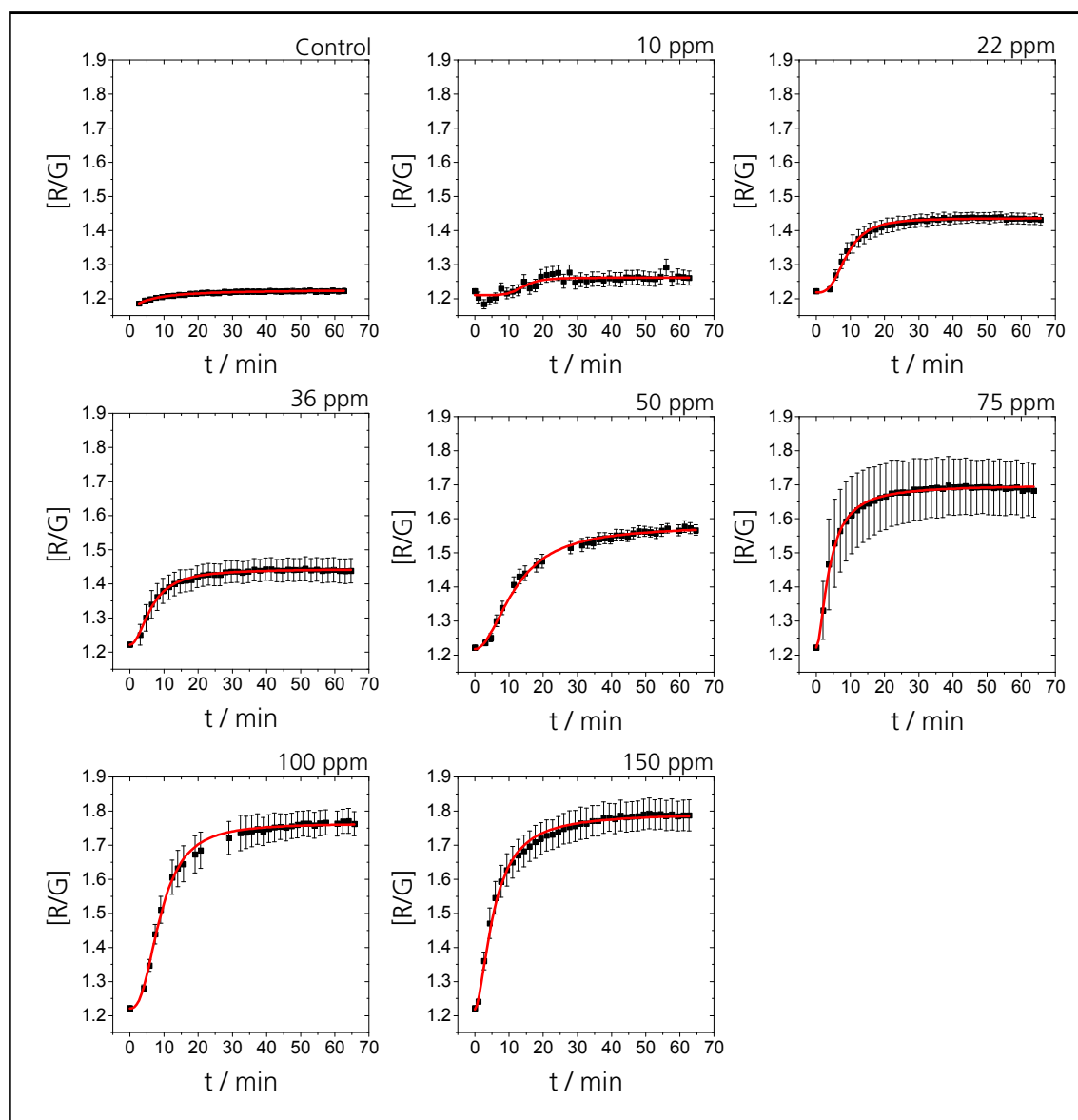
**Figure E18.** Color of sensor textile CR-PA after reaching saturation with different concentrations of ammonia.

Figure E18 shows images of the sensor textile CR-PA after reaching the saturation value. Sensor fabric CR-PA exhibits a color-change from yellow to red, all completely visible by naked eye.



**Figure E19.** Time-dependent increase of [B/G] caused by the reaction of sensor fabric CR-PA with different concentrations of ammonia (0-150 ppm). Control was performed with 10  $\mu$ L water and curves were fitted using a logistic fit function. Corresponding fit parameters are shown in the Appendix (Table G19) (mean  $\pm$  SDM; N = 5).

The observed signal saturations of either [B/R], [B/G], or [R/G] for all ammonia concentrations under study are attributed to the adjustment of equilibrium. Reaching this equilibrium takes about 20-30 minutes becoming noticeable since all signals are nearly constant after this time (Figure E17, E19, and E20).



**Figure E20.** Time-dependent increase of [R/G] induced by reaction of CR-PA fabric with various concentrations of ammonia (0-150 ppm). Control was performed with 10  $\mu$ L water and curves were fitted using a logistic fit function. Fit parameters are shown in the Appendix (Table G20) (mean  $\pm$  SDM; N = 5).

Utilizing the data of measurements described in this chapter calibration curves were plotted for [B/R], [B/G], and [R/G]. For this purpose saturation values for all calibration plots were determined by forming the mean of the last ten data points (45-60 min). The values were plotted against ammonia concentrations resulting in the graphs depicted in Figure E21 (graph A for [B/R], graph B

for [B/G] and graph C for [R/G]). All curves were fitted with an exponential association ( $R^2 = 0.97$  for A,  $R^2 = 0.99$  for B, and  $R^2 = 0.98$  for C). Since small ammonia concentrations show a linear signal response additional linear fits were applied for concentrations between 0 and 50 ppm (Figure E21, graphs D, E, and F). The parameters of these linear fit functions for graph D ( $R^2 = 0.96$ ), E ( $R^2 = 0.99$ ), and F ( $R^2 = 0.99$ ) are depicted in Table E4.

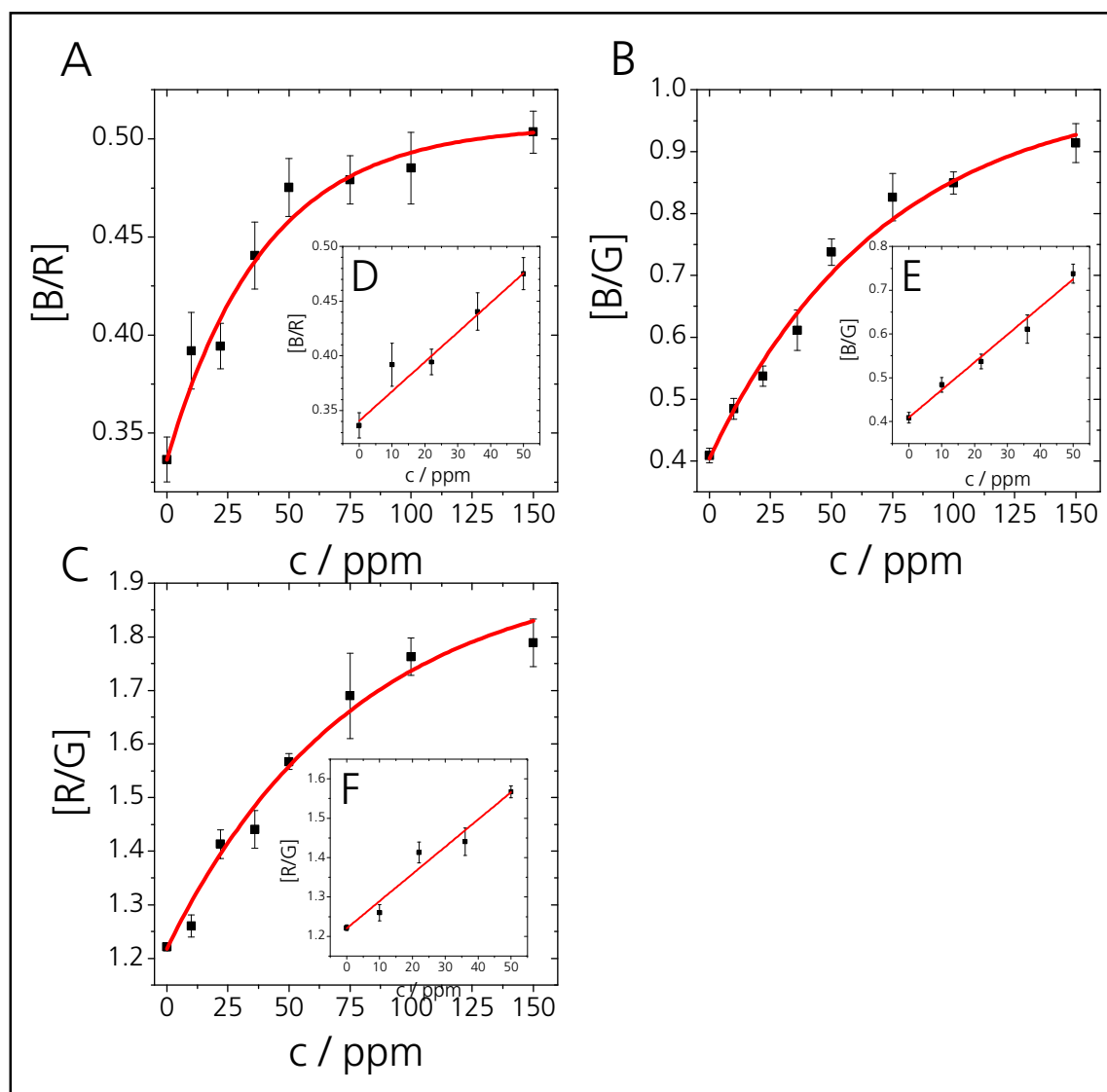


**Figure E21.** Ammonia calibration plots of sensor textile CR-PA. **A:** calibration curve for data evaluation by [B/R], **B:** calibration plot [B/G], and **C:** calibration plot for [R/G] values. The plotted data derives from calculating the mean of the last ten data points of time-dependent curves (Figure E17, E18, and E19). Small graphs D ([B/R]), E ([B/G]), and F ([R/G]) show the linear response of CR-PA to low ammonia concentrations (mean  $\pm$  SDM;  $N = 5$ ).

It can be seen from Table E4 that the lowest slope of the linear fit functions is obtained in Figure E21, graph D ( $0.0027 \pm 0.0003 \text{ ppm}^{-1}$ ). Values of graph E and F, however, are in the same

range with  $0.0063 \pm 0.0004 \text{ ppm}^{-1}$  and  $0.0069 \pm 0.0004 \text{ ppm}^{-1}$ . Consequently, lower limits of detection are expected for data evaluation by [B/G] (graph E) and [R/G] (graph F).

**Table E4.** Parameters calculated from linear fits of Figure E21, graphs D, E, and F.

Graph	Slope $\pm$ error / $\text{ppm}^{-1}$	Intercept $\pm$ error
Fig. E21; D	$0.0027 \pm 0.0003$	$0.351 \pm 0.008$
Fig. E21; E	$0.0063 \pm 0.0004$	$0.409 \pm 0.008$
Fig. E21; F	$0.0069 \pm 0.0004$	$1.220 \pm 0.009$

### 4.1.3 Methyl red dyed polyamide (MR-PA)

For sensor textile MR-PA only data evaluation by [G/R] gave a suitable response as already mentioned in chapter 3.4.3. Quantifying the color change of MR-PA was performed applying seven different ammonia concentrations between 0 and 150 ppm. Since all measurements can be described by sigmoidal curves each curve was fitted with a logistic fit function (Equation E2). The time-dependent plots are shown in Figure E23 and corresponding fit parameters are depicted in the Appendix, Table G21.

Figure E22 represents images of the sensor fabric MR-PA after achieving saturation in the presence of ammonia. Increasing the ammonia concentrations provoke a change of MR-PA from orange to yellow.



**Figure E22.** Color of sensor textile MR-PA after reaching saturation in the presence of different ammonia concentrations.

The observed signal saturation of sensor textile MR-PA for all ammonia concentrations is attributed to the adjustment of equilibrium. Reaching this equilibrium takes about 10-20 minutes since signals [G/R] are constant after this time for all concentrations under study (Figure E23).

Figure E23 shows the time-dependent increases of signal [G/R] during reaction of MR-PA with varying concentrations of ammonia (0 - 150 ppm). Increasing the ammonia concentration causes

a raise of the saturation value. However, beyond 100 ppm no further increase is observed. This indicates a complete reaction of all indicator dye molecules in the textile without further signal change at concentrations beyond 100 ppm.

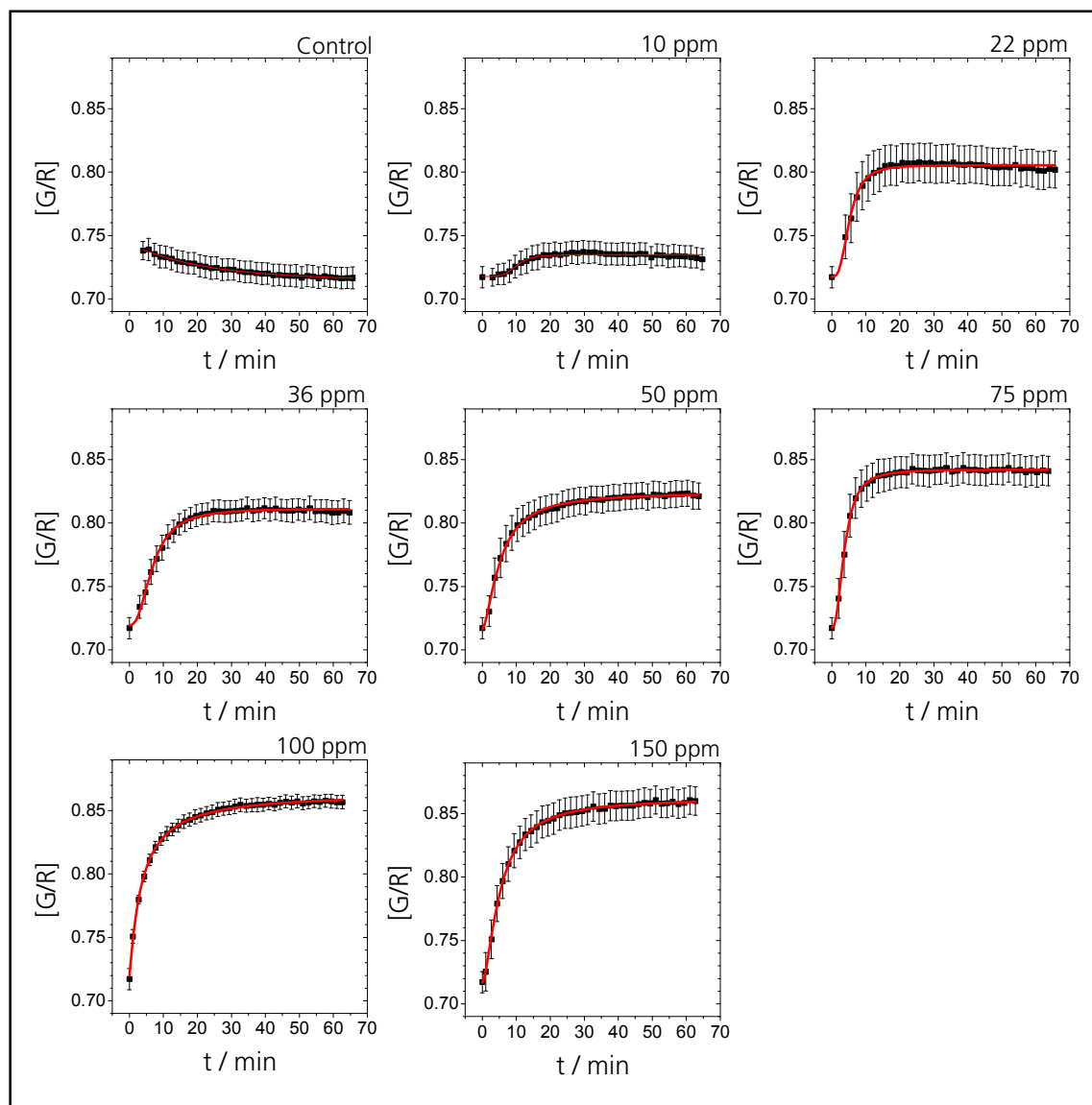


**Figure E23.** Time-dependent increase of the signal  $[G/R]$  induced by reaction of MR-PA sensor fabric with different concentrations of ammonia (0-150 ppm). Control was performed with 10  $\mu\text{L}$  water and curves were fitted using a logistic fit function. Fit parameters are shown in the Appendix (Table G21) (mean  $\pm$  SDM;  $N = 5$ ).

Based on the measurements with varying ammonia concentrations calibration curves were plotted. For this purpose the saturation value for each time-dependent plot was determined by calculating the mean of the last ten data points as described in chapter 3.5. Afterwards the values of  $[G/R]$  were plotted against the ammonia concentrations (Figure E24, A) and fitted with an exponential association ( $R^2 = 0.97$ ).



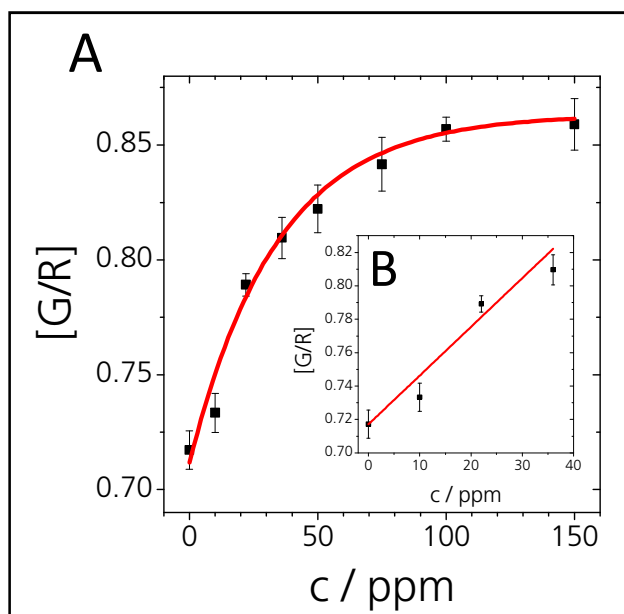


**Figure E24.** Ammonia calibration plot for sensor textile MR-PA. **A:** exponential calibration curve, plotted values derive from calculating the last ten data points of all saturation curves (Figure E23). **B:** the graph shows the linear signal response towards low ammonia concentrations (mean  $\pm$  SDM; N = 5).

For small ammonia concentrations (0-36 ppm) a linear signal response was observed (Figure E24, B) and were thus fitted applying a linear fit function. The parameters of linear fit function ( $R^2 = 0.88$ ) are depicted in Table E5.

**Table E5.** Parameters of linear fit function (Figure E24, graph B).

Graph	Slope $\pm$ error / ppm <sup>-1</sup>	Intercept $\pm$ error
Fig. E24; B	$0.0029 \pm 0.0006$	$0.72 \pm 0.01$

## 4.2 Limits of detection (LOD), sensitivity, and response times

Limits of detection (LOD) and associated errors  $s_{xLOD}$  were determined as described in chapter 3.5. The calculation of LODs was performed for the three sensor textiles BTB-PA, CR-PA, MR-PA. Additionally, LOD determination was carried out for all suitable ratiometric data evaluation methods. The respective values are given in Table E6.

The response times were calculated as  $t_{90}$  values in this case. They represent the time when 90% of overall signal change is achieved. For this purpose logistic fit functions of time-dependent calibration measurements were evaluated as described in chapter 3.5. Data in Table E6 results as mean of  $t_{90}$  times of all seven ammonia concentrations under study.

**Table E6.** Limits of detection (LODs), sensitivities, and response times for three sensor textiles under study. Values were calculated for all suitable evaluation methods (see chapter 3.5)

Sensor textile	Method of data evaluation	LOD $\pm$ error / ppm	Sensitivity / ppm <sup>-1</sup>	Response time $t_{90} \pm$ error / min (N = 7)
<b>BTB-PA</b>	[B/R]	$2 \pm 1$	$0.048 \pm 0.003$	$16 \pm 2$
	[B/G]	$3.5 \pm 0.9$	$0.0190 \pm 0.0008$	$17 \pm 2$
<b>CR-PA</b>	[B/R]	$11 \pm 3$	$0.0027 \pm 0.0003$	$15 \pm 3$
	[B/G]	$5 \pm 1$	$0.0063 \pm 0.0004$	$21 \pm 4$
	[R/G]	$3 \pm 1$	$0.0069 \pm 0.0004$	$22 \pm 3$
<b>MR-PA</b>	[G/R]	$9 \pm 5$	$0.0029 \pm 0.0006$	$17 \pm 2$

BTB-PA exhibits a limit of detection of about 3 ppm, independently from the data evaluation method applied. [B/R], however, leads to a slightly lower LOD value than [B/G]. This observation corresponds to the sensitivity values since linear calibration plots with higher sensitivity yield, of course, in lower LOD values. CR-PA exhibits a quite high LOD of  $11 \pm 3$  ppm for data evaluation by the ratio [B/R]. The lowest LOD of  $3 \pm 1$  ppm is received with the ratio [R/G]. This tendency is again reflected by the corresponding sensitivity values of  $0.0069 \pm 0.0004$  ppm<sup>-1</sup> for [R/G] and  $0.0027 \pm 0.0003$  ppm<sup>-1</sup> for [B/R]. LOD received from data [B/G], however, is  $5 \pm 1$  ppm, and thus very similar to [R/G]. Sensor textile MR-PA was only evaluated by calculating ratios from green and red color channels [G/R], yielding a LOD of  $11 \pm 3$  ppm and sensitivity of  $0.0029 \pm 0.0006$  ppm<sup>-1</sup>.

As response times turned out to be rather independent from ammonia concentration the mean of  $t_{90}$  values received from the seven different ammonia concentrations was calculated. This was again performed for all data evaluation methods. The calculated times are depicted in Table E6.

As it can be shown in Table E6, response times are all in the same order of magnitude taking errors into account. Lowest value of  $15 \pm 3$  min was obtained for CR-PA evaluated by [B/R] whereas the highest  $t_{90}$  value of  $22 \pm 3$  min was received from CR-PA and [R/G]. Additionally, errors of response times are in the same range (about 15%). However, it is important to know that response times are highly dependent on the surrounding temperature and measurements in our case were not performed in an air-conditioned room. Nevertheless, all measurements were conducted within a short time frame exhibiting similar ambient temperatures. Hence, comparison between our measurements is reasonable, whereas the comparison to other measurements might be difficult.

The response times for all ammonia concentrations are similar and rather independent from the type of indicator dye. Thus, the response of sensor textiles is probably highly affected by the evaporation time of ammonia and polyamide permeability. As a result from Table E6 most suitable data evaluation methods are [B/R] for sensor textile BTB-PA and [R/G] for CR-PA. MR-PA has to be evaluated by [G/R] as there is no feasible alternative. Comparing all sensor textiles BTB-PA exhibits the lowest LOD. Consequently, BTB-PA currently seems to be the most suitable sensor textile at that time.

### 4.3 Response and reverse behavior of sensor fabrics

For investigations towards reverse behavior of sensor fabrics two different concentrations (36 and 150 ppm) were investigated. These concentrations were chosen as they provoke different sensor responses. While 150 ppm ammonia leads to complete saturation of the textiles, signal increase at 36 ppm ammonia is in the linear zone of the calibration curves (Figure E25, E26, and E27). Response behavior was investigated for the three sensor textiles BTB-PA, CR-PA, and MR-PA. Data evaluation was performed using the suitable methods for each sensor textile as described in chapter 3.5. Images were taken in time intervals of 60 seconds for a measuring time of 38 minutes. After this time glass vials were removed and screw caps were placed in the measuring chamber again. After further 38 minutes 10  $\mu$ L of stock solutions was pipetted in new glass vials and subsequently closed with the screw caps. This procedure was repeated six times and carried out in five replicates each.

### 4.3.1 Bromothymol blue dyed polyamide

Response curves for BTB-PA are depicted in Figure E25 for data evaluation by the ratios  $[B/R]$  (graphs A and B) and  $[B/G]$  (graphs C and D). For both evaluation methods the curves for 36 ppm (graphs A and C) and 150 ppm ammonia (graph B and D) are represented.

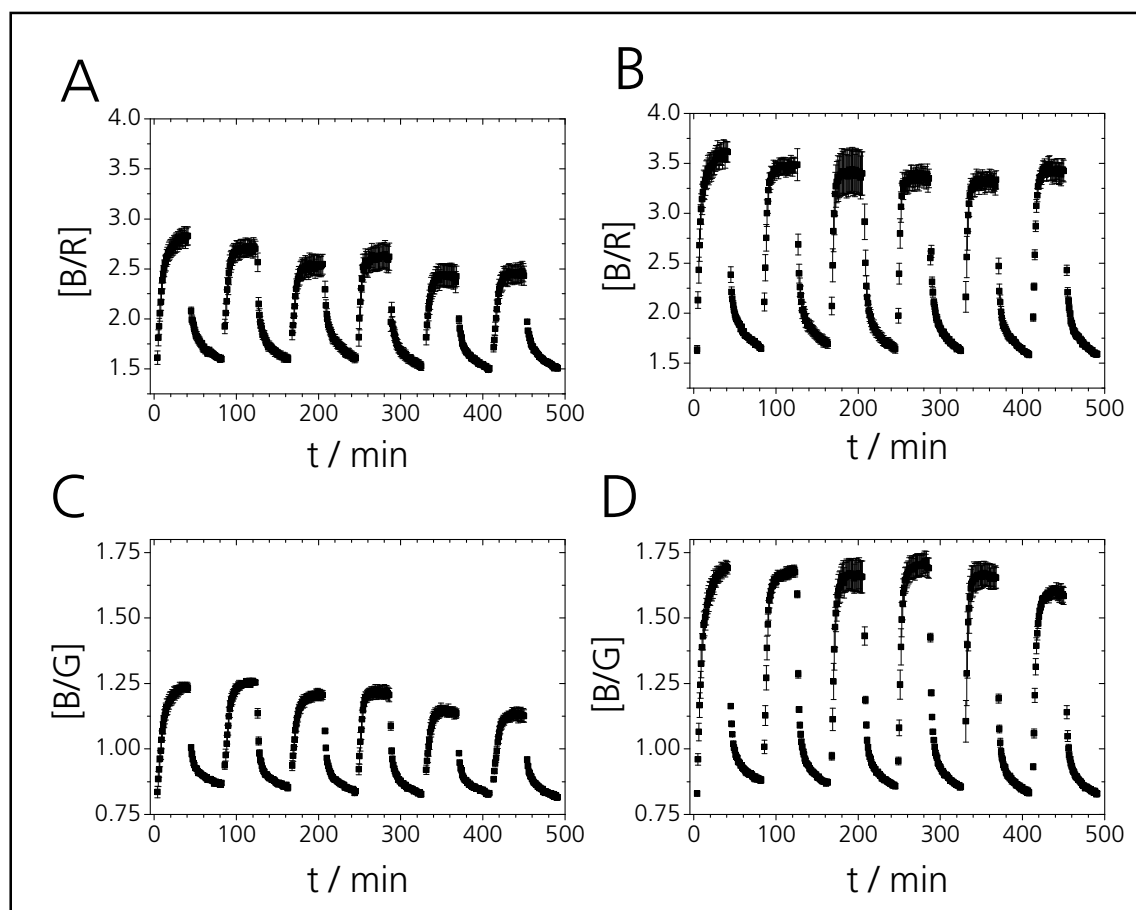


**Figure E25.** Ammonia response curves of bromothymol blue dyed polyamide fabric. Two different ammonia concentrations were investigated. Curves for 36 ppm are shown by **A** and **C**. Signal changes provoked by 150 ppm are depicted in **B** and **D**. Two different methods of data evaluation were carried out. Changes in  $[B/R]$  are represented by graphs **A** and **B**. Signal changes of  $[B/G]$  are shown by **C** and **D** (mean  $\pm$  SDM;  $N = 5$ ).

The response of sensor textile BTB-PA with ammonia as well as the reverse reaction is completed within a measuring period of 38 min for 36 and 150 ppm. While the signal  $[B/R]$  changes between 1.5 and 2.75 in the presence of 36 ppm ammonia (Figure E25, A) the signal response for 150 ppm is between 1.5 and 3.5 (Figure E25, B). For data evaluation by  $[B/G]$  a signal shift from 0.75 to 1.2 is obtained for 36 ppm ammonia (Figure E25, C) and signals for 150 ppm are in the range between 0.75 and 1.7 (Figure E25, D).

### 4.3.2 Cresol red dyed polyamide

Figure E26 represents the response curves of sensor textile CR-PA to 36 and 150 ppm ammonia. Data evaluation was performed by signals [B/R] (graphs A and B), [B/G] (graphs C and D), and [R/G] (Figure E and F). For all evaluation methods curves for 36 ppm (graphs A, C, and E) and 150 ppm ammonia (graph B, D, and F) are represented.

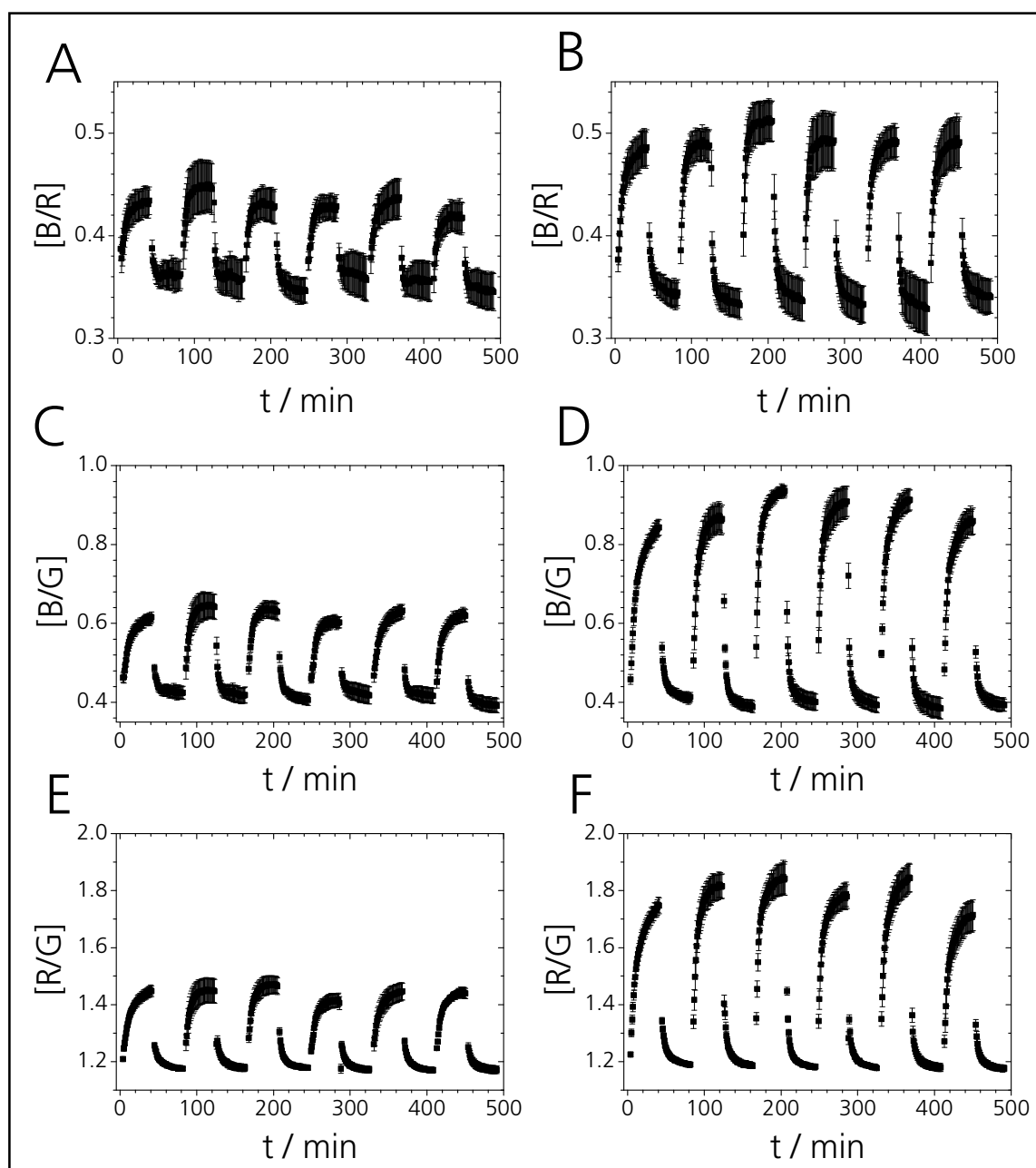


**Figure E26.** Ammonia response curves of CR-PA. Curves for 36 ppm are shown in **A**, **C**, and **E**. Signal changes for 150 ppm are depicted in graphs **B**, **D**, and **F**. Three different methods of data evaluation were carried out. Signal changes of [B/R] are represented by graphs **A** and **B**, whereas signal shift of [B/G] is shown by curves **C** and **D**. Intensity changes of [R/G] are depicted in graphs **E** and **F** (mean  $\pm$  SDM;  $N = 5$ ).

The reaction of sensor textile CR-PA with ammonia is completed for 36 as well as 150 ppm within the measuring time of 38 min. In addition, the reverse reaction is finished after the measuring time being recognized from Figure E26. Signals for [B/R] show a shift between 0.35 and 0.45 in the presence of 36 ppm (Figure E26, A). For 150 ppm the signal variation ranges between 0.35 and 0.5 (Figure E26, B). Data evaluation by [B/G] results in a signal change between 0.4 and 0.6 for 36 ppm ammonia (Figure E26, C) and a shift from 0.4 to 0.9 for 150 ppm (Figure E26, D). Moreover, [B/G] exhibits a signal change between 1.2 and 1.4 for 36 ppm (Figure E26, C) and from 1.2 to 1.8 applying 150 ppm ammonia (Figure E26, D).

### 4.3.3 Methyl red dyed polyamide

Response and reverse curves of sensor textile MR-PA are represented in Figure E27 for [G/R] since it is the sole reasonable method of data evaluation in this case. While Figure E27, A depicts the response towards 36 ppm graph B represents the data for applying 150 ppm ammonia. The response as well as the reverse reaction of sensor textile MR-PA with ammonia is completed within a measuring period of 38 minutes for 36 and 150 ppm. This is concluded from stable signals after every 38 min, as shown in Figure E27. Signal changes between 0.72 and 0.80 are provoked by 36 ppm ammonia (Figure E27, A). For 150 ppm the signal response is between 0.72 and 0.83 (Figure E27, B).

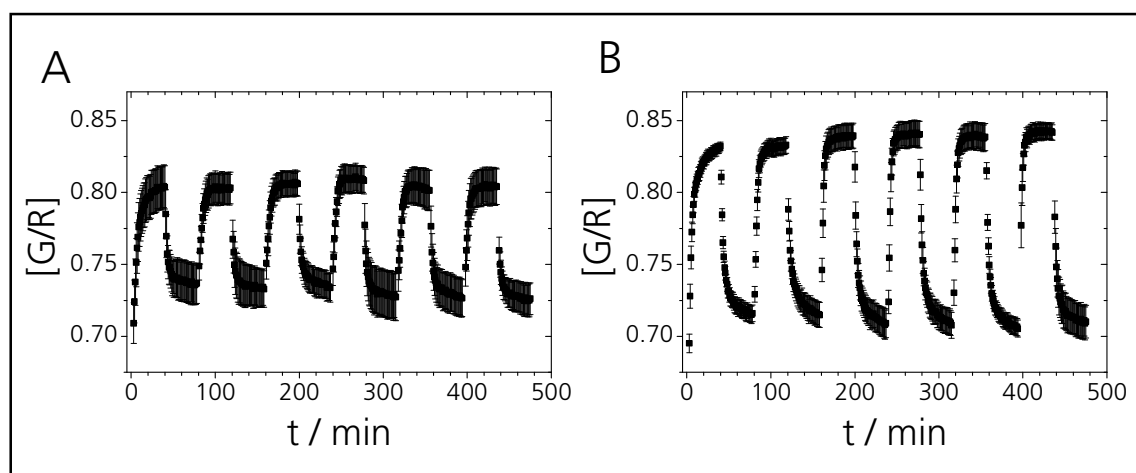


**Figure E27.** Ammonia response curves for methyl red dyed polyamide fabric. Data for 36 ppm is represented by graph **A** whereas signal changes by 150 ppm ammonia are depicted in graph **B** (mean  $\pm$  SDM; N = 5).

### 4.3.4 Response and reverse times

Based on investigations the experiments shown in the preceding paragraphs for the sensor textiles BTB-PA, CR-PA, and MR-PA (chapter 4.3.1, 4.3.2, and 4.3.3) response and reverse times were calculated as  $t_{90}$  values (for details see chapter 3.5). Table E7 represents the calculated times of

the sensor fabrics for the two ammonia concentrations 36 and 150 ppm. Furthermore, response and reverse times were determined for all reasonable data evaluation methods.

Values for response and reverse times shown in Table E7 derive from the mean of all associated measuring cycles. However, the first cycle (0 – 38 min) was not included for calculation as no blank was measured. Consequently, values of response times originate from the mean of five measurement cycles and values of reverse times from six cycles. Additionally, indicated errors represent the standard deviations.

**Table E7.** Response and reverse times ( $t_{90}$ ) for three sensor fabrics BTB-PA, CR-PA, and MR-PA under study. Values are depicted for the ammonia concentrations of 36 and 150 ppm and for each suitable method of data evaluation.

Sensor textile	Method of data evaluation	$c(\text{NH}_3)$ / ppm	Response time $t_{90} \pm \text{SDM}$ / min (N = 5)	Reverse time $t_{90} \pm \text{SDM}$ / min (N = 6)
<b>BTB-PA</b>	Ratio B/R	36	$9.3 \pm 0.5$	$18.2 \pm 0.8$
		150	$12.0 \pm 0.8$	$15.0 \pm 0.2$
	Ratio B/G	36	$10.1 \pm 0.3$	$15.0 \pm 0.9$
		150	$13.6 \pm 0.8$	$11.3 \pm 0.4$
<b>CR-PA</b>	Ratio B/R	36	$11.4 \pm 0.9$	$8.4 \pm 0.7$
		150	$13 \pm 1$	$9.9 \pm 0.4$
	Ratio B/G	36	$13.8 \pm 0.5$	$8.4 \pm 0.5$
		150	$15 \pm 2$	$7.4 \pm 0.4$
	Ratio R/G	36	$14 \pm 1$	$10.4 \pm 0.2$
		150	$14 \pm 1$	$8.3 \pm 0.2$
<b>MR-PA</b>	Ratio G/R	36	$7.3 \pm 0.3$	$8.6 \pm 0.7$
		150	$9.9 \pm 0.3$	$11.3 \pm 0.7$

For sensor textile BTB-PA response times of roughly 10 minutes are received measuring 36 ppm ammonia. For 150 ppm the values are slightly higher (13 minutes). These times are independent from evaluation methods and, thus, the same for [B/R] and [B/G]. Reverse times are generally

higher than response times whereby a difference is also observed between the two ammonia concentrations. A reverse time of 18 minutes is observed for 36 ppm determined by [B/R] whereas 15 min are obtained for 150 ppm ammonia. The same tendency is obtained by data [B/G] whereas values received by [B/G] are slightly lower (15 and 11 minutes).

Sensor textile CR-PA shows response times of about 14 minutes independent from ammonia concentration and data evaluation method. Reverse times again are slightly lower than response times. E.g. for data evaluation method [B/R] the response time is 11 minutes for 36 ppm ammonia whereas the corresponding reverse time is about 8 minutes. A dependency on the ammonia concentration could not be observed for this sensor textile.

Response and reverse times of sensor fabric MR-PA appear to be dependent on the ammonia concentration. While response times are 7 min for 36 ppm and 10 min for 150 ppm reverse times are slightly higher. For 36 ppm a value of about 9 min was obtained, whereas reverse time is 11 minutes applying 150 ppm ammonia.

Altogether response and reverse times can be assumed to be almost independent from data evaluation method. Additionally, reverse times are slightly higher than response times except for CR-PA. Lowest response times were obtained from MR-PA closely followed by BTB-PA. Reverse times are almost equivalent for MR-PA and CR-PA (9-10 minutes) whereas BTB-PA exhibits an higher value of 15 minutes on average.

As a result, the response times for all ammonia concentrations are similar and rather independent from type of indicator dye and data evaluation method. In contrast, reverse time are slightly dependent on the indicator dye. While CR-PA and MR-PA exhibit values of about 10 minutes, reverse times are about 15 min for the BTB-PA fabric. Moreover, reverse times are not depending on the data evaluation method. Consequently, CR-PA and MR-PA seem to be the most suitable sensor textiles regarding response and reversibility properties.

#### **4.4 Assessment of cross sensitivities to acids**

Responses of sensor fabrics exposed to different acids were investigated in order to obtain information about the opportunity to distinguish between ammonia and acids. For this purpose acetic acid (100%) and hydrochloric acid (37 wt%) were applied to obtain qualitative information. Measurements were performed in triplicate using 10  $\mu$ L of pure substance. The acids were added into glass vials which were subsequently closed by screw caps with integrated sensor textile. Afterwards, image acquisition was performed every 100 seconds for a measuring period of



65 minutes (for details see chapter 3.3) applying the camera settings described for previous measurements. Investigations were carried out applying the three sensor fabrics BTB-PA, CR-PA, and MR-PA by performing all suitable methods of data evaluation.

#### 4.4.1 Bromothymol blue dyed polyamide

In presence of ammonia sensor textile BTB-PA exhibits a color change from green to blue (Figure E13) with a response time of about 13 minutes (Table E7). In contrast, sensor response towards acetic acid is noticeable by a color change from green to yellow. Figure E28, A shows the color of the sensor textile after reaction with acetic acid. Indicator dye bromothymol blue exhibits a  $pK_a$ -value of 7.1 and an indication range of pH 5.8-7.6. Protonated BTB is yellow colored whereas its color changes to blue for higher pH. In neutral form BTB exhibits a green color.

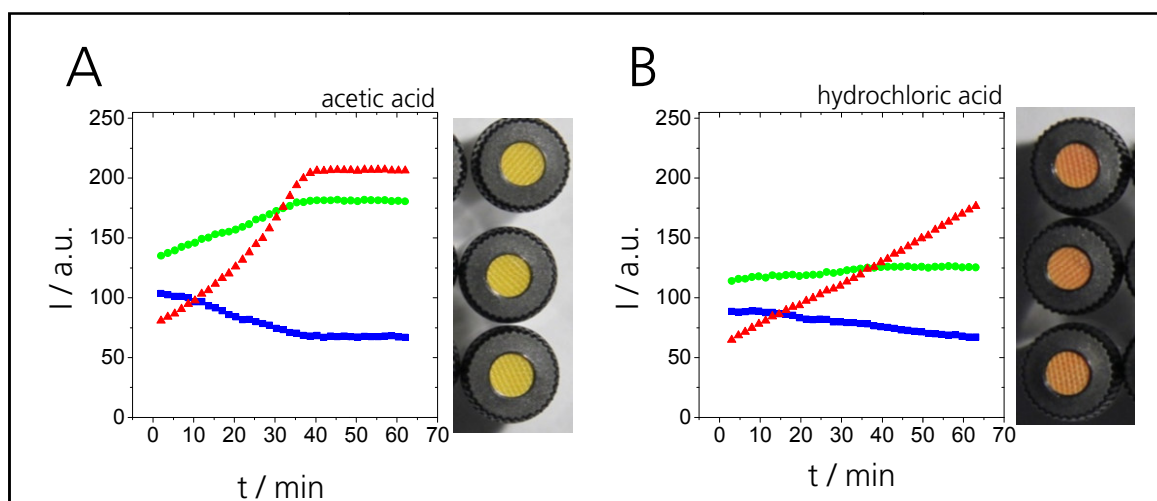


**Figure E28. A:** Graph shows the changes of red (▲), green (●), and blue (■) color channel intensities of sensor textile BTB-PA during reaction with acetic acid. Pictures indicate the color of three measuring samples after reaction under identical conditions. **B:** Graph shows the changes of red (▲), green (●), and blue (■) color channel intensities of sensor textile BTB-PA during reaction with hydrochloric acid. Pictures indicate the color of three measuring samples after reaction under identical conditions.

During the reaction of BTB-PA sensor textile with gaseous acetic acid the intensity of red color channel becomes at least doubled. Simultaneously, intensity of green color channel increases slightly and blue color channel is decreased from about 100 to 60 a.u. After 40 minutes intensities of color channels stay constant attributed to a completed reaction (Figure E28, A). The saturation can be either caused by lack of free acetic acid or by complete consumption of present bromothymol blue indicator.

Hydrochloric acid causes a color change of BTB-PA from green to orange (Figure E28, B). Figure E28, B shows the color of sensor textile after reaction with hydrochloric acid. This observation comes along with an almost linear increase of red channel intensity and a slight signal

increase of green color channel. Simultaneously, blue color channel intensity decreases from about 90 to 50 a.u. In contrast to acetic acid the signals for hydrochloric acid do not saturate even after a measuring time of 65 minutes (Figure E28, B).

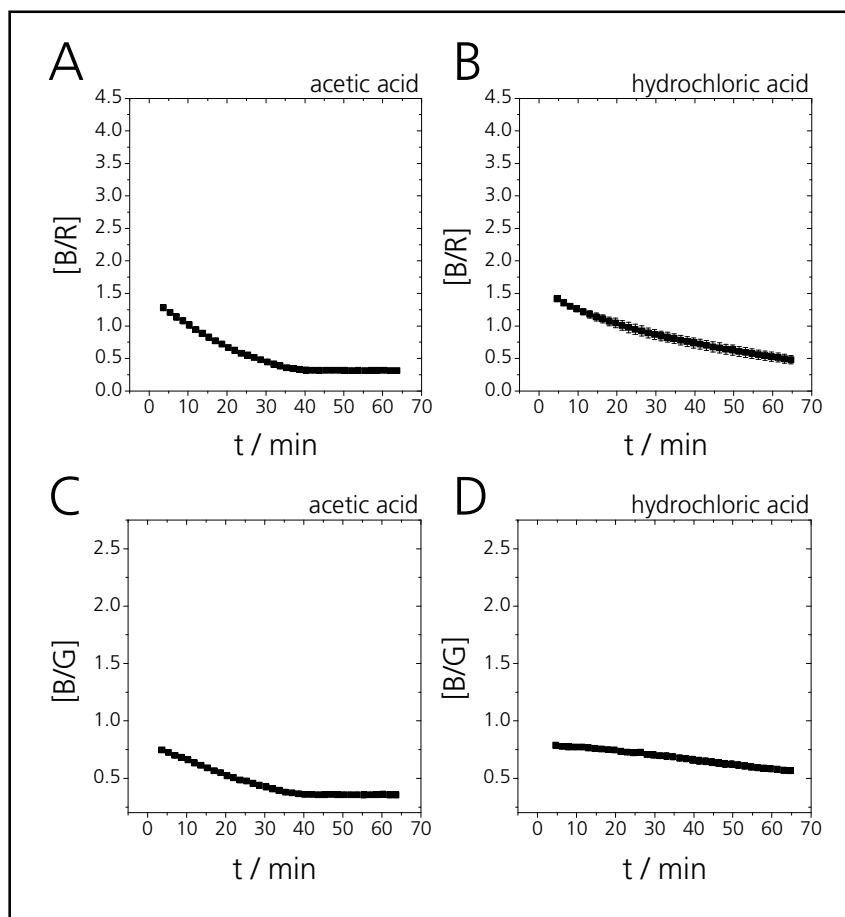


**Figure E29.** Time-dependent changes of signals [B/R] and [B/G] during reaction of BTB-PA with acetic acid (graph **A** and **C**) and hydrochloric acid (graph **B** and **D**). Graphs **A** and **B** display the data evaluation by [B/R], graphs **C** and **D** the signal changes of [B/G] (mean  $\pm$  SDM;  $N = 3$ ).

Figure E29 depicts the time-dependent signal changes of [B/R] and [B/G] of BTB-PA during reaction with acetic and hydrochloric acid. Data evaluation was performed as previously carried out for ammonia calibration measurements. Acetic acid shows a decrease in signal [B/R] as well as for [B/G] during reaction with BTB-PA (Figure E29, A and C) in the gas phase. After approximately 40 minutes signals remain constant as already observed in Figure E29, A. A signal decrease is also observed for hydrochloric acid (Figure E29, B and D). In contrast to acetic acid, however, no saturation is reached after 65 min indicating either an incomplete reaction or a degradation of polyamide fabric, since strong acids, such as hydrochloric acid, might provoke a hydrolysis of amide-bonds and influence hydrogen bonds.

Using the color information of sensor textile BTB-PA it can be nicely distinguished between a signal response triggered by solely ammonia or acids using either [B/R] or [B/G]. While ammonia causes a signal increase of [B/R] and [B/G] (chapter 4.1.1) acetic and hydrochloric acid provoke decreasing signals (Figure E29).

#### 4.4.2 Cresol red dyed polyamide

Sensor textile CR-PA exhibits a color change from yellow over orange to red with increasing ammonia concentration in the gas phase (Figure E18). In the presence of acetic acid CR-PA exhibits a yellow color after 65 minutes (Figure E30, A) as well. During the measuring time red and green channel intensities increase slightly whereas blue channel signal decreases from roughly 75 to 50 (Figure E30, A).

Cresol red is a pH indicator exhibiting a yellow color at pH values between 2 and 6.5. While it switches to violet at higher pH values, the dye is red colored at pH values  $<2$ .<sup>46</sup> After the preparation of the CR-PA fabric the indicator is existent in its neutral, yellow structure. Consequently, no color response is expected in the presence of acetic acid exhibiting a  $pK_a$ -value of 4.75. Figure E30, graph A depicts the signals of red, green, and blue color channels in the presence of acetic acid which show weaker variations. As the sensor textile fabrication was performed at pH 6.5 (for details see chapter 3.1) partial deprotonation of indicator dye might happen here. As a result, the described color channel changes (Figure E30, A) can be caused by protonation of these CR molecules.

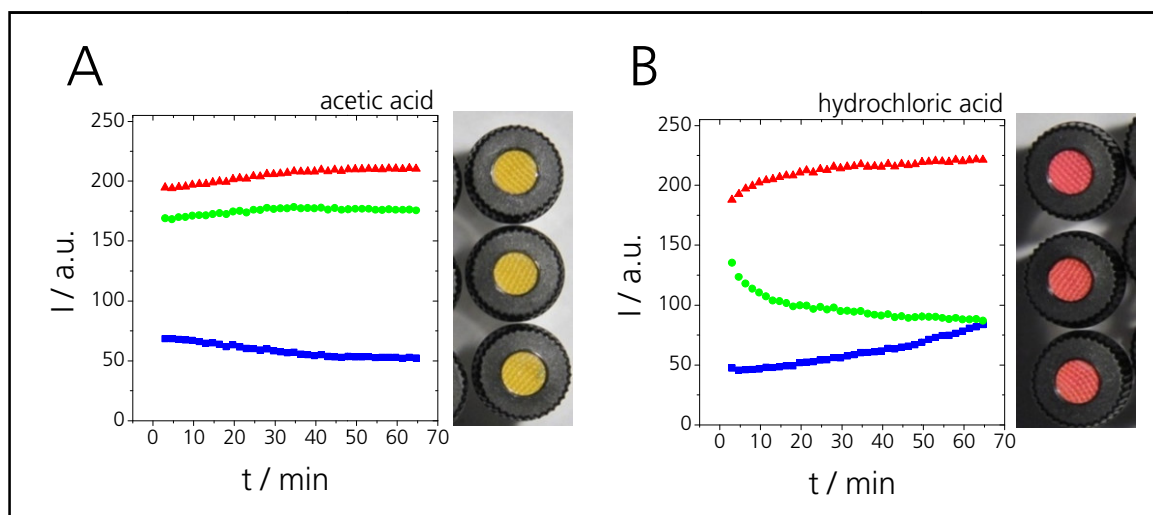


**Figure E30. A:** Graph shows the changes of red (▲), green (●), and blue (■) color channel intensities of sensor textile CR-PA during reaction with acetic acid. Pictures indicate the color of three measuring samples after reaction under identical conditions. **B:** Graph shows the changes of red (▲), green (●), and blue (■) color channel intensities of sensor textile CR-PA during reaction with hydrochloric acid. Pictures indicate the color of three measuring samples after reaction under identical conditions.

In contrast to acetic acid, hydrochloric acid possesses a  $pK_a$ -value of -6. Thus, CR-PA exhibits a color change to red during reaction with hydrochloric acid (Figure E30, B). The reaction comes along with an increase in red and blue color channel intensities and a decrease of green color channel (Figure E30, B). While red and green color channels exhibit a reasonably constant signal after about 30 minutes, the blue color channel intensity increases during the whole measuring time.

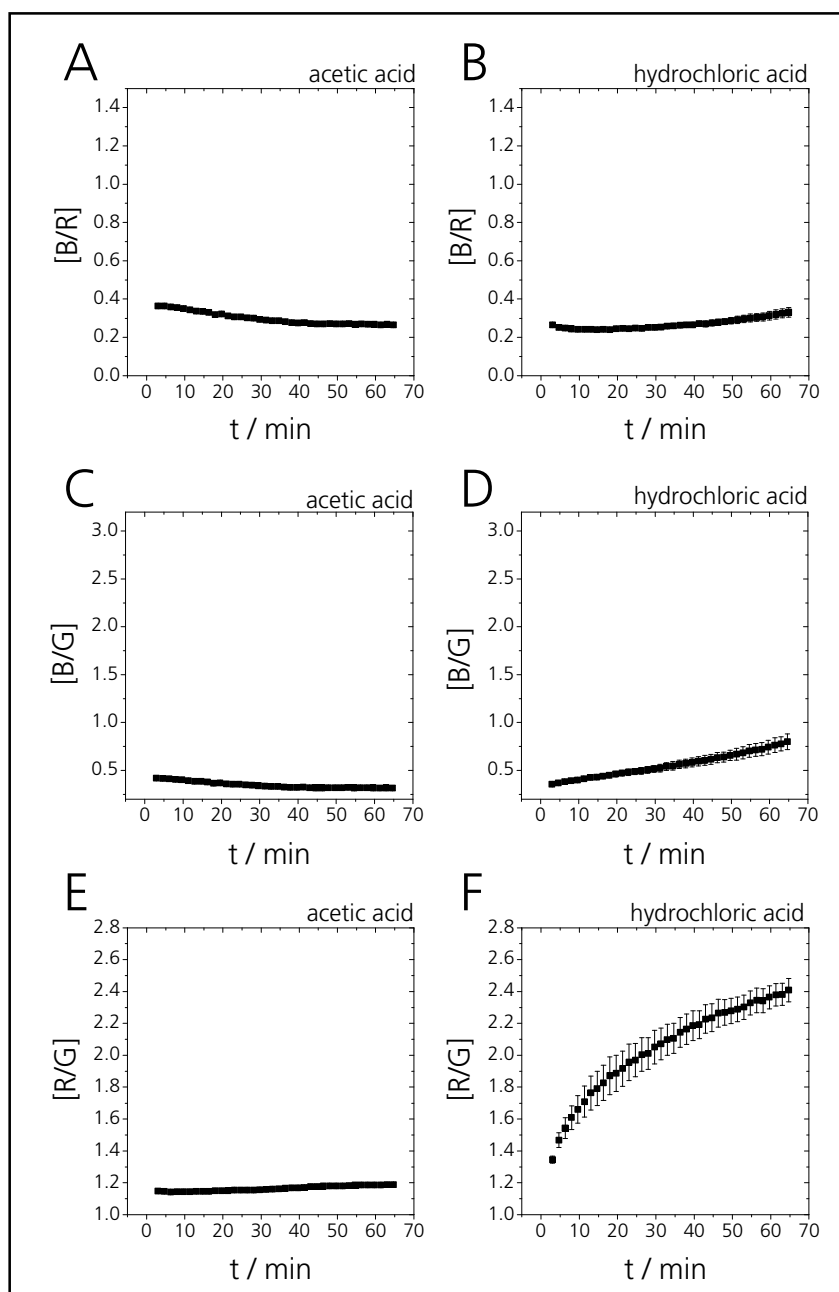


**Figure E31.** Time-dependent changes of [B/R], [B/G], and [R/G] during reaction of CR-PA with acetic acid (graph A, C, and E). Graph B, D, and F reflect the changes caused by hydrochloric acid. Graphs A and B display data evaluation by [B/R], graphs C and D signal changes of [B/G], and graphs E and F data of [R/G] (mean  $\pm$  SDM;  $N = 3$ ).

Figure E31 depicts the time-dependent signal changes caused by reaction of sensor textile CA-PA with acetic and hydrochloric acid. Data evaluation was performed by [B/R], [B/G], and [R/G] as previously carried out for ammonia calibration measurements. Graphs of signal changes caused by acetic acid show a slight time-dependent growth of [B/R] (Figure E31, A) and [B/G] (Figure E31, C) and, furthermore, are constant after 40 minutes. In contrast, the graph of [R/G] (Figure E31, E) displays an almost constant signal over the whole measuring time.

Reaction with hydrochloric acid provokes an almost constant signal of [B/R] (Figure E31, B) whereas [B/G] shows a linear increase (Figure E31, D) during the whole measuring time. For data evaluation by [R/G] an signal increase is observed without showing saturation after 65 minutes.

For acetic acid almost no signal response of CR-PA was observed, thus demonstrating the absence of a cross sensitivity. In contrast, hydrochloric acid provokes a color change to red very similar to the color change caused by reaction of CR-PA ammonia. Consequently, there is the need to differentiate between both sensor responses.

While the red color channel decreases for the reaction with ammonia, it is increased for hydrochloric acid. In contrast, green and blue color channels show the same tendency for both analytes – a decrease for green and an increase for blue. However, while ammonia provokes a sigmoidal increase of the blue channel an almost linear increase is observed in the presence of hydrochloric acid.

Consequently, discrimination between purely ammonia and acids is possible by evaluation of [B/R] and [B/G] signals. While graphs for ammonia show a sigmoidal increase the graphs for hydrochloric acid exhibit an almost linear growth. However, calculation of [R/G] does not allow a clear differentiation between ammonia and hydrochloric acid due to a sigmoidal increase for both analytes. Therefore, conclusion from chapter 4.2 needs to be refined.

In chapter 4.2 data evaluation by [R/G] was concluded to be the most suitable for quantifying the sensor response of CR-PA. The reason was the low LOD of  $3 \pm 1$  ppm calculated from these two color channels. However, since [B/G] offers a similar LOD of  $5 \pm 1$  ppm and with regard to the possible differentiation between acids and ammonia this method becomes favored.

#### 4.4.3 Methyl red dyed polyamide

The reaction of MR-PA with acetic acid leads to a color shift from orange to red. Figure E32, A shows the color of three measuring samples after reaction with acetic acid in the gas phase. The observed color change comes along with an intensity decrease of green color channel from 140 to 80 a.u. while signals of blue and red color channel nearly remain constant. Reaction of sensor fabric MR-PA with hydrochloric acid results in a color change from orange to rose (Figure E32, B). In this case an intensity increase of blue color channel can be observed. The signal of the green color channel decreases while the red color channel stays roughly constant. After about

50 minutes all color channels show constant values which is either attributed to equilibrium (Figure E32, A and B) or a complete conversion of present methyl red indicator.

In the presence of gaseous ammonia the sensor fabric MR-PA exhibits a color change from orange to yellow (Figure E22) with a response time of about 10 minutes. In contrast, sensor response towards acetic acid and hydrochloric acid can be perceived by a color change from orange to orange-red or rose (Figure E32, A and B), respectively. The dye methyl red exhibits an indication range of pH 4.4-6.2. While pH values below 4.4 provoke a red color, values beyond 6.2 lead to a yellow colored dye.

Since sensor fabrication is accomplished at pH 6.5 (for details see chapter 3.1) most of methyl red molecules exist in their deprotonated form. Additionally, acetic and hydrochloric acid have  $pK_a$  values lower than the indicator range of methyl red. Thus, both acids provoke a sensor response of the original orange-colored MR-PA. While acetic acid causes a color change to orange-red hydrochloric acid is leading to a rose color.

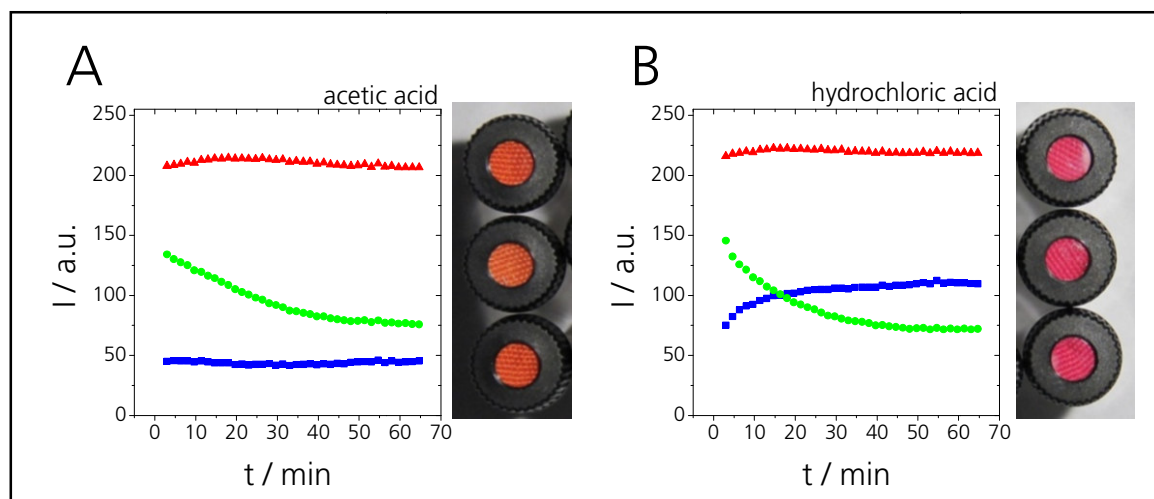


**Figure E32. A:** Graph shows the changes of red (▲), green (●), and blue (■) color channel intensities of sensor textile MR-PA during reaction with acetic acid. Pictures indicate the color of three measuring samples after reaction under identical conditions. **B:** Graph shows the changes of red (▲), green (●), and blue (■) color channel intensities of sensor textile MR-PA during reaction with hydrochloric acid. Pictures indicate the color of three measuring samples after reaction under identical conditions.

Figure E33 depicts the time-dependent signal changes provoked by reaction of MR-PA with acetic and hydrochloric acid. Data evaluation was performed by calculating  $[G/R]$  as previously carried out for ammonia calibration measurements as well.

Graphs for acetic and hydrochloric acid show a quite similar trend starting with a decrease and ending up in saturation. (Figure E33, A and B). For acetic acid a decrease from about 0.7 to 0.4 is observed whereas  $[G/R]$  is reduced to a value of 0.3 provoked by hydrochloric acid.

Differentiation between signal response of purely ammonia or acids is possible by comparing the color change. While sensor response towards ammonia is observable by a color change to yellow, both acids cause a red color. Since both acids show a decreased [G/R] signal while ammonia provokes an increase, the differentiation is feasible by the [G/R] data evaluation as well.

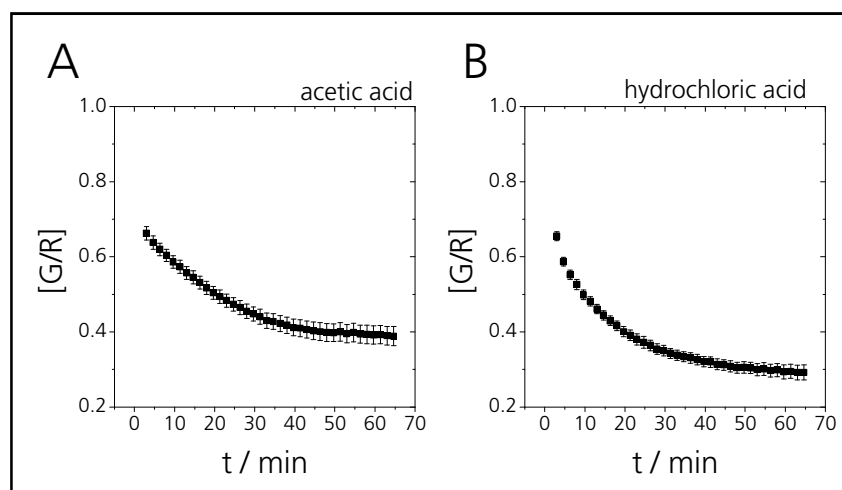


**Figure E33.** Time-dependent changes of [G/R] during reaction of MR-PA with acetic acid (graph **A**) and hydrochloric acid (graph **B**) (mean  $\pm$  SDM; N = 3).

In summary, hydrochloric acid provokes a color change of sensor textiles BTB-PA, CR-PA, and MR-PA. However, in the presence of acetic acid only BTB-PA and MR-PA show a sensor response as the indication range of cresol red is too low for a response towards acetic acid. Nevertheless, responses provoked by purely acetic and hydrochloric acid can clearly be differentiated from response provoked by purely ammonia. This is possible either by simple color changes of sensor textile or by suitable data evaluation methods.

#### 4.5 Response of sensor textiles to various amines

In order to obtain information about the response of sensor textiles BTB-PA, CR-PA, and MR-PA towards organic amines the following substances were investigated: ammonia, ethylamine, diethylamine, triethylamine, dimethylamine, and trimethylamine. For this purpose aqueous amine solutions were prepared. Composition of solutions were chosen to establish concentrations of 685 ppm in glass vials after adding and evaporating 10  $\mu$ L solution (for details see chapter 3.4). After addition of the respective solutions, glass vials were sealed by screw caps with integrated sensor textiles. Image acquisition was performed applying camera settings previously used for ammonia calibration (for details see chapter 3.3). All measurements were performed in triplicate and applying high amine concentrations of 685 ppm in order to obtain fast sensor responses. The aim of these measurements was to receive qualitative information about the dependence of signal response on  $pK_a$  values of sensor dyes and analytes as well as on analyte molecule sizes.

Measurements for each sensor textile and analyte were performed as described in the following: after adding amine solutions into the glass vials, the vials were closed with the fabric-equipped screw caps and the color change of the fabric provoked by respective amines was measured up to a constant signal value. Subsequently, glass vials were removed and color change documentation of the sole screw caps was continued. In this way the reverse reaction was analyzed. Additionally, a picture of sensor textile was taken after 20 and 45 hours. Black data points (■) in Figures E34, E35, and E36 depict the sensor responses towards amines whereas red data points (●) show the reverse reaction after removal of the glass vial. Additionally, blue (▼) and green (▲) data points represent the color after two or three days, respectively.

Color information was only evaluated by ratiometric calculation which previously turned out to be the most suitable one for the sensor textiles under study (see chapter 4.2. and 4.4), e.g. [B/R] for BTB-PA, [B/G] for CR-PA, and [G/R] for MR-PA. However, the tendencies discussed in the following chapters can also be observed for the other data evaluation methods. The parameters of additional data evaluations are presented in Appendix (Tables G22 and G23).

Absolute signal changes of response and reverse reactions are depicted in corresponding tables for all amines. Additionally, response times were calculated as  $t_{80}$  indicating the reaction time until 80% of signal response has occurred. Calculation of  $t_{80}$  times is described in detail in chapter 3.5.



#### 4.5.1 Bromothymol blue dyed polyamide

Figure E34 depicts the response of sensor fabric BTB-PA towards ethylamine (EA), diethylamine (DEA), triethylamine (TEA), ammonia, dimethylamine (DMA), and trimethylamine (TMA). All graphs show a signal increase of [B/R] during reaction with the respective amines. The highest signal change is observed for EA followed by DEA. TEA causes a slightly lower signal change and a higher response time. Additionally, EA, DEA, and TEA provoke no signal change during reverse reaction even after two (blue data points, ▲) or three days (green data points, ▼). While DMA induces a slightly lower signal response than DEA, the response caused by TMA is higher than those by TEA. Moreover, the signal change for TMA is higher than the change provoked by DMA. With regard to reversibility, removal of TMA generates no signal difference between two and three days. However, DMA measurement exhibits a signal decrease during the whole measuring period of three days. The signals of DMA and TMA do not return to their starting intensity value as already observed for EA, DEA, and TEA. In contrast to all alkylated amines, the response for ammonia is completely reversible and the reverse reaction is much faster.

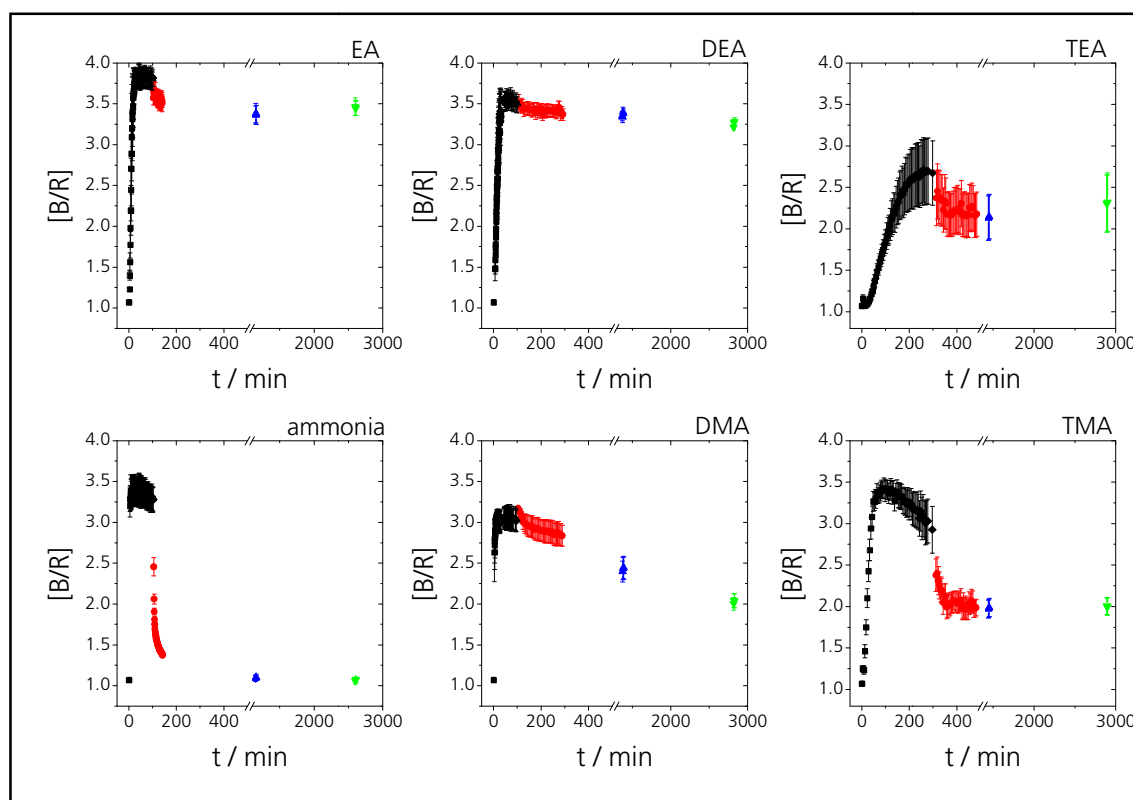


**Figure E34.** Signal changes of [B/R] during reaction of BTB-PA with 10  $\mu$ L ethylamine, diethylamine, triethylamine, ammonia, dimethylamine, and trimethylamine solution (685 ppm, black data points, ■). Red data points (●) indicate the signal change of reverse reaction after removing glass vial with amine solution. Blue data points (▲) show the signal after one day and green data point (▼) after two days at amine-free atmosphere (mean  $\pm$  SDM; N = 3).

As previously discussed ammonia exhibits a different sensor response compared to all other amines under study. Data in Table E8 further emphasizes this fact by showing absolute signal change values for response and reverse reaction. Comparing the signal change provoked by the reaction of BTB-PA with EA, DEA, and TEA a decrease can be recognized from EA ( $2.75 \pm 0.07$ ) to DEA ( $2.41 \pm 0.06$ ) and TEA ( $1.6 \pm 0.2$ ). Moreover, reactions of the three ethylated amines do not show complete reversibility even after three days. Values for completion of the reverse reaction are all in the same range (9%-25%) especially if the errors of absolute  $\Delta$  completion (reverse reaction) values are taken into account. In addition, response times of sensor textile BTB-PA increase from EA (14 min) to DEA (21 min), and TEA (186 min).

Comparing parameters for DMA and TMA a higher signal change is observed for TMA ( $2.36 \pm 0.08$ ). However, the signal change of reverse reaction is almost identical for both amines as the maximum response signal is roughly halved after three days. One obvious difference between TMA and DMA is the time until the reverse reaction reaches equilibrium. While TMA leads to saturation within minutes the signal for DMA does not show saturation at all even after three days. Response times behave in the same way as previously observed for DEA and TEA since response time is higher for TMA (40 min) compared to DMA (5 min).

Ammonia shows a high maximum signal change of  $2.21 \pm 0.09$  and a completed reverse reaction after two days. Moreover, ammonia has the shortest response time of all amines (3 min) and is therefore similar to DMA (5 minutes).

**Table E8.** Parameters of BTB-PA reacting with EA, DEA, TEA, ammonia, DMA, and TMA for data evaluation by [B/R]. Absolute signal changes are depicted for maximum response (black data points, Figure E34) and for signal change of reverse reaction (difference of maximum signal with signal after three days). Completion of reverse reaction is additionally given in percentage. The last column depicts the response time  $t_{80}$  for the respective amines.

Amine	$\Delta$ Signal (response)	$\Delta$ Signal (reverse reaction)	$\Delta$ Completion (reverse reaction) / %	Response time $t_{80}$ / min
EA	$2.75 \pm 0.07$	$0.4 \pm 0.1$	15	14
DEA	$2.41 \pm 0.06$	$0.21 \pm 0.07$	9	21
TEA	$1.6 \pm 0.2$	$0.4 \pm 0.4$	25	186
Ammonia	$2.21 \pm 0.09$	$2.21 \pm 0.09$	100	3
DMA	$1.96 \pm 0.08$	$1.0 \pm 0.1$	51	5
TMA	$2.36 \pm 0.08$	$1.4 \pm 0.1$	59	40

### 4.5.2 Cresol red dyed polyamide

In Figure E35 the response of sensor fabric CR-PA to ethylamine (EA), diethylamine (DEA), triethylamine (TEA), ammonia, dimethylamine (DMA), and trimethylamine (TMA) is depicted. All graphs show a signal increase of [B/G] while reacting with the respective amines. The highest signal change is observed for EA followed by DEA. TEA provokes a distinctly lower signal change and a higher response time. Moreover, EA, DEA, and TEA induce signal decreases when removing the amine atmosphere. EA and DEA cause a decrease over three days whereas reverse reaction of TEA is finished after a few minutes shown by red data points (●) exhibiting the same signal value as blue (▲) and green (▼) data points. However, signal responses of all amines do not return to their respective initial intensity in the absence of analyte even after three days. DMA and TMA induce a slightly lower maximum signal change in comparison to DEA and TEA. Additionally, signal change by DMA is higher than change by TMA and removal of both amines cause an almost completed reverse reaction after three days. However, for DMA measurement the signal decreases during three days. Ammonia provokes a relatively low signal change in comparison to e.g. EA and DEA, however, ammonia reaction is completely reversible after a few minutes.

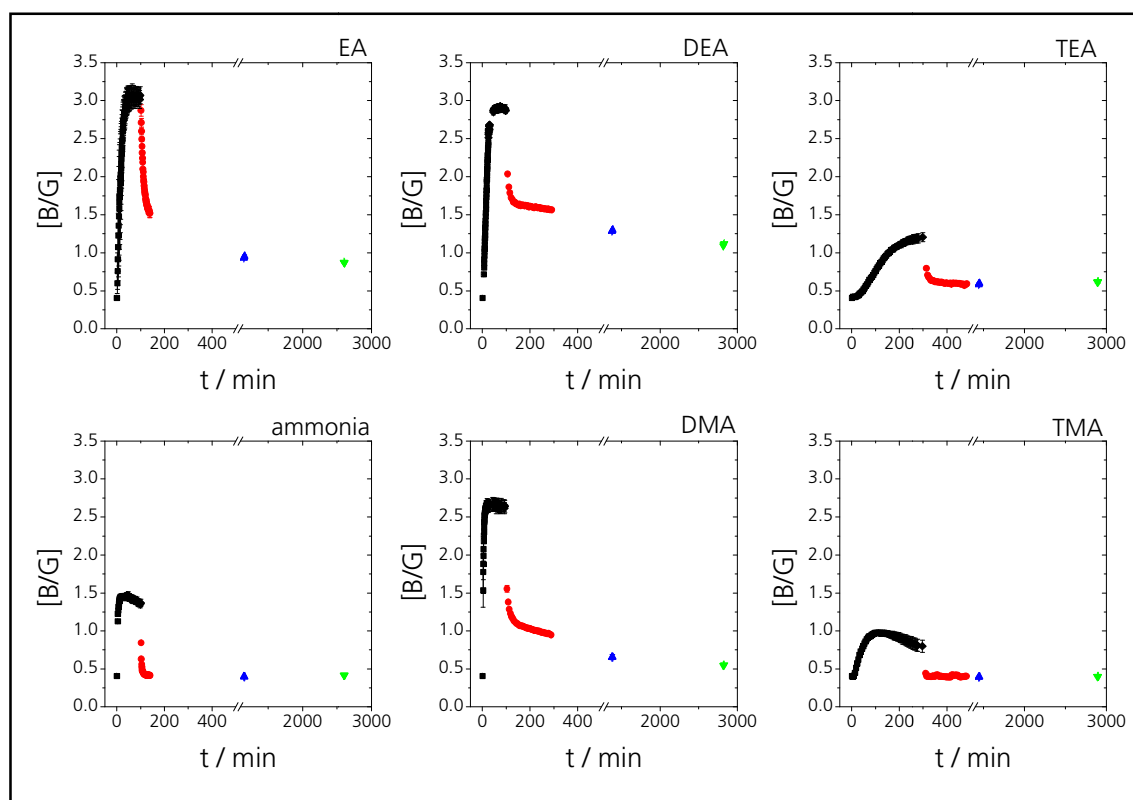


**Figure E35.** Signal changes of [B/G] during reaction of CR-PA with 10  $\mu$ L ethylamine, diethylamine, triethylamine, ammonia, dimethylamine, and trimethylamine solution (685 ppm, black data points, ■). Red data points (●) indicate the signal change of the reverse reaction after removing the glass vial and thus amine atmosphere. Blue data points (▲) show the signal after two and green data point (▼) after three days at amine-free atmosphere (mean  $\pm$  SDM; N = 3).

**Table E9.** Parameters of CR-PA upon reaction with EA, DEA, TEA, ammonia, DMA, and TMA for data evaluation by [B/G]. Absolute signal changes are depicted for maximum response (black data points, Figure E35) and for signal change of reverse reaction (difference of maximum signal and signal after three days). The completion of reverse reaction is additionally given in percentage. Last column depicts the response time  $t_{80}$  for the respective amines.

Amine	$\Delta$ Signal (response)	$\Delta$ Signal (reverse reaction)	$\Delta$ Completion (reverse reaction) / %	Response time $t_{80}$ / min
EA	$2.66 \pm 0.6$	$2.12 \pm 0.06$	80	22
DEA	$2.46 \pm 0.03$	$1.75 \pm 0.02$	71	26
TEA	$0.79 \pm 0.04$	$0.59 \pm 0.04$	75	214
Ammonia	$0.96 \pm 0.03$	$0.95 \pm 0.02$	99	5
DMA	$2.23 \pm 0.05$	$2.09 \pm 0.05$	94	6
TMA	$0.57 \pm 0.02$	$0.57 \pm 0.01$	100	69

CR-PA exhibits different behavior towards the six amines which is shown in Table E9. Comparing the maximum signal change during reaction with EA, DEA, and TEA a tendency towards smaller signal increases can be recognized from EA ( $2.66 \pm 0.6$ ) to DEA ( $2.46 \pm 0.03$ ) and TEA ( $0.79 \pm 0.04$ ). Moreover, reverse reactions of the three ethylated amines do not show completion even after three days. Values for completion of the reverse reaction are all in the same range (71%-80%). In addition, response times of sensor textile CR-PA increase from EA (22 min) to DEA (26 min), and TEA (214 min).

Comparing parameters for DMA and TMA a higher signal change is observed for DMA ( $2.23 \pm 0.05$ ). The reverse reaction is almost identical for both amines since starting values are achieved after three days if considering the errors of absolute values in the second and third column (Table E9). However, one difference between DMA and TMA is reflected by the time until reverse reaction reaches equilibrium. While TMA reaches saturation within minutes the signal for DMA does not show any saturation at all even after three days. Response times behave in the same way as observed for DEA and TEA. They are clearly higher for TMA (69 min) than for DMA (6 min).

Ammonia exhibits a moderate maximum signal change of  $0.96 \pm 0.03$  and a completed reverse reaction within a few minutes (Figure E35). Moreover, ammonia has the shortest response time of all amines (5 min) and is therefore comparable to DMA (6 min).

### 4.5.3 Methyl red dyed polyamide

The response of MR-PA to ethylamine (EA), diethylamine (DEA), triethylamine (TEA), ammonia, dimethylamine (DMA), and trimethylamine (TMA) is depicted in Figure E36. All graphs show a signal increase  $[G/R]$  during reaction with the respective amines. Highest signal changes are observed for EA, DEA, and DMA. TEA provokes a distinctly lower signal change and a higher response time. Moreover, EA, DEA, and TEA cause almost no signal decrease when removing the amine atmosphere even after three days. In contrast, DMA and TMA induce a signal decrease after removing the glass vials. For TMA the reverse reaction is almost finished within minutes, whereas removal of DMA causes a signal decrease during three days. However, neither the signals of DMA nor TMA return to their initial value after this time.

Ammonia provokes a high signal change of sensor fabric MR-PA similar to EA and DEA. Furthermore, the response of the sensor textiles towards ammonia is completely reversible after three days.

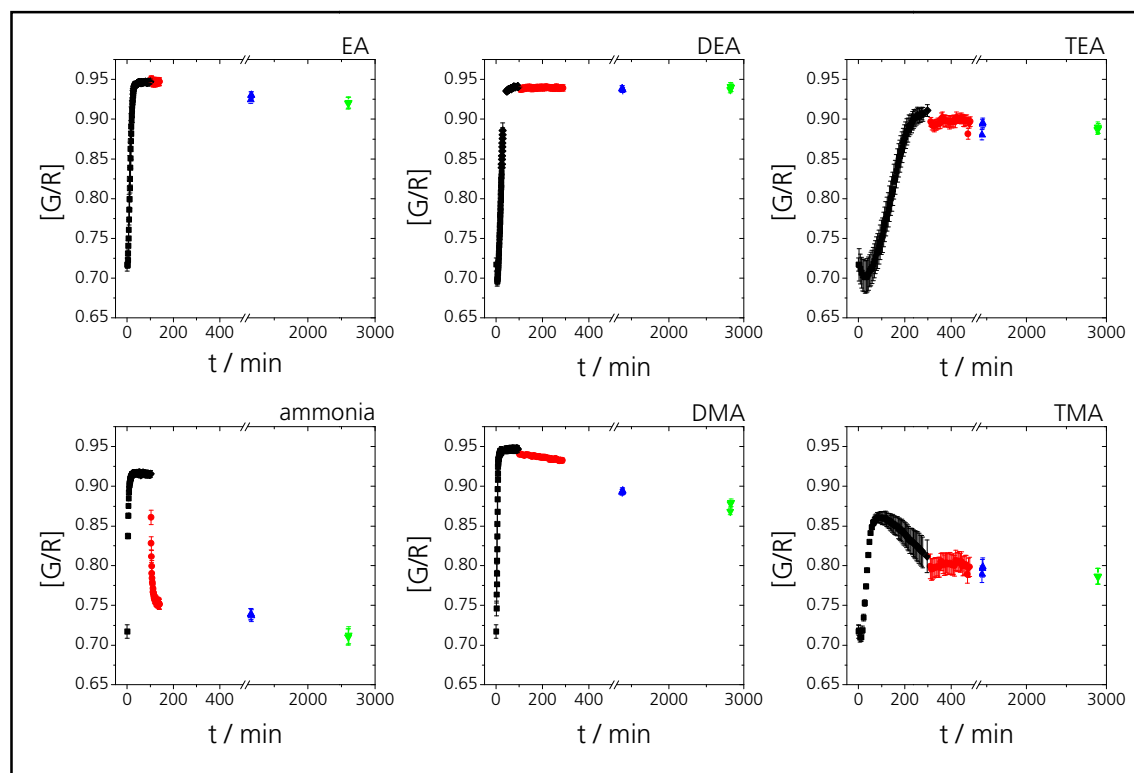


**Figure E36.** Signal changes of  $[G/R]$  during reaction of MR-PA with 10  $\mu\text{L}$  ethylamine, diethylamine, triethylamine, ammonia, dimethylamine, and trimethylamine solutions (685 ppm, black data points,  $\blacksquare$ ). Red data points ( $\bullet$ ) indicate the signal change of reverse reaction after removing glass vials. Blue data points ( $\blacktriangle$ ) show the signal after one day and green data point ( $\blacktriangledown$ ) after two days at amine-free atmosphere (mean  $\pm$  SDM;  $N = 3$ ).

**Table E10.** Parameters of MR-PA reacting with EA, DEA, TEA,  $\text{NH}_3$ , DMA, and TMA for data evaluation by [G/R]. Absolute signal changes are depicted for maximum response (black data points, Figure E36) and for signal change of back reaction (difference between maximum signal and signal after three days). Completion of reverse reaction is additionally given in percent. Last column depicts the response time  $t_{80}$  towards the respective amines.

Amine	$\Delta$ Signal (response)	$\Delta$ Signal (reverse reaction)	$\Delta$ Completion (reverse reaction) / %	Response time $t_{80}$ / min
EA	$0.2 \pm 0.1$	$0.03 \pm 0.01$	13	17
DEA	$0.224 \pm 0.005$	$0.001 \pm 0.003$	0.5	31
TEA	$0.19 \pm 0.01$	$0.023 \pm 0.007$	12	209
Ammonia	$0.199 \pm 0.006$	$0.203 \pm 0.007$	102	6
DMA	$0.20 \pm 0.01$	$0.068 \pm 0.004$	34	7
TMA	$0.15 \pm 0.01$	$0.07 \pm 0.01$	47	50

Sensor fabric MR-PA exhibits different behavior compared to BTB-PA and CR-PA towards the amines under study which is shown in Table E10. Comparing the maximum signal change during reaction with EA, DEA, and TEA a slight decrease can be recognized from EA ( $0.2 \pm 0.1$ ) and DEA ( $0.224 \pm 0.005$ ) to TEA ( $0.19 \pm 0.04$ ). Moreover, response of MR-PA towards EA, DEA, and TEA is practically not reversible as just 0.5 - 13% signal reduction is observed even after three days in amine free atmosphere. In addition, response times of sensor textile MR-PA increase from EA (17 min) to DEA (31 min), and TEA (209 min).

By comparing parameters of DMA and TMA a higher signal change is observed for DMA ( $0.20 \pm 0.01$ ). For both amines reverse reactions are almost identical since 34 – 47% signal reduction was received after three days. However, a difference can be found comparing the reversibility of both reactions. While reverse reaction of TMA is finished within minutes, the signal of DMA decreases over a time span of three days. Response times behave similarly to DEA and TEA since response time for TMA (50 min) is clearly higher than for DMA (7 min).

Ammonia provokes a high maximum signal change of  $0.15 \pm 0.01$  and a complete reversibility of the reaction after three days (Figure E36). Moreover, ammonia has the shortest response time of all amines (6 min) being similar to DMA (7 min).

#### 4.5.4 Comparison of sensor responses to various amines

A crucial point for comparing signal responses of sensor textiles is the pH indication ranges of the sensor dyes or their  $pK_a$  values, respectively. Table E11 depicts the relevant pH ranges whereby cresol red exhibits a indication range at very high pH values (pH 6.5 - 8.5) followed by bromothymol blue (pH 5.8 – 7.6) and methyl red (pH 4.4 – 6.2). Since the pH range influences the reversibility of sensor responses based on the different states of equilibrium of indicator dyes, CR-PA is expected to exhibit the best reversibility. The extent of deprotonation of indicator dyes with high  $pK_a$  values by ammonia is less pronounced which might come along with a faster reverse reaction. Consequently, sensor fabric BTB-PA might exhibit a worse reversibility than CR-PA followed by MR-PA.

This assumption is confirmed by previously shown experiments. CR-PA exhibits the best reversibility when sensing amines (e.g. 75% signal recovery for TEA and 100% for TMA, see Table E9) while BTB-PA (25% for TEA, 59% for TMA, see Table E8) and MR-PA (12% for TEA, 47% for TMA, see Table E10) show significant lower values. Moreover, TMA induces better reversibility compared to TEA as is can be seen from all three sensor fabrics under study. This fact can be attributed to different  $pK_a$  values and/or sizes of the amines. The deprotonation of indicator dyes is more likely for TEA, since it exhibits a higher  $pK_a$ -value compared to TMA (Table E12). Moreover, TEA is a larger molecule which hampers its polyamide permeability. According to this explanation TEA should have a worse reversibility as well as longer response times. These facts are true for all sensor textiles as shown by Table E8, E9, and E10. The same trends are observed for the comparison of DEA and DMA.

**Table E11.** pH indication ranges of sensor dyes used for sensor fabric preparation. <sup>46</sup>

Sensor dye	pH indication range
Cresol red	6.5 – 8.5
Bromothymol blue	5.8 – 7.6
Methyl red	4.4 - 6.2

Direct information about the size dependency of analytes can be received for EA, DEA, and TEA. Since  $pK_a$ -values of all three amines are quite similar (Table E12), the response times of sensor textiles can give a direct indication of the size effects. Response times for DEA are slightly higher than for EA, being valid for all three sensor textiles. However, values for TEA are significantly higher in all of the three cases. E.g. response times are 22 min (EA), 26 min (DEA), and 186 min

(TEA) for CR-PA or 14 min (EA), 21 min (DEA), and 214 min (TEA) for BTB-PA, respectively. The results demonstrate a strong size dependency of response times which might be due to a worse permeability of polyamide for larger molecules.

Moreover, the hydrophilicity of analytes can also play a role and would emphasize the same result. Hydrophilicity decreases in the following order: ammonia > EA > DEA > TEA. Since polyamide is quite hydrophilic its permeability might also be higher for more hydrophilic molecules.

**Table E12.**  $pK_a$ -values of amines under study. <sup>47,48</sup>

Analyte	$pK_a$
EA	10.75
DEA	10.98
TEA	10.75
ammonia	9.24
DMA	10.71
TMA	9.81

Response times for TMA show also higher values compared to DMA. E.g. response times are 6 min for DMA and 69 min for TMA in case of CR-PA fabric (Table E9). This is surprising on the one hand since the  $pK_a$  of TMA (9.81) is lower compared to DMA (10.71). However, on the other hand it demonstrates that size and hydrophilicity are likely to have a stronger effect on the respective response times. Shortest response times are received for ammonia in all three sensor textiles. Ammonia represents the smallest and most hydrophilic molecule of the amines under study and, moreover has the lowest  $pK_a$ -value.

Consequently, the experiments give evidence that sensor responses are primarily dependent on analyte molecule size and/or hydrophilicity.  $pK_a$ -Values of amines play only a minor role with regard to response of the sensor textiles.



#### 4.6 Calibration of bromothymol blue dyed polyamide fabric with ethylamine, diethylamine, and triethylamine

Ethylamine (EA), diethylamine (DEA), and triethylamine (TEA) were further investigated to gain quantitative information on their detectability with the individual sensor textiles. For this purpose calibrations were performed with BTB-PA as it displays a suitable sensor textile regarding response time, limit of detection, and color change when exposed to ammonia (see chapter 4.1. and 4.2).

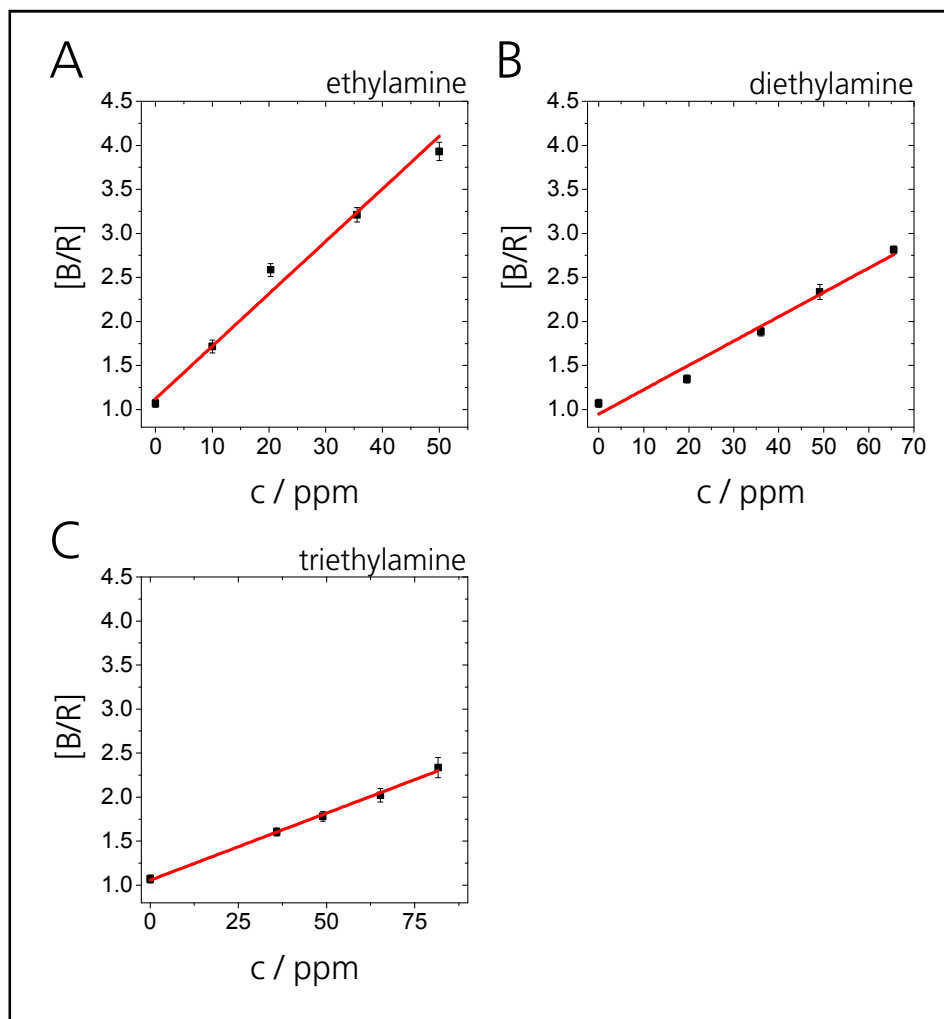


**Figure E37.** Calibration curves of BTB-PA sensor fabric with **A:** ethylamine, **B:** diethylamine, and **C:** triethylamine. Curves were fitted by linear fit functions. Saturation values of associated time-dependent curves were determined by calculating the mean of last ten data points (mean  $\pm$  SDM;  $N = 5$ ).

Measurements were performed in five replicates with amine concentrations of 0 to 80 ppm. Time dependent response curves of the investigated amine concentrations are depicted in Appendix (Figure G7 – G9). Saturation values were determined by calculating the mean of last ten data points. Afterwards, the obtained values were plotted against the amine concentrations

resulting in graphs depicted in Figure E37. Calibration curves were fitted with linear fit functions (Figure E37). The corresponding fit parameters are represented in Table E13. All calibration curves exhibit excellent coefficients of determination being 0.98 for EA, 0.97 for DEA, and 0.99 for TEA. Furthermore, time-dependent curves were fitted with logistic fit functions enabling determination of response times ( $t_{90}$ ) (for details see chapter 3.5). Parameters of logistic fit functions are represented in Appendix (Table G24 –G26).

**Table E13.** Linear fit function parameters of BTB-PA calibration with ethylamine (EA), diethylamine (DEA), and triethylamine (TEA).

Amine	Slope $\pm$ error / ppm <sup>-1</sup>	Intercept $\pm$ error	R <sup>2</sup>
EA	0.060 $\pm$ 0.004	1.12 $\pm$ 0.09	0.98
DEA	0.028 $\pm$ 0.002	0.9 $\pm$ 0.1	0.97
TEA	0.0152 $\pm$ 0.0005	1.06 $\pm$ 0.03	0.99

Limits of detection were calculated based on the parameters depicted in Table E14 (for details see chapter 3.5). Ethylamine displays a lower LOD than diethylamine and triethylamine (Table E14). Taking the calculated errors into account, LOD values for DEA and TEA are in the same range. The high difference between the LOD of EA (1  $\pm$  2 ppm) and those of DEA and TEA (9  $\pm$  4 ppm and 10  $\pm$  2 ppm) can be attributed amongst others to a higher slope of the EA linear calibration curve. Thus, sensitivity is higher for EA (0.060  $\pm$  0.004 ppm<sup>-1</sup>) compared to DEA (0.028  $\pm$  0.002 ppm<sup>-1</sup>) and TEA (0.0152  $\pm$  0.0005 ppm<sup>-1</sup>) (Table E14).

**Table E14.** Limits of detection, sensitivities, and response times  $t_{90}$  for calibration of BTB-PA with ethylamine (EA), diethylamine (DEA), and triethylamine (TEA). Response times  $t_{90}$  were calculated as time averages of the different amine concentrations (mean  $\pm$  SDM; N = 25).

Amine	LOD / ppm	Sensitivity / ppm <sup>-1</sup>	$t_{90}$ / min
EA	1 $\pm$ 2	0.060 $\pm$ 0.004	91 $\pm$ 19
DEA	9 $\pm$ 4	0.028 $\pm$ 0.002	182 $\pm$ 17
TEA	10 $\pm$ 2	0.0152 $\pm$ 0.0005	227 $\pm$ 5

Table E14 lists the response times ( $t_{90}$ ) which were calculated as mean of response times received from the five amine concentrations, since a concentration dependency was not observed in this case. While EA exhibits a  $t_{90}$  of  $91 \pm 19$  min, DEA and TEA reflect significantly higher values of  $182 \pm 17$  min and  $227 \pm 5$  min. Hence, an increase of response times is observed from EA to DEA and TEA which might attributed to the size increase and simultaneous decrease of hydrophilicity of the analyte molecules. This observation correlates well with the results presented in chapter 4.5.

In summary, the lowest LOD and response time was observed for EA whereas DEA and TEA exhibit similar LOD values. However, the response time is higher for TEA. The results are an evidence for a size-dependency of the sensor response as EA displays the smallest molecule, thus, permeating the polyamide fabric faster than DEA or TEA. Simultaneously, hydrophilicity decreases from EA to TEA which also influences the polymer permeability. Since polyamide is a relatively hydrophilic polymer it is better permeable for the more hydrophilic EA.

#### 4.7 Long-term stability of sensor textiles

Long-term stability is a crucial factor for the application of sensor textiles for work safety applications since short-term stabilities imply high costs for users. Moreover, commercialization becomes difficult if sensor textile applications or even whole working clothes need to be replaced after a short period of time.

Signal changes of BTB-PA, CR-PA, and MR-PA were investigated when exposed to ammonia in order to obtain information about the shelf-life of sensor textiles. Sensor textiles were immobilized into screw caps (see chapter 3.2) and the color change provoked by three different concentrations of ammonia was determined in time intervals of roughly one month. Concentrations were 22, 75, and 150 ppm ammonia whereas all measurements were performed in five replicates. Data evaluation was performed by the most suitable ratiometric calculation method (see chapter 4.1 and 4.2) and corresponding plots of sensor textiles are depicted in Figure E38. Thus,  $[B/R]$  was calculated for BTB-PA,  $[B/R]$  for CR-PA, and  $[G/R]$  for MR-PA sensor fabric.

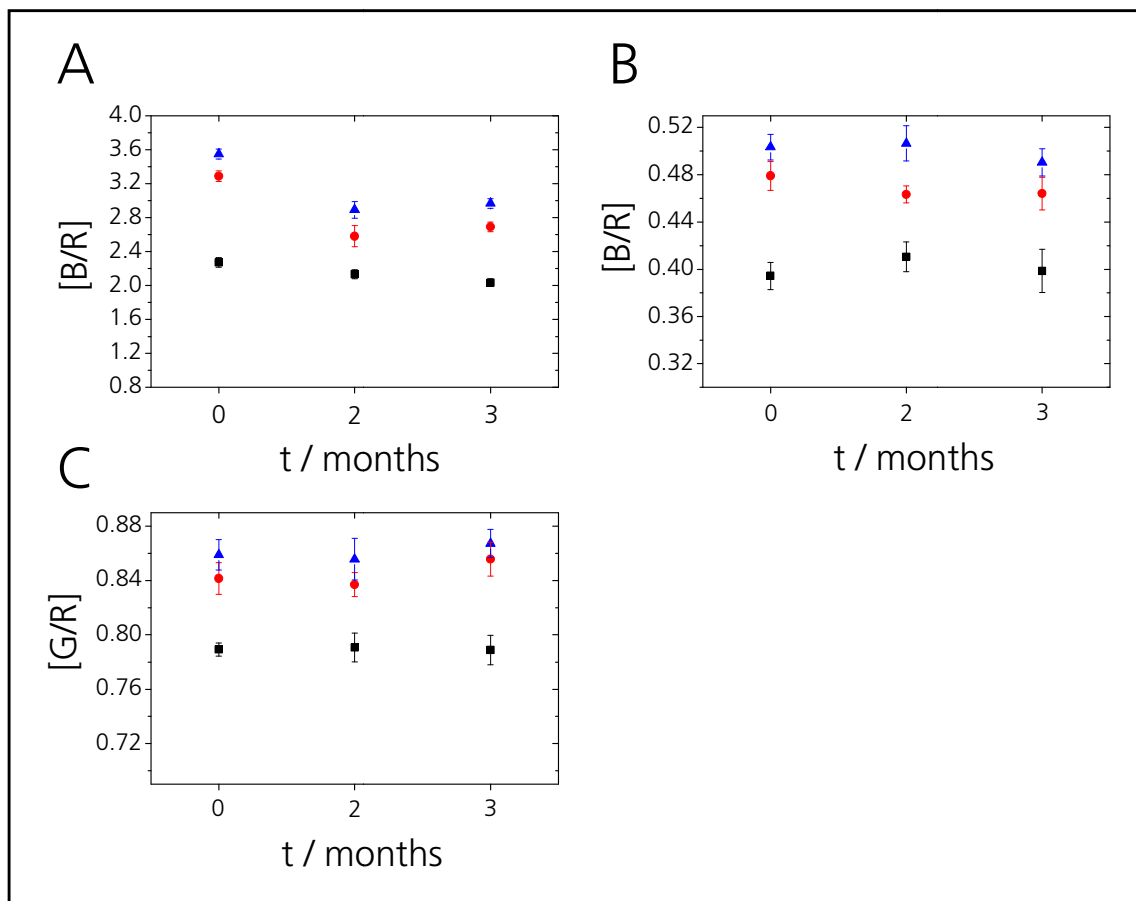


**Figure E38.** Plots represent the long-term stability of **A:** BTB-PA, **B:** CR-PA, and **C:** MR-PA. The sensor textiles were exposed to three different ammonia concentrations (22 ppm, ■, black; 75 ppm, ●, red; and 150 ppm, ▲, blue) over three months (mean  $\pm$  SDM; N = 5).

Signals are rather stable over three months for CR-PA (Figure E38, B) and MR-PA (Figure E38, C). Small alterations in signal intensities are due to errors originating from preparing and pipetting calibration solutions. Nevertheless, a stable signal was obtained for each ammonia concentration and no significant degradation of the two sensor textiles was observed.

However, sensor fabric BTB-PA shows a signal drop for 75 and 150 ppm ammonia after two or three months, respectively. The drop can be either provoked by the degradation of the sensor textile or by pipetting steps during the measurements. In the context of this assumption long-term stability investigation needs to be continued. However, this is not within the scope of this thesis.

## 5 Summary and conclusion

The preparation of three different sensor textiles for colorimetric detection of ammonia for work safety applications was described in this chapter. Commercially available pH indicator dyes bromothymol blue, cresol red, and methyl red were investigated for the dyeing of polyamide fabrics. For quantifying the color changes of the sensor textiles the design of an experimental setup for RGB imaging was accomplished. This setup consists of a custom-made calibration chamber with an integrated light source combined with a SLR camera. By automatic camera control digital color images were taken in defined time intervals with subsequent RGB color evaluation applying ratiometric analysis techniques.

Ammonia calibration measurements reveal limits of detection between 2 and 10 ppm depending on the sensor textile. Different methods for data evaluation were compared and verified regarding response times and limits of detection. Furthermore, reversibility studies of sensor responses towards ammonia were performed applying two different ammonia concentrations. All sensor fabrics exhibit response times between 10 and 14 minutes and all reactions were completely reversible after about 10 to 18 minutes.

Additionally, qualitative cross sensitivity studies of sensor textiles towards acetic and hydrochloric acid were carried out. Both acids provoke a response of sensor textiles which can be differentiated from ammonia response by naked eye since sensor textile exhibit different color changes depending on the respective analyte. Additionally, differentiation of individual, pure analytes is possible by evaluating RGB color information for all sensor textiles.

Finally, experiments on the cross sensitivities of the fabrics towards other amines were carried out for analyzing the influence of molecule size and hydrophilicity of the analytes in combination with the  $pK_a$ -values of indicator dyes. In this context an increase of response times was observed by increasing the analyte size or decreasing the hydrophilicity. Moreover, sensor reversibility highly depends on the indication range of pH indicators. A high  $pK_a$ -value causes higher sensor reversibility than indicator dyes with lower  $pK_a$ . Additionally, calibration with ethylamine, diethylamine, and triethylamine confirmed these observations.

Until now no sensor textiles are commercially available for signaling ammonia by colorimetric methods. Limits of detection lower than the ammonia threshold limit of 20 ppm and response times in the range of minutes were achieved by all sensor textiles under study. Thus, to the best of my knowledge, the sensor textiles developed here are the first ones practical for application.

## 6 References

- (1) LUBW Landesanstalt für Umwelt, Messungen und Naturschutz Baden-Württemberg, Ed. *Ammoniak in der Umwelt*, 2008.
- (2) Timmer, B.; Olthuis, W.; van Berg, A. d. *Sens. Actuators, B* **2005**, *107* (2), 666–677.
- (3) Rodríguez, A. J.; Zamarreño, C. R.; Matías, I. R.; Arregui, F. J.; Cruz, R. F. D.; May-Arrioja, D. A. *Sensors* **2014**, *14* (3), 4060–4073.
- (4) Bosoi, C. R.; Rose, C. F. *Metab. Brain Dis.* **2009**, *24* (1), 95–102.
- (5) Abel, T.; Ungerböck, B.; Klimant, I.; Mayr, T. *Chem. Cent. J.* **2012**, *6* (1), 124.
- (6) Courbat, J.; Briand, D.; Damon-Lacoste, J.; Wöllenstein, J.; Rooij, N. F. de. *Sens. Actuators, B* **2009**, *143* (1), 62–70.
- (7) Mader, H. S.; Wolfbeis, O. S. *Anal. Chem.* **2010**, *82* (12), 5002–5004.
- (8) Trinkel, M.; Trettnak, W.; Reininger, F.; Benes, R.; O'Leary, P.; Wolfbeis, O. S. *Anal. Chim. Acta* **1996**, *320* (2-3), 235–243.
- (9) Peeters, R.; Berden, G.; Apituley, A.; Meijer, G. *Appl. Phys. B: Lasers Opt.* **2000**, *71* (2), 231–236.
- (10) Sutar, D. S.; Padma, N.; Aswal, D. K.; Deshpande, S. K.; Gupta, S. K.; Yakhmi, J. V. *Sens. Actuators, B* **2007**, *128* (1), 286–292.
- (11) Vidotti, M.; Dall'Antonia, L. H.; Córdoba de Torresi, Susana I.; Bergamaski, K.; Nart, F. C. *Anal. Chim. Acta* **2003**, *489* (2), 207–214.
- (12) Ip, Y. K.; Chew, S. F.; Wilson, J. M.; Randall, D. J. *J. Comp. Physiol., B* **2004**, *174* (7), 565–575.
- (13) Lin, Y.-C.; Chen, J.-C. *J. Exp. Mar. Biol. Ecol.* **2001**, *259* (1), 109–119.
- (14) Werner, T.; Klimant, I.; Wolfbeis, O. S. *Analyst* **1995**, *120* (6), 1627.
- (15) Pyatt, F. B. *J. Occup. Environ. Med.* **2003**, *60* (12), 986–988.
- (16) Sazhin, S. G.; Soborover, E. I.; Tokarev, S. V. *Russ. J. Nondestr. Test.* **2003**, *39* (10), 791–806.
- (17) Galbarra, D.; Arregui, F. J.; Matias, I. R.; Claus, R. O. *Smart Mater. Struct.* **2005**, *14* (4), 739–744.
- (18) Jin, Z.; Su, Y.; Duan, Y. *Sens. Actuators, B* **2001**, *72* (1), 75–79.
- (19) Chabukswar, V.; Pethkar, S.; Athawale, A. A. *Sens. Actuators, B* **2001**, *77* (3), 657–663.
- (20) Castrellon-Urbe, J.; Nicho, M. E.; Reyes-Merino, G. *Sens. Actuators, B* **2009**, *141* (1), 40–44.
- (21) Kosterev, A. A.; Tittel, F. K. *Appl. Opt.* **2004**, *43* (33), 6213.
- (22) Claps, R.; Englich, F. V.; Leleux, D. P.; Richter, D.; Tittel, F. K.; Curl, R. F. *Appl. Opt.* **2001**, *40* (24), 4387.
- (23) Gauglitz, G. *Anal. Bioanal. Chem.* **2005**, *381* (1), 141–155.
- (24) Stich, Matthias I. J.; Nagl, S.; Wolfbeis, O. S.; Henne, U.; Schaeferling, M. *Adv. Funct. Mater.* **2008**, *18* (9), 1399–1406.

- (25) Waich, K.; Borisov, S.; Mayr, T.; Klimant, I. *Sens. Actuators, B* **2009**, *139* (1), 132–138.
- (26) Lobnik, A.; Wolfbeis, O. S. *Sens. Actuators, B* **1998**, *51* (1-3), 203–207.
- (27) Vasileiadis, M.; Athanasekos, L.; Meristoudi, A.; Alexandropoulos, D.; Mousdis, G.; Karoutsos, V.; Botsialas, A.; Vainos, N. A. *Opt. Lett.* **2010**, *35* (9), 1476–1478.
- (28) Wolfbeis, O. S. *Anal. Chem.* **2006**, *78* (12), 3859–3874.
- (29) Delmarre, D.; Bied-Charreton, C. *Sens. Actuators, B* **2000**, *62* (2), 136–142.
- (30) Yimit, A.; Itoh, K.; Murabayashi, M. *Sens. Actuators, B* **2003**, *88* (3), 239–245.
- (31) Yimit, A.; Rossberg, A. G.; Amemiya, T.; Itoh, K. *Talanta* **2005**, *65* (5), 1102–1109.
- (32) von der Weiden, S. *Smarte Textilien überstehen selten den Waschgang*. 2013 [cited: 2015 october 17]; available from: <http://www.ingenieur.de/Themen/Chips-Sensoren/Smarte-Textilien-ueberstehen-selten-Waschgang>.
- (33) hi-fun. *hi-Call*. 2015 [cited: 2015 october 17]; available from: <http://www.hi-fun.com/it/pagina/1547-hi-call-family>.
- (34) Weir, J. *Swany Texsys G-Cell Bluetooth Gloves*. 2008 [cited: 2015 october 17]; available from: <http://www.crunchwear.com/swany-texsys-g-cell-bluetooth-gloves/>.
- (35) KIT -Institut für Technik der Informationsverarbeitung. *Wearable Computing - Smart Clothes Technologien*. 2013 [cited: 2015 october 17]; available from: <https://www.itiv.kit.edu/218.php>.
- (36) Hochschule Niederrhein - FTB. *Textile Strukturen, Sensorik, Wissensmanagement, Simulation*. 2015 [cited: 2015 october 17]; available from: <http://www.hs-niederrhein.de/forschung/ftb/forschungsschwerpunkte/textile-strukturen-sensorik/>.
- (37) Handelsblatt. *Herz-Kreislauf-Monitoring für Jogger - Mobile EKG-Messung per T-Shirt und Handy*. 2004 [cited: 2015 october 17]; available from: <http://www.handelsblatt.com/technik/it-internet/herz-kreislauf-monitoring-fuer-jogger-mobile-ekg-messung-per-t-shirt-und-handy/2303300.html>.
- (38) Kreiszeitung. *Intelligente Kleidung schützt*. 2011 [cited: 2015 october 17]; available from: <http://www.kreiszeitung.de/lokales/bremen/intelligente-kleidung-schuetzt-1196815.html>.
- (39) Dietl J. *Intelligente Schutzkleidung aus Bremen - Neue Latzhose "Horst" schützt Waldarbeiter*. 2012 [cited: 2015 october 17]; available from: [http://www.weser-kurier.de/bremen/bremen-stadtreport\\_artikel,-Neue-Latzhose-Horst-schuetzt-Waldarbeiter-\\_arid,107886.html](http://www.weser-kurier.de/bremen/bremen-stadtreport_artikel,-Neue-Latzhose-Horst-schuetzt-Waldarbeiter-_arid,107886.html).
- (40) Hövding. *Airbag für Radfahrer*. 2015 [cited: 2015 october 17]; available from: [http://www.hovding.de/?utm\\_expId=37988497-0.onzg4jq0RsKvXrgwOlw3lw.0](http://www.hovding.de/?utm_expId=37988497-0.onzg4jq0RsKvXrgwOlw3lw.0).
- (41) Velo Plus. *Velo Plus - Ausrüstung für Abenteuer*. 2015 [cited: 2015 october 17]; available from: <http://www.veloplus.ch/alleprodukte/velohelme.aspx>.
- (42) Waak, A. - Die Welt. *Im Test – der Airbag-Helm für Radfahrer*. 2014 [cited: 2015 october 18]; available from: <http://www.welt.de/icon/article128104218/Im-Test-der-Airbag-Helm-fuer-Radfahrer.html>.

- (43) Fraunhofer IZM. *Textilintegrierte elektronische Systeme*. 2015 [cited: 2015 october 17]; available from: [http://www.izm.fraunhofer.de/de/abteilungen/system\\_integrationinterconnectiontechnologies/arbeitsgebiete/elektronikintegrationinalternativmaterialien/projekte/integration\\_von\\_elektronikintextilien.html](http://www.izm.fraunhofer.de/de/abteilungen/system_integrationinterconnectiontechnologies/arbeitsgebiete/elektronikintegrationinalternativmaterialien/projekte/integration_von_elektronikintextilien.html).
- (44) Infineon. *Wearable Electronics - umfangreiche Expertise in Halbleiterfertigungs- und Verbindungstechnik ermöglicht robuste und zuverlässige Chip-Integration*. 2002 [cited: 2015 october 17]; available from: <http://www.infineon.com/cms/de/about-infineon/press/press-releases/2002/130751.html>.
- (45) Infineon. *Wearable Electronics - umfangreiche Expertise in Halbleiterfertigungs- und Verbindungstechnik ermöglicht robuste und zuverlässige Chip-Integration*. 2002 [cited: 2015 october 17]; available from: [http://interactive-wear.de/cms/front\\_content.php?idcat=49&idart=52](http://interactive-wear.de/cms/front_content.php?idcat=49&idart=52).
- (46) Merck KGaA. *pH-Tests im Überblick*. 2005 [cited: 2015 october 30]; available from: [http://www.mibius.de/out/oxbaseshop/html/0/images/wysiwigpro/pH\\_Brosch\\_d%281%29.pdf](http://www.mibius.de/out/oxbaseshop/html/0/images/wysiwigpro/pH_Brosch_d%281%29.pdf).
- (47) Papandreu, G.; Tong, M. K.; Ganem, B. J. *Am. Chem. Soc.* **1993**, 115 (25), 11682–11690.
- (48) Perrin, D. D.; Dempsey, B.; Serjeant, E. P. *pKa prediction for organic acids and bases*; Chapman and Hall: London, 1981.



## F Summary

### 1 Summary in English

The aim of this thesis was the development and characterization of colorimetric indicators for food and work safety applications. For this several immobilization techniques and measurement setups were examined.

The first part of this work discusses a novel application of Schiff's reagent as indicator for substances generated by the deterioration of fat-containing food. Here the indicator was immobilized on the surface of silica particles and was characterized analytically regarding its feasibility for the detection of hexanal as a quality indicator for fats. An experimental setup for measuring the color change by RGB readout was successfully designed and calibration measurements were performed for hexanal, propionaldehyde, and acetaldehyde. Based on these, the indicator was characterized regarding its limits of detection which was 0.5 ppm for hexanal and propionaldehyde and 1 ppm for acetaldehyde. Furthermore, the indicator particles showed an excellent long-term stability of at least 6 months. Cross sensitivity measurements were also investigated towards substances without aldehyde groups. By using a principal component analysis approach all compounds could be clearly distinguished from hexanal. Finally, in collaboration with Fraunhofer IVV, the indicator was immobilized in polyvinylacetate as matrix polymer and was successfully integrated into food packaging. Thus, further experiments on real food samples with high content of linoleic acid were conducted. As a result the indicator shows an excellent performance for detecting the rancidity of hazelnuts and peanuts. However, also limitations were observed since the detection of rancid sunflower oil is not possible due to insufficient volatilization of dissolved hexanal.

The second part of this thesis describes a colorimetric sensor for work safety applications. For this previously developed sensor systems for carbon monoxide were subjected to further analytical characterization and optimization. Here, two different Co(III)-corrole compounds were immobilized in matrix polymers, cast onto a transparent solid support, and studied towards their performance for carbon monoxide sensing. A suitable measurement setup was designed enabling an on-line monitoring of the absorbance changes and therefore, the characterization of the sensors. Developed sensor foils were stable for at least 120 min, and did not show any signs of photodegradation. They furthermore exhibited outstanding properties for carbon monoxide sensing in ambient air, with response times in the range of seconds and good reversibility. Both sensor systems exhibited limits of detection lower than the threshold limit in Germany (30 ppm) and no cross sensitivities towards CO<sub>2</sub> (up to 3000 ppm) and NO<sub>2</sub> (up to 10 ppm). The system

with CoTPFPC as sensor dye showed a slightly faster response (and best reversibility) whereas CoTDCPC provided a slightly lower detection limit for carbon monoxide. As a result two excellent CO sensors for different areas of application have been developed.

Another sensor for work safety application is finally presented in the third part of the thesis. Here, commercially available pH-indicator dyes were used as dyeing agents for polyamide fabrics. This enabled the production of intelligent sensor textiles for visualizing gaseous ammonia in working places. Quantifying the color of intelligent textiles was accomplished via a custom-built measurement setup and ratiometric evaluation of the RGB color channels here. Obtained sensor textiles were characterized by their response times, limits of detection, and reversibility. All sensor fabrics were found to exhibit good response times (10 - 14 min) and reversibility (10 - 18 min) for ammonia. Measurements of various other amines showed an increase of response times with increasing analyte size and decreasing hydrophilicity. The sensor reversibility also depends on the type of pH indicator. For all sensor textiles ammonia concentrations below the threshold (20 ppm) have been detected. In conclusion, the first practical application of sensor textiles for a colorimetric detection of gaseous ammonia has been presented.

## 2 Summary in German

Das Ziel der vorliegenden Arbeit war die Entwicklung und Charakterisierung kolorimetrischer Indikatoren für die Anwendung in der Lebensmittelkontrolle sowie im Arbeitsschutz. Dabei wurden sowohl verschiedene Techniken zur Farbstoffimmobilisierung, als auch verschiedene Messaufbauten zur Charakterisierung eingesetzt.

Der erste Teil dieser Arbeit beschäftigt sich mit neuen Anwendungsmöglichkeiten des Schiff's Reagenzes. Dieses wird als Indikator für den Nachweis von Substanzen angewendet, die durch den Verderb fetthaltiger Lebensmittel entstehen. Der Indikator wurde dafür auf der Oberfläche von Silikapartikeln immobilisiert und hinsichtlich der Einsatzmöglichkeiten zum Nachweis von Hexanal charakterisiert. Hexanal ist eine Substanz, die als Indikator für die Qualität und Frische von Fetten dient. Für die Messung des Farbwechsels wurde ein Messaufbau entwickelt, der die Dokumentation von RGB Farbwerten ermöglichte. Damit wurden Kalibrationsmessungen mit den Aldehyden Hexanal, Propionaldehyd und Acetaldehyd durchgeführt und der Indikator bezüglich seiner Detektionsgrenzen charakterisiert. Diese betrugen 0,5 ppm für Hexanal und Propionaldehyd und 1 ppm für Acetaldehyd. Die entwickelten Indikatorpartikel zeigen eine exzellente Langzeitstabilität von mindestens 6 Monaten. Darüberhinaus wurden Querempfindlichkeitsprüfungen gegenüber Substanzen durchgeführt, die keine Aldehyd-Gruppe tragen. Mit Hilfe einer Hauptkomponentenanalyse konnten dabei alle Substanzen klar von Hexanal unterschieden werden. In Kooperation mit Fraunhofer IVV wurden die Indikatorpartikel schließlich in Polyvinylacetat als Matrixpolymer eingebettet, in Lebensmittelverpackungen integriert und Untersuchungen an realen Lebensmittelproben mit hohem Gehalt an Linolsäure durchgeführt. Der Indikator zeigt herausragende Eigenschaften für die optische Anzeige ranziger Haselnüsse und Erdnüsse. Es stellte sich jedoch heraus, dass das kolorimetrische Indikatorsystem auch Grenzen in seiner Anwendung aufweist. In Sonnenblumenöl verflüchtigte sich das gebildete Hexanal nicht in ausreichender Menge, was eine Detektion nicht möglich machte.

Der zweite Teil der Arbeit beschreibt einen kolorimetrischen Sensor für die Anwendung im Bereich des Arbeitsschutzes. Dabei wurden Sensorsysteme angewendet, die bereits in früheren Arbeiten untersucht wurden. Diese wurden optimiert und analytisch charakterisiert. Zwei verschiedene Co(III)-Corrole wurden dabei als Sensorfarbstoffe eingesetzt und in Matrixpolymere immobilisiert. Anschließend wurden transparente Trägersubstanzen mit diesen Farbstoff-Polymer-Mischungen beschichtet und die Eigenschaften der dadurch hergestellten Sensorfolien als Kohlenstoffmonoxid-Sensoren getestet. Dafür wurde ein geeigneter Messaufbau für die on-line Dokumentation von Absorbanzänderungen entwickelt. Die hergestellten Sensorfolien waren mindestens 120 Minuten stabil und zeigten keinerlei Anzeichen von Fotoalterung. Darüberhinaus waren sie hervorragend zum Nachweis von Kohlenstoffmonoxid in Umgebungsluft geeignet. Beide Sensorsysteme wiesen Ansprechzeiten im Sekundenbereich, gute Reversibilität und

Nachweisgrenzen unter dem Arbeitsplatzgrenzwert in Deutschland von 30 ppm auf. Außerdem zeigten sie keine Querempfindlichkeiten gegenüber CO<sub>2</sub> (bis zu 3000 ppm) und NO<sub>2</sub> (bis zu 10 ppm). Das Sensorsystem mit dem Farbstoff CoTPFPC wies eine etwas schnellere Ansprechzeit und eine bessere Reversibilität auf, wobei das System mit CoTDCPC eine geringere Nachweisgrenze hat. Dadurch wurden zwei hervorragende CO-Sensoren entwickelt, die für verschiedene Einsatzgebiete geeignet sind.

Abschließend wird im dritten Teil der Arbeit ein weiterer Sensor für die Anwendung im Arbeitsschutz vorgestellt. Hierbei wurden kommerziell erhältliche pH-Indikatoren zum Färben von Polyamidtextilien eingesetzt. Dadurch wurden intelligente Textilien zur Visualisierung von gasförmigem Ammoniak hergestellt. Die Quantifizierung des Farbumschlages der Sensortextilien wurde durch einen selbst entwickelten Messaufbau ermöglicht, durch den RGB Farbkanäle ratiometrisch ausgewertet werden konnten. Die hergestellten Sensortextilien wurden hinsichtlich ihrer Ansprechzeit, Nachweisgrenzen und ihrer Reversibilität untersucht. Alle Sensortextilien zeigten dabei gute Ansprechzeiten (10 -14 min) und Reversibilitäten (10 -18 min) gegenüber gasförmigem Ammoniak. Die Messung unterschiedlicher Amine zeigte darüberhinaus eine Erhöhung der Ansprechzeit mit steigender Molekülgröße und abnehmender Hydrophilität. Die Reversibilität des Sensors ist darüber hinaus auch abhängig von dem eingesetzten pH-Indikator. Mit allen Sensortextilien konnten Ammoniakkonzentrationen klar angezeigt werden, die sich unterhalb des Arbeitsplatzgrenzwertes von 20 ppm befinden. Im Rahmen dieses Projektes wurden die ersten Sensortextilien entwickelt, die für die kolorimetrische Anzeige von gasförmigem Ammoniak geeignet sind.

## G Appendix

### 1 Abbreviations and symbols

ATR	attenuated total reflection
[B/G]	intensity ratio of blue and green color channels
[B/R]	intensity ratio of blue and red color channels
BTB	bromothymol blue
BTB-PA	bromothymol blue dyed polyamide fabric
c	concentration
CCD	charge-coupled device
CDCl <sub>3</sub>	deuterated chloroform
CH <sub>4</sub>	methane
CHCl <sub>3</sub>	chloroform
CI-ELISA	competitive indirect enzyme-linked immunosorbant assay
cm	centimeter
cm <sup>2</sup>	square centimeter
CMOS	complementary metal-oxide-semiconductor
CO	carbon monoxide
CO <sub>2</sub>	carbon dioxide
Co(OAc) <sub>2</sub>	cobalt(II) acetate
CoTDCPC	5,10,15-[tris(2,6-dichlorophenyl)corrole] cobalt(III)
CoTPFPC	5,10,15-[tris(2,3,4,5,6-pentafluorophenyl)corrole] cobalt(III)
CR	cresol red
CR-PA	cresol red dyed polyamide fabric
DCM	dichloromethane
DDQ	2,3-dichloro-5,6-dicyano-1,4-benzoquinone
DEA	diethylamine
DIN	German Institute for Standardization
DMA	dimethylamine
DNPH	2,4-dinitrophenylhydrazine
DSC	differential scanning calorimetry
DSLR	digital single-lens reflex
EA	ethylamine
[e.d.]	euclidean distance

EE	ethyl aceate
EC	ethyl cellulose
ECG	electrocardiogram
Eq.	equation
equiv.	equivalents
ESR	electron spin resonance
FID	flame ionization detector
FRET	fluorescence resonance energy transfer
g	gramm
GC	gas chromatography
[G/R]	intensity ratio of green and red color channels
h	hour
HS	head-space
hPa	hectopascal (100 Pa)
HPLC	high performance liquid chromatography
Hz	hertz
IR	infrared
K	Kelvin
Kg	kilogram ( $10^3$ gram)
kJ	kilojoule ( $10^3$ joule)
LDPE	low-density polyethylene
lm	lumen
LOD	limit of detection
LOI	limit of identification
LOQ	limit of quantification
LUMO	lowest unoccupied molecular orbital
$\lambda_{\max}$	absorption maximum
m	mass
M	molar concentration (mol/l)
m <sup>2</sup>	square meter
Mb-CO	carboxy-myoglobin
MeOH	methanol
mg	milligram ( $10^{-3}$ gram)
MgSO <sub>4</sub>	magnesium sulfate
MHz	megahertz ( $10^6$ hertz)
min	minutes

ml	milliliter ( $10^{-3}$ liter)
mm	millimeter ( $10^{-3}$ meter)
mM	millimolar ( $10^{-3}$ mol/l)
mol	mole
MR	methyl red
MR-PA	methyl red dyed polyamide fabric
MS	mass spectrometry
$M_w$	molecular weight
$\mu\text{g}$	microgram ( $10^{-6}$ gram)
$\mu\text{L}$	microliter ( $10^{-6}$ liter)
N	number
$\text{NH}_3$	ammonia
$\text{NH}_4\text{NO}_3$	ammonium nitrate
$(\text{NH}_4)_2\text{SO}_4$	ammonium sulfate
NIR	near infrared
nm	nanometer ( $10^{-9}$ meter)
NMR	nuclear magnetic resonance
$\text{NO}_2$	nitrogen dioxide
$\text{NO}_3^-$	nitrate
$\text{NO}_x$	mono-nitrogen oxides
$\text{O}_2$	oxygen
OSI	oil stability index
Pa	pascale
PA	polyamide
<i>p</i> -AnV	<i>p</i> -anisidine value
PANI	polyaniline
PA/PE	polyamide/polyethylene
PE	petroleum ether
PET	polyethylene terephthalate
poly(TMSP)	poly[1-(trimethylsilyl)-1-propyne]
ppb	parts per billion
ppm	parts per million
PS	polystyrene
PTFE	polytetrafluoroethylene
PV	peroxide value
PVA	polyvinylacetate
PVC	polyvinylchloride

r	Pearson product-moment correlation coefficient
R <sup>2</sup>	coefficient of determination
R <sub>a</sub>	color rendering index
[R/G]	intensity ratio of red and green color channels
RGB	red, green, blue
rpm	revolutions per minute
r.t.	room temperature
s	second
sccm	standard cubic centimeter per minute
SD	standard deviation
SDM	standard deviation of the mean
SH <sub>2</sub>	hydrogen sulfide
SLR	single-lens reflex
SnO <sub>2</sub>	tin dioxide
SO <sub>2</sub>	sulfur dioxide
SR@Si	Schiff's reagent adsorbed on surface of silica particles
t	time
T	temperature
t <sub>80</sub> , t <sub>90</sub>	time until 80% (90%) of overall signal change is achieved
TaCl <sub>5</sub>	tantalum pentachloride
TBA	thiobarburic acid
TDCPC	5,10,15-tris(2,6-dichlorophenyl)corrole
TEA	triethylamine
TFA	trifluoroacetic acid
TG	thermogravimetry
THF	tetrahydrofuran
TiO <sub>2</sub>	titanium dioxide
TLC	thin layer chromatography
TMA	trimethylamine
TPFPC	5,10,15-tris(2,3,4,5,6-pentafluorophenyl)corrole
UV	ultraviolet
V	volume
Vis	visible
W	watt
wt	weight
YFT	yellow fluorescent protein
% (w/v)	weight per volume



## 2 Reagents and materials

1,2,3,4,5-Pentafluorobenzaldehyde	Sigma Aldrich CHEMIE GmbH, Steinheim
2,6-Dichlorobenzaldehyde	Sigma Aldrich CHEMIE GmbH, Steinheim
Acetaldehyde	Sigma Aldrich CHEMIE GmbH, Steinheim
Acetic Acid	Carl Roth GmbH + Co KG, Karlsruhe
Ammonium hydroxide 28-30%	Sigma Aldrich CHEMIE GmbH, Steinheim
Bromothymol blue	Sigma Aldrich CHEMIE GmbH, Steinheim
Chloroform 99% p.a.	Carl Roth GmbH + Co KG, Karlsruhe
Cobalt(II) acetate dihydrate	Sigma Aldrich CHEMIE GmbH, Steinheim
Cresol red	Sigma Aldrich CHEMIE GmbH, Steinheim
DDQ	Sigma Aldrich CHEMIE GmbH, Steinheim
Deuterated chloroform 99.8 atom% D	Carl Roth GmbH + Co KG, Karlsruhe
Dichloromethane 99% p.a.	Carl Roth GmbH + Co KG, Karlsruhe
Diethylamine 99.5 %	Sigma Aldrich CHEMIE GmbH, Steinheim
Dimethylamine solution 40 wt%	Sigma Aldrich CHEMIE GmbH, Steinheim
Ethanol 99.8% p.a.	Carl Roth GmbH + Co KG, Karlsruhe
Ethylcellulose (49% ethoxy content)	Sigma Aldrich CHEMIE GmbH, Steinheim
Ethyl acetate 99.5% p.a.	Carl Roth GmbH + Co KG, Karlsruhe
Ethylamine solution 70 wt%	Sigma Aldrich CHEMIE GmbH, Steinheim
Formic Acid	Sigma Aldrich CHEMIE GmbH, Steinheim
Hexan 99% p.a.	Carl Roth GmbH + Co KG, Karlsruhe
Hexanal 98%	abcr GmbH, Karlsruhe
Hydrochloric Acid 37%	VWR International GmbH, Darmstadt
Imacol PAM	J .G. Knopf's Sohn GmbH, Helmbrechts
Lyogen NH	J .G. Knopf's Sohn GmbH, Helmbrechts
Methanol 99.9% p.a.	Carl Roth GmbH + Co KG, Karlsruhe
Methyl red	Sigma Aldrich CHEMIE GmbH, Steinheim
Petroleum ether 40-60°C, p.a.	Carl Roth GmbH + Co KG, Karlsruhe
Polystyrene	Carl Roth GmbH + Co KG, Karlsruhe
Polyvinylacetate ( $M_w = 55000-70000$ g/mol)	Carl Roth GmbH + Co KG, Karlsruhe
Propionaldehyde 97%	Sigma Aldrich CHEMIE GmbH, Steinheim
Pyrrole	Sigma Aldrich CHEMIE GmbH, Steinheim
Schiff's reagent for microscopy	Sigma Aldrich CHEMIE GmbH, Steinheim
Silica Gel (0.06-0.2 mm)	Carl Roth GmbH + Co KG, Karlsruhe
Sodium hydroxide	Merck KGaA, Darmstadt

Sodium dihydrogenphosphate dihydrate	Sigma Aldrich CHEMIE GmbH, Steinheim
Tantal pentachloride	Sigma Aldrich CHEMIE GmbH, Steinheim
Tetrahydrofuran 99.5% p.a.	Carl Roth GmbH + Co KG, Karlsruhe
Toluene 99.5% p.a.	Carl Roth GmbH + Co KG, Karlsruhe
Triethylamine 99.5%	Sigma Aldrich CHEMIE GmbH, Steinheim
Trifluoroacetic acid 99%	Sigma Aldrich CHEMIE GmbH, Steinheim
Trimethylamine solution 45 wt%	Sigma Aldrich CHEMIE GmbH, Steinheim
[1-(trimethylsilyl)-1-propyne]	Sigma Aldrich CHEMIE GmbH, Steinheim

### 3 Instrumentation and consumable

Argon (100%)	Linde AG, Munich
Carbon dioxide (3000 ppm in synthetic air)	Linde AG, Munich
Carbon monoxide (10% in nitrogen)	Linde AG, Munich
Carbon monoxide (300 ppm in synthetic air)	Linde AG, Munich
Drying oven (Heraeus Oven T6)	Thermo Scientific, Braunschweig
HPLC-Vials (1.5 mL, 32 x 11.6 mm)	VWR International, Darmstadt
Nitrogen dioxide (10 ppm in synthetic air)	Linde AG, Munich
Mylar®-foil (thickness of 125 µm)	Goodfellow GmbH, Bad Nauheim
PTFE tape (width 1 cm, thickness 100 µm)	Bauhaus, Regensburg
Screw caps (8 mm screw cap, PP black, centre hole, silicone blue/PTFE white 45°, 1.3 mm)	VWR International, Darmstadt
Tube rotator (fixed rotation speed at 18 rpm)	VWR International, Darmstadt
Ultrasonic bath (USC600T)	VWR International, Darmstadt
pH meter (pH 211 Microprocessor pH Meter)	HANNA Instruments, Vöhringen
Synthetic air (80% N <sub>2</sub> , 20% O <sub>2</sub> )	Linde AG, Munich

### 4 Software

DigiCamControl	<a href="http://digicamcontrol.com/">http://digicamcontrol.com/</a>
Image J	<a href="http://imagej.nih.gov/ij/">http://imagej.nih.gov/ij/</a>
Origin 8.5 and Origin 9	<a href="http://www.originlab.de">www.originlab.de</a>

## 5 Supplementary figures and tables

**Table G1.** Mass of water determined for the quantification of total volume of glass vials. Vials were weighed, completely filled with distilled water and reweighed since the mass of water is directly proportional to the vial volume ( $\rho_{\text{water}} = 1 \text{ mg/mL}$ ). The procedure was performed for a total of five glass vials and repeated three times for each vial.

	1 <sup>st</sup> Measurement m / mg	2 <sup>nd</sup> Measurement m / mg	3 <sup>rd</sup> Measurement m / mg
Vial 1	1.8181	1.7997	1.7901
Vial 2	1.8452	1.8222	1.8051
Vial 3	1.8319	1.8434	1.8234
Vial 4	1.8310	1.8330	1.8131
Vial 5	1.8515	1.8524	1.8347

**Table G2.** Logistic fit function parameters of time-dependent increase of signal [B/R] during reaction of indicator particles SR@Si 2 with different concentrations of hexanal (4-250 ppm).

c(hexanal) / ppm	Chi Squ	R <sup>2</sup>	A1	σ(A1)	A2	σ(A2)	x0	σ(x0)	p	σ(p)
4	1.80927	0.97319	0.79342	0.00405	0.97757	0.00536	72.81364	1.77806	7.41053	1.19129
14	0.67170	0.99419	0.82785	0.00217	1.11939	0.00426	61.71085	1.24282	6.64523	0.71322
23	0.96816	0.99735	0.78992	0.00660	1.30641	0.00658	47.80679	0.93008	2.36415	0.11917
33	0.99500	0.99388	0.81861	0.00276	1.30558	0.00898	60.59928	0.95301	5.58885	0.37930
44	1.87809	0.99363	0.85552	0.00493	1.47323	0.00947	35.71904	1.23833	3.13835	0.27028
55	0.48012	0.99892	0.84553	0.00240	1.51310	0.00661	50.95544	0.40937	2.92062	0.07314
110	1.82467	0.99314	0.87711	0.00654	1.58556	0.01294	35.60856	0.98035	3.46415	0.27620
150	0.60687	0.99881	0.87041	0.00290	1.56279	0.00379	29.39526	0.38981	3.14593	0.10780
200	0.28813	0.99893	0.87607	0.00140	1.59760	0.00483	32.21024	0.47486	3.04714	0.08568
250	0.33003	0.99865	0.89390	0.00301	1.65443	0.00610	26.20364	0.42241	2.51301	0.07682

**Table G3.** Logistic fit function parameters of time-dependent increase of signal [B/G] during reaction of indicator particles SR@Si<sub>2</sub> with different concentrations of hexanal (4–250 ppm).

c(hexanal) / ppm	Chi Squ	R <sup>2</sup>	A1	σ(A1)	A2	σ(A2)	x0	σ(x0)	p	σ(p)
4	2.49006	0.40796	1.34349	0.02449	1.44213	0.00955	33.36440	2.93773	24.27013	34.23757
14	0.64097	0.99802	1.15224	0.00258	1.70811	0.00589	32.09315	0.63515	2.73206	0.14649
23	0.16925	0.99562	1.31351	0.01946	2.00494	0.01144	27.78306	0.90140	1.93855	0.13899
33	0.43489	0.99638	1.15224	0.00213	2.25477	0.02754	46.66586	1.46204	2.38215	0.10057
44	0.14869	0.99755	1.14903	0.00235	2.54534	0.02195	20.21998	0.42969	2.15776	0.14923
55	0.36670	0.99665	1.23512	0.01367	2.65995	0.02211	40.39372	0.72597	2.40641	0.11606
110	0.78019	0.99477	1.16613	0.00635	3.12007	0.04057	26.39369	1.27632	2.05110	0.11992
150	2.76682	0.99077	1.20211	0.00417	2.75877	0.03761	23.84785	1.17982	2.15804	0.15014
200	0.91109	0.98974	1.13514	0.00328	3.23302	0.06402	31.43333	1.84555	1.84241	0.08789
250	0.18298	0.99687	1.19697	0.00753	3.28585	0.02860	22.75523	0.57301	2.23375	0.09229

**Table G4.** Logistic fit function parameters of time-dependent increase of signal [e.d.] during reaction of indicator particles SR@Si 2 with different concentrations of hexanal (4-250 ppm).

c(hexanal) ppm	Chi Squ	R <sup>2</sup>	A1	σ(A1)	A2	σ(A2)	x0	σ(x0)	p	σ(p)
4	0.57242	0.92297	0.51760	2.42105	41.42807	0.69137	26.92523	1.31874	5.16541	1.30607
14	0.30455	0.99240	-0.11926	1.69632	85.50627	0.84925	37.64499	0.92290	2.85445	0.16162
23	0.02724	0.99940	0.30112	0.52491	115.98147	0.35381	19.57759	0.20215	1.63991	0.02647
33	0.53625	0.99303	-0.24587	2.21894	121.80572	1.08056	38.74616	0.80405	3.03803	0.16096
44	0.41712	0.99390	2.99190	1.99194	146.10965	1.60451	11.75999	0.57517	1.21272	0.07087
55	0.33456	0.99630	-1.20846	1.74515	136.77511	0.83832	25.69837	0.50717	2.13564	0.07772
110	0.12010	0.99875	1.00007	1.09240	158.46402	0.51146	14.93566	0.22025	1.76877	0.03962
150	0.13832	0.99885	2.22275	0.97781	153.93788	0.43512	15.58636	0.20842	1.84598	0.03874
200	0.05455	0.99954	2.02366	0.57969	153.24417	0.27161	17.42965	0.13811	2.11716	0.02978
250	0.02779	0.99975	-0.04846	0.48158	157.80743	0.22119	13.16215	0.09356	1.78157	0.01892

**Table G5.** Logistic fit function parameters of time-dependent increase of signal [B/R] during reaction of indicator particles SR@Si 2 with different concentrations of propionaldehyde (4-252 ppm).

c(propion- aldehyde) / ppm	Chi Squ	R <sup>2</sup>	A1	σ(A1)	A2	σ(A2)	x0	σ(x0)	p	σ(p)
4	6.01745	0.76165	0.83384	0.00467	0.90255	0.00428	69.67990	6.36627	6.98983	3.88835
9	0.55371	0.99290	0.87893	0.00124	0.98108	0.00128	63.55102	1.24390	4.81960	0.40375
13	1.06805	0.93777	0.89460	0.00404	0.99195	0.00173	36.00492	2.40242	5.47691	1.52233
24	0.45587	0.97600	0.88607	0.00313	1.08123	0.00589	15.98574	1.30812	1.64253	0.20343
35	2.85547	0.97893	0.88777	0.00806	1.21627	0.00854	15.04668	0.88016	1.30908	0.10475
47	0.21657	0.99809	0.88464	0.00221	1.40214	0.01078	26.82990	1.20384	1.13871	0.03772
75	1.28388	0.99558	0.88414	0.00543	1.44982	0.00459	12.89750	0.41581	1.76782	0.09747
110	0.33710	0.99841	0.88226	0.00277	1.58218	0.00791	12.24291	0.39005	1.18176	0.02678
151	1.56556	0.99650	0.88481	0.00599	1.56990	0.00405	5.85866	0.28048	1.73323	0.10424
200	0.14782	0.99959	0.88361	0.00183	1.62605	0.00309	5.22817	0.11450	1.15358	0.02143
252	0.10967	0.99964	0.88413	0.00159	1.67499	0.00286	3.64429	0.07934	1.26175	0.02690

**Table G6.** Logistic fit function parameters of time-dependent increase of signal [B/G] during reaction of indicator particles SR@Si 2 with different concentrations of propionaldehyde (4-252 ppm).

c(propion- aldehyde) / ppm	Chi Squ	R <sup>2</sup>	A1	σ(A1)	A2	σ(A2)	x0	σ(x0)	p	σ(p)
4	26.05166	0.65680	1.15186	0.01650	1.34056	0.01287	3.25964	0.89442	4.77629	13.19117
9	0.44483	0.99832	1.15203	0.00213	1.66536	0.00442	14.92484	0.27153	2.17049	0.06417
13	0.75905	0.99649	1.15233	0.00281	1.79364	0.01181	12.37500	0.36119	1.90576	0.07317
24	0.47407	0.99216	1.15156	0.00222	1.89908	0.01122	7.47748	0.39719	2.29032	0.20536
35	0.21563	0.99765	1.15191	0.00150	2.23662	0.00907	10.17135	0.36806	2.19137	0.12015
47	0.05956	0.99916	1.15191	0.00079	2.83253	0.01498	12.87750	0.30031	1.43752	0.02993
75	1.21360	0.99634	1.15238	0.00355	3.09215	0.01969	9.64129	0.20786	2.93107	0.09248
110	0.09785	0.99911	1.15185	0.00101	3.55947	0.01541	6.49312	0.13080	1.90799	0.04498
151	1.59048	0.99311	1.15186	0.00408	3.38796	0.03243	3.72666	0.25304	3.05038	0.73487
200	1.74687	0.99351	1.15191	0.00427	3.16157	0.03284	2.18031	0.15343	1.97987	0.15921
252	2.14146	0.99367	1.15190	0.00473	3.91411	0.04097	2.25582	0.20995	2.01143	0.20401



**Table G7.** Logistic fit function parameters of time-dependent increase of signal [e.d.] during reaction of indicator particles SR@Si 2 with different concentrations of propionaldehyde (4-252 ppm).

c(propion- aldehyde) / ppm	Chi Squ	R <sup>2</sup>	A1	σ(A1)	A2	σ(A2)	x0	σ(x0)	p	σ(p)
4	4.68783	0.60856	0.88882	6.90579	50.68515	1.48453	4.63709	1.16115	3.55320	2.26745
9	0.09863	0.99730	0.33289	0.94704	93.18408	0.33932	15.44199	0.28323	2.18253	0.06881
13	0.18993	0.99416	0.54434	1.39074	104.04749	0.52570	10.04915	0.28884	1.96357	0.09414
24	0.01854	0.99957	0.22850	0.42712	123.68012	0.15468	7.34578	0.07293	1.57917	0.01970
35	0.29778	0.99474	-1.51315	1.72817	132.37703	0.52832	9.34909	0.28621	1.88193	0.07868
47	0.00694	0.99988	-0.04299	0.26681	148.52700	0.13109	5.89887	0.03829	1.25120	0.00972
75	0.95989	0.98838	-2.93531	3.09221	154.59408	0.69695	7.21462	0.30174	2.15444	0.13468
110	0.02011	0.99973	-0.07416	0.45426	164.83533	0.15203	2.99429	0.03339	1.26141	0.01499
151	0.07538	0.99890	-0.06773	0.87976	162.26219	0.31047	2.11509	0.06358	1.16779	0.03420
200	0.00404	0.99995	-0.02934	0.20365	165.62555	0.06100	1.39080	0.00757	1.12648	0.00541
252	0.04258	0.99944	-0.05854	0.66114	164.40783	0.20304	1.15308	0.02147	1.08898	0.01904

**Table G8.** Logistic fit function parameters of time-dependent increase of signal [B/R] during reaction of indicator particles SR@Si 2 with different concentrations of acetaldehyde (4–252 ppm).

c(acet- aldehyde) / ppm	Chi Squ	R <sup>2</sup>	A1	σ(A1)	A2	σ(A2)	x0	σ(x0)	p	σ(p)
4	4.77416	0.31684	0.85694	0.00787	0.90352	0.01120	83.68027	11.76652	9.91027	12.56295
8	26.29103	0.65510	0.83755	0.00846	0.90752	0.01012	78.73423	21.30652	6.15598	7.51077
13	18.27956	0.42435	0.86817	0.00815	0.92000	0.01010	80.03417	12.24697	8.74810	11.19295
24	0.79970	0.91850	0.89276	0.00236	0.95145	0.00160	50.23678	2.41576	7.80283	2.51422
35	0.50838	0.92590	0.88760	0.00238	0.94596	0.00210	39.21940	1.74994	12.58893	6.45915
47	0.63555	0.85365	0.95077	0.00312	1.00697	0.00249	31.75652	1.37094	10.68240	4.01614
76	0.33746	0.99407	0.88442	0.00278	1.27885	0.01480	12.38634	1.24653	1.14514	0.10252
110	1.40649	0.98216	0.88740	0.00563	1.34553	0.01701	11.43289	1.00140	1.23849	0.10781
142	0.48156	0.99769	0.88462	0.00332	1.54329	0.01305	12.88413	0.61015	1.18744	0.05479
171	0.04221	0.99969	0.88383	0.00431	1.58784	0.00398	8.60356	0.14919	1.39845	0.02320
197	2.13625	0.99115	0.88724	0.00692	1.48494	0.00897	7.55053	0.40650	1.70740	0.16252
252	0.19653	0.99948	0.88353	0.00212	1.63777	0.00302	7.73474	0.11167	1.76066	0.03446

**Table G9.** Logistic fit function parameters of time-dependent increase of signal [B/G] during reaction of indicator particles SR@Si 2 with different concentrations of acetaldehyde (8-252 ppm).

c(acet- aldehyde) / ppm	Chi Squ	R <sup>2</sup>	A1	σ(A1)	A2	σ(A2)	x0	σ(x0)	p	σ(p)
4	-	-	-	-	-	-	-	-	-	-
8	18.55003	0.80243	1.14833	0.00820	1.38890	0.02639	5.82648	2.61741	9.83239	154.75083
13	19.25378	0.83666	1.15460	0.00936	1.45618	0.02351	5.90538	0.96781	6.96060	49.84855
24	3.10147	0.90615	1.15198	0.00569	1.42856	0.01359	3.49954	0.73896	2.69899	0.96586
35	2.13309	0.95138	1.15192	0.00472	1.60697	0.02127	3.42388	0.64709	2.25291	0.71536
47	6.65040	0.96189	1.15678	0.00812	1.67057	0.01581	5.06490	0.68149	2.15096	0.48181
76	3.28487	0.99277	1.15239	0.00586	2.53933	0.03787	8.67511	0.76836	1.56376	0.15437
110	1.26726	0.98804	1.15227	0.00364	2.64616	0.04184	8.63363	0.49966	1.58127	0.12190
142	0.12374	0.99803	1.15187	0.00114	3.45350	0.04080	11.99933	0.55226	1.39007	0.04727
171	0.04780	0.99874	1.15184	0.00071	3.70625	0.02532	9.11130	0.26616	1.61916	0.04561
197	2.17799	0.99308	1.15280	0.00477	3.14208	0.04295	6.77454	0.26479	1.63751	0.05511
252	0.10877	0.99899	1.15185	0.00107	3.59741	0.01652	6.43670	0.11301	2.29247	0.07661

**Table G10.** Logistic fit function parameters of time-dependent increase of signal [e.d.] during reaction of indicator particles SR@Si 2 with different concentrations of acetaldehyde (8-252 ppm).

c(acet- aldehyde) / ppm	Chi Squ	R <sup>2</sup>	A1	σ(A1)	A2	σ(A2)	x0	σ(x0)	p	σ(p)
4	-	-	-	-	-	-	-	-	-	-
8	8.53885	0.40544	1.89862	7.15443	38.66584	2.56318	5.88426	9937.44813	24.14379	20.93250
13	6.35017	0.69061	3.35267	6.24830	56.40587	2.26620	6.10360	1.28330	4.12677	4.71763
24	1.12904	0.91848	2.26878	2.75294	62.36860	0.96971	7.01996	0.65971	3.73974	1.45855
35	1.46670	0.96068	1.83346	3.85074	94.98872	1.48453	4.29729	0.55696	1.69130	0.25417
47	0.60983	0.98523	2.83578	1.97891	101.68366	0.63592	7.01072	0.38282	2.10817	0.20078
76	0.11657	0.99868	0.27535	1.08806	148.23324	0.59823	6.02435	0.13981	1.27151	0.03368
110	0.10897	0.99836	0.38266	1.05451	150.16588	0.39832	4.89579	0.11428	1.31823	0.03286
142	0.17511	0.99810	-0.04524	1.33977	163.43222	0.90198	5.36070	0.17227	1.19395	0.04793
171	0.03925	0.99955	-0.10246	0.63417	162.84139	0.26945	4.10018	0.05998	1.38151	0.02351
197	0.01575	0.99980	0.13695	0.40050	159.57022	0.12741	3.77142	0.03278	1.41052	0.01233
252	0.25244	0.99719	-0.18117	1.60966	166.64602	0.63122	3.69262	0.14458	1.35430	0.06386

**Table G11.** Score data of principal component analysis.

Source Data			Scores Labels	Scores	
[B/R]	[B/G]	[e.D.]	Substance	Principal component 1	Principal component 2
0.09775	0.24739	38.91282	H 4.1	-0.76472	-0.29301
0.24033	0.54552	84.23639	H 13.7	0.13518	0.03975
0.39382	0.81224	111.84586	H 23	0.851	0.11702
0.43228	1.02962	119.92637	H 32.9	1.15831	0.13792
0.58833	1.3115	139.12199	H 43.8	1.80593	0.09564
0.61424	1.42131	133.94605	H 55	1.87884	-0.03024
0.71028	1.83427	155.34177	H 110	2.55798	0.0506
0.66742	1.60452	152.27268	H 150	2.28431	0.10629
0.70482	1.84919	152.29434	H 200	2.53081	0.01767
0.74979	2.01396	156.23591	H 250	2.76617	-0.02385
0.04861	-0.10637	16.38442	Propanone	-1.33772	-0.47736
0.08048	-0.04182	22.50085	Acetonitrile	-1.17818	-0.457
-0.51586	-0.50337	76.78997	Formic acid	-1.90542	1.37039
-0.00288	0.26942	25.40185	Butan-2-one	-1.03609	-0.3002
-0.00836	-0.03264	11.71158	Chloroform	-1.41435	-0.44701
0.04966	0.23549	31.49463	Acetic acid	-0.92132	-0.30732
0.05378	-0.10472	28.11643	Ethyl acetate	-1.21165	-0.3282
0.06316	0.04605	13.63834	Ethanol	-1.22503	-0.55442
0.03284	-0.03462	19.88465	Water	-1.27148	-0.40906
0.04942	-0.10112	11.24377	Methanol	-1.38364	-0.5487
-0.55433	-0.34623	86.02279	Ammonia	-1.75076	1.54808
-0.15175	0.45489	80.81607	Toluene	-0.56815	0.693

**Table G12.** Correlation matrix of principal component analysis.

	[B/R]	[B/G]	[e.D.]
[B/R]	1	0.92509	0.68822
[B/G]	0.92509	1	0.87339
[e.D.]	0.68822	0.87339	1

**Table G13.** Eigenvalues of principal component analysis.

	Eigenvalue	Percentage of Variance	Cumulative
1	2.66177	88.73%	88.73%
2	0.31449	10.48%	99.21%
3	0.02374	0.79%	100.00%

**Table G14.** Extracted Eigenvectors of principal component analysis.

	Coefficients of PC1	Coefficients of PC1
[B/R]	0.56813	-0.65509
[B/G]	0.60784	-0.07397
[e.D.]	0.55476	0.75192

**Figure G1.** Long-term stability of SR@Si 2 evaluated by [B/R]. Three different hexanal concentrations were measured (14 ppm, ■, black; 33 ppm, ●, red; 110 ppm, ▲, blue) over six months (mean  $\pm$  SDM; N = 5).

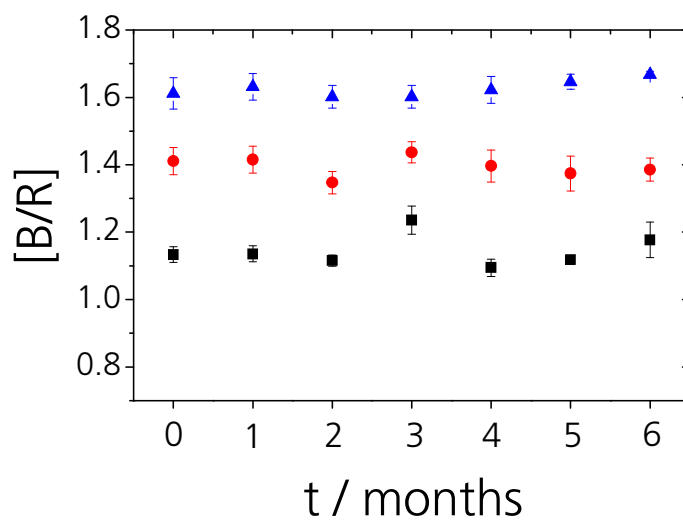


**Figure G1.** Long-term stability of SR@Si 2 evaluated by [e.d.]. Three different hexanal concentrations were measured (14 ppm, ■, black; 33 ppm, ●, red; 110 ppm, ▲, blue) over six months (mean  $\pm$  SDM; N = 5).

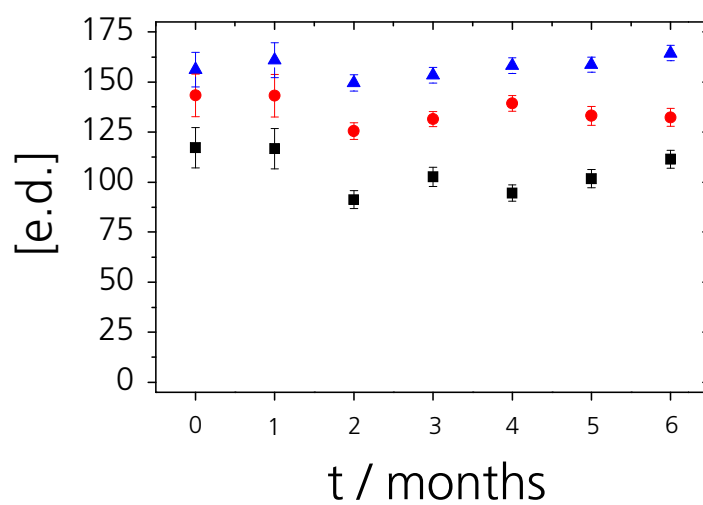


**Table G15.** Tabular values for Neumann's trend-test. <sup>1</sup>

<i>n</i>	0.1 %	1 %	5 %	<i>n</i>	0.1 %	1 %	5 %
4	0.5898	0.6256	0.7805	33	1.0055	1.2283	1.4434
5	0.4161	0.5379	0.8204	34	1.0180	1.2386	1.4511
6	0.3634	0.5615	0.8902	35	1.0300	1.2485	1.4585
7	0.3695	0.6140	0.9359	36	1.0416	1.2581	1.4656
8	0.4036	0.6628	0.9825	37	1.0529	1.2673	1.4726
9	0.4420	0.7088	1.0244	38	1.0639	1.2763	1.4793
10	0.4816	0.7518	1.0623	39	1.0746	1.2850	1.4858
11	0.5197	0.7915	1.0965	40	1.0850	1.2934	1.4921
12	0.5557	0.8280	1.1276	41	1.0950	1.3017	1.4982
13	0.5898	0.8618	1.1558	42	1.1048	1.3096	1.5041
14	0.6223	0.8931	1.1816	43	1.1142	1.3172	1.5098
15	0.6532	0.9221	1.2053	44	1.1233	1.3246	1.5154
16	0.6826	0.9491	1.2272	45	1.1320	1.3317	1.5206
17	0.7104	0.9743	1.2473	46	1.1404	1.3387	1.5257
18	0.7368	0.9979	1.2660	47	1.1484	1.3453	1.5305
19	0.7617	1.0199	1.2834	48	1.1561	1.3515	1.5351
20	0.7852	1.0406	1.2996	49	1.1635	1.3573	1.5395
21	0.8073	1.0601	1.3148	50	1.1705	1.3629	1.5437
22	0.8283	1.0785	1.3290	51	1.1774	1.3683	1.5477
23	0.8481	1.0958	1.3425	52	1.1843	1.3738	1.5518
24	0.8668	1.1122	1.3552	53	1.1910	1.3792	1.5557
25	0.8846	1.1278	1.3671	54	1.1976	1.3846	1.5596
26	0.9017	1.1426	1.3785	55	1.2041	1.3899	1.5634
27	0.9182	1.1567	1.3892	56	1.2104	1.3949	1.5670
28	0.9341	1.1702	1.3994	57	1.2166	1.3999	1.5707
29	0.9496	1.1830	1.4091	58	1.2227	1.4048	1.5743
30	0.9645	1.1951	1.4183	59	1.2288	1.4096	1.5779
31	0.9789	1.2067	1.4270	60	1.2349	1.4144	1.5814
32	0.9925	1.2177	1.4354	∞	2.0000	2.0000	2.0000

(1) Funk. W.; Dammann. V.; Donnevert. G. *Quality assurance in analytical chemistry*. 2nd edn.; Wiley-VCH: Weinheim. 2007.



**Figure G3.** Representative graphs for the determination of absorption coefficients of TPFPc in  $\text{CHCl}_3$ . Diverse dye concentrations were measured and plotted against the absorbance maximum at different wavelength (left: 407 nm; middle: 562 nm; right: 605 nm).

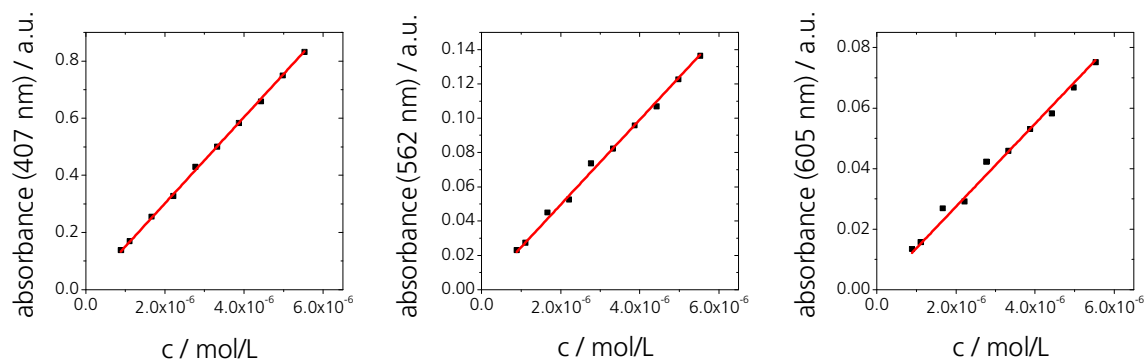


**Figure G4.** Representative graphs for the determination of absorption coefficients of TDCPC in  $\text{CHCl}_3$ . Diverse dye concentrations were measured and plotted against the absorbance maximum at different wavelength (left: 410 nm; middle: 566 nm; right: 605 nm).

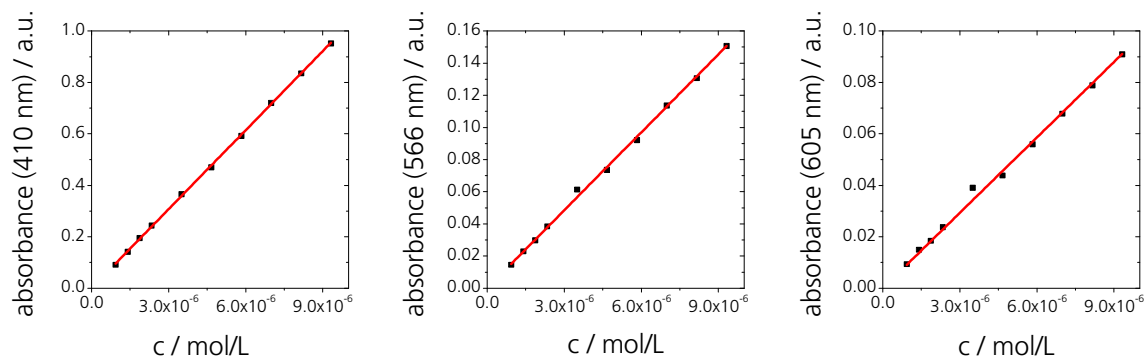


**Figure G5.** Representative graphs for the determination of absorption coefficients of CoTPFPc in  $\text{CHCl}_3$ . Diverse dye concentrations were measured and plotted against the absorbance maximum at different wavelength (left: 401 nm; right: 538 nm).

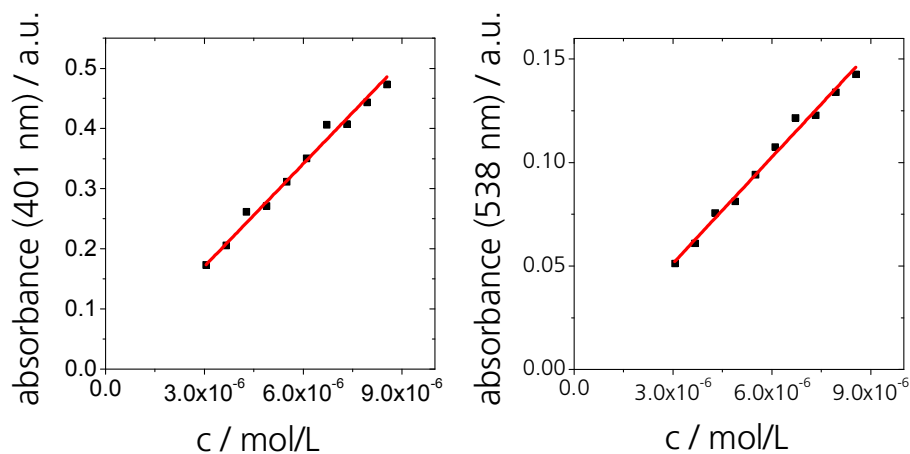


**Figure G6.** Representative graphs for the determination of absorption coefficients of CoTDCPC in  $\text{CHCl}_3$ . Diverse dye concentrations were measured and plotted against the absorbance maximum at different wavelength (left: 393 nm; right: 525 nm).

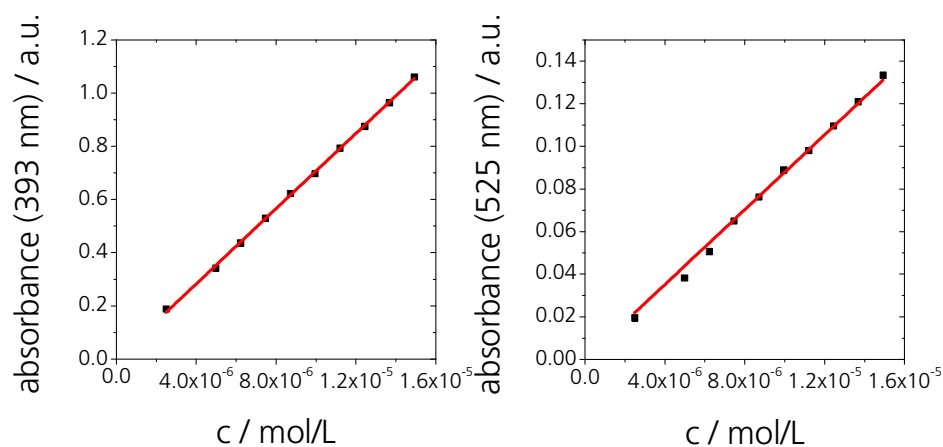


**Table G16.** Logistic fit function parameters of time-dependent signal [B/R] increase during reaction of bromothymol blue dyed polyamide fabric (BTB-PA) with different concentrations of ammonia (0-150 ppm).

$c(\text{NH}_3) / \text{ppm}$	Chi Squ	$R^2$	A1	$\sigma(\text{A1})$	A2	$\sigma(\text{A2})$	x0	$\sigma(\text{x0})$	p	$\sigma(\text{p})$
0	0.02454	0.99443	1.57724	0.11716	1.01279	0.01572	5.13737	2.07633	0.89958	0.15760
10	1.30812	0.92651	1.10779	0.03500	1.65165	0.01687	5.96293	0.66049	1.55235	0.25822
22	0.32836	0.99209	1.07256	0.01790	2.30272	0.01080	4.36822	0.14580	1.81826	0.15658
36	0.91944	0.98791	1.07142	0.02996	2.78580	0.01075	3.58386	0.41954	2.11962	0.28146
50	0.44803	0.99546	1.07304	0.02089	3.17986	0.01963	3.74584	0.18889	1.57348	0.10514
75	1.09833	0.99179	1.07484	0.03270	3.33288	0.02108	3.20219	0.18337	1.51741	0.10735
100	0.65867	0.99474	1.07939	0.02527	3.64416	0.03568	3.00265	0.20088	1.28346	0.08404
150	1.05824	0.99444	1.07591	0.02989	3.65758	0.03028	2.61673	0.15272	1.08989	0.06608

**Table G17.** Logistic fit function parameters of time-dependent signal [B/G] increase during reaction of bromothymol blue dyed polyamide fabric (BTB-PA) with different concentrations of ammonia (0-150 ppm).

c(NH <sub>3</sub> ) / ppm	Chi Squ	R <sup>2</sup>	A1	σ(A1)	A2	σ(A2)	x0	σ(x0)	p	σ(p)
0	0.10324	0.92184	1.80967	22.05698	0.59927	0.09099	0.03113	1.75096	0.44133	1.07313
10	0.47998	0.90285	0.65801	0.01223	0.82179	0.00445	6.48254	0.83586	1.81651	0.34241
22	0.15587	0.99102	0.64257	0.00723	1.10022	0.00318	4.13108	0.14458	1.98041	0.16123
36	0.22041	0.99389	0.64229	0.00860	1.32482	0.00190	3.53387	0.23227	2.67614	0.26147
50	0.16110	0.99705	0.64572	0.00732	1.40266	0.00637	4.43009	0.16489	1.37357	0.05454
75	0.83404	0.99042	0.64722	0.01659	1.54275	0.00304	3.97666	0.22661	1.68308	0.09055
100	0.32412	0.99601	0.65183	0.01029	1.69375	0.01494	4.04308	0.24533	1.20211	0.05906
150	0.92332	0.99520	0.67362	0.01625	1.76514	0.00773	3.77901	0.15148	1.30353	0.04832

**Table G18:** Logistic fit function parameters of time-dependent signal [B/R] increase during reaction of cresol red dyed polyamide fabric (CR-PA) with different concentrations of ammonia (0–150 ppm).

c(NH <sub>3</sub> ) / ppm	Chi Squ	R <sup>2</sup>	A1	σ(A1)	A2	σ(A2)	x0	σ(x0)	p	σ(p)
0	0.02047	0.91130	0.37677	0.04560	0.32771	0.01283	4.97496	11.04923	0.63507	0.68787
10	0.01714	0.96920	0.33654	0.00151	0.41841	0.03847	2.55173	9.66527	0.24196	0.17186
22	0.05407	0.96768	0.33671	0.00267	0.42289	0.00094	4.20447	0.25866	2.15996	0.28285
36	0.06904	0.96840	0.33663	0.00302	0.44118	0.00115	3.00515	0.31533	1.89887	0.31238
50	0.02472	0.99600	0.33639	0.00180	0.48034	0.00142	5.51100	0.17600	1.36646	0.06747
75	0.08157	0.98189	0.33665	0.00329	0.48044	0.00092	2.06980	0.14320	1.73945	0.18565
100	0.03615	0.99432	0.33559	0.00217	0.48608	0.00084	6.18807	0.16597	2.58078	0.15094
150	0.18526	0.98197	0.33728	0.00485	0.50830	0.00203	2.65716	0.21186	1.19826	0.09218

**Table G19.** Logistic fit function parameters of time-dependent signal [B/G] increase during reaction of cresol red dyed polyamide fabric (CR-PA) with different concentrations of ammonia (0-150 ppm).

c(NH <sub>3</sub> ) / ppm	Chi Squ	R <sup>2</sup>	A1	σ(A1)	A2	σ(A2)	x0	σ(x0)	p	σ(p)
0	0.02921	0.68151	0.50949	7.38765	0.37738	1.06749	0.01554	9.77101	0.14191	6.06305
10	0.10565	0.92723	0.41331	0.00368	0.49030	0.00316	5.70842	0.79356	1.34810	0.26709
22	0.04584	0.99461	0.40888	0.00252	0.61812	0.00147	6.32691	0.16634	2.17201	0.11512
36	0.05970	0.99138	0.40901	0.00289	0.61766	0.00164	3.60297	0.20469	2.36557	0.27086
50	0.02324	0.99900	0.40851	0.00177	0.75291	0.00208	8.92193	0.13985	1.56462	0.03497
75	0.02531	0.99890	0.40881	0.00188	0.83019	0.00175	2.42686	0.09386	1.76792	0.11607
100	0.14025	0.99664	0.40630	0.00439	0.86479	0.00313	9.18461	0.23798	1.87249	0.08049
150	0.06317	0.99891	0.40957	0.00289	0.92775	0.00288	4.02181	0.10784	1.42342	0.03770

**Table G20.** Logistic fit function parameters of time-dependent signal [R/G] increase during reaction of cresol red dyed polyamide fabric (CR-PA) with different concentrations of ammonia (0–150 ppm).

$c(\text{NH}_3) / \text{ppm}$	Chi Squ	$R^2$	A1	$\sigma(\text{A1})$	A2	$\sigma(\text{A2})$	x0	$\sigma(\text{x0})$	p	$\sigma(\text{p})$
0	0.02099	0.98982	1.17272	0.00541	1.22621	0.00131	6.62182	1.04346	1.19886	0.16083
10	0.44262	0.79353	1.20999	0.00338	1.26088	0.00305	14.21918	1.35444	5.56473	2.60957
22	0.09668	0.99696	1.21763	0.00216	1.43559	0.00120	8.91209	0.19798	3.01924	0.14089
36	0.01308	0.99904	1.22169	0.00085	1.44348	0.00118	6.42100	0.12248	2.03344	0.07200
50	0.23209	0.99752	1.21786	0.00330	1.57965	0.00434	12.02839	0.36016	1.99234	0.09901
75	0.00437	0.99978	1.22191	0.00049	1.69901	0.00179	3.95700	0.08138	1.64151	0.04916
100	0.05619	0.99934	1.22101	0.00173	1.76409	0.00249	8.94512	0.12411	2.55204	0.06228
150	0.08739	0.99897	1.21783	0.00206	1.79396	0.00396	5.56616	0.14421	1.72249	0.04932

**Table G21** Logistic fit function parameters of time-dependent signal [G/R] increase during reaction of cresol red dyed polyamide fabric (MR-PA) with different concentrations of ammonia (0–150 ppm).

c(NH <sub>3</sub> ) / ppm	Chi Squ	R <sup>2</sup>	A1	σ(A1)	A2	σ(A2)	x0	σ(x0)	p	σ(p)
0	0.00463	0.99240	0.74161	0.00122	0.71148	0.00147	20.28850	1.07562	1.39476	0.16289
10	0.02443	0.94938	0.71778	0.00072	0.73490	0.00027	10.17510	0.46493	4.90353	0.90225
22	0.02189	0.99252	0.71747	0.00124	0.80547	0.00045	5.20286	0.14969	3.00343	0.21814
36	0.03044	0.99541	0.71930	0.00135	0.81148	0.00041	6.87648	0.14829	2.39302	0.08952
50	0.01310	0.99768	0.71622	0.00094	0.82427	0.00049	5.29837	0.11660	1.59181	0.04751
75	0.00619	0.99907	0.71729	0.00065	0.84221	0.00020	3.78281	0.04922	2.40133	0.05339
100	0.03744	0.99879	0.71980	0.00150	0.86430	0.00059	3.60551	0.07850	1.10670	0.02255
150	0.00671	0.99935	0.71673	0.00065	0.86209	0.00040	5.31467	0.06184	1.57938	0.02738



**Table G22.** Parameters of BTB-PA reacting with EA, DEA, TEA, ammonia, DMA, and TMA for data evaluation by [B/R] and [B/G]. Absolute signal changes are depicted for maximum response and for signal change of reverse reaction (difference of maximum signal with signal after three days). Completion of reverse reaction is additionally given in percentage. The last column depicts the response time  $t_{80}$  towards the respective amines (mean  $\pm$  SDM; N = 3).

	Method of data evaluation	$\Delta$ Signal (response)	$\Delta$ Signal (reverse reaction)	$\Delta$ Signal (reverse reaction) / %	Response time $t_{80}$ / min
EA	[B/R]	$2.75 \pm 0.07$	$0.4 \pm 0.1$	15	14
	[B/G]	$1.65 \pm 0.03$	$0.32 \pm 0.05$	19	19
DEA	[B/R]	$2.41 \pm 0.06$	$0.21 \pm 0.07$	9	21
	[B/G]	$1.80 \pm 0.04$	$0.28 \pm 0.04$	16	34
TEA	[B/R]	$1.6 \pm 0.2$	$0.4 \pm 0.4$	25	186
	[B/G]	$0.7 \pm 0.1$	$0.2 \pm 0.2$	29	284
Ammonia	[B/R]	$2.21 \pm 0.09$	$2.21 \pm 0.09$	100	3
	[B/G]	$1.22 \pm 0.03$	$1.14 \pm 0.04$	93	4
DMA	[B/R]	$1.96 \pm 0.08$	$1.0 \pm 0.1$	51	5
	[B/G]	$1.47 \pm 0.02$	$0.94 \pm 0.03$	64	5
TMA	[B/R]	$2.36 \pm 0.08$	$1.4 \pm 0.1$	59	40
	[B/G]	$1.15 \pm 0.01$	$0.83 \pm 0.02$	72	40

**Table G23.** Parameters of CR-PA reacting with EA, DEA, TEA, ammonia, DMA, and TMA for data evaluating by [B/R], [B/G], and [R/G]. Absolute signal changes are depicted for maximum response and for signal change of reverse reaction (difference of maximum signal and signal after three days). Completion of reverse reaction is additionally given in percentage. Last column depicts the response time  $t_{80}$  towards the respective amines (mean  $\pm$  SDM; N = 3).

	Method of data evaluation	$\Delta$ Signal (response)	$\Delta$ Signal (reverse reaction)	$\Delta$ Signal (reverse reaction) / %	Response time $t_{80}$ / min
EA	[B/R]	$0.68 \pm 0.01$	$0.49 \pm 0.01$	72	13
	[B/G]	$2.66 \pm 0.6$	$2.12 \pm 0.06$	80	22
	[R/G]	$1.90 \pm 0.08$	$1.36 \pm 0.05$	72	16
DEA	[B/R]	$0.64 \pm 0.02$	$0.40 \pm 0.02$	63	29
	[B/G]	$2.46 \pm 0.03$	$1.75 \pm 0.02$	71	26
	[R/G]	$1.74 \pm 0.05$	$1.02 \pm 0.08$	59	22
TEA	[B/R]	$0.28 \pm 0.01$	$0.15 \pm 0.01$	54	163
	[B/G]	$0.79 \pm 0.04$	$0.59 \pm 0.04$	75	214
	[R/G]	$0.64 \pm 0.07$	$0.56 \pm 0.08$	89	230
Ammonia	[B/R]	$0.28 \pm 0.02$	$0.27 \pm 0.02$	96	4
	[B/G]	$0.96 \pm 0.03$	$0.95 \pm 0.02$	99	5
	[R/G]	$1.04 \pm 0.03$	$1.08 \pm 0.04$	104	7
DMA	[B/R]	$0.60 \pm 0.01$	$0.50 \pm 0.01$	83	6
	[B/G]	$2.23 \pm 0.05$	$2.09 \pm 0.05$	94	6
	[R/G]	$1.47 \pm 0.08$	$1.47 \pm 0.08$	97	6
TMA	[B/R]	$0.16 \pm 0.02$	$0.15 \pm 0.02$	94	42
	[B/G]	$0.57 \pm 0.02$	$0.57 \pm 0.01$	100	69
	[R/G]	$0.59 \pm 0.02$	$0.61 \pm 0.02$	103	46

**Figure G7.** Time-dependent response curves of BTB-PA sensor fabric during reaction with different concentrations of ethylamine (0 - 50 ppm). Control was performed with distilled water (mean  $\pm$  SDM; N = 5).

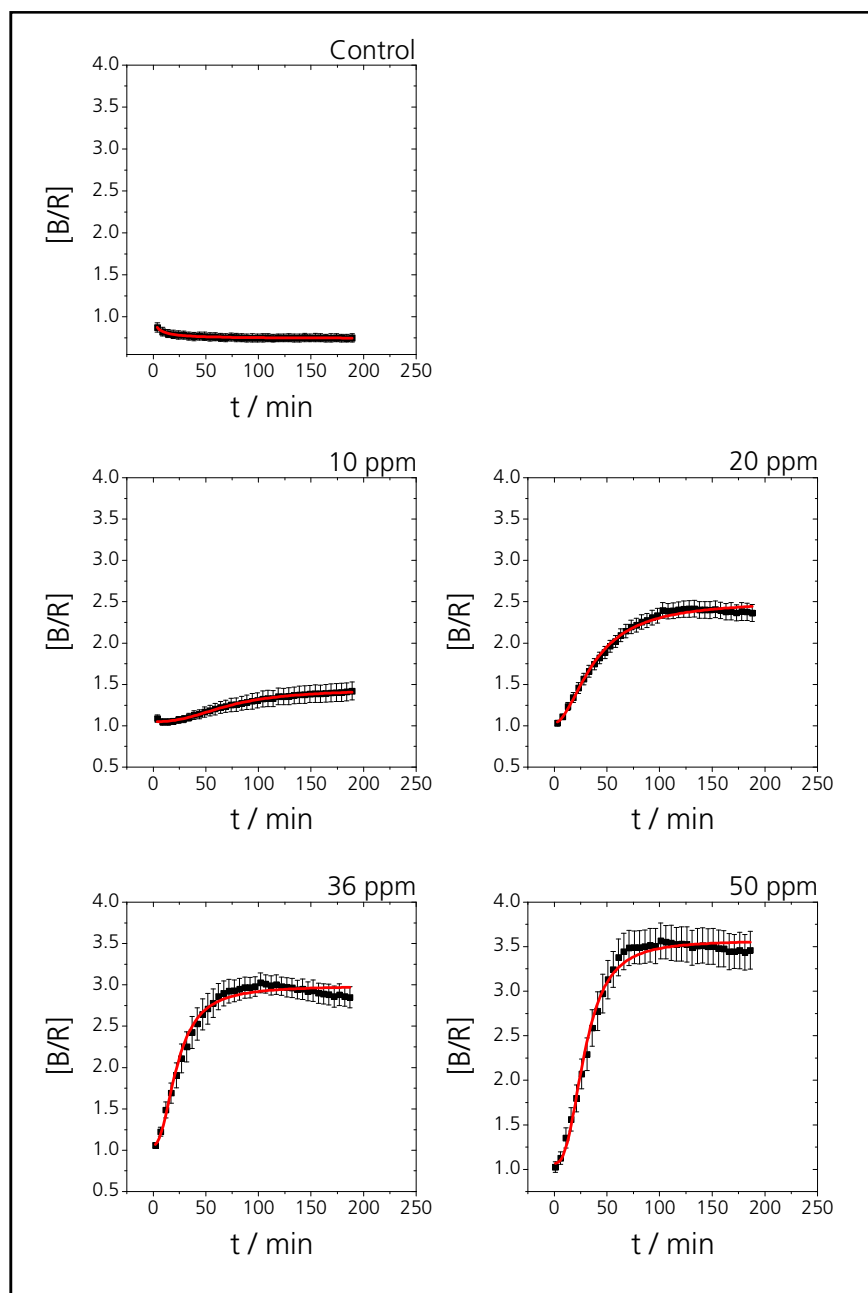


**Figure G8.** Time-dependent response curves of BTB-PA sensor fabric during reaction with different concentrations of diethylamine (20 - 66 ppm). Control with distilled water is shown in Figure G7 (mean  $\pm$  SDM; N = 5).

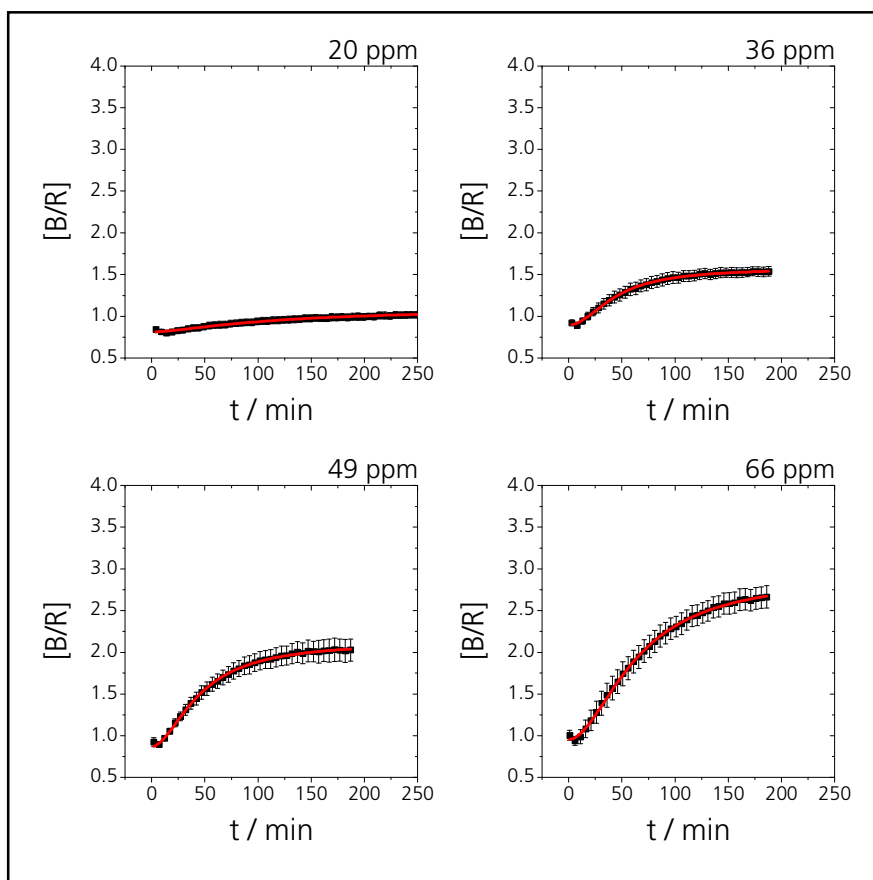


**Figure G9.** Time-dependent response curves of BTB-PA sensor fabric during reaction with different concentrations of triethylamine (36 - 82 ppm). Control with distilled water is shown in Figure G7 (mean  $\pm$  SDM; N = 5).

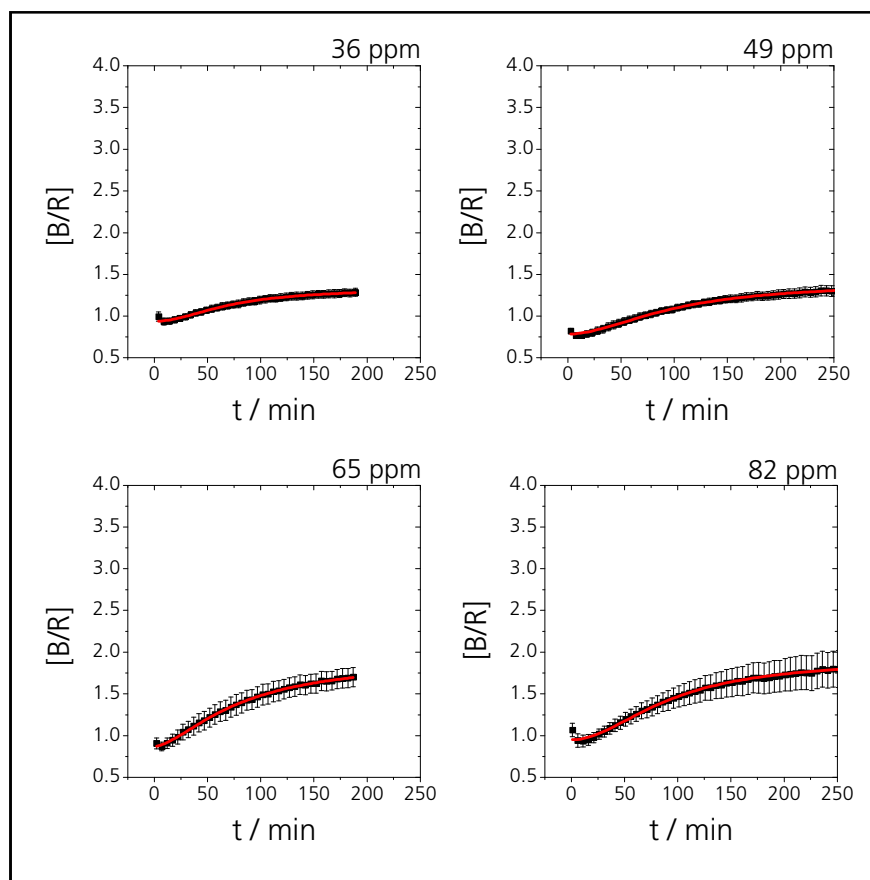


**Table G24.** Logistic fit function parameters of time-dependent signal [B/R] increase during reaction of bromothymol blue dyed polyamide fabric (BTB-PA) with different concentrations of ethylamine (0-50 ppm).

c(EA) / ppm	Chi Squ	R <sup>2</sup>	A1	σ(A1)	A2	σ(A2)	x0	σ(x0)	p	σ(p)
0	0.00514	0.97909	0.98970	0.07422	0.73906	0.00353	4.57632	2.69933	0.95136	0.16913
10	0.03170	0.99093	1.05009	0.00440	1.43996	0.01526	72.54287	3.03900	2.44167	0.18547
20	0.18690	0.99686	1.03316	0.01354	2.51643	0.02350	38.34469	0.96666	1.86936	0.08957
36	0.30620	0.99599	1.06060	0.01729	2.98842	0.02089	22.84317	0.85794	2.23423	0.15115
50	0.19640	0.99613	1.06802	0.02093	3.56948	0.02526	28.98228	0.69718	2.66361	0.15001

**Table G25.** Logistic fit function parameters of time-dependent signal [B/R] increase during reaction of bromothymol blue dyed polyamide fabric (BTB-PA) with different concentrations of diethylamine (0-66 ppm).

c(DEA) / ppm	Chi Squ	R <sup>2</sup>	A1	σ(A1)	A2	σ(A2)	x0	σ(x0)	p	σ(p)
0	0.00514	0.97909	0.98970	0.07422	0.73906	0.00353	4.57632	2.69933	0.95136	0.16913
20	0.05951	0.98482	0.81131	0.00497	1.08969	0.01652	115.73458	9.59623	1.48606	0.14592
36	0.04086	0.99782	0.89718	0.00595	1.57762	0.00830	44.42330	0.93149	1.96679	0.07963
49	0.05061	0.99870	0.86906	0.00744	2.13211	0.01794	45.55612	0.92870	1.80626	0.05579
66	0.05419	0.99845	0.95330	0.00983	2.91034	0.03765	63.95121	1.62421	1.85570	0.07200

**Table G26.** Logistic fit function parameters of time-dependent signal [B/R] increase during reaction of bromothymol blue dyed polyamide fabric (BTB-PA) with different concentrations of triethylamine (0-82 ppm).

c(TEA) / ppm	Chi Squ	R <sup>2</sup>	A1	σ(A1)	A2	σ(A2)	x0	σ(x0)	p	σ(p)
0	0.00514	0.97909	0.98970	0.07422	0.73906	0.00353	4.57632	2.69933	0.95136	0.16913
36	0.04368	0.99379	0.93784	0.00650	1.33001	0.01379	71.30999	2.76608	1.95462	0.14218
49	0.08621	0.99440	0.78444	0.00506	1.39932	0.01438	100.01653	2.85457	1.87760	0.08815
65	0.01769	0.99805	0.87132	0.00641	1.90919	0.03386	80.40806	3.58655	1.60456	0.07358
82	0.04524	0.99241	0.95003	0.00870	1.91649	0.02035	92.73707	2.64440	1.93289	0.09049



## H Curriculum vitae

### Julia Linhardt (née Sporer)

---

University of Regensburg

Institute of Analytical Chemistry, Chemo- and Biosensors

E-Mail: Julia.Sporer@chemie.uni-regensburg.de

#### Personal Data

---

Date and place of birth: September 03 1987, Bad Koetzting

Nationality: German

#### Education

---

01/2013 - 12/2015 **PhD thesis** at the Fraunhofer EMFT under supervision of Prof. Dr. Joachim Wegener, Institute of Analytical Chemistry, Chemo- and Biosensors, University of Regensburg:

*"Colorimetric detection of selected gases for work and food safety applications"*

10/2010 - 09/2012 **Master of Science** (M.Sc.) in Chemistry (1.3)

Master thesis at the Fraunhofer EMFT under supervision of Prof. Dr. Burkard König, Institute for Organic Chemistry, University of Regensburg:

*"Synthesis of indicator dyes and development of new sensor systems for carbon monoxide sensing"*

09/2010	<p><b>Bachelor of Science</b> (B.Sc.) in Chemistry (2.0)</p> <p>Bachelor thesis under supervision of Prof. Dr. Oliver Reiser, Institute for Organic Chemistry, University of Regensburg:</p> <p><i>“Organische Reaktionen mit auf C/Co-Nanopartikeln immobilisierten Katalysatoren”</i></p>
06/2007	<p><b>University Entrance Diploma</b> at the Willibald-Gluck-Gymnasium Neumarkt i. d. Opf., Germany (1.7)</p>

### Professional Experience

---

01/2013 - 09/2013	Research assistant, Institute of Analytical Chemistry, Chemo- and Biosensors, University of Regensburg, Germany
10/2012 - 12/2012	Industrial placement at Bionorica SE, Neumarkt i. d. Opf.: <i>“Quality control and analysis of active pharmaceutical ingredients of plants and plant extracts”</i>
05/2011 - 10/2012	Research assistant, Fraunhofer EMFT, work group Sensor Materials, Regensburg, Germany

### Advanced Education

---

07/2015 – 08/2015	<b>Quality Assurance</b> in Analytical Chemistry
07/2015	TechnoLogisch – Module <b>Semiconductor Technologies</b>
09/2014 - 12/2014	<b>Business Studies</b> for Developer
09/2014	Softskills: Convincing and Effective <b>Communication</b>

### Patent and Publication

---

- J. Linhardt, B. Gruber, S. Trupp, J. Wegener, *Colorimetric Detection of Volatile Aldehydes: A Sensor Concept for Food Quality Control*, Analytical Chemistry, manuscript submitted.
- J. Sporer, M. Stich, S. Trupp, DE102013218997 A1, *Sensorelement zur Kohlenmonoxid-Detektion*, 03 / 2015.

**Scientific Presentations**

---

- J. Sporer, M. Stich, S. Trupp, J. Wegener, *Entwicklung eines optischen Sensors für Kohlenstoffmonoxid*, Doktorandenseminar der GDCh und DECHEMA, Arbeitskreis Prozessanalytik, 02 / **2015**, Oral.
- J. Sporer, S. Trupp, *Sensormaterialien und Sensorsysteme*, Seminar zur Entwicklung neuer Arbeitsschutztechniken, Institut für Arbeitsschutz der DGUV, St. Augustin, 10 / **2014**, Oral.
- J. Sporer, M. Stich, S. Trupp, J. Wegener, *Corroles as Indicator Dyes for Optical Carbon Monoxide Sensing*, XII Conference on Optical Chemical Sensors & Biosensors, Athens (Greece), 04 / **2014**, Poster.
- J. Sporer, M. Stich, S. Trupp, *A Novel Fluorescent Sensor for Amine Sensing*, 13th Conference on Methods and Applications of Fluorescence, Genoa (Italy), 09 / **2013**, Poster.
- J. Sporer, M. Stich, S. Trupp, *Development of Novel Optical Probes and Sensor Systems for Volatile Amines*, GDCh Wissenschaftsforum, Darmstadt (Germany), 09 / **2013**, Poster.
- J. Sporer, M. Stich, S. Trupp, *Corroles as Indicator Dyes for Optical Sensing of Volatile Amines*, 18th European Symposium on Organic Chemistry, Marseille (France), 07 / **2013**, Poster.



## I Acknowledgements

Ich bedanke mich hiermit ganz herzlich bei Prof. Dr. Joachim Wegener für seine Unterstützung in jeder Situation und für die wissenschaftlichen Diskussionen und Ideen hinsichtlich meiner Arbeit - **DANKE Joe!**

Bei den Mitarbeitern der EMFT, vor allem bei Herrn Prof. Dr. Christoph Kutter, bedanke ich mich, dass ich meine Doktorarbeit bei Fraunhofer anfertigen durfte und für die Begutachtung meiner Arbeit.

Des weiteren gilt mein Dank dem gesamten Prüfungskomitee.

Allen Mitarbeiterinnen und wenigen Mitarbeitern ;) der „wegeners“: DANKE! Die Stimmung bei euch war immer top. Und danke für diverse Grillabende, Stammtische und sonstige Aktivitäten.

Ein herzliches Dankeschön nach Freising an Dr. Klaus Rieblinger und Kateryna Krisanova für ihre unkomplizierte und erfolgreiche Zusammenarbeit im Rahmen des Projektes Hexanal-Detektion.

Meinen Bachelor-Studenten und Forschungspraktikanten Lisa-Marie Wiesholler, Anton Kröner, Lisa Stadler und Christina Liedlbier möchte ich ganz herzlich für die engagierte und sorgfältige Arbeit danken und für den Spaß den wir zusammen hatten.

Danke an Dr. Thomas Hirsch und Dr. Alexander Zöpfl dafür, dass ich Messungen an ihrer Gasmischanlage durchführen konnte. Danke Alex für das kreative Zusammenbasteln sämtlicher Schläuche.

An alle Mädels des 4. Stocks: ihr seid SUPERGEIL!

TAUSEND DANK an Dr. Matthias Stich, Dr. Benjamin Gruber und Dr. Roland Linhardt für das gewissenhafte und zügige Korrekturlesen meiner Arbeit - ihr seid die Allerbesten!

Spezieller Dank geht auch an meine Freunde und Kollegen Christian („Götzi“) Götz, Romy (unser Mädchen) Freund und nochmal an Dr. Benjamin (Benno) Gruber. Danke dass ihr immer da wart, für die stundenlangen Diskussionen und den Spaß den wir zusammen hatten!

Ganz besonderen und sicherlich den **größten Dank** schulde ich jedoch meiner Familie, besonders meinen Eltern sowie meinem Mann Roland. ohne eure anhaltende Unterstützung wäre weder mein Studium möglich gewesen, noch würde irgendjemand diese Arbeit in Händen halten können.

## Eidesstattliche Erklärung

Ich erkläre hiermit an Eides statt, dass ich die vorliegende Arbeit ohne unzulässige Hilfe Dritter und ohne Benutzung anderer als der angegebenen Hilfsmittel angefertigt habe; die aus anderen Quellen direkt oder indirekt übernommenen Daten und Konzepte sind unter Angabe des Literaturzitats gekennzeichnet.

Weitere Personen waren an der inhaltlich-materiellen Herstellung der vorliegenden Arbeit nicht beteiligt. Insbesondere habe ich hierfür nicht die entgeltliche Hilfe eines Promotionsberaters oder anderer Personen in Anspruch genommen. Niemand hat von mir weder unmittelbar noch mittelbar geldwerte Leistungen für Arbeiten erhalten, die im Zusammenhang mit dem Inhalt der vorgelegten Dissertation stehen.

Die Arbeit wurde bisher weder im In- noch im Ausland in gleicher oder ähnlicher Form einer anderen Prüfungsbehörde vorgelegt.

---

Ort, Datum

Unterschrift